THE UNIVERSITY OF ADELAIDE

Department of Mechanical Engineering

A STUDY OF MODAL SOUND RADIATION

by

C.H. Hansen, B.E. (Hons.)

Thesis for the Degree of Doctor of Philosophy

April 1979

Awarded April 1980

SUMMARY

The work described in this thesis is concerned with the development and verification of techniques useful for the investigation of modal sound radiation from vibrating surfaces.

For the purpose of developing and verifying techniques it has been useful to consider in detail the radiation properties of a simple model capable of exact mathematical description. For the latter purpose the clamped edge circular flat plate mounted in an infinite baffle and vibrating in one of its low order modes has been chosen for study, as it is a model that can be both simulated and mathematically described.

The general applicability of the techniques developed is demonstrated for three models which are not readily described by mathematical analysis. The models used for the latter demonstration are the clamped edge circular flat plate mounted on the end of a long tube, the same plate mounted in an infinite baffle but vibrating in a non-classical mode and the side walls of several in-line internal combustion engine blocks.

The modal responses of flat circular plates with both clamped and simply supported edge conditions are calculated using both Classical and Mindlin-Timoshenko plate theories. Numerical results for the modal resonant frequencies, mode shapes and mean square surface velocities are calculated using each theory and presented for the first seven plate modes.

The results obtained for the plate response are used to calculate the corresponding sound radiation efficiencies for each mode, where the

radiation efficiency is defined as a complex quantity with both real and imaginary parts, and may be considered as a normalised form of the surface radiation impedance. The acoustic field adjacent to the vibrating plate is described in terms of oblate spheroidal coordinates. Use of these coordinates allows matching of the acoustic velocity in the fluid adjacent to the plate with the normal plate surface velocity, enabling both real and imaginary parts of the radiation efficiency to be calculated. The predictions obtained in this way for the real part of the radiation efficiency are compared with numerical results obtained by solving the Rayleigh Integral in the acoustic far field. Excellent agreement is demonstrated.

Measurements of the real part of the circular plate modal radiation efficiencies are made using time averaged holography to determine the mean square plate surface velocity. A reverberant room is used for the direct measurement of the radiated sound power. A range of plates differing in size and thickness and vibrating in each of their six lowest order vibration modes are tested. Reasons for discrepancies between experimentally measured and theoretically predicted radiation efficiencies are suggested.

In the second part of the thesis the suitability of a reverberant room (containing a rotating diffuser) for the pure tone sound power measurements mentioned earlier is investigated. In particular the average radiation impedance presented to a number of pure tone sound sources is experimentally determined and compared with free field predictions and measurements.

The sound sources considered initially are the mouths of two impedance tubes of different diameters and a conical horn whose throat is attached to the mouth of the smaller impedance tube. The impedance

presented to the tube mouth is determined as a function of frequency and diffuser angular position and speed by sampling the sound field in the impedance tube at a suitable rate and over a suitable period of time. The impedance averaged over one complete diffuser revolution is then calculated as a function of diffuser speed and frequency and compared with the free field predictions.

Finally, several different size simply supported square plates, each vibrating in their fundamental resonant mode are used as sound sources. Both the real and imaginary parts of the radiation efficiency are measured for each plate as a function of diffuser angular position. The measurement procedure uses a time averaged hologram to store information about the velocity amplitude distribution over the vibrating surface, which may be related to a single acceleration measurement on the surface. A near field microphone scan of the vibrating surface allows determination of the amplitude and phase distribution of the acoustic pressure in the fluid adjacent to the surface, which again is related to the single acceleration measurement. A computer program is used to combine the velocity and pressure information to give the real and imaginary parts of the radiation efficiency.

Values of the measured radiation efficiency averaged over the plate surface are averaged over one complete diffuser revolution and compared with free field predictions and similar measurements in an anechoic room.

It is demonstrated that the rotating diffuser does have a significant effect on the sound power radiated by a pure tone sound source in a reverberant room and that the radiation impedances presented to the pure tone test sources, when averaged over one complete diffuser revolution, are close to the free field values.

TABLE OF CONTENTS

STATEMENT OF ORIGINALITY

This thesis contains no material which has been accepted for the award of any other degree or diploma in any University. To the best of the author's knowledge and belief, this thesis contains no material previously published or written by another person, except where due reference is made in the text.

C.H. Hansen

April, 1979

ACKNOWLEDGEMENTS

I wish to express my sincere thanks and gratitude to my supervisor Dr. D.A. Bies for his constant encouragement and stimulating help throughout the duration of the research and for the many hours he spent giving critical advice with this thesis. His assistance was always readily forthcoming and in the form of helpful criticism and suggestion.

I am very grateful to many members of both the Mechanical and Electronics Workshop staff for their much needed assistance in the assembly of the equipment used for the experimental work. In particular I wish to thank the following people: Messrs. P. Walker and A. Davis for their patient guidance during the construction of the electronics necessary for controlling the microphone scanner. Mr. P. Hull for his care and effort in the construction of the microphone scanner; Mr. G. Osborne for his untiring efforts in keeping the laser in operation and his assistance in the construction of some of the experimental equipment; and Mr. I. Modistach whose outstanding cooperation and enthusiasm in his work on the microphone scanner, peak detector circuit, filters and repair of faulty equipment was very much appreciated. During the course of the experimental work, Mr. D. Morrison was a constant and willing source of help in the design and construction of the equipment, and for this I wish to express my thanks and gratitude.

I also wish to thank my aunt, Mrs. J. Woodroffe who spent many tedious hours using a planimeter to analyse holograms in the initial stages; my mother for financial assistance for the production of the thesis and my wife for her continuous patience and encouragement.

I am indebted to the Heads of the Mechanical Engineering Department, Professor H.H. Davis initially, and Professor R.E. Luxton finally, for providing both the opportunity to conduct the research described in this thesis and the support so necessary for its successful completion.

Finally, I acknowledge the generous financial assistance of the Australian Research Grants Committee, without which much of the experimental work would not have been possible.

SYMBOLS

a	Plate radius
$\bar{a}$	Mean length defined in Table 5.1b
$\hat{a}$	Acceleration amplitude (m/s^2)
a_1	Length of one side of a rectangular surface (m)
a_2	Length of other side of a rectangular surface (m)
A	Surface area of vibrating plate or area of sound source in reverberant room (m^2)
A_g	r.m.s. acceleration amplitude in terms of "g", acceleration due to gravity (dimensionless)
A_{mn}	Sum of all of the coefficients A_{mnj}, $j = 1 \rightarrow \infty$
A_{mnj}	Coefficient corresponding to the plate vibrating in mode mj and defined by equation (2.85)
B	Constant of equation (7.1) dependent on amplitude of sound field within tube
B_1	Constant defined by Equation (2.54)
B_2	Constant defined by Equation (2.55)
c_o	Speed of sound in air (m/s)
c_s	Shear wave speed in clamped plate (m/s) = $(G/\rho)^{\frac{1}{2}}$
c_L	Longitudinal wave speed in plate (m/s) = $[E/\rho(1-\nu^2)]^{\frac{1}{2}}$
C_{2x}^{mn}	Coefficient defined by equation (2.78) and Flammer (1957
d_N	Distance from impedance tube mouth to nearest sound pressure level minimum in the tube (m)
$d_r^{mn}(-ic)$	Oblate spheroidal coefficient defined by Flammer (1957)
D	Constant dependent on amplitude of plate vibration
D_m	Distance from impedance tube mouth to nearest sound pressure level maximum in the tube (m)
D_{mj}	Constant of Equation (2.3), (2.11) dependent on amplitude of plate vibration
D_1, D_2, D_3	Constants dependent on amplitude of plate vibration
e_{mnj}	Coefficient defined by equations (2.80) to (2.82)
E	Young's modulus of elasticity (N/m^2)

$E_{mx}(\alpha)$	Function defined by equation (2.83)
f	Frequency of plate vibration (Hz)
f_c	Schroeder large room frequency limit defined by equation (6.1) (Hz)
f_{mj}	Frequency of plate vibrating in resonant mode mj (Hz)
$F_m(x)$	Bessel Function of the first kind if equation (2.38) is satisfied and modified Bessel Function of the first kind if equation (2.39) is satisfied
F_{mj}	Coefficient defined by equation (A1.16) or equation (A1.
g	Acceleration due to gravity (m/s^2)
g_{mj}	Function defined by equation (2.49) or (2.50)
G	Modulus of rigidity (N/m^2)
$G_{mx}(\alpha)$	Function defined by equation (2.84)
h	Plate thickness (m)
$H_{mj}(u)$	Function defined by equation (2.4)
$H_{tmj}(u)$	Function defined by equation (2.42)
I_i	Reactive acoustic intensity
$I_m(x)$	Modified Bessel Function of the first kind of order m and argument x
I_o	Light intensity of a vibration node on a reconstructed image from a hologram of a vibrating surface
I_R	Resistive acoustic intensity
I_v	Light intensity at a point on an image reconstructed from a hologram
j	Number of circular nodes for a given mode of plate vibration
$J_m(x)$	Bessel Function of the first kind of order m and argument x
k	Acoustic wavenumber in air ($= 2\pi/\lambda$)
k_b	Plate bending wavenumber
k_T	Constant defined by equation (2.33)
K	Constant defined by equation (2.34)
ℓ	Distance from horn apex to a point on a horn sectional plane (m)

ℓ_w	Wavenumber ratio defined by equation (2.98)
L_{max}	Maximum sound pressure level in impedance tube (dB re $2 \times 10^{-5} N/m^2$)
L_{min}	Minimum sound pressure level in impedance tube (dB re $2 \times 10^{-5} N/m^2$)
L_p	Sound pressure level (dB re $2 \times 10^{-5} N/m^2$)
L_w	Sound power level (dB re 10^{-12} watts)
$\bar{L}$	Distance from observer to sound source (m)
m	Number of diametral nodes for a given mode of circular plate vibration, or number of nodal lines in x direction for a resonantly vibrating rectangular plate
n	Index used in summations or number of nodal lines in y direction for a resonantly vibrating rectangular plate
N_{mn}	Coefficient defined by equation (2.74)
p	Acoustic pressure (N/m^2)
p(x)	Acoustic pressure amplitude at a point x in the impedance tube (N/m^2)
$\hat{p}$	Acoustic pressure amplitude (N/m^2)
p_{mj}	Acoustic pressure generated in the acoustic medium by the plate vibrating in mode mj (N/m^2)
$\hat{p}_{mj}$	Acoustic pressure amplitude generated in the acoustic medium by the plate vibrating in mode m,j (N/m^2)
p_{max}	Maximum r.m.s. acoustic pressure measured in the impedance tube (N/m^2)
p_{min}	Minimum r.m.s. acoustic pressure measured in the impedance tube (N/m^2)
p_1	r.m.s. acoustic pressure of outgoing wave in impedance tube (N/m^2)
p_2	r.m.s. acoustic pressure of reflected wave (N/m^2)
P	Barometric pressure (mm of Hg)
P_{mj}	Function defined by equation (2.15)
Q_{mj}	Coefficient defined by equations (2.97)
r_o	Radial polar coordinate (for plate or horn mouth)
r'	Defined in Fig. A1.1

R	Spherical radial coordinate in plate analysis or resistive radiation impedance (MT^{-1})
$R_{mn}(-ika,i\xi)$	Oblate spheroidal radial function
$R_{mn}^{(\ell)}(-ika,i\xi)$	Oblate spheroidal radial function of the ℓ^{th} kind
S	Total surface area of reverberant room boundaries (m^2)
$S_{mn}(-ika,\eta)$	Oblate spheroidal angular function
$S_{mn}^{(\ell)}(-ika,\eta)$	Oblate spheroidal angular function of the ℓ^{th} kind
t	Time (seconds)
T	Temperature (°C)
T_{60}	60dB decay time (secs)
u	Dimensionless radial polar coordinate in plate analysis ($=r_o/a$)
v	Acoustic particle velocity (m/s)
$\hat{v}$	Acoustic particle velocity amplitude (m/s)
v_{mj}	Acoustic particle velocity corresponding to the plate vibrating in mode mj (m/s)
$\hat{v}_{mj}$	Acoustic particle velocity amplitude corresponding to the plate vibrating in mode mj (m/s)
$\hat{v}_{ref}$	Velocity amplitude at the location of the reference accelerometer, (m/s)
$\hat{v}_A$	Antinodal plate velocity amplitude (m/s)
$\hat{v}(r_o,\theta)$	Acoustic velocity amplitude at point (r_o,θ) on vibrating plate (m/s)
$\langle v^2 \rangle_{st}$	Mean square velocity averaged in time and space (m^2/s^2)
$\langle v_{mj}^2 \rangle_{st}$	Mean square plate surface velocity averaged over the plate surface and in time for plate vibration mode mj (m^2/s^2)
V	Volume of reverberant room (m^3)
$V_{\xi mj}$	Dimensionless acoustic velocity generated by the plate vibrating in mode m,j on a given surface defined by ξ = constant
w	Coefficient defined by equation (2.29)
W	Radiated acoustic power (watts)

W_i	Reactive acoustic power
W_R	Resistive acoustic power
W_{mj}	Acoustic power radiated by the plate vibrating in mode mj (watts)
x	Cartesian coordinate or distance from mouth of impedance tube to plane of measurement (m)
X	Reactive radiation impedance
$X(u,\theta)$	Plate displacement function defined by equation (2.37) (m)
y	Plate displacement function (m)
$\hat{y}$	Plate displacement amplitude (m)
$\hat{y}_A$	Displacement amplitude at antinode of plate vibration (m)
$\langle\hat{y}^2\rangle_s$	Mean square plate displacement amplitude averaged over the plate surface (m^2)
Y	Dimensionless plate displacement amplitude
$Y(u,\theta,t)$	Dimensionless plate displacement function
$Y_{mj}(u,\theta)$	Dimensionless plate displacement amplitude function for mode mj
$Y_1(u,\theta)$	Plate displacement amplitude function defined by equation (2.35)
$Y_2(u,\theta)$	Plate displacement amplitude function defined by equation (2.36)
$\langle\hat{Y}^2_{mj}\rangle_s$	Dimensionless mean square displacement amplitude averaged over vibrating plate surface for vibration mode mj
z	Cartesian coordinate
Z	Complex radiation impedance (MT^{-1})
α	Spherical angular coordinate in plate analysis or absorption coefficient for impedance tube
β	Variable of equation (2.2) proportional to the plate radial bending wavenumber
β_{mj}	m-j^{th} solution of equation (2.6) or equation (2.9)
$\bar{\beta}$	Quantity defined by equation (2.22)
γ	Variable in equations (7.16) and (7.17) representing the phase difference between an outgoing and reflected wave within the horn

$\bar{\gamma}$	Ratio defined by equation (2.30)
δ_1	Coefficient defined by equation (2.28)
δ_2	Coefficient defined by equation (2.28)
$\delta_{1_{mj}}$	Coefficient corresponding to mode mj and defined by equation (2.28)
$\delta_{2_{mj}}$	Coefficient corresponding to mode mj and defined by equation (2.28)
Δ	Function defined by equation (A1.11)
ε_m	$= \begin{cases} 1 \text{ when } m = 0 \\ 2 \text{ when } m \neq 0 \end{cases}$
η	Oblate spheroidal coordinate
θ	Angular polar coordinate on plate and oblate spheroidal angular coordinate
θ_i	Angle between illuminating wave and normal to the vibrating plate surface in holography (radians)
θ_r	Angle between reflected wave and normal to the plate surface in holography (radians)
$\Theta_m(\theta)$	$= \begin{cases} \cos m\theta \text{ if } m = 0 \\ \sin m\theta \text{ if } m \neq 0 \end{cases}$
λ	Wavelength of sound (m)
λ_ℓ	Wavelength of laser light (m)
Λ	Constant of equation (2.2)
μ	Variable of equations (7.16) and (7.17) representing the amplitude ratio of the outgoing and reflected acoustic waves within the horn
ν	Poisson's ratio
ξ	Oblate spheroidal coordinate
ρ	Density of plate material (steel) (kg/m^3)
ρ_0	Density of acoustic medium (air) (kg/m^3)
σ	Plate acoustic radiation efficiency
σ_{mj}	Plate acoustic radiation efficiency for mode mj
σ_1	Coefficient defined by equation (2.31)
σ_2	Coefficient defined by equation (2.32)

ϕ	Velocity potential in dimensional form (L^2T^{-1})
$\phi_{p\text{-}a_{ref}}$	Phase angle between the acoustic pressure adjacent to a given point on a surface and the acceleration of the surface at the location of the reference accelerometer
$\phi_{p\text{-}v}$	Phase angle between acoustic pressure and velocity; referred to in Chapter 8
$\phi_{y\text{-}y_{ref}}$	Phase angle between the surface displacement at a given point and the displacement at the location of the reference accelerometer
Φ	Velocity potential in dimensionless form
$\hat{\Phi}$	Dimensionless velocity potential amplitude
ψ_1, ψ_2	Unknown constants of equation (7.1)
ψ_θ	Angular plate displacement function defined by equation (2.25)
ψ_u	Radial plate displacement function defined by equation (2.24)
ω	Angular frequency (radians/sec)
∇	Laplacian operator

CHAPTER 1

SOME PRELIMINARY CONSIDERATIONS AND GENERAL INTRODUCTION

1.1 COMPLEX RADIATION EFFICIENCY

The relationship between the vibration characteristics of a surface and the sound power produced remains a problem worth investigation although much has already been accomplished. Knowledge of this relation or a good approximation to it is a necessary prerequisite for the successful prediction of the sound power radiated by a surface vibrating with known phase and amplitude. The degree of acoustic coupling between a vibrating surface and the surrounding medium may be expressed in mathematical terms as the surface radiation efficiency σ, which is a measure of how much more or less acoustic power is radiated by the surface than would be radiated by an equal area of an infinite plane wave.

As the quantity σ may in certain cases exceed unity, it is realised there may be some conceptual problems in referring to it as radiation efficiency. Indeed for this reason some authors (e.g. Beranek, 1971b) refer to it as radiation ratio. On the other hand other authors (e.g. Lyon, 1975 and Cremer, Heckl and Ungar, 1973a) have referred to it as radiation efficiency. As the quantity σ is a measure of the efficiency with which a particular surface radiates sound, the latter terminology is considered to be suitable and is adopted in this thesis.

The radiation efficiency, σ, may be defined in terms of the space time average mean square normal surface velocity $\langle v^2 \rangle_{st}$, the surface area A and the acoustic power W radiated into the surrounding medium (which has a characteristic impedance of $\rho_o c_o$) as follows, (Cremer, Heckl and Ungar, 1973):

$$\sigma = \frac{W}{\langle v^2 \rangle_{st} A \rho_o c_o} \qquad (1.1)$$

In equation (1.1) we shall assume that both W and σ are complex.

As shown by Alper (1970), the radiated acoustic power may be described as a complex quantity, the real part of which represents power radiated into the far field and the imaginary part of which represents power flow back and forth between the surface and the acoustic near field. Thus it is convenient to define a complex radiation efficiency with real and imaginary parts corresponding to the real and imaginary parts respectively of the radiated acoustic power. The complex radiation efficiency of a surface may be considered as a normalised form of the complex radiation impedance. Although the concept of complex radiation efficiency has not been discussed by other authors, it is used in this thesis because it is a consistent and convenient way in which to present numerical and experimental results.

In the high frequency range, where many vibration modes are excited on a surface at once, a statistical approach has been shown to give satisfactory results for the purpose of estimating the radiation efficiency of thin panels (Maidanik, 1962). However for the statistical approach to yield reliable results the number of resonant modes of the surface in the measurement frequency band must exceed some minimum number. Thus at low frequencies, where only one or a few modes are excited, the sound radiation of each mode must be considered. Furthermore most surfaces which might be of interest are too complex to be conveniently analysed theoretically. Thus an experimental method for determining radiation efficiencies for low order modes of any vibrating surface could serve a useful purpose. The latter consideration has motivated the research presented in this thesis.

1.2 OBJECTIVES

An initial and important objective of this thesis is the proposal and verification of experimental techniques for the determination of the radiation efficiency of a modally vibrating surface as defined by equation

(1.1). Bies (1974) and James (1976) showed qualitatively that optical holography might be used, in conjunction with appropriate acoustical measurements, to study the phenomenon of acoustic radiation from vibrating surfaces. In this thesis it is shown how their experimental technique may be adapted to obtain good quantitative results for the modal radiation efficiency of a vibrating surface.

Initially the first six low order modes of some clamped edge circular plates are considered. Experimental results are compared with theoretical predictions derived from the analysis of this thesis. The real part of modal radiation efficiency is calculated using equation (1.1), holographic measurements to determine $\langle v^2 \rangle_{st}$ and reverberant room measurements to determine the real part of W.

A second objective of this thesis is to demonstrate the extension of the experimental technique for the measurement of modal radiation efficiency, to vibrating surfaces not readily amenable to mathematical analysis.

A third objective is to investigate the suitability of a reverberant room containing a rotating diffuser for sound power measurements required for the determination of modal radiation efficiencies. In particular, the radiation impedance presented by the room to pure tone sound sources is investigated for a number of different sources and diffuser rotational speeds.

1.3 GENERAL INTRODUCTION TO REMAINDER OF THESIS

In Part I of this thesis a thorough theoretical description is presented of the response and radiation characteristics of a resonantly vibrating circular plate with both clamped and simply supported edges. This is followed by a description of the holographic procedure used for the determination of the quantity $\langle v^2 \rangle_{st}$ of equation (1.1). The procedure for the measurement of the real part of the radiated sound power W of equation

(1.1) is then described. Using these experimentally determined values for W and $\langle v^2 \rangle_{st}$, and equation (1.1), values are calculated for the resistive part of the radiation efficiency and compared with theoretical predictions. The experimental technique is then extended to the determination of the resistive parts of the radiation efficiencies for surface vibrations not readily amenable to mathematical analysis. These include some low order engine block vibration modes and some non-classical plate vibration modes.

Part II of this thesis is concerned with the investigation of the suitability of the reverberant room for the measurements described in Part I. In particular the radiation impedance presented to a number of pure tone sound sources by the room containing a rotating diffuser is considered. The sources used are the mouths of two different diameter straight tubes, the mouth of a conical horn whose throat is attached to a straight tube, and some simply supported edge square plates of five different sizes. The complex radiation impedance presented to the tube and horn mouth sound sources is measured by sampling the sound field in the tube. The complex radiation efficiency for the plate sources is calculated from holographic measurements and a near field microphone scan of the vibrating surface. Verification of this experimental technique using clamped edge circular plates and side surfaces of some in line engine blocks in an anechoic room has been previously reported by the author and his thesis advisor (Hansen and Bies, 1979).

The main purpose of the investigations in the reverberant room is to establish whether or not a rotating diffuser enables the room to present on average free field radiation impedance to a pure tone sound source. The variations in radiation impedance caused by the rotating diffuser are evaluated experimentally as a function of source size and diffuser angular position and rotational speed. The average radiation impedance is calculated by averaging over one complete diffuser revolution and is then compared with free field measurements and predictions.

PART 1: INVESTIGATION OF SOUND RADIATION FROM MODALLY VIBRATING SURFACES

CHAPTER 2

THE MODEL: THE CIRCULAR FLAT PLATE

2.1 GENERAL INTRODUCTION

The edge clamped circular flat plate mounted in an infinite rigid baffle and radiating into an echo free field is relatively simple to describe analytically and thus was chosen as a model for verification of the experimental measuring techniques investigated in this thesis. The model had the advantage that direct comparison could readily be made between experimental results and theoretical predictions. The model provided the additional important advantage that its geometry made possible considerable simplification in the interpretation of the time averaged holograms. The simplification was possible because the direction of vibration for the clamped edge flat plate is normal to the surface so that the angles between the three vectors, the direction of positive displacement, the direction of illumination, and the direction of observation, could be arranged to essentially coincide. Under these circumstances the surface displacement vector and the optical sensitivity vector are essentially coincident everywhere over the surface of the model, so that the surface displacement amplitude is directly related to the fringe number on the reconstructed image. By contrast if the surface were curved or irregular and the direction of vibration were in consequence unknown, at least three different holograms containing different orientations of the sensitivity vector would be required to unambiguously determine the

vibration amplitude of any point on the surface (Tonin and Bies, 1977).

In the following chapter the modal responses and radiation efficiencies of the first seven low order modes of the circular flat plate with both clamped edge and simply supported edge are considered theoretically and numerical results are given in detail for later reference. Comparisons are made for the clamped edge plate between thin plate theory (Classical theory) and thick plate theory (Mindlin-Timoshenko theory) to determine the range of usefulness of the simpler thin plate theory. Numerical results are given for mode shapes, resonant frequencies, mean square surface velocity amplitudes and radiation efficiencies.

2.2 PREDICTED PLATE RESPONSE

2.2.1 Introduction to Plate Response Analysis

The flexural vibrations of circular plates were first considered by Poisson as early as 1829 but the first detailed analysis for various edge conditions was not presented until 1878 by Rayleigh (1878a). Rayleigh's analysis is generally referred to as Classical plate theory and as it ignores the effects of shear and rotatory inertia its use is restricted to thin isotropic plates with a large radius to thickness ratio.

In more recent times, Mindlin (1951) has presented a two dimensional solution for plate motion derived from three dimensional equations of elasticity which consider the effects of shear and rotatory inertia on plate vibrations and resonant frequencies. His analysis is based on a similar one dimensional theory for bars in which Rayleigh (1878b) is credited for including the effect of rotatory inertia and Timoshenko (1921) is credited for including the effect of transverse shear.

For plate motion, the shear effect is shown by Mindlin to be much more significant than the rotatory inertia effect. Consequently the theory of plate motion presented by Mindlin in 1951 is generally referred to as Mindlin-Timoshenko Plate Theory (or M-T Plate Theory).

In 1954 Mindlin and Deresiewicz extended the two dimensional general plate theory to include the flexural vibrations of an isotropic free edge circular plate. Recently, the forced vibrations of an edge clamped circular plate have been considered by Alper and Magrab (1970).

In the following section both M-T plate theory and Classical plate theory are presented for clamped edge plates for the purpose of obtaining expressions for the plate normal velocity distribution and the mean square plate surface velocity. These quantities are required for the theoretical determination of the plate modal radiation efficiency. Both theories are presented so that the range of validity of the much simpler Classical plate theory may be determined by comparison with the more exact M-T theory. The comparison will show that the Classical plate theory gives valid results over a range of thickness to radius ratios up to about 0.1 for the first few low order modes.

Classical plate theory presented by Morse and Ingard (1968a) is repeated here for the purpose of correcting an error in their analysis (equation 2.12) and for the purpose of simplifying their expression for the characteristic equation to make numerical computation easier. For comparison, the analysis for a clamped edge plate using the more precise M-T plate theory is also presented. For this purpose the analysis of Alper and Magrab (1970) is repeated and extended to obtain expressions for the modal mean square plate surface velocity.

The case of the simply supported circular plate, is also considered using Classical plate theory.

An expression is derived for the mean square surface velocity of the plate from the characteristic equation (equation 2.9). This characteristic equation is given by Leissa (1969) and may be derived from the equations describing the plate boundary conditions given by Rayleigh (1878a). The simply supported edge analysis is presented to show what trend might be expected in the cases encountered experimentally where the clamped edge condition for some of the thick plates tested (at high frequencies) could not be well met and the edge condition in these cases probably lay somewhere between clamped and simply supported.

2.2.2 Classical Plate Theory

When in-plane motion may be ignored and only normal plate motion need be considered, the general equation of motion for a plate vibrating in an acoustic medium with negligible mass loading is,

$$\nabla^4 y + \frac{12\rho(1-\nu^2)}{Eh^2} \frac{\partial^2 y}{\partial t^2} = 0 \ .$$

This equation and its solution for a circular plate were first given by Rayleigh (1878a). His solution may be written in dimensionless form as,

$$Y(u,\theta,t) = D\,\Theta_m(\theta)[J_m(\pi\beta u) + \Lambda I_m(\pi\beta u)]e^{i\omega t} \qquad (2.1)$$

where the notation is consistent with that used later by Morse and Ingard (1968a) (with the exception of the sign of the time dependence) and that used throughout the remainder of this thesis.

For both simply supported and edge clamped plates equation (2.1)

can be simplified by making use of the first boundary condition that the normal plate displacement at the edge is always zero.

$$Y = 0 \quad \text{at} \quad u = 1. \tag{2.2}$$

Use of equation (2.2) allows equation (2.1) to be written in a more compact form for a plate vibrating in mode (m,j) as,

$$\hat{Y}_{mj}(u,\theta) = D_{mj}\Theta_m(\theta)H_{mj}(u) \tag{2.3}$$

where $$H_{mj}(u) = J_m(\pi\beta_{mj}u) - J_m(\pi\beta_{mj})I_m(\pi\beta_{mj}u)/I_m(\pi\beta_{mj}). \tag{2.4}$$

For clamped edge plates the second boundary condition requires that the displacement slope must be zero at the edge. Thus,

$$\frac{\partial Y}{\partial u} = 0 \quad \text{at} \quad u = 1. \tag{2.5}$$

Solutions for β_{mj} of equation (2.4) corresponding to particular modes (m,j) are found using the second boundary condition, equation (2.5). Substitution of equation (2.3) into (2.5) gives the following result which defines β_{mj} and which is equivalent to the equation given by Leissa (1969).

$$J_{m+1}(\pi\beta_{mj})I_m(\pi\beta_{mj}) + J_m(\pi\beta_{mj})I_{m+1}(\pi\beta_{mj}) = 0. \tag{2.6}$$

In writing equation (2.6) the following Bessel Function identities (McLachlan, 1941) have been used;

$$\frac{\partial}{\partial z} J_m(pz) = (m/z)J_m(pz) - pJ_{m+1}(pz) \tag{2.7a}$$

$$\frac{\partial}{\partial z} I_m(pz) = (m/z)I_m(pz) + pI_{m+1}(pz). \tag{2.7b}$$

For simply supported plates the second boundary condition as given by Rayleigh (1878a) and expressed in dimensionless form is,

$$\frac{\partial^2 Y}{\partial u^2} + \nu \left(\frac{1}{u} \frac{\partial Y}{\partial u} \right) = 0 \quad \text{at } u = 1. \tag{2.8}$$

Substituting equation (2.3) into (2.8) and rearranging terms, gives the following result which is equivalent to the expression given by Leissa (1969).

$$\frac{J_{m+1}(\pi\beta_{mj})}{J_m(\pi\beta_{mj})} + \frac{I_{m+1}(\pi\beta_{mj})}{I_m(\pi\beta_{mj})} - \frac{2\pi\beta_{mj}}{(1-\nu)} = 0 \tag{2.9}$$

where in addition to (2.7a) and (2.7b), the following identities have been used;

$$I_m(z) = [(2m+2)/z]\, I_{m+1}(z) + I_{m+2}(z) \tag{2.10a}$$

$$J_m(z) = [(2m+2)/z]\, J_{m+1}(z) - J_{m+2}(z). \tag{2.10b}$$

The β_{mj} solutions obtained for simply supported [equation (2.9)] and clamped edge [equation (2.6)] plates are listed in table 2.1 for the first few vibration modes.

The mean square surface displacement amplitude averaged over the plate surface for vibration mode mj may be found by substituting the mj^{th} solution of equation (2.6) or (2.9) into equation (2.3), squaring and then integrating over the surface area.

That is,

$$\langle \hat{Y}^2_{mj} \rangle_s = \frac{a^2}{A} \int_0^{2\pi} \int_0^1 D^2_{mj} \Theta^2_m(\theta) H^2_{mj}(u)\, u\, du\, d\theta. \tag{2.11}$$

For clamped edge plates vibrating in mode (m,j) equation (2.11) may be simplified by expanding and integrating term by term. The result is,

$$\langle \hat{Y}^2_{mj} \rangle_s = (2D^2_{mj}/\varepsilon_m)\, J^2_m(\pi\beta_{mj}) \tag{2.12}$$

where $$\varepsilon_m = \begin{cases} 1 \text{ when } m = 0 \\ 2 \text{ when } m \neq 0. \end{cases}$$

This result was obtained by using equation (2.6) and the following Bessel

Table 2.1 : Classical Plate Theory Solutions of the Characteristic Equation (Equations 2.6 and 2.9) Describing Plate Motion for the First Few Vibration Modes.

Mode (m,j)	β_{mj} (clamped edge)	β_{mj} (simply supported edge)
0,1	1.0174	0.7071
0,2	2.0074	1.7353
0,3	3.0047	2.7411
0,4	4.0034	3.7436
1,1	1.4677	1.1867
2,1	1.8798	1.6110
3,1	2.2739	2.0121
4,1	2.6568	2.3999

Function identities (McLachlan, 1941).

$$\int_0^1 J_m^2(Bz)z\,dz = 0.5[J_m'^2(B) + (1 - m^2/B^2)J_m^2(B)] \tag{2.13a}$$

$$\int_0^1 I_m^2(Bz)z\,dz = -0.5[I_m'^2(B) - (1 + m^2/B^2)I_m^2(B)] \tag{2.13b}$$

$$\int_0^1 I_m(Bz)J_m(Hz)z\,dz = [1/(B^2 + H^2)][BJ_m(H)I_m'(B) - HI_m(B)J_m'(H)], \tag{2.13c}$$

where the prime denotes differentiation with respect to the Bessel Function argument.

For simply supported edge plates equation (2.11) may be simplified to give,

$$\langle \hat{Y}_{mj}^2 \rangle_s = (2D_{mj}^2/\epsilon_m)J_m^2(\pi\beta_{mj})P_{mj} \tag{2.14}$$

where, $P_{mj} = 1 - [2\pi^2\beta_{mj}^2/(1-\nu)^2] - [2\pi\beta_{mj}/(1-\nu)][(m/\pi\beta_{mj})$

$$+ (1/\pi\beta_{mj}) - J_{m+1}(\pi\beta_{mj})/J_m(\pi\beta_{mj})]. \tag{2.15}$$

In this case the result was obtained by using equation (2.9) and the Bessel Function identities 2.7a, 2.7b, 2.10a, 2.10b, 2.13a,b and c.

The dimensional mean square normal plate surface velocity for vibration mode m,j averaged in time and over the plate surface, may be obtained from the non-dimensional mean square normal surface displacement amplitude of equations (2.12) and (2.14) using the following relation,

$$\langle v_{mj}^2 \rangle_{st} = 0.5\,\omega^2 a^2 \langle \hat{Y}_{mj}^2 \rangle_s. \tag{2.16a}$$

For the clamped edge plate we obtain,

$$\langle v_{mj}^2 \rangle_{st} = D_{mj}^2 a^2 \omega^2 J_m^2(\pi\beta_{mj})/\varepsilon_m, \tag{2.16b}$$

and for the simply supported edge plate we obtain,

$$\langle v_{mj}^2 \rangle_{st} = D_{mj}^2 a^2 \omega^2 J_m^2(\pi\beta_{mj}) P_{mj}/\varepsilon_m. \tag{2.16c}$$

The constant D_{mj} of equations (2.12) and (2.14) may be conveniently evaluated in terms of the velocity amplitude at a modal antinode. Referring to equation (2.3) we choose θ such that $\Theta_m(\theta)$ is unity and differentiate $\hat{Y}_{mj}$ with respect to u. We then determine u_A from the equation which results from setting the derivative equal to zero,

$$dH_{mj}(u)/du = 0 \quad \text{at } u = u_A . \tag{2.17}$$

Equation (2.17) was solved by successive iteration on a computer for those values for which m was non zero. Where m was zero the amplitude at the centre of the plate was used. The value of u_A obtained by this process was then substituted into equation (2.3) and the square of the velocity amplitude in dimensional form was computed,

$$\hat{v}_A^2 = D_{mj}^2 a^2 \omega^2 H_{mj}^2(u_A). \tag{2.18}$$

Dividing equations (2.16) by (2.18) and using either equations (2.12) or (2.14) gives the following results.

For clamped edge plates,

$$\langle v_{mj}^2 \rangle_{st}/\hat{v}_A^2 = J_m^2(\pi\beta_{mj})/[\varepsilon_m H_{mj}^2(u_A)], \tag{2.19}$$

and for simply supported edge plates,

$$\langle v_{mj}^2 \rangle_{st}/\hat{v}_A^2 = J_m^2(\pi\beta_{mj}) P_{mj}/[\varepsilon_m H_{mj}^2(u_A)]. \tag{2.20}$$

An expression due to Rayleigh (1878a) which may be used to calculate modal resonant frequencies and which will be useful later is,

$$f_{mj} = [\pi\beta_{mj}^2 h/4a^2][E/3\rho(1-\nu^2)]^{\frac{1}{2}}. \qquad (2.21)$$

2.2.3 Mindlin-Timoshenko Plate Theory

For the purpose of the following analysis the plates considered are assumed to be isotropic and the mass loading of the acoustic medium is assumed to be negligible. As shown by Lax (1944) the mass loading of the medium is negligible when the following condition is satisfied,

$$\bar{\beta} = (\rho_0/\rho)(a/h) << 1 . \qquad (2.22)$$

For a steel plate vibrating in air the density ratio (ρ_0/ρ) is approximately 1.5×10^{-4} while the largest value of the radius to thickness ratio (a/h) is approximately 10^3. A larger value of the radius to thickness ratio is not possible since membrane stresses, neglected in the analysis, would then become important; thinner plates would behave like stretched stiff membranes. We conclude that the largest value of $\bar{\beta}$ is of the order of 0.15 or less and hence for the case of steel plates vibrating in air, the mass loading of the medium is negligible.

The equations of motion for the isotropic circular flat plate with negligible mass loading of the surrounding fluid, expressed in dimensionless form, are as follows (Mindlin and Deresiewicz, 1954).

$$Y = [\hat{Y}_1 + \hat{Y}_2]e^{i\omega t}, \qquad (2.23)$$

$$\psi_u = \{(\sigma_1-1)\frac{\partial \hat{Y}_1}{\partial u} + (\sigma_2-1)\frac{\partial \hat{Y}_2}{\partial u} + \frac{1}{u}\frac{\partial \hat{X}}{\partial \theta}\}e^{i\omega t}, \qquad (2.24)$$

and

$$\psi_\theta = \{(\sigma_1-1)\frac{1}{u}\frac{\partial \hat{Y}_1}{\partial \theta} + (\sigma_2-1)\frac{1}{u}\frac{\partial \hat{Y}_2}{\partial \theta} - \frac{\partial \hat{X}}{\partial u}\}e^{i\omega t}. \qquad (2.25)$$

The effects of rotatory inertia and shear have been considered and polar coordinates with origin at the plate centre have been used.

The functions $\hat{Y}_1$, $\hat{Y}_2$ and X satisfy the following differential equations characterising bending waves in a flat plate.

$$(\nabla^2 + \delta_1^2)(\nabla^2 + \delta_2^2) Y = 0, \tag{2.26}$$

and

$$(\nabla^2 + w^2) X = 0. \tag{2.27}$$

The quantities in equations (2.24) to (2.27) may be expressed in dimensionless form as follows.

$$(\delta_i a)^2 = 0.5(c_o/c_s)^2(ka)^2\{(k_T^{-2} + K) - (-1)^i[(k_T^{-2}-K)^2 + 4K(c_s/\bar{\gamma}\, c_o\, ka)^2]^{\frac{1}{2}}\}$$

$$i = 1,2 \tag{2.28}$$

$$(wa)^2 = (c_o/c_s)^2(ka)^2 - (k_T/\bar{\gamma})^2 \tag{2.29}$$

$$\bar{\gamma} = h/a\sqrt{12} \tag{2.30}$$

$$\sigma_1 = \delta_2^2/(w^2K) \tag{2.31}$$

$$\sigma_2 = \delta_1^2/(w^2K) \tag{2.32}$$

$$k_T = 0.3\nu + 0.76 \tag{2.33}$$

$$K = G(1-\nu^2)/E = (1-\nu)/2 \text{ for isotropic material.} \tag{2.34}$$

Solutions to equations (2.26) and (2.27) were given by Mindlin and Deresciewicz (1954) and may be written in dimensionless form as follows,

$$\hat{Y}_1(u,\theta) = D_1 J_m(\delta_1 au), \tag{2.35}$$

$$\hat{Y}_2(u,\theta) = D_2 F_m(\delta_2 au), \tag{2.36}$$

and

$$\hat{X}(u,\theta) = D_3 F_m(wau)\, \Theta_m(\theta + \pi/2). \tag{2.37}$$

In equations (2.36) and (2.37), $F_m(x)$ is a Bessel Function of the first kind if

$$ka \geqslant (k_T c_s/\bar{\gamma} c_o), \tag{2.38}$$

and a Modified Bessel Function of the first kind if

$$ka < (k_T c_s / \bar{\gamma} c_0). \tag{2.39}$$

The following boundary conditions must be satisfied for a clamped edge circular plate,

$$\hat{Y}(1,\theta) = \psi_u(1,\theta) = \psi_\theta(1,\theta) = 0. \tag{2.40}$$

Substitution of equation (2.35) and (2.36) into (2.23) and use of the first of the boundary conditions [equation (2.40)] leads to an expression for the dimensionless displacement amplitude for the vibrating plate. Explicit dependence on the mode number (m,j) is indicated;

$$\hat{Y}_{mj}(u,\theta) = D_{mj}\,\Theta_m(\theta)H_{t_{mj}}\ , \tag{2.41}$$

where,

$$H_{t_{mj}} = [J_m(\delta_{1_{mj}} au) - J_m(\delta_{1_{mj}} a)F_m(\delta_{2_{mj}} au)/F_m(\delta_{2_{mj}} a)]\ . \tag{2.42}$$

Next we evaluate the eigen values $\delta_{1_{mj}}$ and $\delta_{2_{mj}}$ for each mode (m,j). Substitution of equations (2.35), (2.36) and (2.37) into equations (2.24) and (2.25) and use of the second and third boundary conditions of equations (2.40) leads to two equations dependent on the constants D_1, D_2 and D_3. Use of the first boundary condition and equation (2.23) enables the constant D_2 to be eliminated. The two equations may then be written as

$$(\sigma_1 - 1)J_m(\delta_1 a)D_1/a - (\sigma_2 - 1)J_m(\delta_1 a)mD_1/a + D_3 wF'(wa) = 0 \tag{2.43}$$

and

$$(\sigma_1 - 1)\delta_1 J'_m(\delta_1 a)D_1 - (\sigma_2 - 1)\delta_2 J_m(\delta_1 a)F'_m(\delta_2 a)D_1/F_m(\delta_2 a) + mF_m(wa)D_3/a = 0 \tag{2.44}$$

where the prime indicates differentiation with respect to the Bessel Function argument and the following Bessel Function identities have been used (McLachlan, 1941);

$$\frac{\partial}{\partial z} J_m(pz) = p \frac{\partial}{\partial (pz)} J_m(pz) \tag{2.45a}$$

$$\frac{\partial}{\partial z} I_m(pz) = p \frac{\partial}{\partial (pz)} I_m(pz). \tag{2.45b}$$

The constants D_1 and D_3 may be eliminated from equations (2.43) and (2.44) to give the following characteristic equation,

$$\frac{(\sigma_1-1)(\delta_1 a)}{J_m(\delta_1 a)} \left[\frac{m}{\delta_1 a} J_m(\delta_1 a) - J_{m+1}(\delta_1 a)\right] - \frac{(\sigma_2-1)(\delta_2 a)}{F_m(\delta_2 a)} \left[\frac{m}{\delta_2 a} F_m(\delta_2 a) \pm F_{m+1}(\delta_2 a)\right]$$

$$+ m^2(\sigma_2-\sigma_1) \frac{F_m(wa)}{wa} \left[\frac{m}{wa} F_m(wa) \pm F_{m+1}(wa)\right]^{-1} = 0. \tag{2.46}$$

The Bessel Function identities of equations (2.7a), (2.7b), (2.45a) and (2.45b) have been used to derive equation (2.46). The negative sign in equation (2.46) is chosen if equation (2.38) is satisfied; the positive sign is chosen if equation (2.39) is satisfied.

Reference to equations (2.28), (2.29), (2.31) and (2.32) shows that equation (2.46) may be expressed as a function of dimensionless frequency, ka. Values of $(ka)_{mj}$ were determined by numerically solving equation (2.46) for its first several roots using a computer. The resonant frequencies of modes (m,j) are given by,

$$f_{mj} = (ka)_{mj} c_o / 2\pi a. \tag{2.47}$$

The mean square displacement amplitude averaged over the plate surface may be determined using equation (2.41), squaring and integrating over the plate surface. The integration is performed by expanding the function and integrating term by term using the Bessel Function identities of equations (2.13a), (2.13b) and (2.13c). The result may be simplified using the Bessel Function identities of equations (2.7a) and (2.7b) together with equation (2.16) to write the following for the mean square velocity averaged in time and over the plate surface;

$$\langle v_{mj}^2 \rangle_{st} = D_{mj}^2 a^2 \omega^2 g_{mj} / \varepsilon_m . \tag{2.48}$$

If equation (2.38) is satisfied then in equation (2.48),

$$g_{mj} = 0.5 J_m^2 \{ 2 + (\frac{J_{m+1}}{J_m})^2 + (\frac{\bar{J}_{m+1}}{\bar{J}_m})^2 - (\frac{J_{m+1}}{J_m})(\frac{2m}{B_1} + \frac{4B_1}{B_1^2 - B_2^2})$$

$$- (\frac{\bar{J}_{m+1}}{\bar{J}_m})(\frac{2m}{B_2} - \frac{4B_2}{B_1^2 - B_2^2}) \} . \tag{2.49}$$

Alternatively if equation (2.39) is satisfied then,

$$g_{mj} = 0.5 J_m^2 \{ 2 + (\frac{J_{m+1}}{J_m})^2 - (\frac{I_{m+1}}{I_m})^2 - (\frac{J_{m+1}}{J_m})(\frac{2m}{B_1} + \frac{4B_1}{B_1^2 + B_2^2})$$

$$- (\frac{I_{m+1}}{I_m})(\frac{2m}{B_2} + \frac{4B_2}{B_1^2 + B_1^2}) \} . \tag{2.50}$$

In equations (2.49) and (2.50)

$$J_i = J_i(\delta_{1_{mj}} a) \tag{2.51}$$

$$\bar{J}_i = J_i(\delta_{2_{mj}} a) \tag{2.52}$$

$$I_i = I_i(\delta_{2_{mj}} a) \tag{2.53}$$

$$B_1 = \delta_{1_{mj}} a \tag{2.54}$$

and

$$B_2 = \delta_{2_{mj}} a . \tag{2.55}$$

Equations (2.41) and (2.42) may be used to evaluate the constant D_{mj} relative to the velocity amplitude at an antinode using the same procedure as described for Classical plate theory. The result allows the velocity ratio $\langle v_{mj}^2 \rangle_{st} / \hat{v}_A^2$ to be computed for each mode (m,j) from

the following relation,

$$\langle v_{mj}^2 \rangle_{st} / \hat{v}_A^2 = g_{mj} / [\epsilon_m H_{tmj}^2 (u_A)]. \qquad (2.56)$$

2.2.4 Numerical Results

The equations presented in the previous section were used to calculate values for resonant frequencies, velocity ratios ($\langle v_{mj}^2 \rangle_{st} / \hat{v}_A^2$) and diametral mode shapes for the first few vibration modes of a circular plate. Clamped edge plate relations were evaluated using equations derived from both Classical and M-T plate theory while simply supported edge plate relations were evaluated using equations derived from Classical plate theory alone.

The first task was the evaluation of the characteristic equations (2.6) and (2.46) which was done using successive iteration. However as the mode order became higher, the argument of the Bessel Functions used became larger until a point was reached where approximation formulae (McLachlan, 1941) had to be used. This point was reached when large arguments generated large terms in the truncated sum used to evaluate the Bessel Functions. Although the sum eventually converged, the differences in magnitude between these large terms and the final result was too great to enable acceptable results to be obtained with the 29 figure accuracy of the available computer. The accuracy of the final result began to be seriously effected for Bessel Function arguments exceeding about 40 corresponding to modes of higher order than the m=10, j=15 mode. The characteristic equation derived using both M-T and Classical Plate Theory was not a continuous function and had an asymtote of $+\infty$ and $-\infty$ on each side of every solution. Thus care was necessary in the iteration procedure to avoid these asymtotes which could yield "phantom" solutions.

From the characteristic equation solutions, it was possible to directly determine the value of the displacement amplitude at any point

on the plate surface, using equations (2.3) and (2.41) for any given mode (m,j), in terms of one unknown constant. In Chapter 3, experimental measurements are compared to theoretical results for the mode shape across plate antinodal diameters for the first six modes of vibration of an edge clamped circular plate.

Values for the velocity ratio ($< v_{mj}^2 >_{st} / \hat{v}_A^2$) were calculated as described earlier, using iteration to find the position and magnitude of the quantity $\hat{v}_A$, and then equations (2.19), (2.20) and (2.56) to determine the ratio. Numerical results for the velocity ratios calculated using equation (2.56) (M-T plate theory), are plotted in Fig. (2.1) as a function of the plate thickness to radius ratio (h/a), for the first six modes of vibration of a clamped edge circular plate. Similar results obtained using Classical plate theory are not shown in the figure for clarity. Classical plate theory would predict constant values of the ratio ($< v_{mj}^2 >_{st} / \hat{v}_A^2$), independent of the value of h/a and the values would be identical with the M-T plate theory results for small values of h/a. Thus the two theories are in agreement over the horizontal portion of the curves shown in the figure. In the experiments described later, plates with thickness to radius ratios of less than 0.08 were used. Values of the velocity ratios for both simply supported and clamped edge plates calculated using Classical plate theory [equations (2.13) and (2.20)] are listed in table 2.2 for the first few vibration modes.

Values of the resonant frequencies of the modes of vibration of both simply supported and clamped edge plates were calculated from the characteristic equation solutions and equations (2.21) and (2.47). Calculated and experimentally measured values are compared in the table in Figs. 2.7 & 2.8. Theoretically predicted values for clamped edge plates are presented in dimensionless form (ka) as a function of the plate thickness to radius ratio (h/a) in Fig. 2.2. In Fig. 2.3 the value of the dimensionless plate bending wave number $k_b a$ is plotted as a function of h/a for the first six vibration modes of a clamped edge

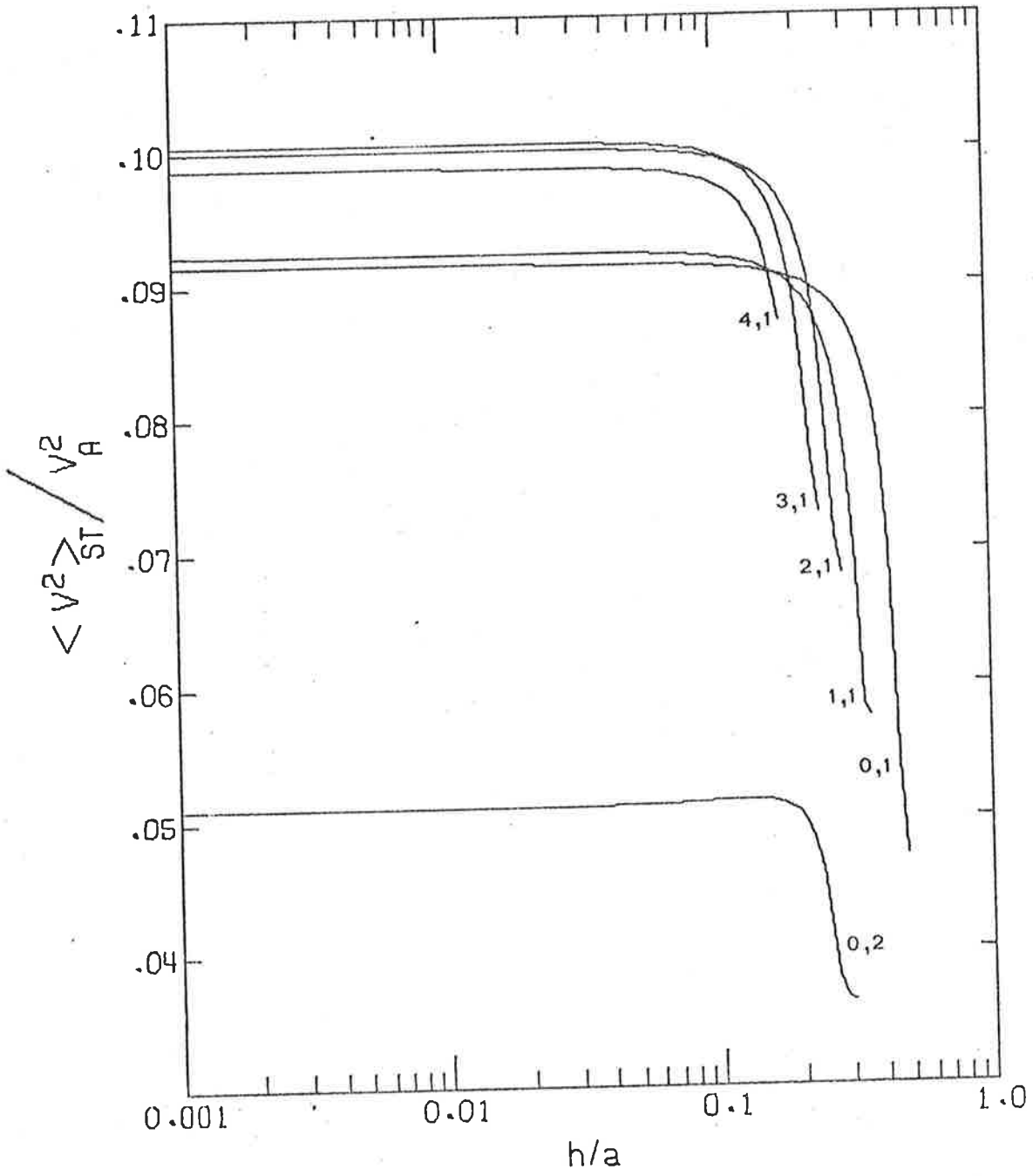

FIG. 2.1 VELOCITY RATIO CALCULATED USING M-T PLATE THEORY (EQUATION 2.56) The curves shown here are for clamped edge plates and h/a is the plate thickness to radius ratio. Classical Theory is in agreement with these calculations over the horizontal portions of the curves. The resonant vibration modes (m,n) may be identified using Fig. 3.2.

Table 2.2 : Values for the Velocity Ratios ($\langle v^2_{mj} \rangle_{st} / \hat{v}^2_A$) Calculated using Classical Plate Theory [Equations (2.19) and (2.20)]

Mode mj	Clamped edge plates $\langle v^2_{mj} \rangle_{st} / \hat{v}^2_A$	Simply supported edge plates $\langle v^2_{mj} \rangle_{st} / \hat{v}^2_A$
0,1	0.0914	0.1425
0,2	0.0509	0.0578
0,3	0.0338	0.0368
1,1	0.0923	0.1224
2,1	0.1000	0.1233
3,1	0.1005	0.1187
4,1	0.0987	0.1133

When M-T plate theory is used the values in the table become dependent on plate thickness as illustrated in Fig. 2.1.

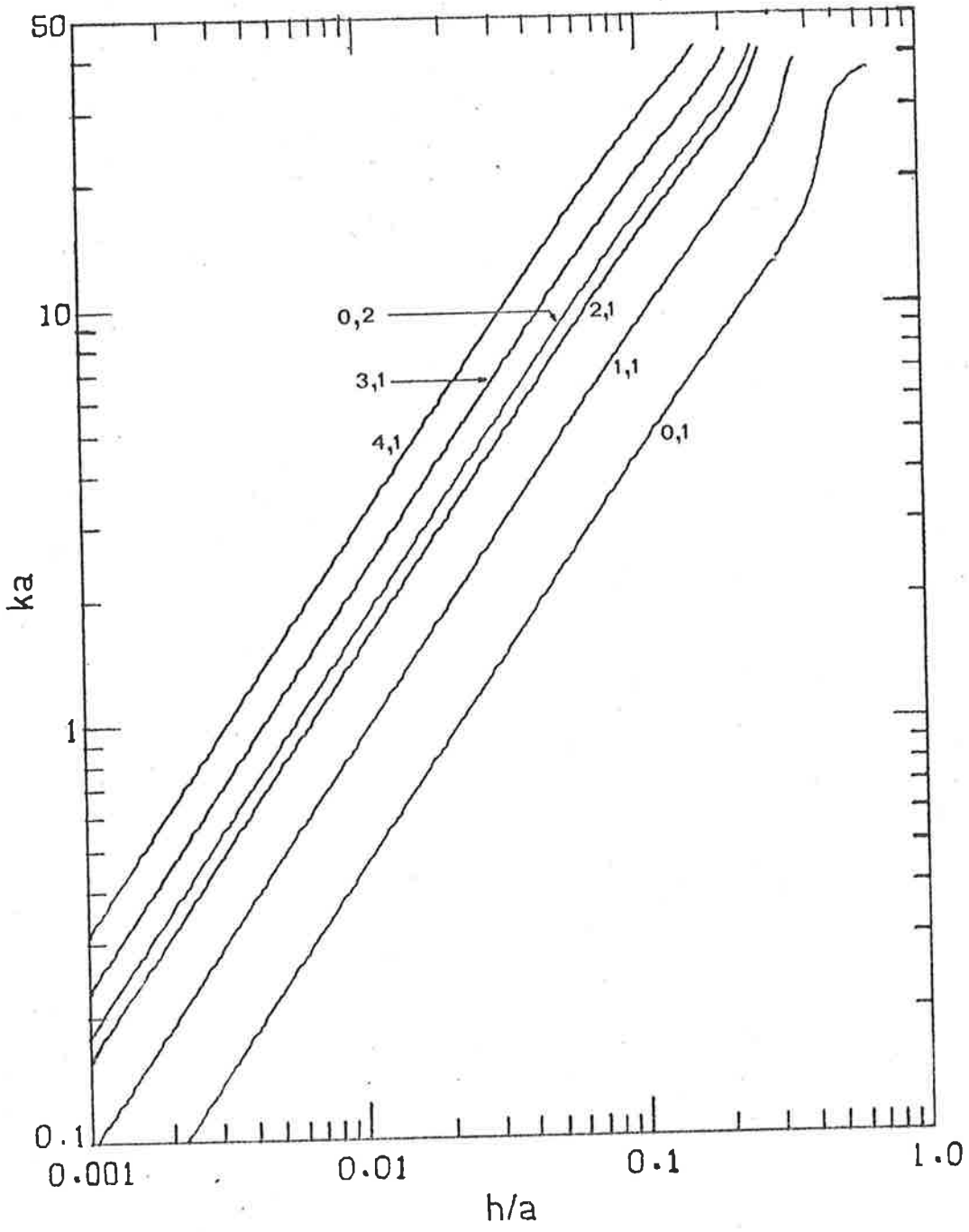

FIG. 2.2 DIMENSIONLESS FREQUENCY AS A FUNCTION OF PLATE SIZE FOR THE FIRST SIX VIBRATION MODES CALCULATED USING M-T PLATE THEORY.

The curves shown here are for clamped edge plates and h/a is the plate thickness to radius ratio. Classical Plate Theory would predict linear relations in agreement with the predictions shown at low values of h/a. The resonant vibration modes (m,n) may be identified using Fig. 3.2.

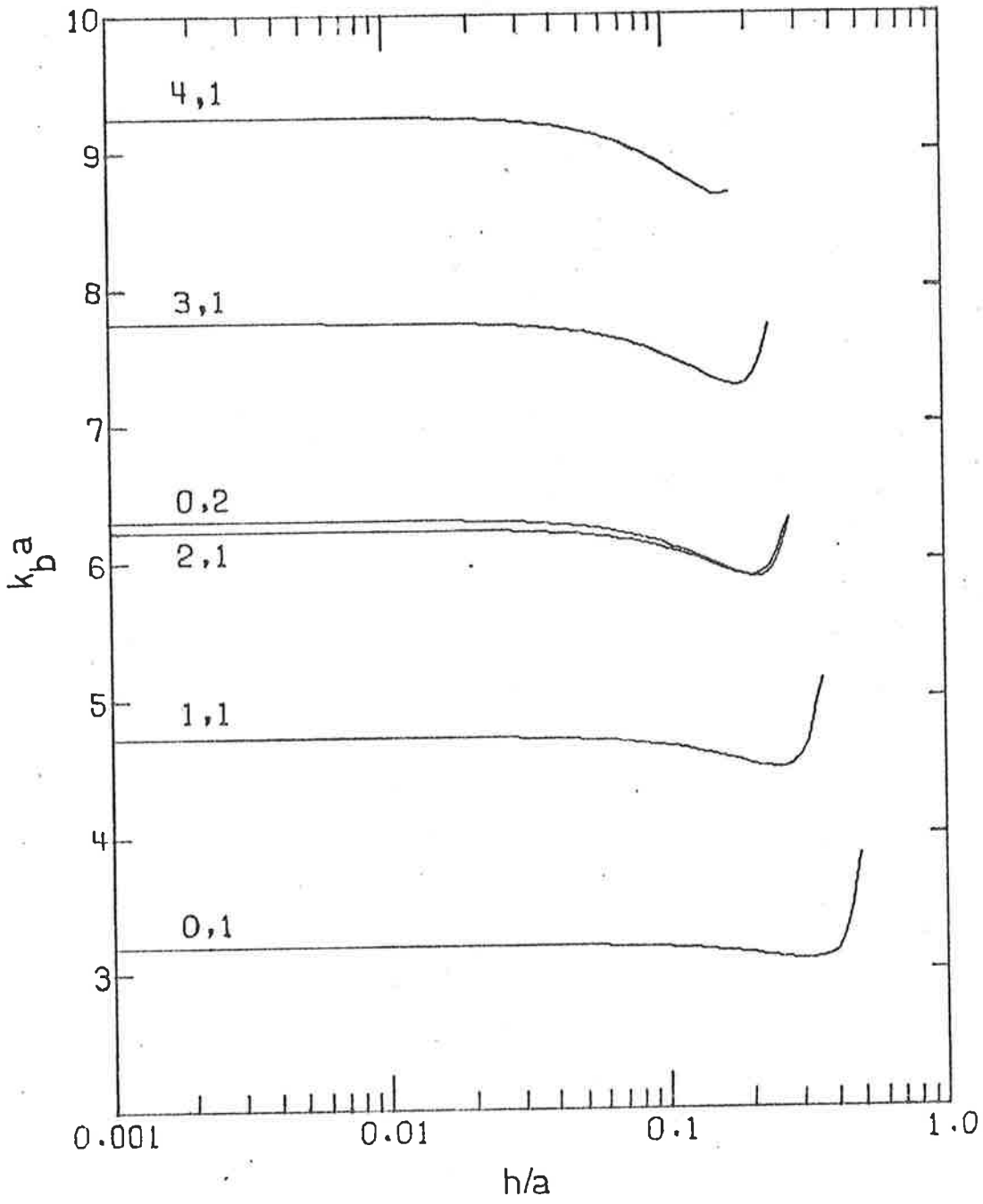

FIG. 2.3 PLATE BENDING WAVE NUMBER FOR RESONANT VIBRATION MODES CALCULATED USING M-T PLATE THEORY (EQUATION 2.57)

The curves shown here are for clamped edge plates and h/a is the plate thickness to radius ratio. Classical Theory would predict constant values in agreement with the predictions shown at low values of h/a. The resonant vibration modes (m,n) may be identified using Fig. 3.2.

plate. The quantity k_b has not been defined for circular clamped edge plates elsewhere in the literature. The expressions given below are derived in a similar way as the corresponding expressions for a rectangular panel. For a given mode (m,j), we define k_b as,

$$k_b a = [(a^2/2)(\delta_{1_{mj}}^2 + \delta_{2_{mj}}^2) + m^2]^{\frac{1}{2}} \tag{2.57}$$

when M-T plate theory is used and,

$$k_b a = [(\pi\beta_{mj})^2 + m^2]^{\frac{1}{2}} \tag{2.58}$$

when Classical plate theory is used.

Only M-T plate theory was used to calculate the values of ka and k/k_b shown in Figs. 2.2 and 2.3. The calculations based on Classical plate theory would produce identical results at low values of h/a but curves based on the latter theory would remain straight lines at high values of h/a, in contrast to the non-linear behaviour predicted in the figures by the M-T theory at high values of h/a.

2.3 PREDICTED ACOUSTIC COUPLING

2.3.1 Introduction to Radiation Coupling Analysis

Rayleigh (1878c) is credited with being the first to present a general solution for the velocity potential describing the field radiated by any surface set in an infinite rigid baffle vibrating with any given velocity distribution. Rayleigh's result given in integral form is extremely difficult to evaluate except for a few special cases.

Using the Rayleigh Integral and Classical plate theory, Lax (1944) has developed a solution for the radiation resistances and reactances of the acoustically coupled symmetric vibration of a clamped edge circular flat plate mounted in an infinite rigid baffle. His results are restricted to the first few axisymmetric vibration modes and a limited frequency range (ka up to 1.1 for 0,1 mode and up to 3.2 for the 0,2; 0,3; and 0,4 modes). Also the method used is not readily amenable to non-axisymmetric vibrations. The work described in this thesis covers both axisymmetric and non-axisymmetric vibration modes for frequencies corresponding to ka values up to 20.0. The results presented at the end of this chapter are in excellent agreement with Lax's results.

Alper and Magrab (1970) have used spheroidal wave function solutions for the Classical wave equation to theoretically analyse the near field pressure distribution and the acoustic power radiated by a clamped edge circular flat plate in forced harmonic vibration. Their work includes a comprehensive review of attempts to solve wave problems associated with circular disc geometry.

In the following analysis oblate spheroidal wave functions are used to obtain solutions to the Classical wave equation for both a clamped edge and a simply supported edge circular plate mounted in an infinite rigid baffle and radiating into an echo free field. Values of ka in the range 0.1 to 20 are considered. As the analysis is concerned with acoustic pressure and velocity distribution in the fluid immediately adjacent to the plate, solutions for both the reactive and resistive parts of the surface radiation efficiency are obtained. Expressions are derived using both Classical plate theory and M-T theory to model the plate response for the clamped plate and Classical plate theory only for the simply supported edge plate.

The analysis outlined below proceeds along lines similar to those presented by Alper and Magrab (1970) for forced plate response. However, as the concern here is with resonant response of individual modes the expressions obtained differ and the analysis is extended beyond that of Alper and Magrab to obtain expressions for both the real and reactive parts of the surface radiation efficiency.

The expressions derived using oblate spheroidal wave functions are difficult to evaluate numerically. If one is interested only in far field radiation (or only the real part of the radiation efficiency) it is possible to obtain much simpler expressions using a different theoretical analysis based on the solution of the Rayleigh Integral in the far field. Analysis of a clamped edge circular plate using this approach which has not been previously reported is presented in Appendix 1. Numerical results obtained for the real part of the modal radiation efficiency using this method are identical to those obtained using the oblate spheroidal wave functions.

2.3.2 Near Field Spheroidal Wave Function Solutions

The method used by Alper and Magrad (1970) for the analysis of forced vibration of circular plates is adapted here to the problem of determining radiation efficiencies (both resistive and reactive) of the first few resonant vibration modes of a circular plate set in an infinite rigid baffle. Both simply supported and clamped edge plates are considered. The problem is solved in four steps as follows:

1. The Classical scalar wave equation is expressed non-dimensionally in terms of oblate spheroidal coordinates (η,ξ,θ) with origin at the plate centre. This particular coordinate system, which is defined in Fig. 2.4, is used because it facilitates the satisfaction of the boundary conditions on the fluid. The general solution to the wave equation in terms of oblate spheroidal wave functions (Flammer, 1957) is simplified using the appropriate fluid boundary conditions.

2. The velocity distribution over the surface of the plate is described for each vibration mode of interest in dimensionless form in terms of one unknown constant dependent on the vibration amplitude. This part of the problem has previously been discussed in detail in section 2.2.

3. Boundary conditions at the plate surface are satisfied. The normal fluid velocity is set equal to the plate surface normal velocity and an expression for the sound power radiated by the plate vibrating in any given resonant mode is obtained.

4. Finally the expressions obtained for the power radiated (step 3) and for the mean square surface velocity (section 2.2) are used to calculate the radiation efficiency for any given resonant vibration mode of the plate.

The general form of the well known scalar wave equation is

$$\nabla^2\phi - (1/c_o^2)\partial^2\phi/\partial t^2 = 0 \ . \qquad (2.59)$$

This equation may be expressed in dimensionless form in terms of the dimensionless velocity potential Φ by replacing ϕ with $\Phi a c_o$ as follows,

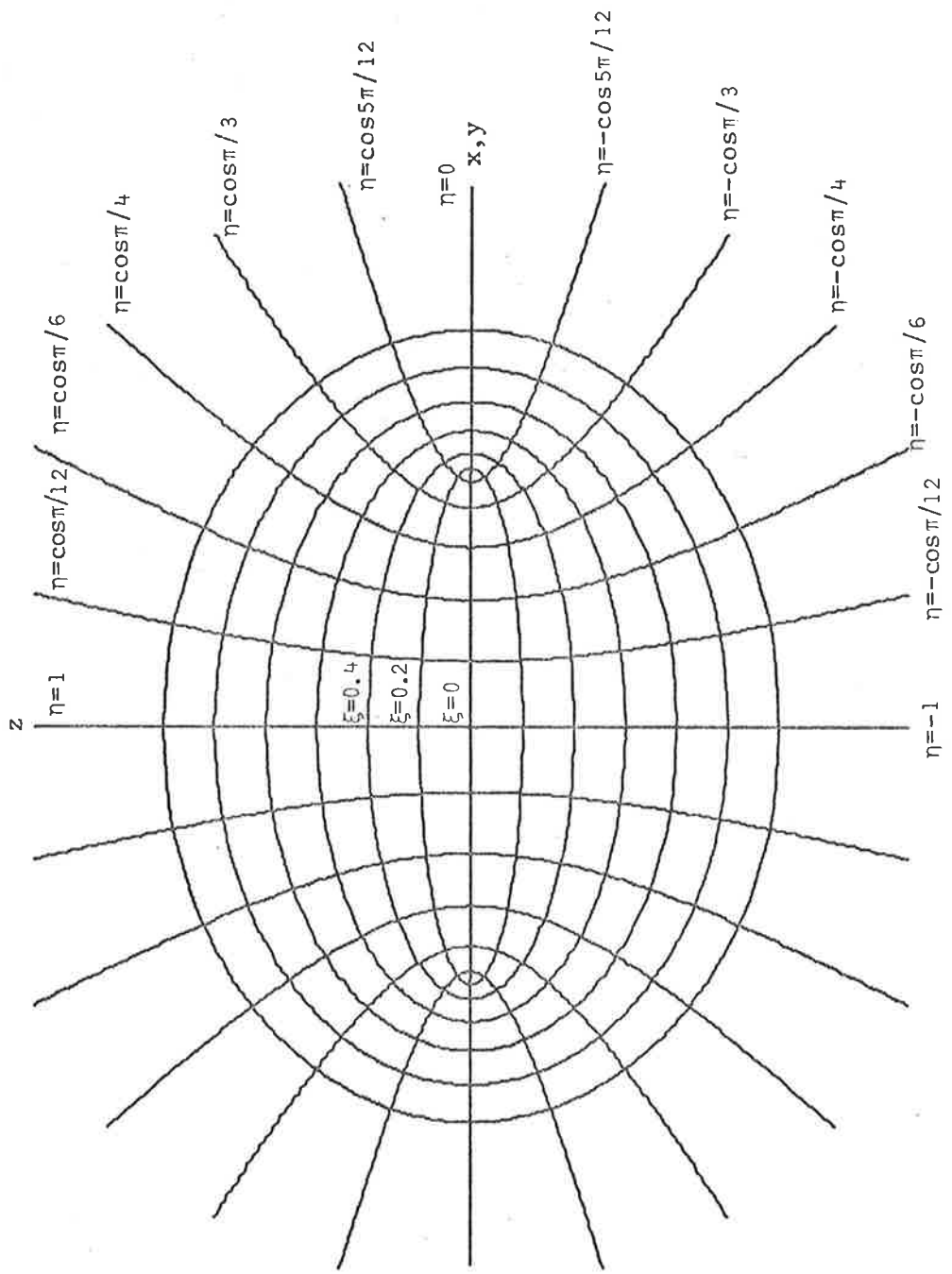

FIG. 2.4 OBLATE SPHEROIDAL COORDINATE SYSTEM

The plane of the plate is perpendicular to the plane of the paper and its circumference passes through the foci of the ellipses, ξ = constant. The θ coordinate is obtained by rotating the above 2-dimensional system through an angle of θ about the $\eta = 1$ or z axis.

$$\frac{1}{a^2}\nabla^2(\Phi a c_o) - (1/c_o^2)\,\partial^2(\Phi a c_o)/\partial t^2 = 0. \qquad (2.60)$$

Equation (2.60) may be simplified and written in terms of the wave number k as,

$$\nabla^2\Phi + (ka)^2\Phi = 0, \qquad (2.61)$$

where positive time dependence ($e^{+i\omega t}$) has been assumed.

Solutions to equation (2.61) which satisfy the boundary conditions governing the fluid are required. Disregarding the plate surface for the moment, the boundary conditions on the fluid are:

1. The fluid velocity normal to the rigid baffle is zero.
2. Only outgoing waves are present.

These boundary conditions are easily satisfied using oblate spheroidal coordinates as it is possible to make the bounding surface of one of the coordinates ($\xi = 0$) represent the circular plate and another ($\eta = 0$) represent the infinite baffle. The third coordinate (θ) is identical to the angular polar coordinate used in the analysis of the plate motion.

In Fig. 2.4 only the η and ξ coordinates are shown. The θ coordinate is obtained by rotating the system about the $\eta = 1$ axis through an angle of θ radians. In Fig. 2.4 the plate is placed coincident with the $\xi = 0$ coordinate so that the plane of the plate is perpendicular to the plane of the figure and the plate centre lies at the centre of the coordinate system. This results in the following relations between the cylindrical coordinate system (r_o,θ,z) and the oblate spheroidal coordinate system (η,ξ,θ):

1. The line $|\eta| = 1$ is coincident with the z axis, perpendicular to the plate surface and passing through the plate centre.
2. The surface $\eta = 0$ is coincident with the $z = 0$ plane except for the circular plate on which $\xi = 0$.
3. The angular coordinate θ is identically the same in both

the field oblate spheroidal coordinate system and in the plate polar coordinate system (degenerate two dimensional cylindrical coordinate system).

The transformation from oblate spheroidal coordinates to cartesian coordinates may be effected using the following equations (Flammer, 1957).

$$x = a[(1-\eta^2)(\xi^2+1)]^{\frac{1}{2}}\cos\theta, \tag{2.62a}$$

$$y = a[(1-\eta^2)(\xi^2+1)]^{\frac{1}{2}}\sin\theta, \tag{2.62b}$$

$$z = a[\eta\xi]. \tag{2.62c}$$

In the above equations (η,ξ,θ) are dimensionless and a, the plate radius, is half the interfocal distances of the confocal ellipses and hyperbolas shown in Fig. 2.4. The domains of η, ξ and θ are as follows,

$$0 \leqslant \eta \leqslant 1, \quad -\infty < \xi < \infty, \quad 0 \leqslant \theta \leqslant 2\pi.$$

Using equations (2.62), and excluding the time dependent term, equation (2.61) may be expressed in dimensionless oblate spheroidal coordinates as (Flammer, 1957),

$$\left[\frac{\partial}{\partial\eta}(1-\eta^2)\frac{\partial}{\partial\eta} + \frac{\partial}{\partial\xi}(\xi^2+1)\frac{\partial}{\partial\xi} + \frac{\xi^2+\eta^2}{(\xi^2+1)(1-\eta^2)}\frac{\partial^2}{\partial\theta^2} + (ka)^2(\xi^2+\eta^2)\right]\hat{\Phi} = 0. \tag{2.63}$$

Following Flammer (1957), the procedure of separation of variables leads to

$$\hat{\Phi}_{mn} = S_{mn}(-ika,\eta)\, R_{mn}(-ika, i\xi)\, \Theta_m(\theta), \tag{2.64}$$

where S_{mn} and R_{mn} represent oblate spheroidal angular and radial functions respectively, and may be written as,

$$S_{mn}(-ika,\eta) = A_{mn}^{(1)} S_{mn}^{(1)}(-ika,\eta) + A_{mn}^{(2)} S_{mn}^{(2)}(-ika,\eta) \tag{2.65}$$

and $$R_{mn}(-ika, i\xi) = B_{mn}^{(3)} R_{mn}^{(3)}(-ika, i\xi) + B_{mn}^{(4)} R_{mn}^{(4)}(-ika, i\xi), \qquad (2.66)$$

where the functions $S_{mn}^{(1)}$, $S_{mn}^{(2)}$, $R_{mn}^{(3)}$ and $R_{mn}^{(4)}$, are defined by Flammer (1957) and discussed in detail in a departmental report, (Hansen, 1979).

Equation (2.64) may be further simplified as follows. As the functions $S_{mn}^{(2)}(-ika,\eta)$ are infinite at $\eta = 1$ and it is necessary that the velocity potential Φ be finite everywhere in the acoustic fluid, the coefficients $A_{mn}^{(2)}$ are set equal to zero. Using the boundary condition that only outgoing waves (from the plate surface) are present, Alper (1970) showed that the radial function solution can be expressed as,

$$R_{mn}(-ika, i\xi) = B_{mn}^{(4)} R_{mn}^{(4)}(-ika, i\xi). \qquad (2.67)$$

By considering the boundary condition that the fluid velocity at the surface of the infinite baffle must be zero, Alper (1970) showed that only the even values of $(n-m)$ are admissible in solutions of equation (2.64). Thus equation (2.64) may be written in simpler form as,

$$\hat{\Phi}_{mn} = A_{mn} S_{mn}^{(1)}(-ika,\eta) . R_{mn}^{(4)}(-ika, i\xi)\, \Theta_m(\theta). \qquad (2.68)$$
$$(n-m) \text{ even.}$$

Summing all of the allowable solutions (and including time dependence) results in the following expression for the velocity potential Φ at a point (η,ξ,θ) in space;

$$\Phi(\eta,\xi,\theta,t) = \sum_{m=o}^{\infty} \sum_{n=m,\, m+2\ldots}^{\infty} A_{mn} S_{mn}^{(1)}(-ika,\eta) . R_{mn}^{(4)}(-ika, i\xi) . \Theta_m(\theta)\, e^{i\omega t}. \qquad (2.69)$$

The coefficients A_{mn} may be represented by $A_{mn} = \sum_{j=1}^{\infty} A_{mnj}$ where A_{mnj} is a coefficient corresponding to a particular resonant vibration mode mj and may be determined in terms of a single unknown constant, D_{mj}. When the plate is vibrating in a single resonant mode mj only the j^{th} coefficient in the infinite sum representation of A_{mn} need be considered

as all others are zero. Thus the velocity potential resulting from the plate vibrating in resonant mode mj may be written as follows,

$$\Phi_{mj}(\eta,\xi,\theta,t) = \sum_{n=m,\, m+2\ldots}^{\infty} A_{mnj} S_{mn}^{(1)}(-ika,\eta).R_{mn}^{(4)}(-ika, i\xi).\Theta_m(\theta)\, e^{i\omega t}. \qquad (2.70)$$

The quantities A_{mnj} may be evaluated by calculating the response of the plate vibrating resonantly in mode m,j and equating the normal fluid velocity (expressed in terms of A_{mnj}) at the plate surface with the plate surface normal velocity.

The dimensionless fluid velocity at the plate surface is found by evaluating the gradient of the velocity potential (given by Moon and Spencer, 1961) in the direction normal to the surface $\xi = 0$. The result, given by Alper, (1970) is as follows,

$$V_{\xi mj} = -(1/\eta)(\partial\Phi_{mj}/\partial\xi)/_{\xi=o} \qquad (2.71)$$

Substituting equation (2.70) into equation (2.71), differentiating and expressing the velocity in dimensional form gives,

$$v_{mj} = -(c_o/\eta) \sum_{n=m,\, m+2\ldots}^{\infty} A_{mnj} S_{mn}^{(1)}(-ika,\eta).R_{mn}^{(4)'}(-ika,0).\Theta_m(\theta)\, e^{i\omega t}. \qquad (2.72)$$

where the prime denotes differentiation with respect to ξ.

An expression for the plate normal surface velocity, calculated using Classical Plate Theory, is obtained by differentiating equation (2.3) with respect to time. The result expressed in dimensional form is,

$$v_{mj} = i\omega a\, D_{mj}\, H_{mj}(u).\Theta_m(\theta)\, e^{i\omega t}. \qquad (2.73)$$

Equating equations (2.72) and (2.73) (for continuity of velocity at the plate surface) gives,

$$-ika\,\eta\, D_{mj} H_{mj}(u) = \sum_{n=m,\, m+2\ldots}^{\infty} A_{mnj} S_{mn}^{(1)}(-ika,\eta).R_{mn}^{(4)'}(-ika,0). \qquad (2.74)$$

As is shown by Flammer (1957), the oblate spheroidal angular wave functions satisfy the following orthogonality property,

$$\int_o^1 S_{mn}^{(1)}(-ika,\eta).S_{mq}^{(1)}(-ika,\eta).d\eta = \begin{cases} o & n \neq q \\ N_{mn} & n = q \end{cases} . \qquad (2.75)$$

An expression for the coefficient N_{mn} is given by Flammer (1957) and is discussed in the report mentioned earlier, (Hansen, 1979a). Flammer has also shown that when (n-m) is even,

$$R_{mn}^{(4)'}(-ika,0) = -iR_{mn}^{(2)'}(-ika,0) . \qquad (2.76)$$

Using the properties expressed by equations (2.75) and (2.76) we may write equation (2.74) as,

$$kaD_{mj} \int_o^1 H_{mj}(u).S_{mn}^{(1)}(-ika,\eta)\eta d\eta = A_{mnj}N_{mn}R_{mn}^{(2)'}(-ika,0) . \qquad (2.77)$$

The cylindrical and oblate spheroidal coordinates are related as follows,

$$u^2 = 1-\eta^2 . \qquad (2.78)$$

Further, Flammer gives for the power series expansion of the oblate spheroidal angular wave function,

$$S_{mn}^{(1)}(-ika,\eta) = \sum_{x=o}^{\infty} C_{2x}^{mn} u^{m+2x} . \qquad (2.79)$$

Here equation (2.78) has been used to express the right hand side of the equation given by Flammer in terms of u instead of η. The coefficients C_{2x}^{mn} are defined by Flammer and discussed in the report mentioned earlier.

Using equations (2.78) and (2.79) the integral on the left hand side of equation (2.77) may be written as,

$$-e_{mnj} = -\sum_{x=o}^{\infty} C_{2x}^{mn} \int_o^1 H_{mj}(u)u^{m+2x+1}du , \qquad (2.80)$$

where the order of integration and summation have been interchanged. If M-T Plate Theory is used, the function $H_{mj}(u)$ is to be replaced by $H_{tmj}(u)$ [defined by equation (2.42)] in equations (2.74), (2.77) and (2.80).

Using equations (2.4) and (2.42) and series expansions for Bessel Functions, the coefficient e_{mnj} may be expressed as follows,

$$e_{mnj} = \sum_{x=o}^{\infty} C_{2x}^{mn} [E_{mx}(\pi\beta_{mj}) - J_m(\pi\beta_{mj}) G_{mx}(\pi\beta_{mj})/I_m(\pi\beta_{mj})]. \tag{2.81}$$

if Classical Plate Theory is used. For M-T Plate Theory the expressions are,

$$e_{mnj} = \sum_{x=o}^{\infty} C_{2x}^{mn} [E_{mx}(\delta_{1_{mj}} a) - J_m(\delta_{1_{mj}} a) E_{mx}(\delta_{2_{mj}} a)/J_m(\delta_{2_{mj}} a)] \tag{2.82}$$

if equation (2.38) is satisfied and,

$$e_{mnj} = \sum_{x=o}^{\infty} C_{2x}^{mn} [E_{mx}(\delta_{1_{mj}} a) - J_m(\delta_{1_{mj}} a) G_{mx}(\delta_{2_{mj}} a)/I_m(\delta_{2_{mj}} a)]. \tag{2.83}$$

if equation (2.39) is satisfied. In equations (2.81) to (2.83) the following relations are implied.

$$E_{mx}(\alpha) = \int_o^1 J_m(\alpha u)\, u^{m+2x+1}\, du = \sum_{r=o}^{\infty} \frac{(-1)^r (\alpha/2)^{m+2r}}{r!(m+r)!2(m+r+x+1)}, \tag{2.84}$$

$$G_{mx}(\alpha) = \int_o^1 I_m(\alpha u)\, u^{m+2x+1}\, du = \sum_{r=o}^{\infty} \frac{(\alpha/2)^{m+2r}}{r!(m+r)!2(m+r+x+1)}. \tag{2.85}$$

Recalling that equations (2.81) to (2.83) describe the left hand side of equation (2.77), we may write the following expression;

$$\frac{A_{mnj}}{D_{mj}} = \frac{-kae_{mnj}}{N_{mn} R^{(2)'}_{mn}(-ika,0)}. \tag{2.86}$$

The complex acoustic power radiated by the plate vibrating in mode (m,j) is obtained by the integration of the product of the acoustic

pressure and normal surface velocity over the plate surface and in time. The temporal integration is performed over one half cycle of vibration and results in a value for the average radiated sound power being given by half the value of the peak radiated sound power, which is obtained by integration over the plate surface of the product of the acoustic pressure and velocity amplitudes. Thus the expression for the average radiated sound power in dimensional form is given by,

$$W_{mj} = (a^2/2) \int_0^{2\pi} \int_0^1 \hat{p}_{mj}(\eta,0,\theta)\, \hat{v}^*_{mj}(\eta,0,\theta)\, \eta\, d\eta\, d\theta, \tag{2.87}$$

where the asterisk denotes the complex conjugate.

The acoustic pressure amplitude may be obtained by differentiating the expression for the dimensionless velocity potential at the plate surface with respect to time;

$$\hat{p}_{mj}(\eta,0,\theta) = i\omega a \rho_o c_o \hat{\Phi}_{mj}(\eta,0,\theta). \tag{2.88}$$

Using equation (2.71), the acoustic velocity amplitude may be written in dimensional form as,

$$\hat{v}_{mj}(\eta,0,\theta) = -(c_o/\eta)(\partial\hat{\Phi}(\eta,0,\theta)/\partial\xi). \tag{2.89}$$

Substitution of equations (2.88) and (2.89) into equation (2.87) gives,

$$W_{mj} = -i(\omega a^3 \rho_o c_o^2/2) \int_0^{2\pi} \int_0^1 \hat{\Phi}_{mj}(\eta,0,\theta)[\partial\hat{\Phi}^*(\eta,0,\theta)/\partial\xi]\, d\eta\, d\theta. \tag{2.90}$$

Using equation (2.76) the differential expression in equation (2.90) may be written as,

$$\partial\hat{\Phi}^*(\eta,0,\theta)/\partial\xi = \sum_{n=m,\, m+2\ldots}^{\infty} iA_{mnj} S^{(1)}_{mn}(-ika,\eta)\, R^{(2)'}_{mn}(-ika,0)\, \Theta_m(\theta). \tag{2.91}$$

The expression for the velocity potential amplitude at the plate surface may be written as,

$$\hat{\Phi}(\eta,0,\theta) = \sum_{n=m,m+2\ldots}^{\infty} A_{mnj} S_{mn}^{(1)}(-ika,\eta).R_{mn}^{(4)}(-ika,0)\Theta_m(\theta). \qquad (2.92)$$

Substituting equations (2.91) and (2.92) into equation (2.90), using the orthogonality properties of the oblate spheroidal angular wave function $S_{mn}^{(1)}(-ika,\eta)$ and rearranging terms we have,

$$W_{mj} = -i(\omega a^3 c_o^2 \rho_o \pi/\varepsilon_m) \sum_{n=m,m+2\ldots}^{\infty} A_{mnj}^2 N_{mn}[R_{mn}^{(4)}(-ika,0).iR_{mn}^{(2)'}(-ika,0)], \qquad (2.93)$$

where $$\varepsilon_m = \begin{cases} 1 \text{ if } m = 0 \\ 2 \text{ if } m \neq 0. \end{cases}$$

To derive equation (2.93) the following orthogonality property of the function $\Theta_m(\theta)$ has been used,

$$\int_0^{2\pi} [\Theta_m(\theta)]^2 \, d\theta = \begin{cases} 2\pi \text{ if } m = 0 \\ \pi \text{ if } m \neq 0. \end{cases} \qquad (2.94)$$

Using expressions given by Flammer (1957), equation (2.93) may be simplified and written as,

$$W_{mj} = (a^2 c_o^3 \rho_o \pi/\varepsilon_m) \sum_{n=m,m+2\ldots}^{\infty} A_{mnj}^2 N_{mn}[1 - ika\, R_{mn}^{(2)}(-ika,0).R_{mn}^{(2)'}(-ika,0)], \qquad (2.95)$$

where the following expressions have been used,

$$R_{mn}^{(4)}(-ika,0) = R_{mn}^{(1)}(-ika,0) - i\, R_{mn}^{(2)}(-ika,0), \qquad (2.96a)$$

$$R_{mn}^{(1)}(-ika,0).R_{mn}^{(2)'}(-ika,0) = 1/ka. \qquad (2.96b)$$

Equation (2.95) is complex and represents both the power flow into the acoustic medium and the power flow back and forth into the reactive near field. If we extend the meaning of power flow to include the reactive near field we may substitute equations (2.95) and either of (2.16b), (2.16c) or (2.48) into equation (1.1) to obtain an expression for the complex radiation efficiency of the (m,j) mode;

$$\sigma_{mj} = [1/(ka)^2 Q_{mj}] \sum_{n=m,m+2\ldots}^{\infty} [A_{mnj}/D_{mj}]^2 N_{mn} [1 - ika\, R_{mn}^{(2)}(-ika,0).R_{mn}^{(2)'}(-ika,0)]. \tag{2.97a}$$

Substitution of equation (2.86) into equation (2.97a) gives,

$$\sigma_{mj} = (1/Q_{mj}) \sum_{n=m,m+2\ldots}^{\infty} [e_{mnj}/R_{mn}^{(2)}(-ika,0)]^2 [1 - ika\, R_{mn}^{(2)}(-ika,0).R_{mn}^{(2)'}(-ika,0)]/N_{mn}, \tag{2.97b}$$

where for clamped edge plates and Classical plate theory,

$$Q_{mj} = J_m^2(\pi\beta_{mj}), \tag{2.98a}$$

for simply supported edge plates and Classical plate theory

$$Q_{mj} = J_m^2(\pi\beta_{mj})\, P_{mj}, \tag{2.98b}$$

and for clamped edge plates and M-T plate theory

$$Q_{mj} = g_{mj}. \tag{2.98c}$$

Equation (2.97b) may also be expressed in terms of the ratio of acoustic wave number k to plate bending wave number k_b calculated using equations (2.57) and (2.58).

We let,

$$k/k_b = \ell_w. \tag{2.99}$$

Substituting equation (2.99) into equation (2.97b) provides the

alternative expression,

$$\sigma_{mj} = (1/Q_{mj}) \sum_{n=m,m+2\ldots}^{\infty} \{[e_{mnj}/R_{mn}^{(2)}(-ik_b a\ell_w,0)]^2$$

$$\times [1-i(k_b a)\ell_w R_{mn}^{(2)}(-ik_b a\ell_w,0)R_{mn}^{(2)'}(-ik_b a\ell_w,0)]/N_{mn} \}. \qquad (2.100)$$

2.3.3 Numerical Results

Equations (2.98) and (2.100) were evaluated using a CDC 6400 computer. Details of the calculation methods and computer programs are contained in a Departmental report (Hansen, 1979a). Calculations were carried out for the first seven low order modes of a clamped edge plate using both Classical and M-T theories for plate response. Calculations were also carried out for a simply supported edge plate for the same modes and over the same frequency range as for the clamped edge plate. However, in this case only Classical plate theory was used to calculate the plate response.

During the course of numerical evaluation of equations (2.98) and (2.100) it was found that the infinite sums in these equations converged more slowly for the imaginary part than for the real part of the radiation efficiency. Furthermore, it became increasingly difficult to calculate high order terms in this infinite sum as the values of ka grew large. Thus there was an upper limit to the value of ka for which it was possible to calculate the radiation efficiency with acceptable accuracy. This upper limit was dependent upon mode order and was above 20 for the real part and between 16 and 20 for the imaginary part of the radiation efficiency when Classical plate theory was used to calculate the plate response. The upper limit was still above 20 for the real part but was reduced to between 12 and 16 for the imaginary part when M-T theory was used to calculate the plate response. By contrast, evaluation of the real part of the radiation efficiency based upon the

Rayleigh integral solution of Appendix 1 suffered from no such limitation and calculations were carried through to a ka of 40. The numerical results for the two methods of calculating the real part of the radiation efficiency are identical.

The convergence of the infinite sums in equations (2.98) and (2.100) is discussed in detail in the previously referenced report (Hansen 1979a). Over the range of ka values for which numerical values were obtained for the real and imaginary parts of the radiation efficiency the difference in values obtained using the Classical plate response and the M-T plate response theories was less than 0.27%. The line plots of the two theories are thus indistinguishable in Figures 2.5 and 2.6.

The numerical results are presented in Figs. 2.5 and 2.6 as plots of radiation efficiency as a function of the wave number ratio (k/k_b) for each of the vibration modes considered. Results are shown for both simply supported and clamped edge plates and for both real and imaginary parts of the radiation efficiency. A value of (k/k_b) equal to unity corresponds to the critical frequency of the plate, and it can be seen from the figures that for all modes the maximum value of the radiation efficiency occurs at a frequency just above the critical frequency.

2.4 THE EXPERIMENTAL MODEL

2.4.1 Choosing a Suitable Range of Plate Sizes

For the purposes of the experimental investigation of the radiation of a circular flat plate it was desirable to carry out tests over as wide a frequency range, ka, as possible, but from the point of view of the construction of the plates and associated mounting fixtures it was desirable to restrict the radii of the plates tested to a few in number.

Examination of the theoretical expressions presented earlier in this chapter shows that for a given mode of vibration, σ_{mj} is a function

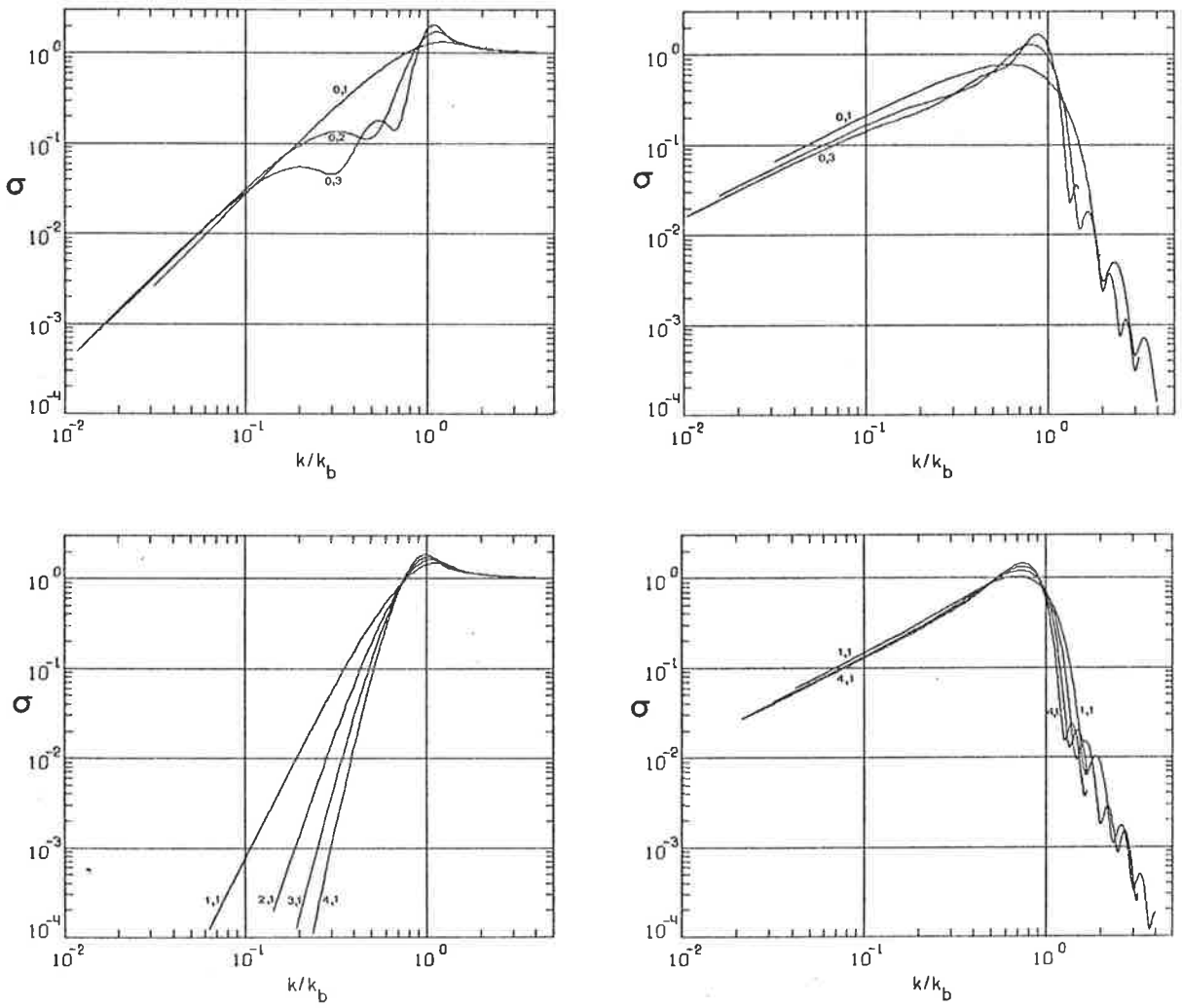

RESISTIVE REACTIVE

FIG. 2.5. PREDICTED RESISTIVE AND REACTIVE RADIATION EFFICIENCIES FOR THE FIRST SEVEN LOW ORDER MODES OF A CLAMPED EDGE CIRCULAR PLATE AS A FUNCTION OF THE WAVE NUMBER RATIO k/k_b.

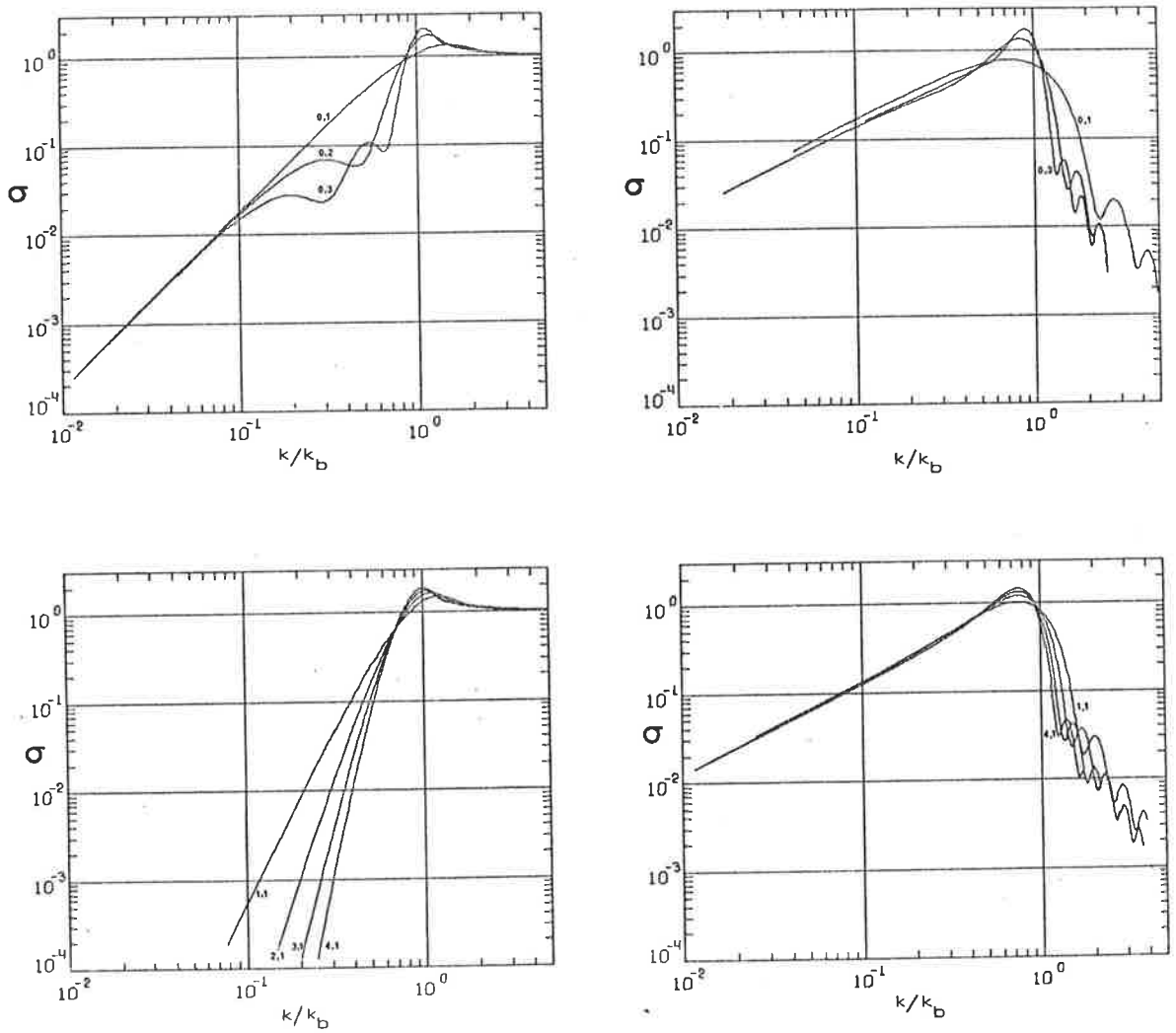

RESISTIVE REACTIVE

FIG. 2.6 PREDICTED RESISTIVE AND REACTIVE RADIATION EFFICIENCIES FOR THE FIRST SEVEN LOW ORDER MODES OF A SIMPLY SUPPORTED EDGE CIRCULAR PLATE AS A FUNCTION OF THE WAVE NUMBER RATIO k/k_b.

of the dimensionless frequency (ka) which, in turn (using equation 2.21), can be shown to be directly proportional to the plate thickness to radius ratio, (h/a). That is,

$$ka = [\pi^2\beta_{mj}^2/2c_o][E/3\rho(1-\nu^2)]^{\frac{1}{2}}[h/a] \quad . \tag{2.101}$$

As a practical alternative it was decided to obtain a range of ka values for a given vibration mode by varying the plate thickness rather than the radius while at the same time keeping the plate properties constant.

The plate material chosen was steel as it could be excited by non-contacting means electromagnetically, thus minimizing the effect of the exciter on the plate response.

The matter of the plate edge condition presented a problem which was not entirely overcome. A compromise was necessary. On the one hand for thin plates it is readily possible to simulate a clamped edge, while for thick plates this is not entirely possible. On the other hand while a construction is possible to implement a supported edge condition for thick plates none seems to be possible for thin plates. Since most of the plates investigated in this thesis were thin, the edge clamped condition was chosen for the test models. However it is recognized that the condition was poorly satisfied for the thickest plates corresponding to the highest frequencies tested. Indeed a tendency is observed for the measured radiation efficiencies at high frequencies to be consistently somewhat higher than predicted. This tendency is discussed in section 5.3.

The optimum plate radius for the experiments was chosen by applying the following limiting conditions.

1. The plate thickness had to be greater than approximately 0.7 mm to ensure that environmental temperature fluctuations did not cause a large enough distortion in the plate to make the modal resonant frequency and hence the plate response alter significantly when either

holograms or sound power measurements were made.

2. The maximum thickness rolled steel plate available was 6.5 mm. Rolled steel plate was preferred because of its small thickness variations which eliminated any need for machining.

3. The maximum driving force was restricted to that obtainable using practical electromagnetic exciters.

4. The minimum value of the modal response amplitude should be about 0.6 micrometers. This corresponds to a vibration amplitude which would produce four interference fringes on a reconstructed image of a time averaged hologram.

5. The plate resonant frequencies should be kept above about 300Hz to ensure that sound power measurements can be made accurately in the available reverberant room.

The plate radius chosen to best satisfy the above constraints was 3 inches or 0.0762 m.

For higher order modes containing one or more diametral nodes, two diametrally opposite exciters were used resulting in twice the driving force as used to excite the 0,1 mode. However, the resonant frequencies of these higher order modes were also greater which resulted in the maximum thickness of the plate which could be excited sufficiently, to decrease as the mode order increased. In some instances it was possible to excite higher order modes on some of the thicker plates sufficiently to make a sensible sound power measurement, even though it was not possible to excite the plates sufficiently for holographic analysis. In these cases it was assumed that the velocity ratio ($\langle v^2 \rangle_{st} / \hat{v}_A^2$) mentioned earlier was identical to that in column 6 of table 3.2. This assumption appears justifiable if the theoretical results shown in Fig. 2.1 are considered, and it is noted that the thickest plate used in the experimental work was 6.5 mm (corresponding to $h/a = 0.085$).

The number of test plates (and corresponding maximum plate thicknesses) used for holographic analysis and sound power measurements

are listed in table 2.3 for each vibration mode considered.

In addition to the 0.0762 m radius plates, there were also some 0.1755 m radius plates available from a previous experiment. The radiation efficiencies of the first few vibration modes of these plates were also measured and the results are included with those for the small plates in the figures of chapter 5.

2.4.2 Experimental Configuration

The plates used in all experiments were clamped at the edges between two clamping rings. The outer clamping ring was chosen to be as thin as possible to minimize any effect on the acoustic radiation and thick enough to provide adequate clamping of the plate edge. The clamping ring thicknesses used are listed in table 2.4.

Table 2.4 : Clamping Ring Thicknesses

Plate Radius (mm)	Plate thickness (mm)	Inner clamping ring thickness (mm)	Outer clamping ring thickness (mm)
76.2	> 3.2	31	12
76.2	⩽ 3.2	31	6.5
175.5	all thicknesses	25	12

The plate, clamped between these two rings was bolted to a heavy iron casting (weighing about 80 kg). This arrangement was used for all holographic measurements and also when the plate was mounted in a side wall of the reverberant room. For some sound power measurements the clamping rings and plate were bolted to one end of a tube (closed at the opposite end). The tube used for the large plates was approximately 1.5 m long and weighed about 115 kg,while the tube used for the small plates was the same

Table 2.3 : Experimental Test Plates

Mode	h_1(mm)	h_2(mm)	$(ka)_1$	$(ka)_2$	$(ka)_{min}$	N_1	N_2
0,1	6.5	6.5	3.32	3.32	0.38	11	11
0,2	3.2	6.5	6.66	12.12	1.63	9	11
1,1	1.83	3.20	2.11	3.59	0.91	7	9
2,1	1.83	2.51	3.45	4.60	1.43	7	8
3,1	1.46	2.51	4.05	6.72	2.17	5	8
4,1	1.12	1.46	4.36	5.55	2.98	3	5

h_1 = Maximum thickness of plate which can be excited with the available driver system to an amplitude corresponding to four holographic fringes.

h_2 = Maximum thickness of plate which can be excited with sufficient amplitude to give a sound pressure level in the reverberation room at least 8dB above the background SPL. for the particular $\frac{1}{3}$ - octave band.

$(ka)_1$ = Value of ka corresponding to plate with a thickness of h_1.

$(ka)_2$ = Value of ka corresponding to plate with thickness h_2.

$(ka)_{min}$ = Value of ka corresponding to thinnest plate to be used (.79 mm thick).

N_1 = Number of different plates of radius 76.2 mm used in holographic analysis.

N_2 = Number of different plates of radius 76.2 mm used for sound power measurements.

length and weighed about 18 kg.

The plate exciting mechanism consisted of an electro-magnet surrounded by a permanent magnet. The electro-magnet, when driven sinusoidally by an oscillator, modulated the magnetic field of the permanent magnet in a cyclic manner, thus allowing the plate to vibrate at the same frequency as the signal from the oscillator.

When modes with no diametral nodes were driven, a single electromagnetic driver mounted at the plate centre was used. When modes with diametral nodes were driven, two electro-magnetic drivers were used; one on each of two diametrally opposite antinodes. When the vibration mode had an odd number of diametral nodal lines, the exciters were driven in phase and when the mode had an even number of diametral nodal lines, the exciters were driven 180° out of phase.

The angular position of the antinodes was theoretically arbitrary but in practice it depended on the properties of the particular plate and clamping rings and thus varied from plate to plate. It was therefore desirable to be able to rotate the driving mechanism to any required angular position. This was achieved using two bars.

One of the bars was fixed across a diameter of the inner plate clamping ring and the other bar (to which the exciters were attached) was joined to the first with a single bolt at the centre and thus was free to rotate. As the support for the plate exciters was attached to the inner plate clamping ring, it was possible to move the clamped plate from the casting to the pipe without changing the boundary conditions or exciter positions.

The plate exciters were driven through a 25 watt audio amplifier by a Muirhead model D-650-B oscillator which had an hourly frequency stability of 0.02% and an amplitude stability of better than 1%. The system stability was sufficient to ensure a stable enough plate response for holographic analysis. Temperature stability in the medium surrounding

the plate had a major influence on the stability of the plate response. Temperature fluctuations caused stresses to be induced in the clamped plate which caused slight changes in modal resonant frequency resulting in changes in vibration amplitude when a constant excitation frequency was used. Temperature fluctuations of fractions of a degree centigrade were sufficient to affect the plate response by more than 3dB in some cases. As might be expected the thinner plates were affected to a greater extent than were the thicker ones. In the optical laboratory, where the holography experiments were conducted, the temperature stability was sufficient to ensure negligible effect on the plate response during the hologram exposure time of a few seconds. However when sound power measurements were made in the reverberant room, it was found necessary to continually adjust the plate exciting frequency to maintain maximum plate response for a given exciter input voltage.

When higher order vibration modes were being driven, it was necessary to ensure that lower order modes (which, in general, had a higher radiation efficiency) were not being forced and the motion superimposed on that of the higher order mode. This requirement was satisfied most effectively by exciting the mode of interest at one or more of its vibration antinodes. As a check, the acceleration at the plate centre was monitored to ensure that the response of the lowest order mode (which was likely to be the chief forced contributor) was negligible.

Positioning the exciters at antinodes of vibration for modes containing diametral nodal lines presented a problem, as the angular position of the nodal diameters varied from plate to plate. The angular position of the nodal diameters was found experimentally for each mode of interest on each plate investigated by scanning the acoustic field near the plate with a ¼ inch Bruel and Kjaer condenser microphone. The microphone output was amplified and monitored together with the input signal to the plate exciters on a dual beam oscilloscope. The nodal diameters were located

where the phase between the two signals underwent a 180° shift.

The angular positions of the antinodes were found by bisecting the angle between two adjacent nodal diameters. The radial positions of the antinodes measured experimentally (using an accelerometer) agreed well with theoretical predictions for the plates which were tested. These values (calculated using Classical Plate Theory) may be found in table 2.5. Values for simply supported edge plates are included for interest. For the range of plate thicknesses considered, the difference between Classical Plate Theory and M-T Plate Theory predictions was always less than ½%.

Table 2.5 : Radial Positions of Vibration Antinodes for Simply Supported and Clamped Edge Circular Plates

Mode (m,j)	u_A (clamped edge)	u_A (simply supported edge)
1,1	0.4102	0.4892
2,1	0.5258	0.6010
3,1	0.5948	0.6631
4,1	0.6424	0.7043

The resonant vibration modes of interest were identified by observing a peak in the response of an accelerometer placed near the position of the expected vibration antinode, as the plate exciting frequency was adjusted above and below the theoretically predicted resonant frequency for the particular mode under consideration.

2.4.3 Modal Resonant Frequencies

The experimentally measured plate resonant frequencies are compared to theoretical predictions for the first six low order plate vibration modes in Figs. 2.7(a) and (b). Theoretical predictions for clamped edge plates using both Mindlin-Timoshenko and Classical plate theory are included for comparison.

It was found desirable to coat the plate surface with a thin layer of retro reflective paint or sheet to obtain good quality holograms. Generally the effect of the surface coating (whether it be adhesive sheet or paint) was to slightly increase the plate stiffness and hence increase the modal resonant frequencies by between 1% and 2% and increase the modal damping by a small amount. The effect, as might be expected, was more noticeable on the thinner plates.

Placing the plate at the end of a tube also increased the resonant frequency, over that measured when the plate was mounted in the room wall, by between 1% and 2%. This was caused by the air in the tube having a stiffening effect on the plates, and this effect increased as the plate thickness decreased. The effect of placing a ½ gram accelerometer on a vibration antinode generally resulted in a decrease in the modal resonant frequency of between ½% and 1% and again the effect was greater for the thinner plates. Most of the experimentally measured resonant frequencies in Fig. 2.7 are much less than those predicted theoretically, which may indicate that the plate edges in the experimental model were not sufficiently clamped. This is supported by the fact that the modal resonant frequencies predicted for simply supported edge plates are much less than those for the same mode on clamped edge plates. The discrepancies between theoretical predictions and experiment are largest for the thicker plates for which it was most difficult to provide a secure clamp.

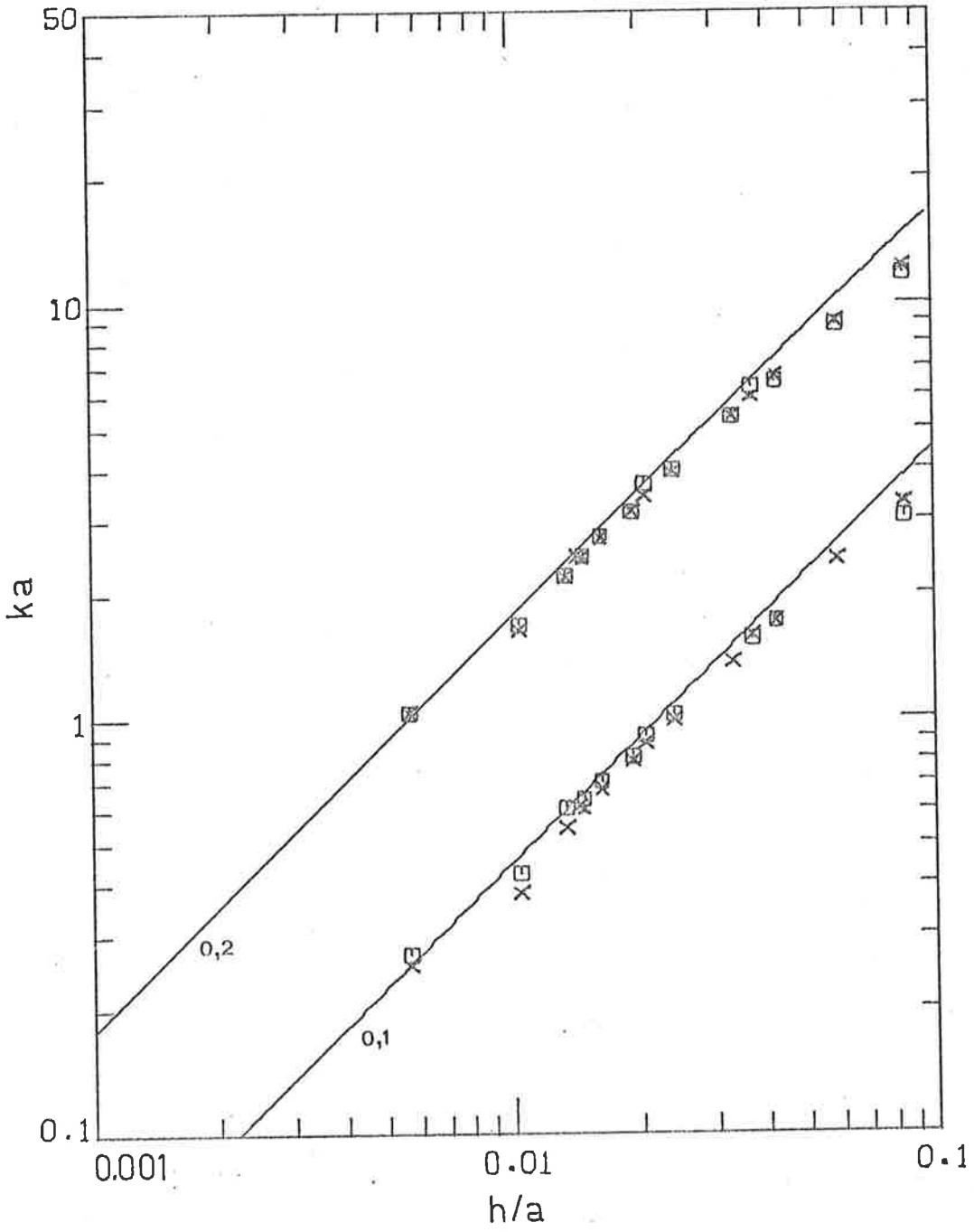

X = DATA FOR PLATES MOUNTED IN REVERBERANT ROOM WALL.
⊡ = DATA FOR PLATES MOUNTED IN END OF TUBE IN REVERBERANT ROOM.
—— = M-T PLATE THEORY.

FIG.2.7a DIMENSIONLESS FREQUENCY AS A FUNCTION OF PLATE SIZE FOR MODES WITH CIRCULAR NODES.

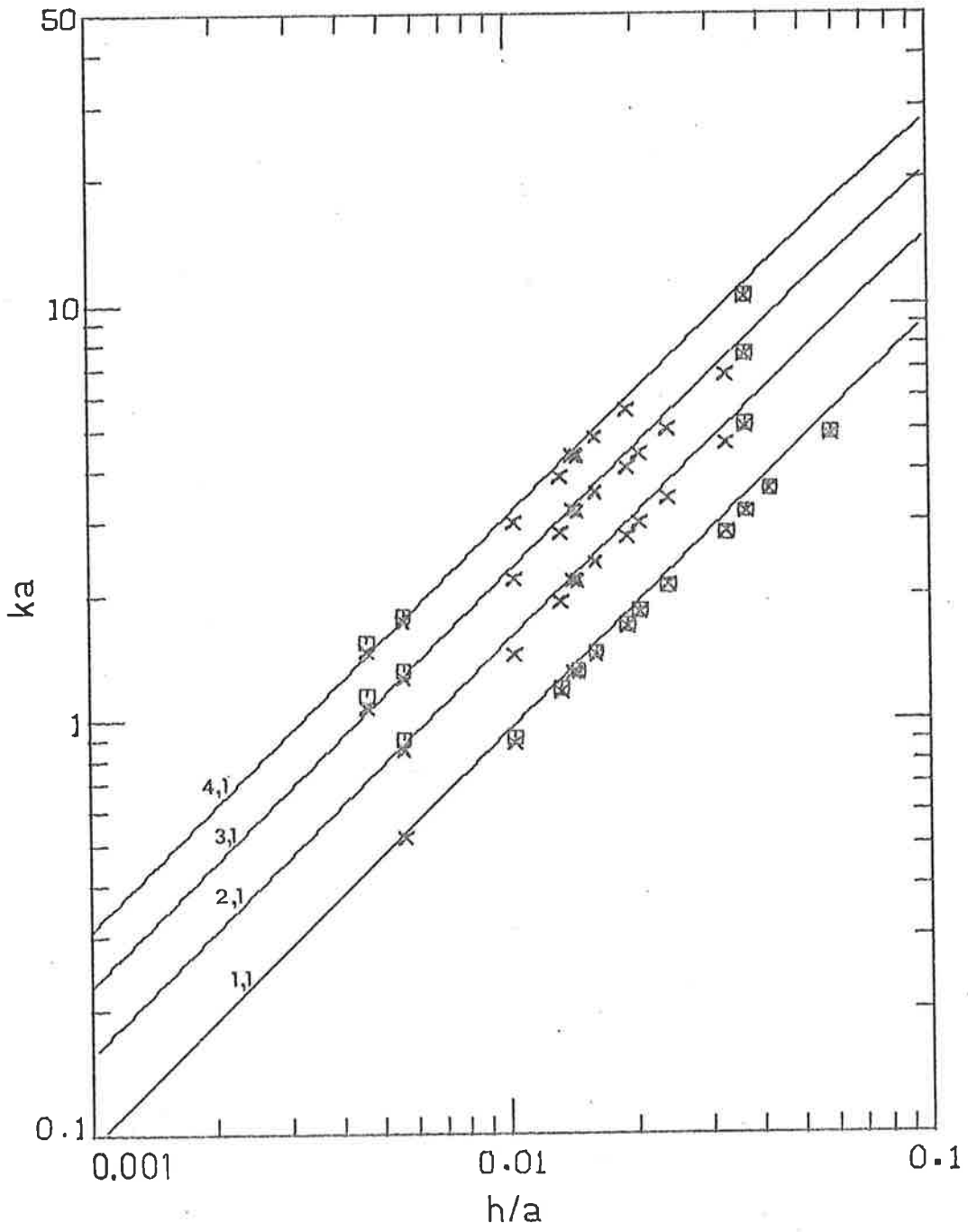

× = DATA FOR PLATES MOUNTED IN REVERBERANT ROOM WALL.
⊡ = DATA FOR PLATES MOUNTED IN END OF TUBE IN REVERBERANT ROOM.
—— = M-T PLATE THEORY.

FIG. 2.7b DIMENSIONLESS FREQUENCY AS A FUNCTION OF PLATE SIZE FOR MODES WITH DIAMETRAL NODES.

2.5 SUMMARY

The theoretical analysis and development of an experimental model of a clamped edge circular flat isotropic plate mounted in an infinite rigid baffle have been discussed in detail. The predictions for the plate response have been made using both Classical and M-T plate theories and expressions have been derived for the plate resonant freqquencies, vibration mode shape functions and modal velocity ratios ($\langle v^2 \rangle_{st} / \hat{v}_A^2$). Numerical results for the mode shape functions and resonant frequencies of the first seven lowest order modes of vibration calculated using Classical plate theory did not significantly differ from those calculated using M-T plate theory. The corresponding experimental values of the modal resonant frequencies did, however, consistently fall below the predicted values by between 0.8% and 18.9% with most values less than 10% below the predicted ones.

This discrepancy between theoretical and experimental resonant frequencies at high frequencies was attributed to the lack of sufficient clamping of the plate edge.

As the experimental results led to the suspicion that the clamped edge condition of the experimental model was not sufficiently realized, it was decided to derive and numerically evaluate expressions for the predicted response of a simply supported edge plate (using only Classical plate theory). These results are compared in the text with both the experimental measurements and theoretical predictions for the clamped edge plates, and tend to support the hypothesis that the plate edges in the experimental model were not sufficiently clamped.

Using the expressions derived for the clamped and simply supported plate responses, expressions were derived for the radiation efficiency of any given mode by solving the scalar wave equation in the acoustic field adjacent to the plate using the oblate spheroidal

coordinate system. The expressions so obtained were evaluated using a computer to obtain numerical results for both the real and imaginary parts of the plate radiation efficiencies. The numerical results for the real part of the radiation efficiency were identical with those calculated using the Rayleigh Integral approach discussed in appendix 1.

CHAPTER 3

TIME AVERAGED HOLOGRAPHY

3.1 INTRODUCTION

Optical holography is the process whereby all the optical information about an object is stored on a photographic plate which can later be used to reconstruct in full three dimensional detail, an image of the original object, simply by illuminating the photographic plate (hologram) with coherent light. Time averaged holography is a special form of optical holography suitable for the study of a cyclically vibrating surface.

Time averaged optical holography has been shown to provide elegant displays of modal response in vibrating structures (Powell and Stetson, 1965; Monahan and Bromley, 1968; Evensen and Aprahamian, 1970; Stetson and Taylor, 1971; Wilson and Strope, 1970; Molin and Stetson, 1969; Liem, Hazell and Blasko, 1973; Khanna, Tonndorf and Janecka, 1973; Fagan, Waddell and McCracken, 1972). If the directions of illumination and observation of a vibrating surface are properly chosen, the optical fringe pattern can be readily interpreted to accurately describe the displacement (or equivalently the velocity) amplitude over the vibrating surface (Brown, Grant and Stroke, 1969; Tonin and Bies, 1977). Time averaged holography thus provides a ready means for mode identification, the determination of mode distortion or equivalently the presence of other forced modes, and for the determination of the mean square normal velocity averaged in time and over the vibrating surface. Although the limited dynamic range may be overcome using strobed illumination of the surface (Watrasiewicz and Spicer, 1968; Shajenko and Johnson, 1968; Archbold and Ennos, 1968; Zaidel, 1969; Fryer, 1970; Vikram, 1972), the

process is limited to a single frequency.

The theoretical basis of holography is discussed in detail in the literature and has been reviewed by the author (1979b) and also by Tonin (1978). Therefore only a description of the photographic process will be given here.

A hologram is formed by the interference, on the surface of a photographic plate, of two light waves originating from a single coherent source. One wave, the object wave, is reflected from the object while the second wave, the reference wave, may be either a plane or spherical wave. If the object has a diffusely reflecting surface, then each point on the surface acts as a point source, contributing some light to each part of the object wave front. The interference pattern formed by combining the object and reference light waves is recorded as a variation in opacity of the developed plate which is referred to as a hologram.

As each point on the diffusely reflecting object surface contributes some light to each part of the object wave front, every point on the hologram must contain all of the optical information about the object Thus if the hologram is damaged in one part, no information is lost and the reconstructed image of the original object, although suffering a loss in intensity and resolution, is no less complete.

When the hologram is illuminated by the original reference beam (reference wave) three light waves are transmitted. One is an undiffracted wave containing no information about the original object. Another is a diffracted wave converging to a real, psuedoscopic (or depth inverted) image of the original object and the third is a diffracted wave diverging from a virtual image of the original object. It is this third wave which is a complete reconstruction of the light reflected by the original object.

When the procedure is repeated as described above for a cyclically vibrating object, a time averaged hologram is formed. The recon-

structed image is a combination of all of the object images between the two extremes of vibration. The positions at which the vibrating object (or surface) spends most of its time (extremes of vibration for a sinusoidally vibrating object) contribute most to the reconstructed image. As the reconstructing light wave is coherent, the combination of all of these different object images results in an image of the original object covered with a series of light and dark fringes. Interpretation of the fringes allows the vibration amplitude at any point on the object surface to be determined. For an object vibrating sinusoidally the resulting intensity distribution on the reconstructed image is (Hansen, 1979b, Tonin, 1978),

$$I_v = I_o J_o^2[(2\pi/\lambda_\ell)\hat{y}\ (\cos\theta_i + \cos\theta_r)]. \qquad (3.1)$$

If a hologram is to have optimum diffraction efficiency and image quality several practical requirements must be satisfied. Firstly there is a need for good thermal and mechanical stability in the experimental arrangement. The stability should be such that during the hologram recording time the relative movement between the reference and object light waves is less than about a tenth of the wavelength of light being used. This usually implies that the experiments should be performed in a carefully air conditioned room on a table well isolated from floor and building vibrations. Secondly, the difference in path length between the reference and object light waves should be as small as possible and certainly well within the coherence length of the laser light source being used. This condition limits the maximum size of objects which can be recorded. Thirdly, the ratio of the intensity of the reference wave to object wave should be large enough to prevent any non-linear recording (resulting in image "noise"). However, it is desirable to have this intensity ratio as small as possible to maximize the hologram diffraction efficiency. The intensity ratio generally accepted for holograms of

stationary objects is between four and seven. For vibrating objects the intensity ratio required to make non-linear effects negligible is smaller and is dependent only on the nodal area of the vibrating surface (Butusov, 1974) and in some cases may be as low as one. Fourthly, the image quality and resolution is degraded by what is referred to as the speckle effect. In general terms this effect causes the image quality and resolution to become poorer as either the size of the hologram or the size of the aperture used to view the image decreases.

3.2 HOLOGRAPHIC TEST ARRANGEMENT

As mentioned earlier, an important requirement in any holographic system is extremely good mechanical and thermal stability, a requirement which cannot be over-emphasised. Good mechanical stability was achieved for the work described in this thesis through the design, construction and use of a large vibration isolated optical table. Thermal stability was achieved by air conditioning the optics laboratory and by giving special attention to the elimination of thermal currents over the surface of the optical table.

The condition of mechanical stability required that the table supporting the optical equipment and vibrating object be effectively isolated from floor vibrations and that the vibrating object be effectively isolated from the table. The existing table top (1.8m×1.2m×.064m) and frame were made of steel and weighed in excess of 1300 kg. Initially ordinary viscous vibration isolators were used to isolate the table from the floor, but these did not provide sufficient isolation from ground vibrations. Good isolation was achieved using an air spring suspension system constructed as follows. The original isolators were replaced with a wooden base board under which were placed four 14 inch diameter car tyre inner tubes supported in cut-a-way tyre casings.

To simplify the task of inflating the tubes from time to time the valves were extended using a plastic tube passed through holes in the base board supporting the table. The total weight supported by the four inner tubes was approximately 1700 kg. The combination of table mass plus inner tube support gave the resonant frequencies for the lowest order table modes of vibration shown in Table 3.1. The times required for these modes to decay by 60 decibels is also shown in the last column of the table. In the table, vertical refers to vibration perpendicular to the table top , transverse refers to vibration side to side in the direction of the table width and longitudinal refers to vibration back and forth along the table length.

Table 3.1 : Resonant frequencies of holographic table and support system

Fundamental Vibration Mode	Resonant frequency (Hz)	Decay time (secs)
Vertical	3.3	6.5
Transverse	0.8	60
Longitudinal	1.2	30

From Table 3.1 it can be seen that equipment on the table is effectively isolated for all floor vibration frequencies above about 5Hz. As the significant part of the floor vibration occurred in the 10Hz to 20Hz frequency range, the system could be used to take good quality holograms any time of the day. The 60dB decay time gives an indication of how long the table takes to settle down if it is accidentally bumped.

The problem of isolating the vibrating object was much easier to solve because of the higher frequencies involved. The vibrating plates were effectively isolated by clamping them to a heavy iron casting which, as previously explained, also helped to provide a clamped, non-moving boundary for the plate edge. The iron casting was allowed to sit directly on the table, as the vibration transmitted by the plate through to the table was negligible. However, when larger objects (such as an engine block) were investigated they were mounted directly on to a heavy cast iron slab (weighing 320 kg) which was isolated from the table top using commercial rubber pads which had good isolating ability for frequencies above about 100 Hz. The load on the isolating pads was about 550 kN/m^2.

Temperature instabilities in the room caused both object deformation and deformation of the table supporting the optics. However, it was found that the former was the most significant, and the thinnest plates suffered the greatest deformation for a given temperature change. Temperature changes of less than $\frac{1}{2}°C$ during the hologram exposure time were found to significantly affect the result (see Fig. 3.8), even for plates with a thickness to radius ratio of 10^{-2}. For this reason it was necessary to cover the laser in such a way that the heat from it was convected well away from the object and table, while at the same time minimizing the escape of stray light. To eliminate the possibility of any other thermal air currents affecting hologram quality, the air conditioner was switched off during the relatively short hologram exposure time. The quality of the holograms produced was further improved by coating the object surface with retro reflective paint and using the experimental arrangement illustrated in Fig. 3.1.

Referring to Fig. 3.1, light from a 15mW HeNe laser 1 is split at

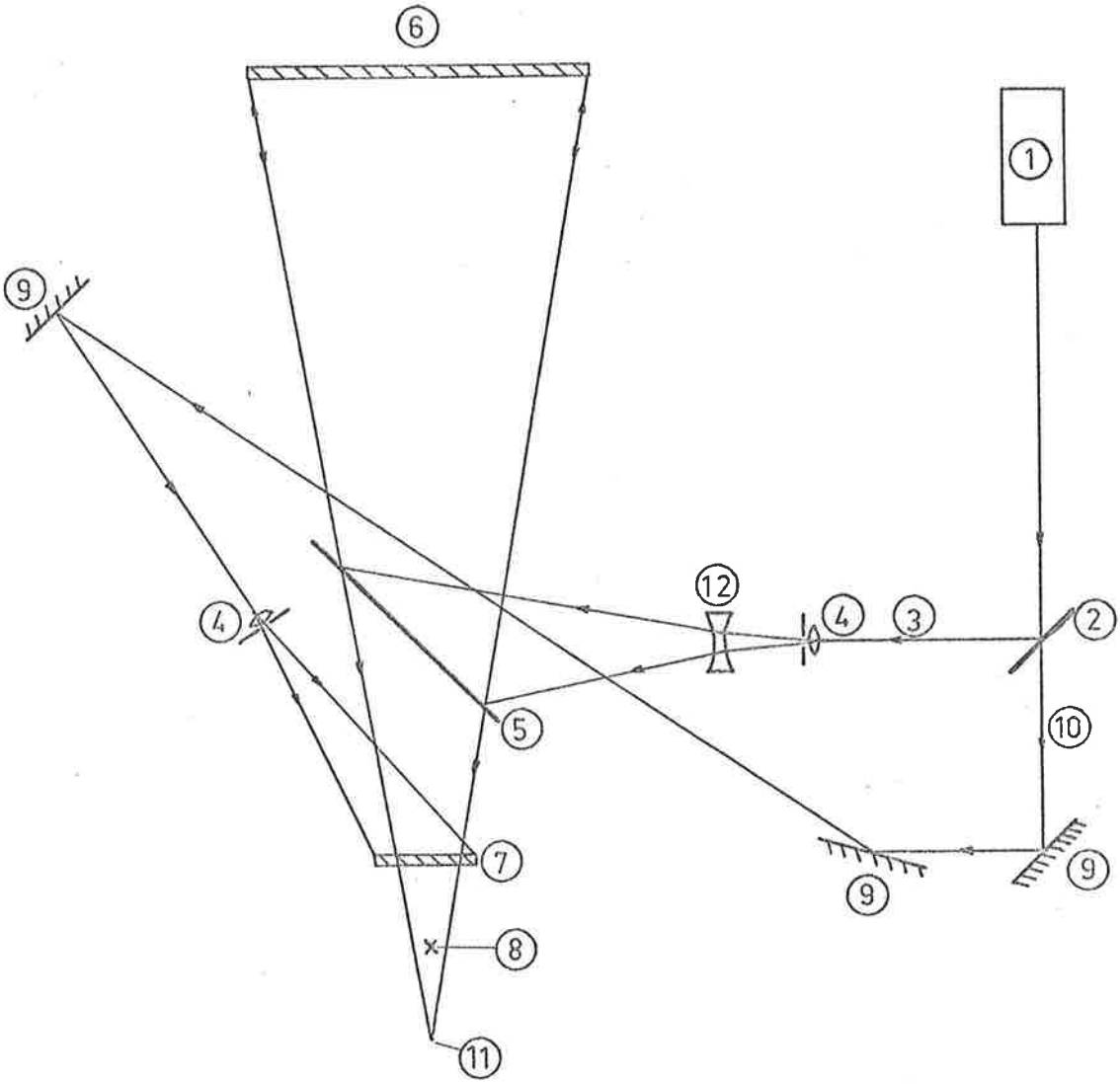

FIG. 3.1 EXPERIMENTAL ARRANGEMENT FOR MAKING TIME AVERAGED HOLOGRAMS.

1.15 milliwatt Helium Neon laser. 2.Variable density beam splitter. 3.Object beam. 4.Spatial filter and beam expander. 5.Partial reflector. 6.Vibrating plate (object). 7.Photographic plate. 8.Viewing point for photographing the holographically reconstructed image. 9.Mirrors. 10.Reference beam (about twice the intensity of the object beam). 11.Focal point of light reflected from retro painted object. 12.Beam expanding lens.

a variable beam splitter 2 into reference and object beams with any required intensity ratio. The object beam is expanded and spatially filtered using a lens pinhole combination 4 and is then reflected by both front and rear surfaces of beam splitter 5 (an ordinary sheet of plate glass placed at a 45 degree angle to the incident beam, reflecting 25% of incident light and transmitting 70%), on to the vibrating surface. Some of the light incident on the vibrating surface is reflected back in the direction from whence it came and again is incident on beam splitter 5 which transmits 70% of it to the photographic plate 7.

The reference beam is first reflected from mirrors 9 then expanded and spatially filtered and finally combined at the surface of the photographic plate with the light reflected from the vibrating object. The hologram is made by exposing the photographic plate for a time dependent on the intensity level at the surface of the photographic plate and the plate sensitivity (see Pierattine and Righini, 1976).

Prior to taking the hologram the following steps were necessary.

1. The object was placed far enough from the photographic plate so that the whole image could be photographed with a 35 mm camera placed immediately behind the photographic plate.

2. A suitable concave lens 12 was then inserted between the spatial filter 4 and beam splitter 5 to ensure that the expansion of the object beam was sufficient to adequately cover the object.

3. The reference to object beam intensity ratio measured at the surface of the photographic plate was adjusted to between one and three (Butusov, 1974) for vibrating objects and to between four and seven for stationary objects.

4. The path difference between the reference and object beams was made as small as possible.

5. A selenium cell connected to a digital volt meter was used to ensure that the illumination was essentially uniform over the surface

of the photographic plate.

6. The required exposure time was determined from a photometer reading at the photographic plate surface and a knowledge of the photographic emulsion sensitivity.

7. The laser shutter was closed, the photographic plate put into position, the air conditioner turned off and the table allowed to settle for some minutes before the photographic plate was exposed and then developed to form a hologram.

The experimental arrangement described above allowed the vibrating surface to be illuminated and viewed normally thus allowing simpler analysis of the fringe pattern on the holographically reconstructed image. It is important to note that in any experimental arrangement it is desirable to minimize the number of spatial filters, beam expanders, beam splitters and mirrors (especially in the object beam) because all result in considerable light intensity losses.

However the main advantage gained by using the arrangement of Fig. 3.1 was that it maximized the intensity of the light reflected from the object when it was coated with retro reflective sheet or paint, (Fagan et al, 1972). This was because the retro reflective surface reflected a large proportion of the incident light back in the direction from whence it came, resulting in higher object beam intensities at the photographic plate than would be possible if non-normal object illumination was used and beam splitter 5 was eliminated, (see Fig. 3.1). Use of the retro reflective paint reduced the required photographic plate exposure time from 15 seconds to 7 seconds for the large plates and from 6 seconds to 3 seconds for the small plates where a reference to object beam ratio of between two and three was used. Use of the reflective sheet instead of the paint reduced the exposure time by a further 50%. As the retro reflective paint and sheet preserves the polarity of the light incident on it, much better fringe contrast is obtained in real time holography

and the reconstructed images from time averaged holograms are much brighter. In addition to preservation of polarity of the reflected light, the retro reflective surface coating focusses the reflected light back to the focal point of the expanding lens but more importantly, with the arrangement of Fig. 3.1, to a point equally distant behind the photographic plate (point 11) and behind the viewing point 8 as illustrated. Thus careful adjustment of the concave lens position ensures optimum brightness of the reconstructed image when viewed or photographed at the viewing point.

As mentioned earlier the effect of the reflective sheet and paint on the plate resonant frequencies was small and as will be shown in the next section the effect on the vibration mode shape was negligible, in fact, it was not measurable. Also it will be shown that the difference in the experimental data describing the modal amplitude distributions along antinodal diameters for both coated and uncoated plates is indistinguishable, at least for plates eight to ten times thicker than the coating thickness (0.15 mm maximum). For thinner plates, no coating was used at all and for the other plates coating was only used when holograms were taken and not when sound power measurements were made.

As only the ratio of mean square surface velocity amplitude to antinodal velocity amplitude squared was required from the holographic analysis and the plate coating did not significantly affect the mode shape, then the effect of the coating on the results obtained for the modal radiation efficiencies was considered to be too small to consider. The use of reflective paint or sheet did affect the angular location of the preferred nodal diameter when modes with nodal diameters were considered, but this was not regarded as important as it did not affect the results obtained for the modal radiation efficiencies.

The plate response was monitored for some holographic measurements and for all sound power measurements using a half gram Bruel and Kjaer

accelerometer, connected through a high impedance amplifier (Bruel and Kjaer type 1606) to a Bruel and Kjaer type 2112 spectrometer. This enabled the plate response to be maintained at a constant level during hologram exposures and also during sound power measurements. The effect of the accelerometer on the mode shape of a particular mode was evaluated by plotting the holographically determined displacement function across an antinodal diameter for plates vibrating with and without an accelerometer attached. To be consistent, the accelerometer was always attached to an antinode of vibration adjacent to one of the plate exciters. The results showed there were no significant variations in the mode shape function caused by using an accelerometer for the range of plate sizes and thicknesses tested. The accelerometer was calibrated using the standard Bruel and Kjaer vibrating table and the results were checked holographically. The check showed that the standard calibration procedure produced an error of less than 0.5 dB. The acceleration level at the accelerometer position was determined from the reconstructed image of a time averaged hologram by counting the number of dark fringes between a vibration node and the accelerometer and then using equation (3.1) with I_v set equal to zero to find the displacement amplitude $\hat{y}$. This procedure is discussed by Brown et al (1969). The acceleration level was then evaluated using the following equation

$$AL = 20 \log_{10} [\hat{y}.\omega^2/g] \quad . \qquad (3.2)$$

Equation (3.2) also allowed easy prediction of the number of dark fringes surrounding a vibration antinode to be expected in the reconstructed image before the hologram was made, ensuring that there would be neither too few nor too many fringes for convenient analysis.

3.3 REVIEW OF HOLOGRAMS

3.3.1 Comparison of Identified Modes with Predictions

Photographs of the reconstructed images from time averaged holograms of an experimental plate vibrating in its six lowest order resonant modes

are shown in Fig. 3.2. The various photographs are identified according to their mode numbers which follow from the analysis of Chapter 2. For example the (0,1) mode has only a single circumferential node at the clamped outer edge of the plate, while the (1,1) mode has a diametral node as well, which is readily identified in the figure. The (0,2) mode has two circumferential nodes with the second one at 0.373 radius out from the centre, which lies between the fourth and fifth dark fringe counting from the perimeter inward in the figure.

Values of measured displacement amplitude as a function of plate radius for all plates tested are compared with theoretical predictions across each antinodal diameter for the first six resonant modes of vibration of the clamped edge plate model in Figs. 3.3 to 3.6. The solid lines in the figures are the predicted amplitude distributions based on Classical plate theory. For the range of plate sizes tested and represented in the figures (up to h/a = 0.085) the Mindlin-Timoshenko and Classical plate theories are indistinguishable. For comparison the predicted amplitude distributions for a simply supported plate are also included in the figures.

In Figs. 3.3c and d, 3.4a and b and 3.6 the mode shapes shown illustrate correctly the magnitudes of the displacement amplitudes but they do not provide information about phase. For example, for mode (0,2) of Fig. 3.3 the outer two peaks will always be exactly out of phase with the inner peak according to the analysis of Chapter 2. Similarly the left and right peaks of mode (1,1) of Fig. 3.4 and mode (3.1) of Fig. 3.6 will also be exactly out of phase. However, the left and right peaks of the remaining modes, for example, modes (2,1) and (4,1) of Figs. 3.4 and 3.5 will all be in phase as may readily be verified by reference to Fig. 3.2.

The experimental data shown in the figures in each case are composites of data taken from several plates. The points correspond to dark fringe crossings along a diametral line through a reconstructed image such as any one of those shown in Fig. 3.2. For convenience all data

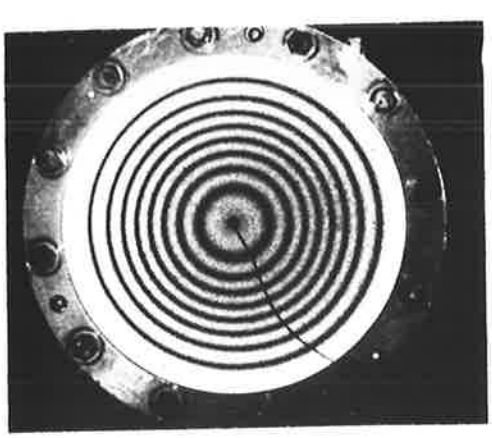

0,1

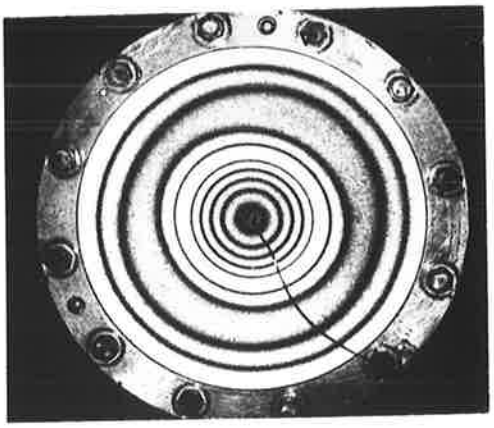

0,2

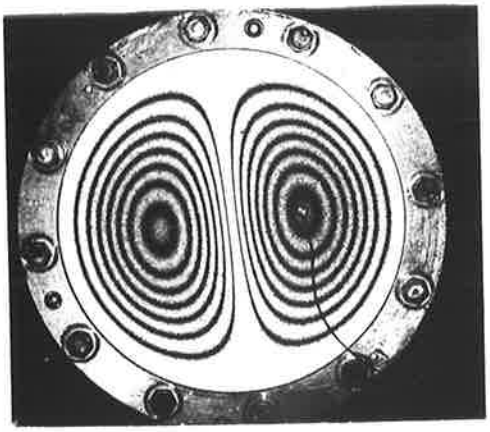

1,1

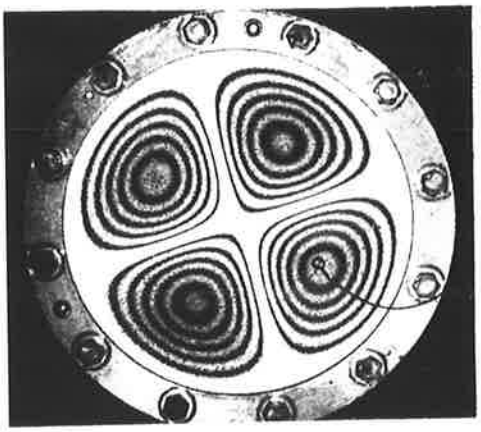

2,1

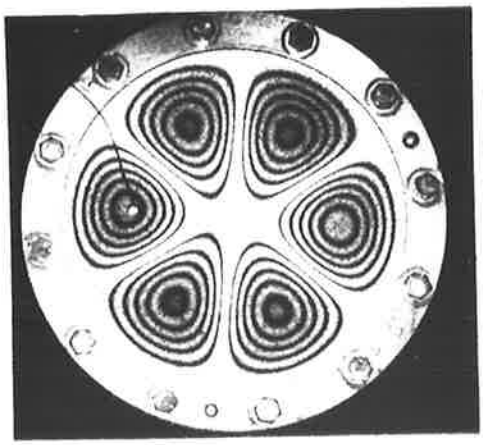

3,1

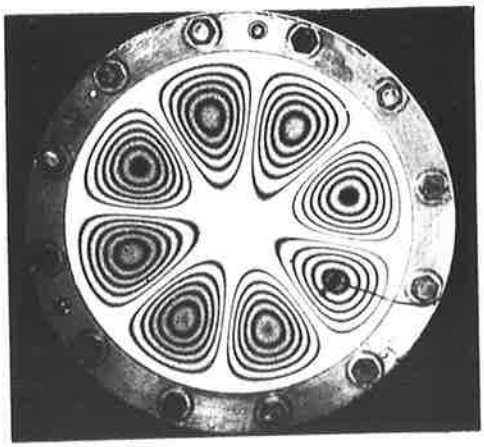

4,1

FIG. 3.2 THE FIRST SIX VIBRATION MODES OF AN EDGE CLAMPED CIRCULAR PLATE.

The modes are identified as (m,n) where m is the number of diametral nodal lines and n is the number of circular nodal lines. The illustrations shown are photographs of the reconstructed images from time averaged holograms.

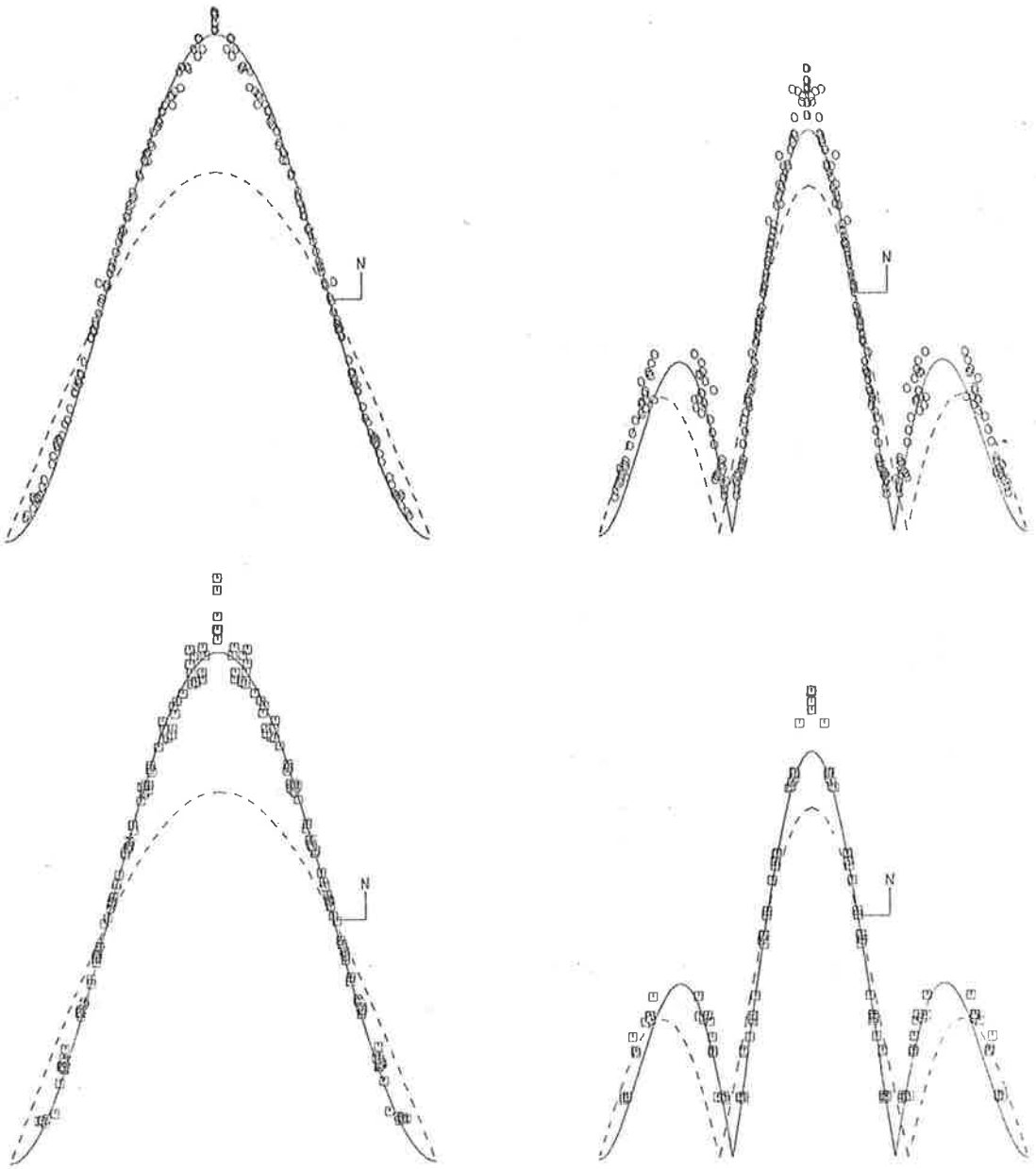

0,1 MODE

0,2 MODE

□ = data for plates painted with reflective liquid
O = data for unpainted plates
- - - = theory for simply supported edge plates
——— = theory for clamped edge plates

FIG.3.3 MODE SHAPE ACROSS A PLATE DIAMETER FOR THE 0,1 AND 0,2 MODES. THE EXPERIMENTAL DATA ARE NORMALISED TO THE THEORY AT THE POINT N.

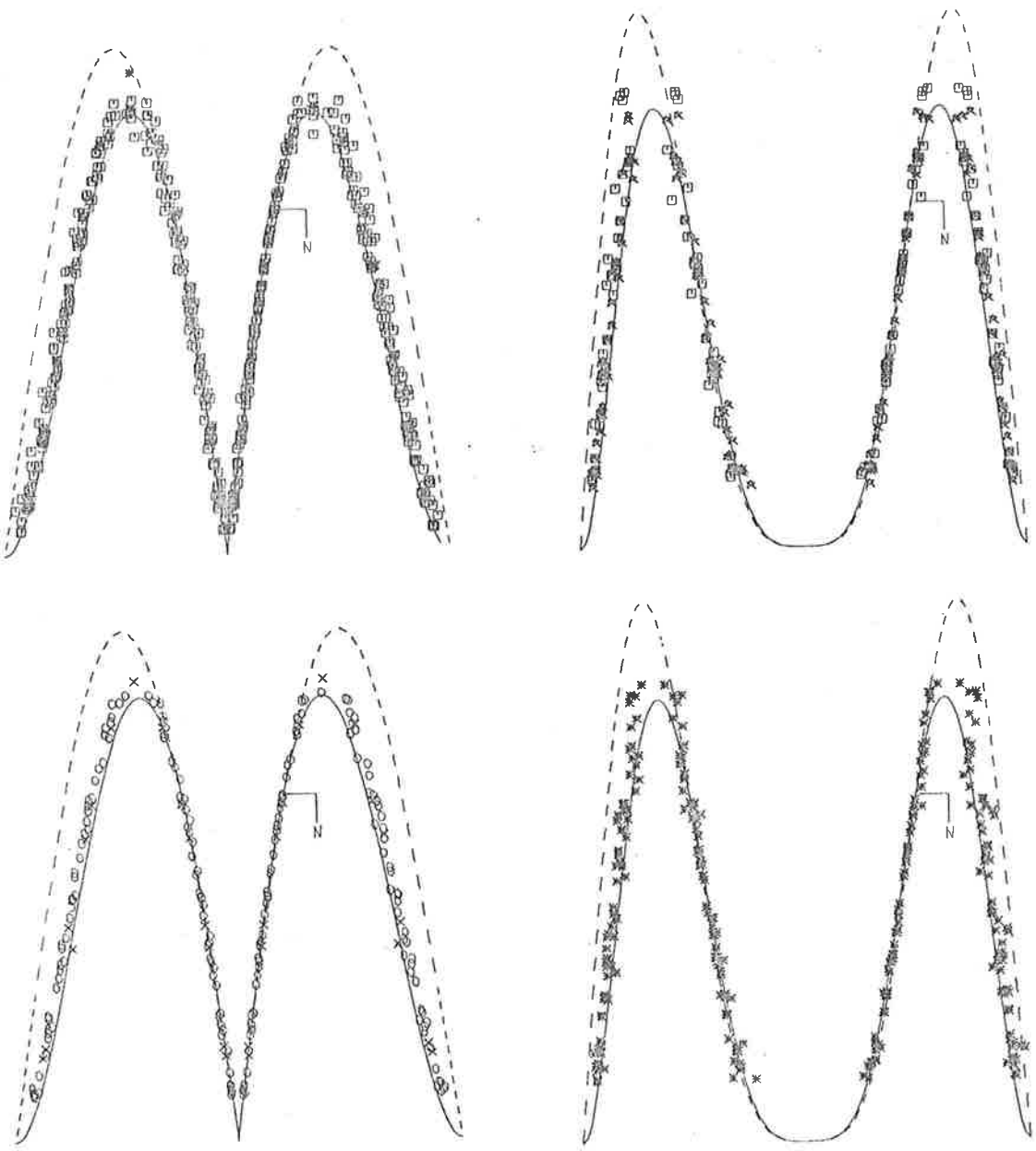

1,1 MODE

4,1 MODE

□ = data for plates painted with reflective paint - accelerometer attached to RHS antinode

✳ = as above but no accelerometer

○ = data for unpainted plates - accelerometer attached to RHS antinode

× = as above but no accelerometer

□ = data measured across antinodal diameter containing exciters

☆ = data measured across antinodal diameter opposite to exciters

✳ = data measured across antinodal diameter adjacent to exciters

– – – – = theory for simply supported edge plates

——— = theory for clamped edge plates

FIG. 3.4 MODE SHAPE ACROSS ANTINODAL PLATE DIAMETERS FOR THE 1,1 AND 4,1 MODES. THE EXPERIMENTAL DATA ARE NORMALISED TO THE THEORY AT POINT N.

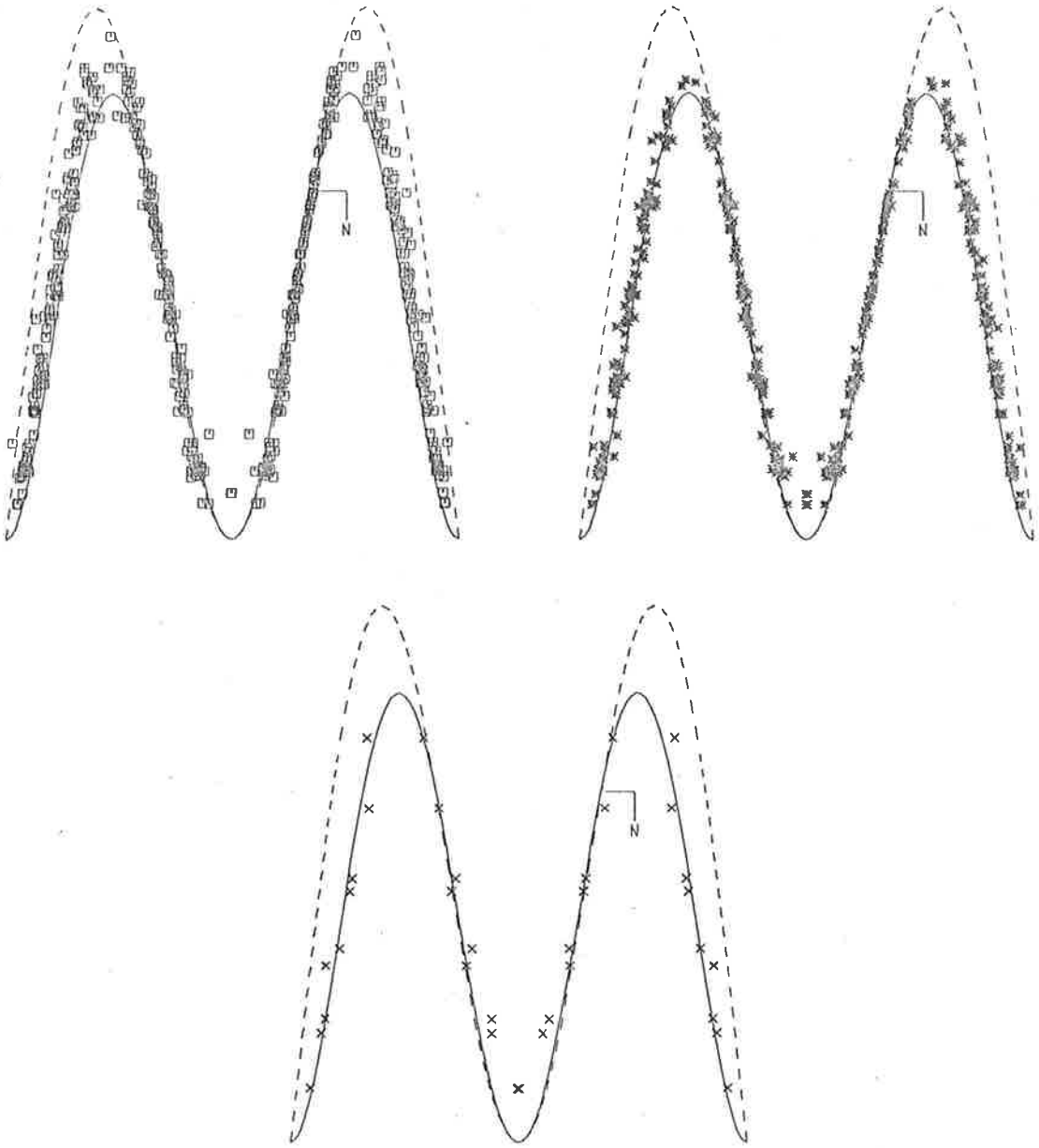

× = data measured across antinodal diameter adjacent to exciters - plates unpainted

✳ = as above but plates painted with reflective paint

□ = data measured across antinodal diameter containing exciters

--- = theory for simply supported edge plates

——— = theory for clamped edge plates

FIG. 3.5 MODE SHAPE ACROSS ANTINODAL PLATE DIAMETERS FOR THE 2,1 MODE. THE EXPERIMENTAL DATA ARE NORMALISED TO THE THEORY AT POINT N.

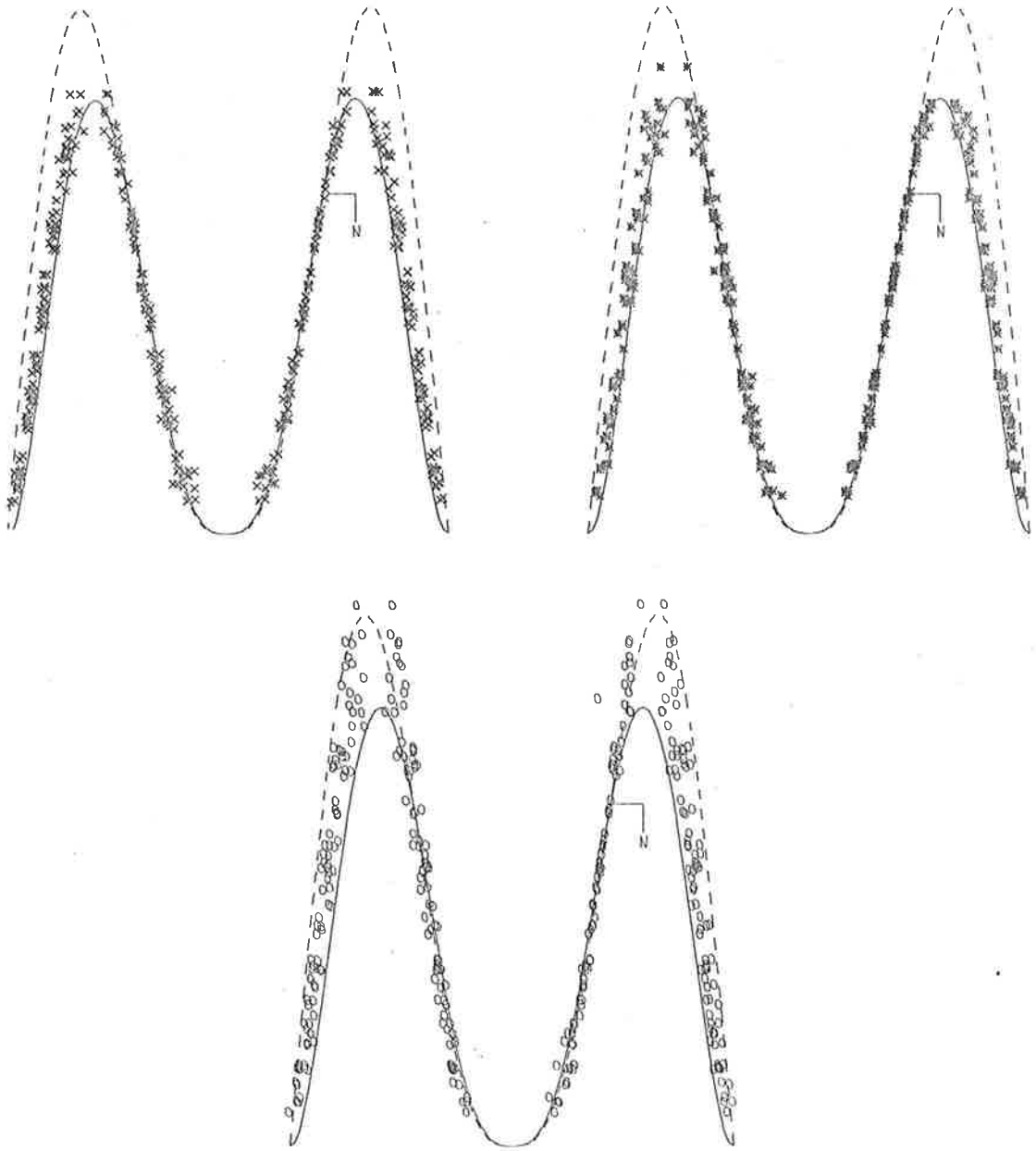

× = data measured across antinodal diameter adjacent to exciters - plates unpainted

✳ = as above but plates painted with reflective paint

O = data measured across antinodal diameter containing exciters

- - - = theory for simply supported edge plates

—— = theory for clamped edge plates

FIG. 3.6 MODE SHAPE ACROSS ANTINODAL PLATE DIAMETERS FOR THE 3,1 MODE. THE EXPERIMENTAL DATA ARE NORMALISED TO THE THEORY AT POINT N.

have been normalized to the theoretical prediction at a single point indicated in the figures as N. Clearly a better overall fit of the data to the predictions might have been obtained using a least squares procedure but for the present purpose the extra computational effort was judged not worth while.

The larger discrepancies between theory and experiment for data points occurring at the centre of a vibration antinode may be attributed to the greater difficulty encountered in assigning the correct displacement amplitude to a dark fringe located at the centre of a fringe system. This difficulty has been discussed by Tuschak and Allaire (1975) who show that the fringe function is only defined at the centre of a dark fringe and cannot be accurately evaluated at other locations.

Some useful conclusions may be drawn from the figures. A comparison of data for unpainted and painted plates in the Figures shows that any effect of the paint on the mode shape is insignificant. Furthermore any effect on the mode shapes produced by the presence of small accelerometers is also insignificant as shown by consideration of Fig. 3.4 parts a and b. Finally the figures show that the comparison between measurement and prediction is best for the two lowest order modes, (0,1) shown in Fig. 3.3 and (1,1) shown in Fig. 3.4.

Reasons for the departure of the measured data from the predicted response for the various higher order modes, for example mode (0,2) of Fig. 3.3 and modes (3,1) and (4,1) of Figs. 3.6 and 3.4 may be advanced. For example it may be expected that the clamped edge condition will become progressively harder to meet as the order of the mode increases. As the mode order increases the corresponding resonant frequency increases and the wavelength to plate thickness grows smaller so that the plate constraint at the clamped edge grows harder to achieve. Generally it was found that the amount by which the data departed from the theory increased as the plate thickness increased for all modes considered. This indicates that

failure to meet the clamped edge condition may contribute to the mode shape distortion measured experimentally. However the principal reason for the apparent mode distortion is that the force applied by the electromagnetic drivers to the plate becomes progressively less well matched to the mode shape as the order of the mode increases. For example a single driver placed at the plate centre was used to drive the (0,1) and (0,2) modes shown in Fig. 3.3. We see that the latter mode is much more distorted than the former. Similarly two drivers out of phase were used to drive modes (1,1) and (3.1) of Figs. 3.4 and 3.6. We note that the agreement between measurement and prediction is fairly good for mode (1,1) where the number of antinodes, two, is equal to the number of drivers. However inspection of parts a, b and c of Fig. 3.6 shows that the mode shape is significantly more distorted along the diametral line through the antinodes containing the drivers. Presumably the addition of two more drivers would have reduced the apparent distortion by providing a better match between the driving force and displacement distribution functions. Similar observations can be made about the remaining modes (2,1) and (4,1) of those studied.

The mode shape distortion considered here is small. For the purpose of determining a surface average mean square velocity, $\langle v^2 \rangle_{st} / \hat{v}_A^2$, the effect of the distortion is quite negligible as shown by reference to columns 3 and 6 of Table 3.2.

3.3.2 Coupled Vibration Modes

If meaningful results are to be obtained for the measured radiation efficiency of a particular vibration mode, it is essential that the resonant mode of interest dominates the plate response to such an extent that any contribution to the overall sound radiation from forced modes is negligible. For the clamped edge circular plate, advantage was taken of knowledge of the displacement distribution functions for the various modes, to place accelerometers at locations to ensure that unwanted

modes were of negligible importance. However it is possible to drive the plate in such a way that its response appears to be resonant but the mode shape is not predictable from Classical Plate Theory (for example, Wilson and Strope, 1970). An example of a non-classical mode is shown in Fig. 3.7. It may be demonstrated that the pattern shown in the figure is made up of a combination and superposition of the responses of two or more forced modes vibrating at frequencies slightly different from their natural resonant frequencies. Although it is relatively easy to ensure that these coupled modes are not significantly excited when measurements are made on a simple, well understood model, the problem of identification of pure modes on a complex surface may be more difficult,as the expected shapes are unknown. However, this problem is beyond the scope of the present investigation.

When modes containing diametral nodes are considered there is an additional problem apart from the possible presence of forced lower order modes. This is the possibility of the presence of more than one mode of the same order but with a different angular orientation of the nodal lines. It was found experimentally that for modes with one or more diametral nodes, each plate had two preferred angular positions for the nodal lines and these were not necessarily orthogonal. These results agree with those presented by Molin and Stetson (1969). The resonant frequencies of the two modes were found to differ by between 1% and 5% depending on the plate thickness and the mode order. As the mode order decreased or the plate thickness increased the percentage difference increased.

It was possible to achieve a resonant condition (peak acceleration level) by suitable adjustment of the exciting frequency and angular location of the exciters, at a frequency between the resonant frequencies of the two preferred modes. However this resonant condition was a combination of the two preferred modes, usually with one dominating (see Figs. 3.9). When one of the preferred modes was excited, the angular position of the

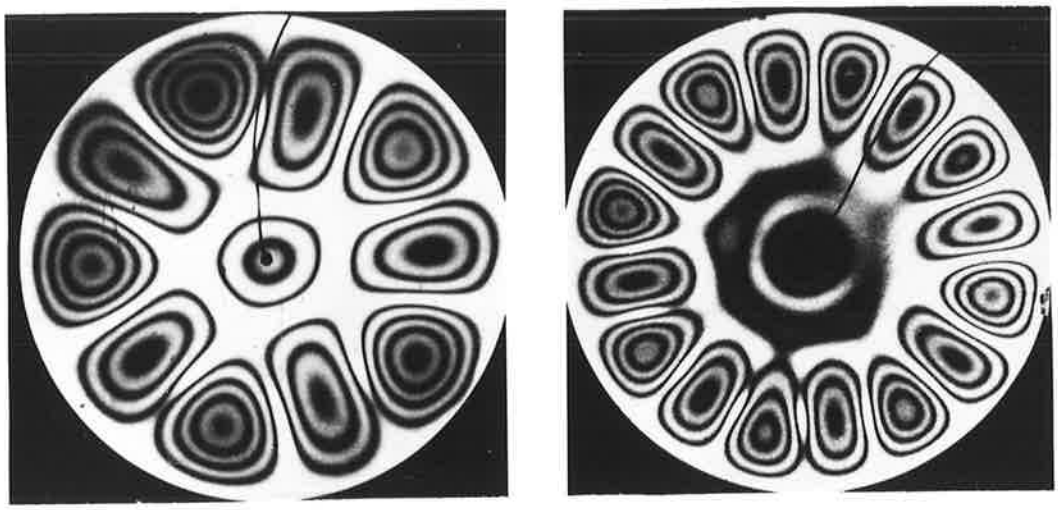

(a) (b)

FIG. 3.7. COMBINATION VIBRATION MODES FOR AN EDGE CLAMPED CIRCULAR PLATE.

These modes cannot be predicted using Classical Plate Theory but may be a combination of two Classical vibration modes.

(a) 0,3 5,1 combination

(b) 0,4 8,1 combination.

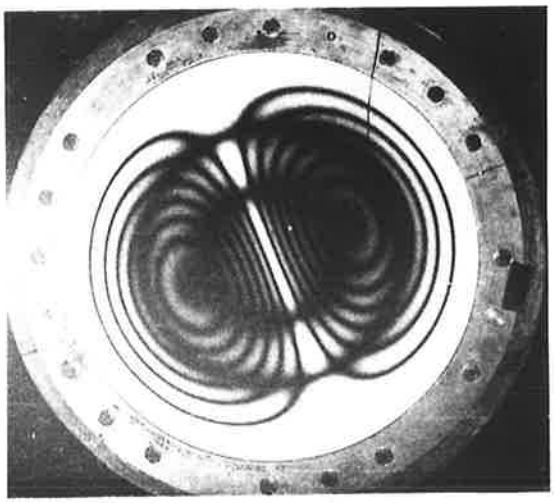

FIG. 3.8. A 1,1 PLATE VIBRATION MODE SHOWING THE EFFECT OF AMBIENT TEMPERATURE VARIATIONS DURING THE HOLOGRAM EXPOSURE.

The temperature variations across the vibrating plate were caused by leaving the air conditioner running during the exposure of the hologram.

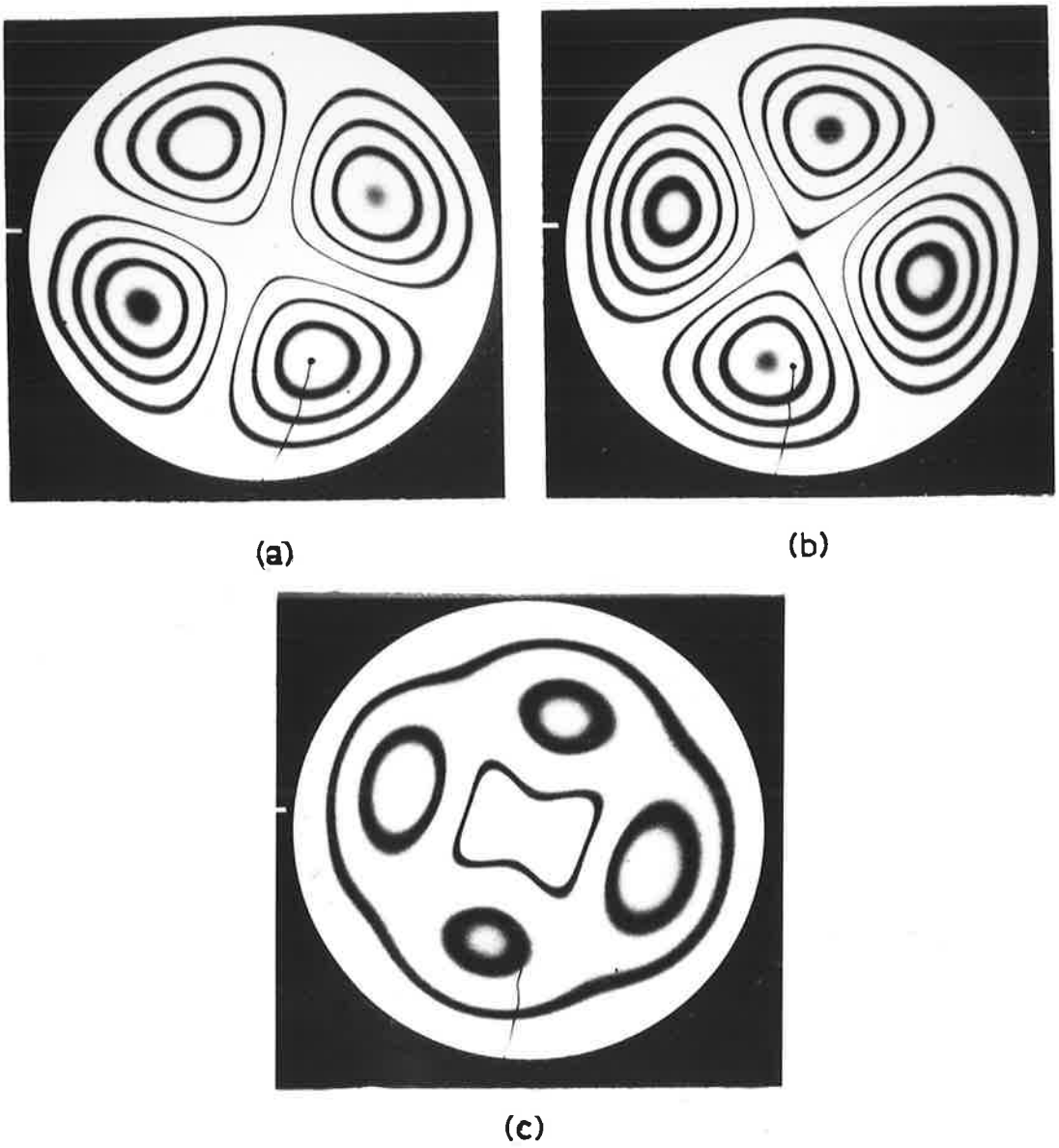

FIG. 3.9. 2,1 VIBRATION MODE OF AN EDGE CLAMPED CIRCULAR PLATE.

These figures show that it is possible to obtain two different preferred angular orientations of the same vibration mode on the same circular plate and that it is possible to excite these two modes together. Note the reference marker in the clamping ring to the left of each photograph, and that the two modes are not exactly orthogonal.

(a) 1st preferred angular orientation

(b) 2nd preferred angular orientation

(c) combination of (a) and (b) using the same excitation system with a different angular orientation and with a resonant frequency between the values for (a) and (b).

exciters was always the same as that of a vibration antinode, but when combination modes were excited, the exciters were usually found to be offset from the antinodal position by a small angle. Thus it was possible to determine by trial and error when only one of the preferred modes was being driven and the contribution from the other to the plate response was negligible. It usually happened that one of the two preferred modes had a greater response for the same driver input power. It was the mode of greatest response which was used in all of the acoustic and holographic measurements.

3.4 MEASUREMENT OF PLATE MEAN SQUARE SURFACE VELOCITY

The reconstructed image from the hologram of a particular vibrating plate, shows the plate covered with a series of interference fringes. When correctly interpreted, these fringes allow the displacement amplitude to be calculated for any point on the plate. Using Equation (3.1) it can be shown (see review by the author, 1979) that for normal illumination and observation of the vibrating surface during the formation of the hologram, the resulting black fringes seen in the reconstructed image satisfy the relation

$$J_0^2 (4\pi\hat{y}/\lambda_\ell) = 0 \ . \qquad (3.3)$$

In the equation $\hat{y}$ is the displacement amplitude at any point covered by a particular fringe and for the HeNe laser used $\lambda_\ell = .6328 \times 10^{-6}$ m. Nodes are identified by bright areas on the reconstructed images while antinodes are identified by the black fringes which surround them. The black fringes immediately adjacent to a node correspond to the first solution of equation (3.3) and the following fringes correspond to successively higher order solutions. When progressing from a (bright) node towards an antinode (or centre of a system of fringes) of vibration, each black fringe passed over represents another solution of equation (3.3). Values for $\hat{y}$ corresponding to particular dark fringe numbers are listed by Brown et al (1969).

The dark fringes are numbered from the node to the antinode. Thus it is straightforward to determine the displacement amplitude at any point covered by a black fringe and the amplitude for the points not covered by black fringes may be found accurately by simple linear interpolation.

The holograms were used to calculate the ratio of mean square plate surface velocity to velocity amplitude squared $(\hat{v}_A^2)$, of an antinode. This ratio was equal to the displacement ratio which was measured directly from the hologram. For example,

$$\frac{\langle v^2 \rangle_{st}}{\hat{v}_A^2} = \frac{\frac{1}{2}\langle \hat{y}^2 \rangle_s}{\hat{y}_A^2} \quad . \tag{3.4}$$

The above ratios were measured from photographs of the reconstructed images of time averaged holograms using a planimeter to measure $\langle \hat{y}^2 \rangle_s$. This was done by measuring the area between two concentric black fringes and then assigning to it a constant displacement amplitude halfway between the two displacement amplitudes corresponding to the centres of the two adjacent black fringes. Areas between a node and the first black fringe were assigned a displacement amplitude of half that corresponding to the first black fringe. Each area so measured was then multiplied by its assigned displacement amplitude squared and the result was summed over the whole plate. The resulting value for the summation was then divided by the plate area (on the photograph) to give the mean square plate displacement averaged in space and then divided by 2 to give its space-time averaged value.

The value of $\hat{y}_A^2$ was obtained from the photograph of the reconstructed hologram image by measuring the radial location across an antinodal diameter of the centre of each dark fringe and assigning a displacement amplitude to it as described earlier. The plate displacement functior derived using Classical plate theory [equation (2.3)] was then fitted to the experimental data using a least squares fit. As the data was

measured across an antinodal diameter the term $\Theta_m(\theta)$ in equation (2.3) was set equal to unity leaving the following equation,

$$\hat{y} = D_{mj}[J_m(\pi\beta_{mj}au) - J_m(\pi\beta_{mj})I_m(\pi\beta_{mj}au)/I_m(\pi\beta_{mj})] \quad . \quad (3.5)$$

The curve fitting procedure used here was similar to that described in Chapter 5 but in this particular case only to two unknowns D_{mj} and β_{mj} were required. Once these two quantities were determined it was possible to determine the plate displacement amplitude at any point (u,θ) on the plate. The position and value of $\hat{y}_A$ was then determined using a simple iteration procedure.

Values of the ratio $\langle v^2\rangle_{st}/\hat{v}_A^2$ equivalent to the ratio $\frac{1}{2}\langle\hat{y}^2\rangle_s/\hat{y}_A^2$ determined experimentally as just described are listed in Table 3.2. They may be compared with Classical plate theory values taken from Table 2.2 and repeated for convenience in Table 3.2, columns 8 and 9. The differences between values calculated using Mindlin-Timoshenko and Classical plate theory were too small (less than 1% for the plates tested) to be measurable experimentally. Thus as Classical plate theory predicts constant values (independent of plate size and thickness) for the ratios, the results are presented as a mean and standard deviation for each vibration mode of interest and averaged over all the plates tested. From Table 3.2 it can be seen that in all cases the experimentally measured values are slightly greater than the theoretically predicted values. This result is consistent with the small mode shape distortion noted earlier in connection with the discussion of the results shown previously in Figs. 3.3 to 3.6.

When modes with one or more diametral nodes were considered the maximum displacement amplitude squared $(\hat{y}_A^2)$ was firstly determined from an average of the values corresponding to each vibration antinode, and the results calculated using this method are listed in columns 2 to 4 of Table 3.2. For the purpose of radiation efficiency measurements, the required

Table 3.2 : Measured and Predicted Values of the Velocity Ratio, $\langle v^2 \rangle_{st} / \hat{v}_A^2$.

Mode Number (m,n)	Experimental Values: $\hat{v}_A$ averaged over all vibration antinodes			Experimental Values: $\hat{v}_A$ measured only at the antinode to which the accelerometer was attached			Theoretical Values from Classical Plate Theory	
	number of measurements	Mean	standard deviation	number of measurements	Mean	standard deviation	edge clamped plate	simply supported plate
0,1	23	0.0950	0.0027	23	0.0950	0.0027	0.0914	0.1425
0,2	23	0.0511	0.0022	23	0.0511	0.0022	0.0509	0.0578
1,1	25	0.0970	0.0040	20	0.0971	0.0046	0.0923	0.1224
2,1	29	0.1066	0.0055	20	0.1092	0.0065	0.1000	0.1233
3,1	20	0.1092	0.0036	11	0.1163	0.0073	0.1005	0.1187
4,1	10	0.1065	0.0025	5	0.1146	0.0104	0.0987	0.1133

values of $\hat{y}_A^2$ were determined only by consideration of the vibration antinode on which the accelerometer was placed and the results calculated with these values are listed in columns 5 to 7 of table 3.2. However only the results listed in columns 2 to 4 should be compared with the theoretical predictions as the results shown in columns 5 to 7 do not represent a true average.

When sound power measurements were made in the reverberant room, the plates were driven harder than they were for holographic analysis so that a good signal to noise ratio could be obtained in the acoustic signal. The mean square surface velocity of the plate vibrating in the reverberant room was determined from the acceleration amplitude measured at a vibration antinode, the values for the velocity ratio obtained from column 6 of table 3.2 and the following equation

$$\langle v^2 \rangle_{st} = \left(\frac{\langle v^2 \rangle_{st}}{\hat{v}_A^2} \right)_h \left(\frac{\hat{a}}{2\pi f} \right)_r^2 \quad , \qquad (3.6)$$

where the subscript h refers to holographic measurements and the subscript r refers to measurements made in the reverberant room.

3.5 SUMMARY

The experimental procedure for determining values of plate modal radiation efficiencies has been separated into two parts. Firstly the mean square surface velocity for a particular mode of interest is determined using time averaged holography and secondly the sound power radiated by the same mode into a reverberant room is measured. The work described in this chapter has been concerned with the holographic determination of the space-time average surface velocity $\langle v^2 \rangle_{st}$. The results for eighteen plates tested have been reviewed and summarized.

In addition to the description of the experimental technique for the determination of $\langle v^2 \rangle_{st}$, the experimentally determined mode shapes

across antinodal diameters have been compared with theoretical predictions. Good agreement was obtained between theory and experiment and slight deviations of the experimental data from the theory were attributed to the effect of the electromagnetic exciters and lack of sufficient plate edge clamping, both of which became more significant as the mode order became higher.

The tendency for lower order forced modes to be present in the plate response is of interest. Even though a high order mode may dominate the plate response (and may in fact be the only one seen holographically) a lower order, more efficient mode, could well dominate the radiated sound power. This consideration shows that use of the experimental method described here for the study of complex surfaces with unknown mode shapes will require extreme care, if more than the first one or two lowest order modes are to be studied with confidence. For the circular plates, the effects of the lower order forced modes were minimized by correctly exciting the plates (at antinodal positions of the resonant mode of interest) and monitoring the antinodal positions of lower order modes with accelerometers.

A phenomenon peculiar to vibrating surfaces of regular symmetry such as square or circular plates is the possibility of degeneracy. In particular the angular locations of diametral nodes will be indeterminate for perfectly flat homogeneous isotropic circular plates. However in practice the ideal plate is never met; slight irregularities will always be present which will result in preferred orientations for diametral nodes and mode splitting. Experimentally two modes of the same order separated slightly in frequency and with different angular orientations will always be encountered. Suitable adjustment of the frequency and angular position of the exciters enables one or the other or a combination of the two modes to be excited. The mode of each degenerate pair with the greater response for the same exciter input power was used for all holographic and acoustic measurements.

CHAPTER 4

REVERBERANT ROOM MEASUREMENT OF RADIATED SOUND POWER

4.1 INTRODUCTION

The experimental determination of the plate modal radiation efficiency requires measurements of both the radiated sound power and the mean square surface velocity for the modally vibrating plate. Measurements of the mean square surface velocity have been described in Chapter 3. This chapter is concerned with the measurement of the pure tone sound power radiated by the plates.

There are two well documented methods which can be used to measure the pure tone sound power radiated by the plates. One method makes use of the free field in an anechoic chamber while the other method makes use of the reverberant field in a reverberant room. Each method has its own advantages and disadvantages. The reverberant room method was chosen because on balance it was considered to have greater advantages and fewer disadvantages. This conclusion is based upon the following considerations.

When measurements are made in an anechoic room many microphone positions are required if the directivity of the source is unknown or complicated. It is expected that the sound fields radiated by modes other than the lowest order plate vibration mode will each be sufficiently complicated to require many free field measurements to determine the radiated sound power. However there is a further problem. In order to unambiguously interpret the measured sound pressures to determine the radiated sound power with precision, it is necessary to avoid Fresnel near field effects. As a general rule (Bies, 1976) for a source of characteristic dimension, a, the minimum distance $\bar{L}$ between source and measurement position must satisfy the following inequality, in order that near field effects be negligible.

$$\overline{L} >> a^2/\lambda \ . \qquad (4.1)$$

Satisfaction of this criterion in the anechoic chamber available would have resulted in test plates which were too small to satisfy the requirements discussed in Chapter 2. The near field problem can be avoided, however, using a reverberant room, since in the reverberant room the domination of the reverberant field restricts source directivity and near field effects to a small volume close to the source. The required reverberant field measurements then are always made outside of this near field dominant small volume.

The acoustic power radiated by a source into a reverberant room can be calculated from sound pressure level measurements in the room provided that the pressure sound field is sufficiently diffuse, using the following equation (Beranek, 1971a).

$$L_w = L_p + 10 \log_{10} V - 10 \log_{10} T_{60} + 10 \log_{10}(1+S\lambda/8V) - 13.5 \ . \qquad (4.2)$$

The accuracy of the value obtained for the sound power level L_w depends on the accuracy of the values obtained for the space average sound pressure level L_p and the reverberation time T_{60}. The accuracy of T_{60} is dependent on the number of room modes excited in the frequency band of interest. The accuracy of L_p depends on the number of discrete sampling points used and the spatial variation of the sound pressure field in the room (which is related to the number of room modes excited). Errors in L_w caused by inaccurate estimations of the quantities L_p and T_{60} are discussed in Part II of this thesis and also in a paper published by the author and his thesis advisor (Bies and Hansen, 1976).

A second problem which has received limited attention in the literature is that of presenting free field radiation impedance to a source under test. Measurement uncertainties resulting from failure of the reverberant room to present free field radiation impedance to a pure tone

test source are a subject of detailed discussion in Part II of this thesis, where the effect of a rotating diffuser in reducing the measurement uncertainties is evaluated for various pure tone sound sources.

4.2 EXPERIMENTAL ARRANGEMENT

The reverberant room used for the sound power measurements was rectangular with a wall surface area of 195 m^2 and a volume of 180 m^3. The room decay times (measured as described in Sect. 4.3) in the $\frac{1}{3}$ octave bands of interest are listed in table 4.1. The rotating diffuser used for these particular experiments was constructed of corrugated fibre glass reinforced with aluminium angle bar stock. The plane of the diffuser surface was tilted at an angle of 30° to the vertical resulting in a swept volume of three cubic metres.

All sound pressure level measurements were made with a half inch type 4134 Bruel and Kjaer condenser microphone connected through a field effect transistor (FET) to a type 2114 Bruel and Kjaer spectrometer. The microphone was carried on a linear traverse back and forth across the room on a diagonal to all wall surfaces. The traverse took 62 seconds to complete one trip in one direction over a distance of 5.6 m, and was positioned so that the microphone never came closer than 1 m to a reflecting surface and was never closer than 2.8 m to the sound source. The test facility is illustrated in Fig. 4.1.

The sound source used for the sound power measurements was the plate model described earlier vibrating at a discrete frequency in one of its resonant modes. Two source positions were considered. First the source was mounted in the side wall of the reverberant room to simulate a radiating clamped edge circular plate mounted in an infinite baffle and second the source was mounted on the end of a long heavy walled tube to simulate a radiating clamped edge circular plate mounted on the end of an infinitely long tube.

Table 4.1: $\frac{1}{3}$ Octave Reverberant Room Decay Times

(Plate Mounted in Wall)

$\frac{1}{3}$ octave band centre Frequency (Hz)	60dB decay time T_{60} (secs)
250	4.6
315	4.3
400	4.2
500	4.5
630	4.5
800	4.2
1000	4.0
1250	3.6
1600	3.6
2000	3.2
2500	3.0
3150	2.9
4000	2.5
5000	2.2
6300	1.6

The first source position was the same as the source position used for the room calibration procedure (see Bies and Hansen, 1976) and is shown in Fig. 4.1. The plate, bolted to the heavy iron casting as described earlier, was mounted in a wooden baffle 0.19 mm thick which in turn was mounted in the room wall. The iron casting and plate were isolated from the baffle by means of a small clearance between the hole in the baffle and the outer edge of the plate clamping rings. The clearance gap was filled with plasticine to prevent sound generated at the rear side of the plate from entering the reverberant room.

For the second sound source position the plate and clamping rings were mounted on the end of a flanged tube which was closed at the other end. The tube was located near a room corner but in such a way that the vibrating plate faced into the room centre and was at all times more than 1.5 m from any room wall.

The plate response in both positions was monitored with accelerometers calibrated as described earlier. The measured acceleration amplitude at a vibration antinode adjacent to one of the drivers was used together with equation (3.6) to determine the plate mean square surface velocity. Both the sound pressure levels and acceleration levels were measured during the experiments using $\frac{1}{3}$ octave filters which were later calibrated to determine the attenuation at each frequency of interest. Use of these filters was essential for the sound pressure level measurements to ensure acceptable signal to noise ratios (greater than 10dB).

4.3 MEASURED MODAL SOUND POWER

The instrumentation used for sound pressure level measurements was calibrated at 250Hz and 124dB re $2 \times 10^{-5} N/m^2$ using a Bruel and Kjaer pistonphone having an accuracy of $\pm$ 0.2dB. The sound pressure level was averaged over several cycles of the microphone traverse using the 300 second averaging circuit on the 2114 model spectrometer. During the sound pressure

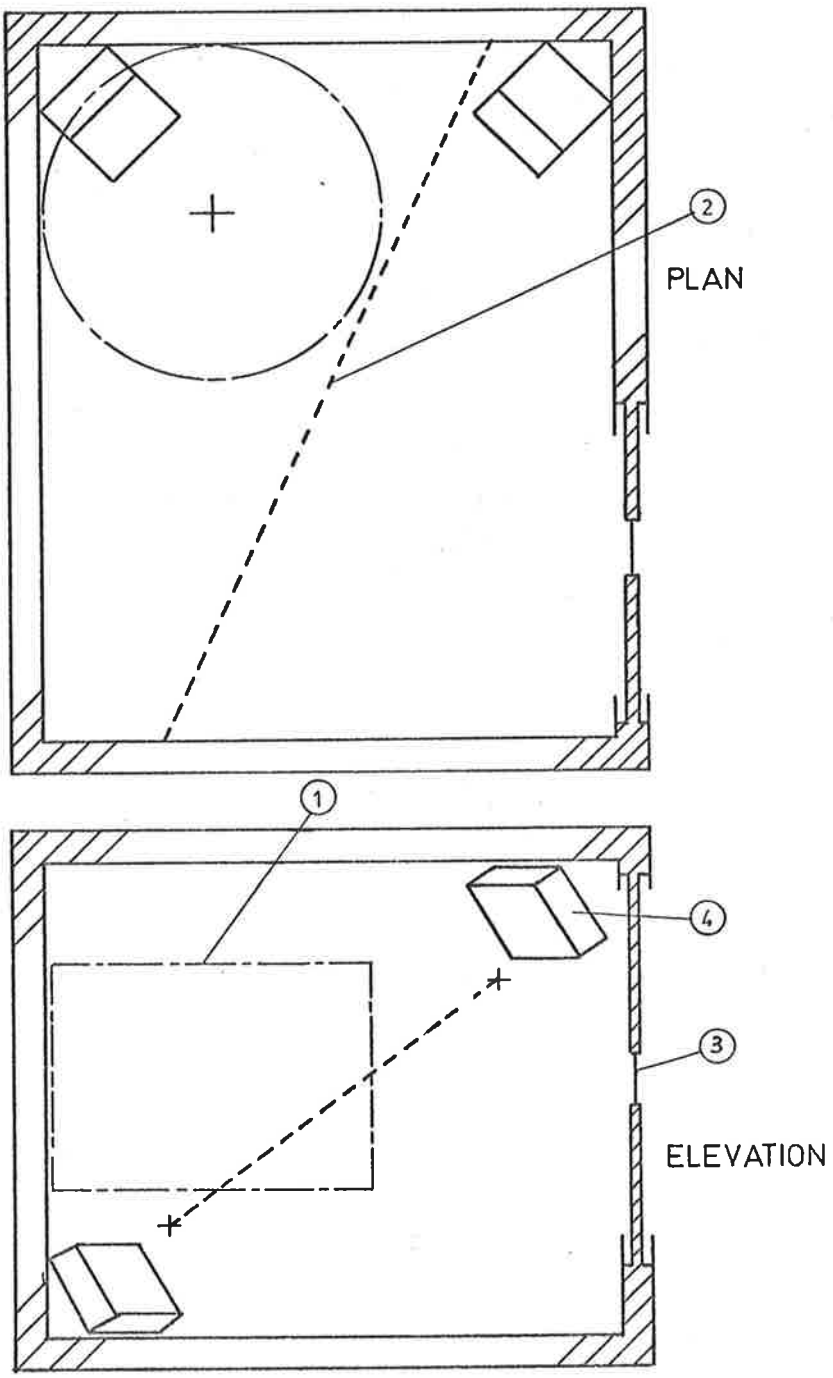

FIG. 4.1 EXPERIMENTAL ARRANGEMENT FOR REVERBERANT ROOM SOUND POWER MEASUREMENTS.

1. Rotating Diffuser
2. Microphone Traverse
3. Vibrating Plate
4. Speaker

level sampling time, the plate exciting frequency was continually manually adjusted to maintain maximum plate response as indicated by maximum voltage output of an accelerometer placed on a vibration antinode.

As the diffuser in the reverberant room rotated, the plate response was observed, by the monitoring accelerometer, to vary cylically as a function of diffuser angular position. The effect was more pronounced for the (0,1) and (0,2) modes than it was for modes with diametral nodes and also became more pronounced as the plates became thinner, with a maximum fluctuation in acceleration level at a vibration antinode, of $\pm$ 3dB for the thinnest plate vibrating in the (0,1) mode. This cyclic variation in plate response for constant driver input power was caused by variations in radiation impedance presented to the source by the rotating diffuser. This matter is discussed in detail in section II of this thesis.

Room reverberation times were measured using the abrupt sound source cut-off method. The sound pressure level was monitored with a stationary half-inch condenser microphone placed near the room centre and connected through a FET to the 2114 model spectrometer. The logarithmic decay curve was recorded for analysis using a level recorder. The 60dB decay time determined from the slope of the level recorder trace was recorded for each $\frac{1}{3}$ octave band of interest and plotted graphically as a function of the centre frequency of the $\frac{1}{3}$ octave band. The decay times corresponding to the frequency of the plate excitation were then obtained by graphical interpolation from measured $\frac{1}{3}$ octave band decay times.

4.4 SUMMARY

An important part of an experimental determination of the radiation efficiency of a resonant mode of vibration of a surface is the accurate measurement of the radiated sound power. In principle the required measurements could be made in the far field of the test source in an anechoic room or alternatively the required measurement could be made in the

reverberant field of a reverberant room. Based upon considerations of the restraints and advantages of the use of each type room the reverberant room was chosen for the measurement of the radiated sound power of the clamped edge circular plate.

The models tested always radiated in pure tones which posed special measurement problems. Furthermore as the models to be tested were placed in one wall of the reverberant room for most of the measurements it was necessary to show that the radiation impedance was at least on average approximately free field at the wall (or at any measurement location). To ensure free field radiation impedance and to smooth the sound field for the purpose of determining a space average sound pressure level, a rotating diffuser was used. The success of the diffuser for this purpose is considered in detail in Part II of this thesis.

CHAPTER 5

RADIATION EFFICIENCY

5.1 INTRODUCTION

The work described thus far has been concerned with the measurement of the parameters required to determine the radiation efficiency of a surface vibrating in one of its resonant modes. In this chapter it is shown how the measured parameters are used to obtain values for the surface radiation efficiency. Results are then presented for the circular clamped edge flat plate vibrating in its first six modes.

Having established confidence in the method it is next shown how the method may be used generally. Two examples are given to show how the experimental method may be used to determine the radiation efficiency of a resonantly vibrating surface in a situation not readily amenable to theoretical analysis. The first class of surface vibration considered is the resonant vibration of a clamped edge circular plate vibrating in a non-classical mode; that is, a mode not predicted by Classical plate theory. The second type of surface considered is the front surface of some in line engine blocks vibrating in some low order modes.

In all radiation efficiency calculations outlined here the following assumptions are implicit.

1. The same vibration mode was excited in the reverberant room as was analysed holographically.

2. The response of all surfaces was linear so that higher excitation levels used during sound power measurement did not result in distortion of the mode shapes studied holographically.

3. The forced response of lower order more efficient modes was small enough to be neglected.

4. The effect of a ½ gram accelerometer on the mode shape and sound power measurements was negligible.

5. The effect of reflective paint on the holographically measured mode shapes was negligible.

Assumptions 3, 4 and 5 have already been discussed in Chapter 3. Assumptions 1 and 2 are considered to be reasonable in the circumstances and are supported by the results shown in Figs. 5.1 and 5.2 for the clamped edge plate test models.

5.2 CALCULATION PROCEDURE

The radiation efficiency for a resonant mode (m,j) of a vibrating plate was defined earlier as,

$$\sigma_{mj} = W_{mj} / \langle v^2 \rangle_{st} A \rho_0 c_0 \quad . \tag{5.1}$$

From the sound power level measurements just described the radiated sound power for a particular vibration mode (m,j) may be calculated using the following relation,

$$W_{mj} = \text{antilog}_{10} [(L_w/10) - 12] \quad . \tag{5.2}$$

The mean square surface velocity $\langle v^2 \rangle_{st}$ is obtained in two steps. First using holographic methods, the ratio $\langle v^2 \rangle_{st} / \hat{v}_A^2$ is determined for all plates tested. Second the square of the antinodal velocity $\hat{v}_A^2$ is obtained from the measured antinodal accelerations A_g. Finally the mean square surface velocity is calculated using the following relationship;

$$[\langle v^2 \rangle_{st}]_r = [\langle v^2 \rangle_{st} / \hat{v}_A^2]_h [A_g / 2\pi f]_r^2 \, g^2 \quad . \tag{5.3}$$

In equation (5.3) the subscript r refers to reverberant room measurements and the subscript h refers to holographic measurements.

An expression given by Beranek (1949) is used to calculate the characteristic impedance. The calculation indicated in equation (5.4) which follows, requires a measurement of the temperature and the barometric pressure in the reverberant room during the measurement of sound power. According to Beranek,

$$\rho_0 c_0 = 42.86[273/(273+T)]^{\frac{1}{2}}[P/760] \qquad (5.4)$$

Equations (5.1) to (5.4) are sufficient to calculate the radiation efficiency σ_{mj}.

5.3 DISCUSSION OF RESULTS FOR THE PLATE MODEL

Experimentally measured values of radiation efficiency for resonant vibration modes of the edge clamped circular plate are shown in Fig. 5.1 for the plate mounted in the side wall of the reverberant room and in Fig. 5.2 for the plate mounted at the end of a closed tube within the reverberant room. In each Figure the solid line represents the theoretical prediction for the clamped edge plate and the dashed line represents the similar theoretical prediction for a simply supported edge plate mounted in an infinite rigid baffle and radiating into free space [equation (2.97b)]. The lines shown in Fig. 5.2 are for comparison purposes only, as no analysis for the case of the plate at the end of a tube is available. Furthermore no analysis has been attempted as the problem is apparently very complicated (Levine and Schwinger, 1948).

From the Figures for the plates mounted in the reverberant room wall it can be seen that the experimental data agree reasonably well with theory for the 0,1 mode and for the mid frequency range of the higher order modes. The deviations of experiment from theory for the 0,2 mode may, in part, be attributed to the forced response of the 0,1 mode which has a higher radiation efficiency in the frequency range tested. This effect

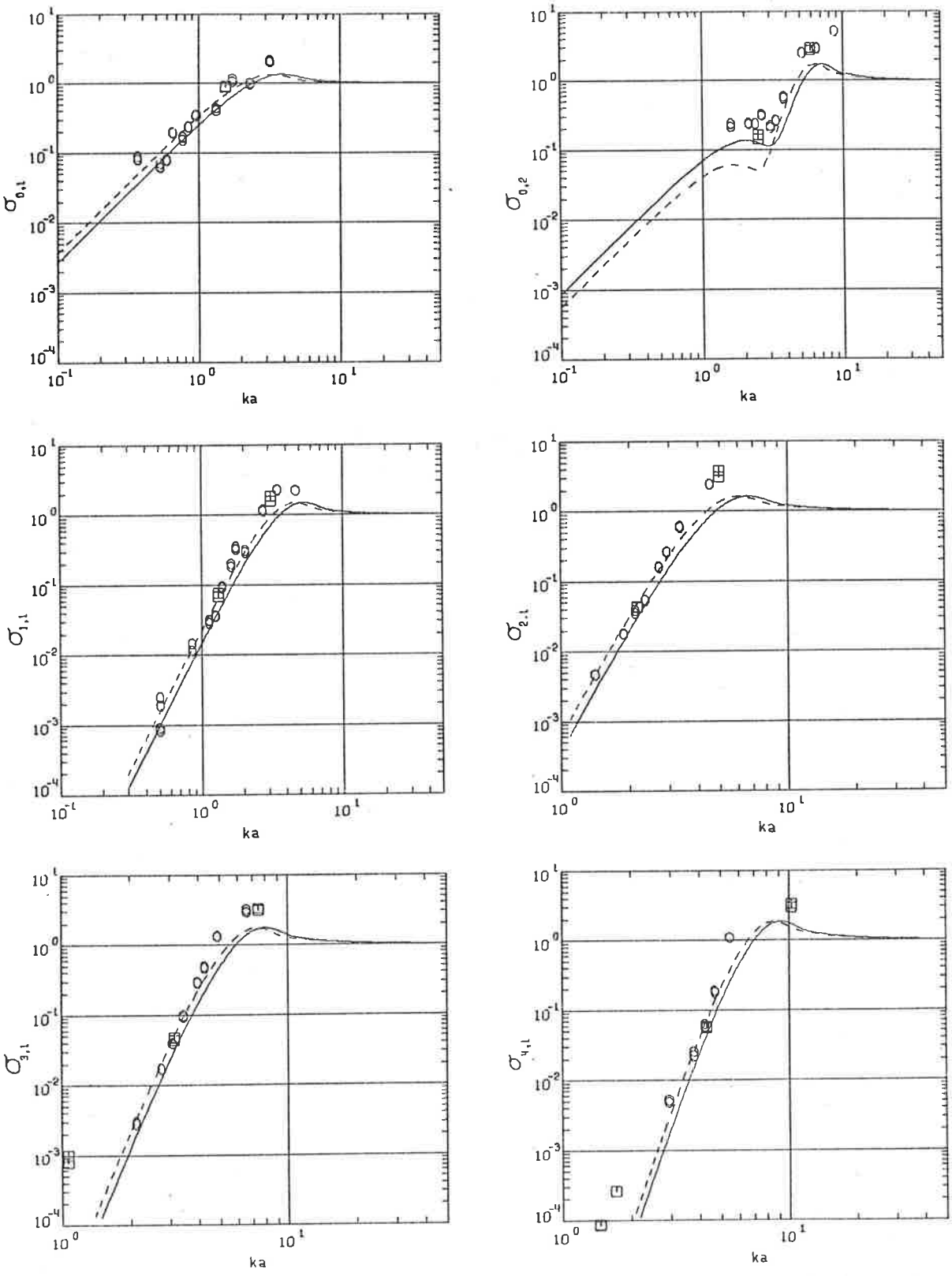

□ = experimental data for 0.1755 m radius plates
○ = experimental data for 0.0762 m radius plates
--- = theory for simply supported edge plates mounted in an infinite baffle
—— = theory for clamped edge plates mounted in an infinite baffle

FIG. 5.1 RESISTIVE RADIATION EFFICIENCIES FOR THE FIRST SIX PLATE MODES. THE PLATES ARE MOUNTED IN THE SIDE WALL OF THE REVERBERANT ROOM.

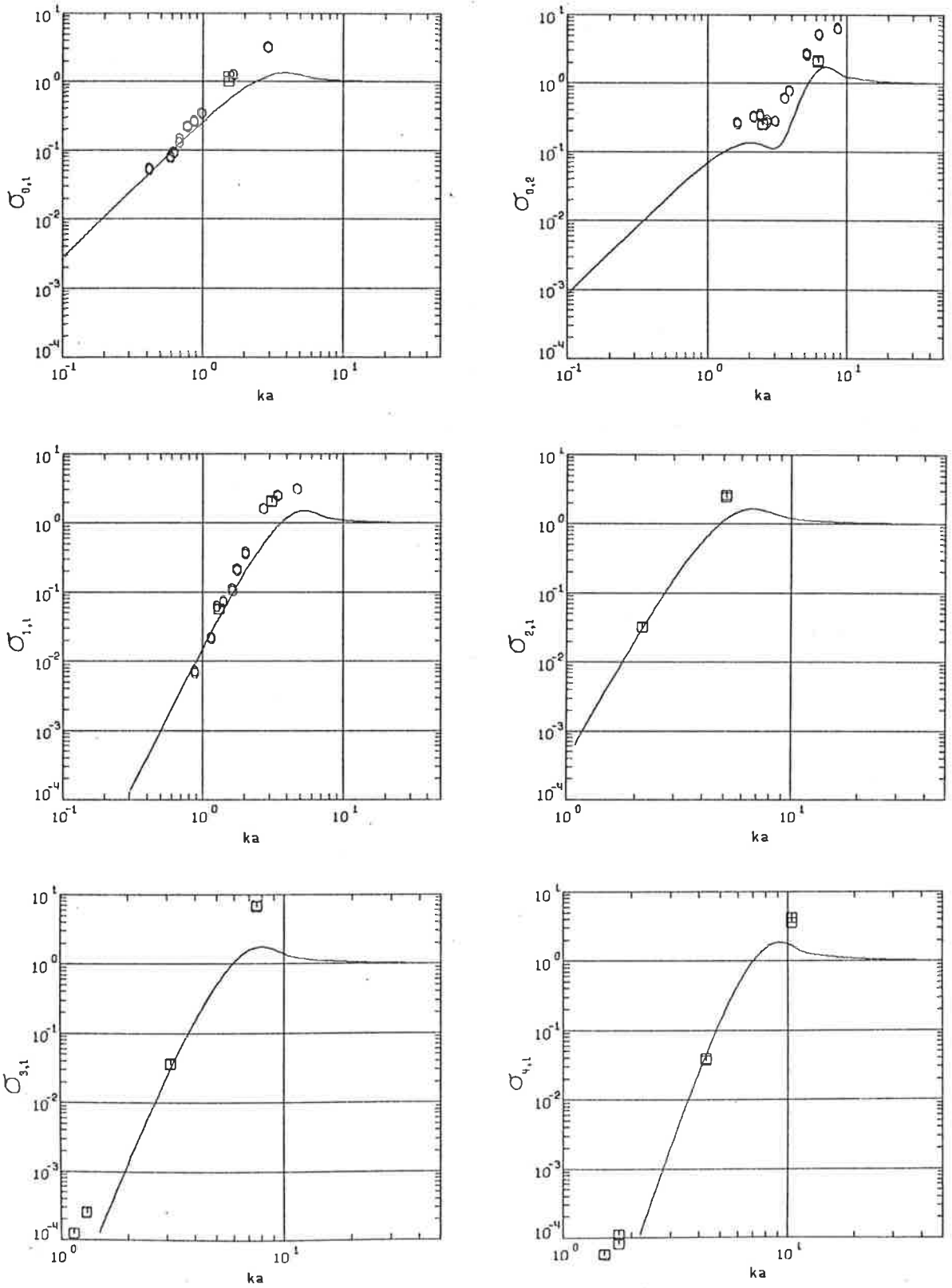

□ = experimental data for 0.1755 m radius plates
O = experimental data for 0.0762 m radius plates
—— = theory for clamped edge plates mounted in an infinite baffle

FIG. 5.2 RESISTIVE RADIATION EFFICIENCIES FOR THE FIRST SIX PLATE MODES. THE PLATES ARE MOUNTED IN THE END OF A HEAVY WALLED TUBE PLACED IN THE REVERBERANT ROOM.

was difficult to avoid as the 0,2 and 0,1 modes were both driven at the same antinode, the plate centre. An additional ring driver at the second annular antinode would have been required to drive the 0,2 mode while suppressing the 0,1 mode.

The deviations at low values of radiation efficiency for the modes with diametral nodes may in part be attributed to the forced response of the lower order modes which was difficult to avoid even though vibration antinodes of successive modes did not coincide. The lowest order modes have progressively greater radiation efficiencies for small values of ka and at these low values of radiation efficiency, the forced response required to over-ride the radiation of a higher order mode is very small.

In the region of high radiation efficiencies (near unity) the experimentally measured values are consistently higher than predicted and the reason for this discrepancy is not understood although some possibly contributing causes can be suggested. High radiation efficiency values were investigated using thick plates in which case it was very difficult to satisfy the clamped edge condition. Indeed for some of the higher order modes, the mode shape plots of Chapter 3 show the edge condition to be somewhere between clamped and simply supported. Failure of the clamped edge condition for the thick plates could result in a larger effective plate surface area than predicted and consequently more sound power radiated than expected. The magnitude of this possible effect is unknown. A second small effect might be mode distortion caused by the plate exciting mechanism. This effect could be significant on the thickest plates vibrating in the higher order modes as some of them could not be driven hard enough to produce sufficient fringes to be investigated holographically In these few cases the mean square plate surface velocity was calculated using the values in Column 6 of Table 3.2. A combination of the two effect

just described could contribute to the higher than predicted radiation efficiencies but whether these effects completely account for the values of radiation efficiency greater than unity is unresolved.

Other possible sources of error which would contribute to scatter in all of the measurements of radiation efficiency are as follows:

(1) The assumption of free field radiation impedance might not be satisfied and as will be shown in Chapter 7 this might contribute an error ±1.0dB.

(2) The possible error in the determination of the mean square normal surface velocity from the optical holograms is estimated to be ±0.7dB.

(3) For frequencies above 400 Hz the possible error in the determination of the space average sound pressure level has been estimated to be ±0.8dB and for frequencies between 300 Hz and 400 Hz the possible error is estimated to be ±1.6dB (Bies and Hansen, 1976). An accumulated error of ±2.5dB can readily be accounted for.

The experimentally measured radiation efficiencies for the plate mounted at the end of a closed tube in the reverberant room are shown in Fig. 5.2 and are included for comparison with values obtained for the plate mounted in the reverberant room wall. In both cases the trend in results is similar. At low frequencies simple source theory predicts that at a given value of ka, the radiation efficiency for the plate mounted in the tube should be 3dB less than that for the plate mounted in the wall. The experimental results show a slight trend to lower values but the trend is less than 3dB.

5.4 EXTENSION OF THE MEASUREMENT TECHNIQUE

For a given surface shape and mode of vibration the radiation efficiency (defined in Chapter 1) is a function of the product of frequency and a characteristic surface dimension (that is, a function of dimensionless frequency ka). The resonant frequency of the mode in turn is determined by the dimensions and physical properties of the surface. Thus if the radiation efficiency can be experimentally determined for the same mode at different resonant frequencies on several different surfaces of the same general shape, it should be possible to generate empirically the relationship between radiation efficiency and dimensionless frequency as a radiation efficiency curve. Use of such an empirical curve should then allow the prediction of the radiation efficiency of the same mode on any other surface of similar shape even though the size might differ greatly from those tested.

In this section the techniques described earlier for the measurement of radiation efficiencies of "classical" resonant modes on a circular plate are used to experimentally investigate the radiation efficiencies of two classes of vibrating surfaces. In one class the radiation efficiencies of a clamped circular plate vibrating in complex non-classical modes which are dependent on the shape of the plate forcing function are investigated. At present these modes are not understood and it is not certain that they can be described using known theoretical techniques. The results thus obtained can be used to predict the radiation efficiencies of edge clamped circular plates of any size or thickness, vibrating in one of these non-classical modes.

In the second class of vibrating surfaces the experimental techniques are used to study the radiation efficiencies of the first few modes of vibration of a complex surface consisting of one side face of an in-line engine block. It should be noted that the purpose here is to show how the experimental technique may be used generally to determine

modal radiation efficiencies. The intent is not to solve any problems or questions concerning in-line engine blocks. The engine blocks were chosen because they were readily available in a range of sizes and they have a side surface with a shape of sufficient complexity for the purposes of this demonstration. For this reason the side surface of interest was baffled when sound power measurements were made so that sound radiation from all the other surfaces of the engine block did not enter the reverberant room.

5.4.1 Theoretical Considerations

The theoretical derivation of the radiation efficiencies for the first six low order classical modes of vibration of an edge clamped circular flat plate has been presented and compared to experiment earlier in this thesis. In this section more complex modes which are not yet fully understood and which cannot be readily described using Rayleigh's Classical Plate Theory (Rayleigh, 1878a) are considered. This is done to demonstrate how experimental measurement on a simple surface shape vibrating in a complex mode may be used to predict the radiation efficiency of other surfaces of similar shape vibrating in the same mode. Similar non-classical modes for membranes have been examined by Ropper (1974) who has shown mathematically that they are functions of the forcing function shape and are not caused by non-circularity or non-uniformity of the plate or edge clamping arrangement. This prediction is supported by experimental results discussed here, in that identical non-classical modes were detected on all the different plates tested.

Ropper (1974) has shown that non-classical modes excited on membranes by a known forcing function may be described as combinations of classical modes. However, these combinations are difficult to predict theoretically. Although the modes considered here appear to be a combination of two classical modes with finely separated resonant frequencies, they are

distinct resonant conditions and not part of a smooth transition between the two classical modes as described by Ropper. Thus in this situation it is of interest to demonstrate how the radiation efficiency curve for these particular modes may be determined from a few experimental measurements.

Generally the theoretical prediction of the radiation efficiency of even simple low order vibration modes on a complex object such as an in-line engine block is a difficult task. Thus it is also of interest in this situation to demonstrate how a radiation efficiency curve (which may be used for almost any in-line engine block) for a given vibration mode may be established from a few experimental measurements on a number of different engine blocks.

Examination of the theoretical results obtained by Wallace (1972) for rectangular panels and those shown in Figs. 2.6 and 2.7 for circular plates suggests that some generalizations about the resistive parts of the radiation efficiencies of the first few low order modes are possible. For this purpose it is advantageous to use the modal bending wavenumber k_b discussed earlier in Chapter 2 where it was shown that for circular plates,

$$k_b^2 = (\pi\beta/a)^2 + (m/a)^2. \tag{5.5}$$

Similarly the modal bending wavenumber for rectangular plates may be written as,

$$k_b^2 = (m\pi/a_1)^2 + (n\pi/a_2)^2. \tag{5.6}$$

For values of k/k_b less than about 0.8 the radiation efficiency is less than unity and its logarithm is generally a linear function of the logarithm of k/k_b with a slope determined by the mode which is excited. For values of k/k_b greater than or equal to 0.8, the radiation efficiency is essentially unity in every case and thus independent of frequency. Thus any available test data that allows determination of the radiation efficiency for values of k/k_b less than 0.8 is sufficient to approximate the radiation

efficiency at all frequencies.

For non-classical plate modes the value of β in equation (5.5) may be approximated from the known values of β_{mj} for the classical modes having the nearest resonant frequencies. For the purpose of calculating k_b for the engine blocks, the surface of interest was assumed to approximate a rectangular panel allowing equation (5.6) to be used.

5.4.2 Experimental Work

The experimental investigation of the radiation of non-classical modes was confined to clamped edge plates having a radius of 0.1755 m and a thickness range from 1 mm to 3.2 mm. Temperature stability determined the lower bound while power limitation of the single electromagnetic driver determined the upper bound on plate thickness. The plates were mounted as described earlier and excited at the centre.

For the second model, in-line engine blocks were chosen, as they represented a complex object and were available in a large range of sizes, all of which had basically similar shapes. The engine blocks were excited by a model V50 Goodmans mechanical vibration transducer which was bolted to them and which in turn was driven by the same oscillator and power amplifier used to drive the electromagnetic plate exciters. Care was required to ensure that engine block resonances were driven and not extraneous resonance due to the presence of the driver and the mounting supports for the engine blocks.

For the purpose of taking holograms it was necessary to isolate the engine blocks from the optical table and at the same time provide a rigid support and a hard mounting surface to minimize damping of resonant modes. This was done by supporting each block sump side uppermost on three small studs, which in turn rested on a cast iron slab weighing about 280 kg. The cast iron slab was isolated from the table using commercial rubber isolation pads which were effective at frequencies above about 100Hz.

It was found that the low order modes investigated had shapes

independent of the driver location or block mounting position, provided that the block was simply supported on studs. The modal resonant frequency and the modal damping changed but the mode shape remained the same when the supporting studs were placed on a softer surface (damping increased) or when the driver position was changed. The engine block surfaces which were investigated are shown in Figs. 5.3. Only the first few low order vibration modes were considered.

The experimental arrangement used for the holographic measurements is similar to the one described in Chapter 3 and is illustrated in Fig. 5.4a. The vibrating surfaces were illuminated and viewed normally. The circular plates were covered with retro reflective sheet and the engine blocks were painted with retro reflective paint thus minimizing the required hologram exposure times. Typical exposure times using Agfa Gevaert 10E75 holographic plates (similar in sensitivity to the Ilford HeNe1 plates used earlier) ranged between 3 seconds for the circular plates to 25 seconds for the engine blocks. The reference to object beam intensity ratio was varied between two and four.

The resonant vibration modes for the engine block were identified using real time holography and a slow frequency sweep through the range of interest while observing the block response with the aid of the real time hologram. Resonant conditions were easily detected when dark interference fringes appeared on the image seen through the hologram. Good quality photographs using real time holography were difficult to obtain and so the modal resonant frequencies were noted and time averaged holograms taken at the frequencies of interest. The non-classical plate modal resonant frequencies were found by observing a peak in the response of an accelerometer placed on the plate centre while the exciting frequency was swept between the two theoretically predicted values for the (5,1) and (0,3) modes or the (8,1) and (0,4) modes respectively.

Sound power measurements were made as described in Chapter 4

(a)

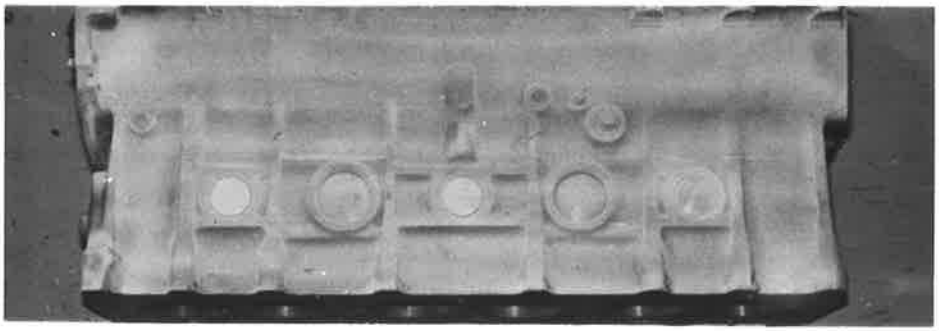

(b)

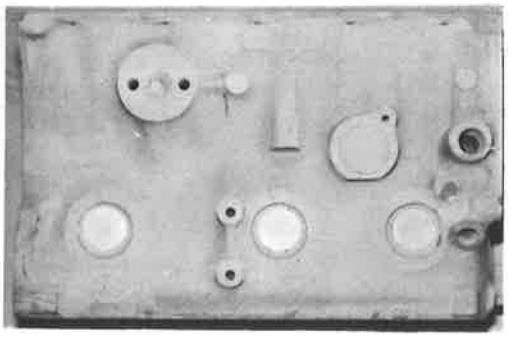

(c)

(d)

FIG. 5.3 ENGINE BLOCK TEST SURFACES (SIDE FACES, SUMP SIDES UP).

(a) 6 cylinder block 1 (Chrysler)

(b) 6 cylinder block 2 (Chevrolet)

(c) 4 cylinder block 3 (Morris)

(d) 4 cylinder block 4 (Galant)

with the vibrating surface mounted in a baffle consisting of a 1.8 m x 2.4 m x .019 m particle board attached to one of the room walls as illustrated in Fig. 5.4b. When the engine blocks were tested care was taken to ensure that the baffle in which the blocks were mounted was not excited through the material used to fill the gaps between the engine block and the baffle surrounding it. Early tests using plasticine to fill the gap between the edge of the block and the baffle showed that the baffle was excited sufficiently to significantly contribute to the radiated sound. This problem was eliminated by using masking tape to cover the gaps instead of plasticine to fill them. A separate test in which the transmission of sound through the gap covered with masking tape was investigated showed that sound leakage through the gap could be expected to be quite small compared to the sound radiated directly from the engine block into the reverberant room. Alternatively the problem was avoided when the circular plates were tested, as the plates were first mounted on a massive iron casting (as described in Chapter 3), which had a small enough vibration amplitude not to significantly excite the wooden baffle board through the plasticine used to fill the gap between the plate clamping rings and the baffle.

5.4.3 Analysis and Discussion of Results

As shown in Fig. 5.3 two six cylinder (blocks 1 and 2) and two four cylinder (blocks 3 and 4) in-line engine blocks were investigated. The displacement amplitude distributions for the first few modes of vibration were determined from photographs of the reconstructed images from time average holograms of the particular modes and are illustrated in Figs. 5.5. Three of the blocks (1,2 and 3) were of generally similar construction and they exhibited similar mode shapes for the first and third modes of vibration (Figs. 5.5a, 5.5b, 5.5d). The second mode (Fig. 5.5c) was only observed on the two six cylinder engine blocks. As may be seen from Figs. 5.5e and 5.5f, the first two modes on block 4 had entirely different mode shapes

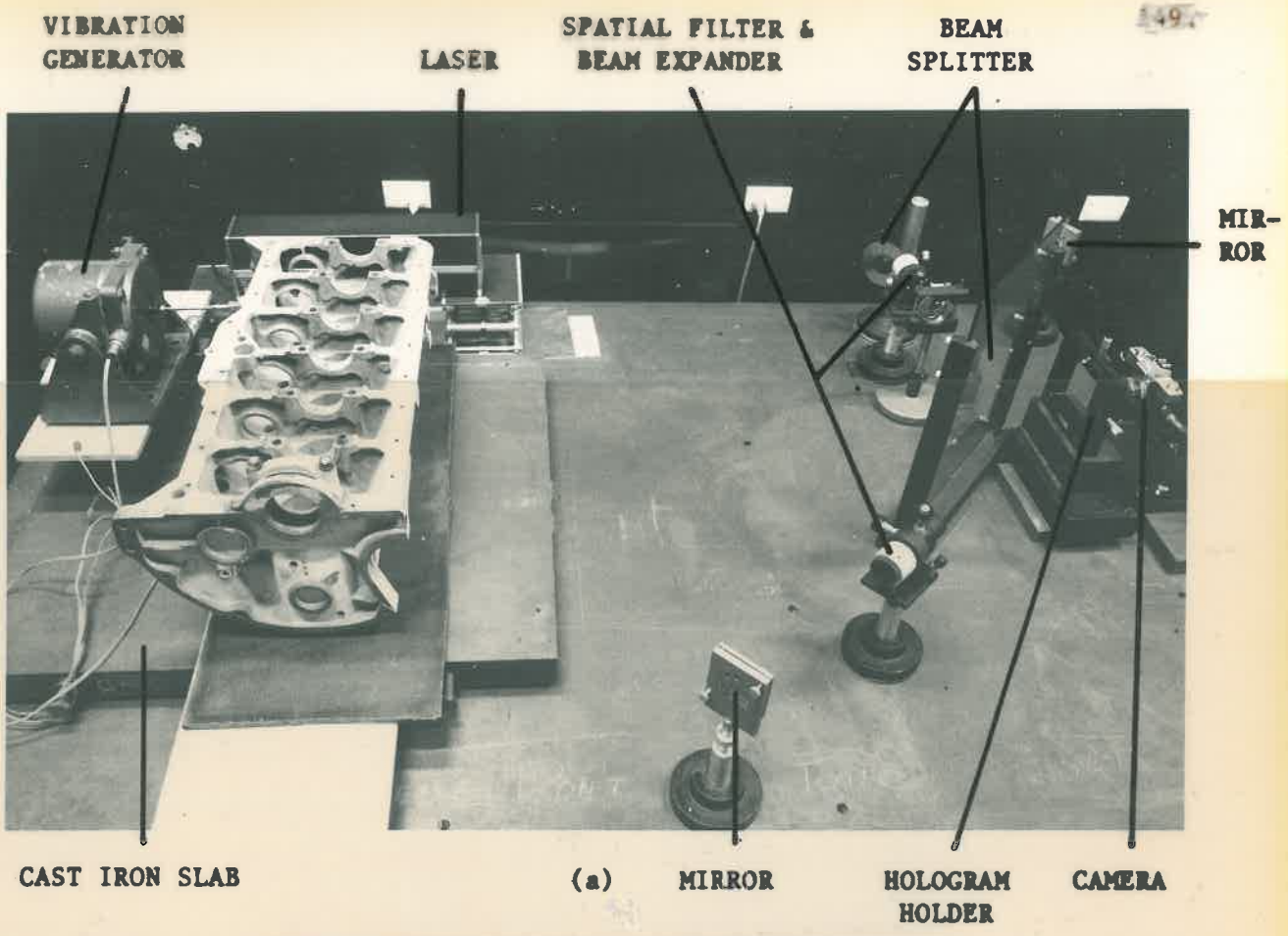

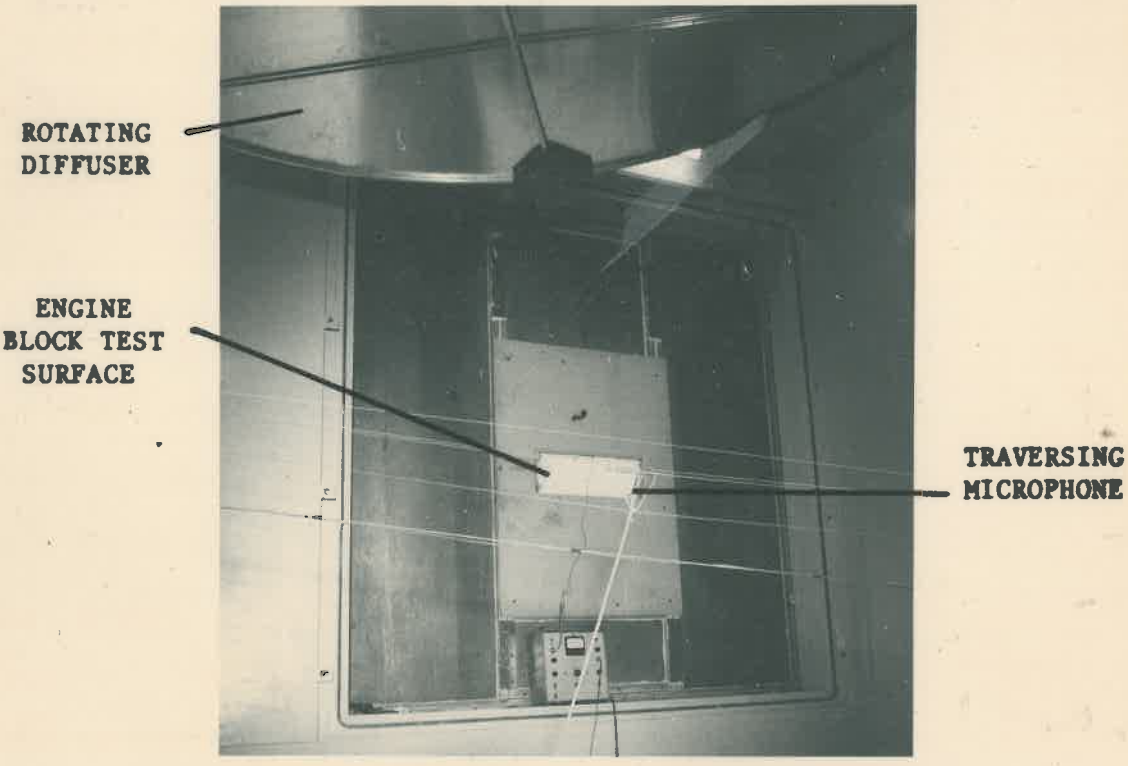

(b)

FIG. 5.4 EXPERIMENTAL ARRANGEMENTS FOR MEASUREMENTS OF THE RADIATION EFFICIENCIES OF THE SIDE SURFACES OF THE IN - LINE ENGINE BLOCKS.
(a) Holographic test arrangement (b) Reverberant room test arrangement.

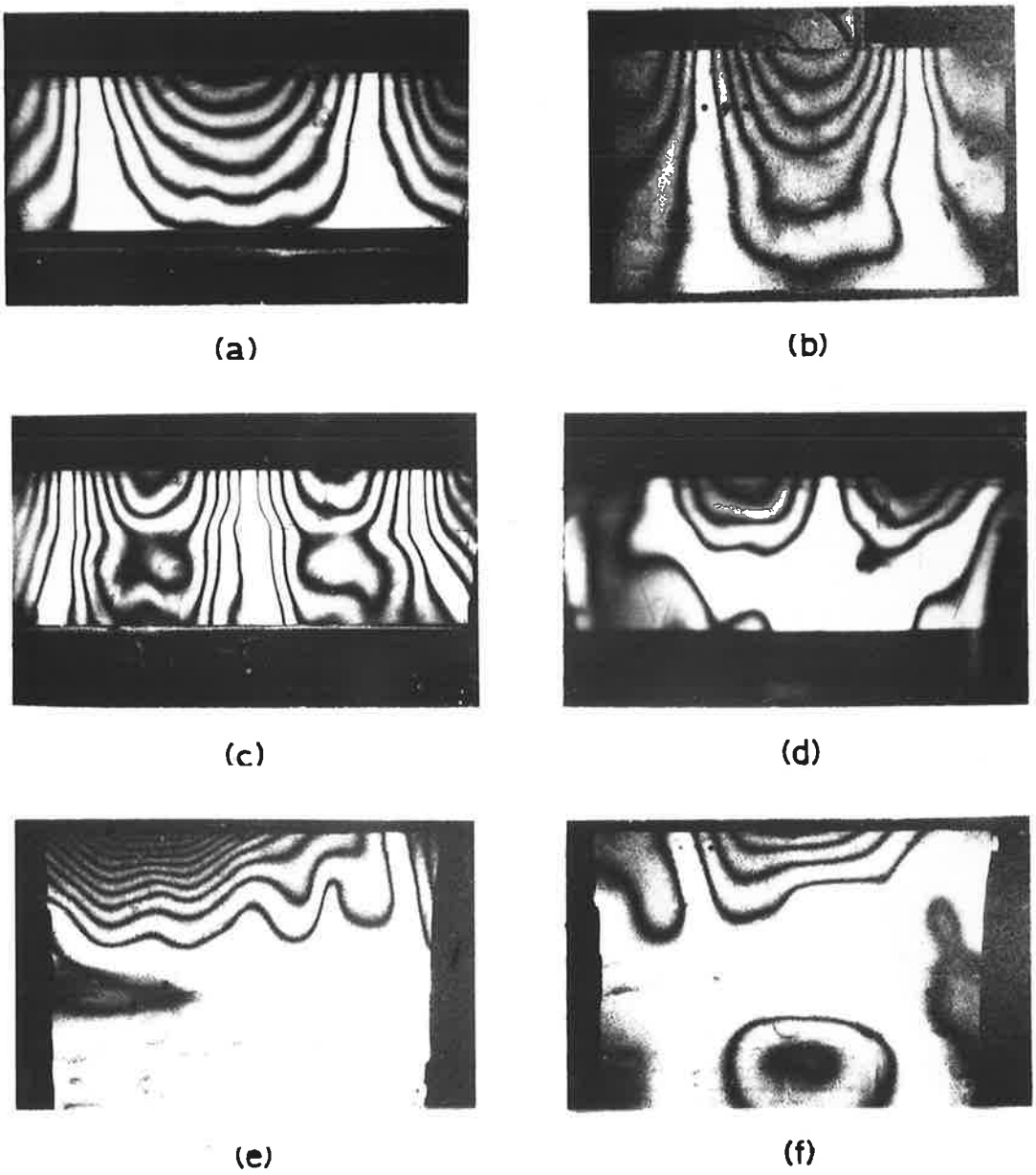

FIG. 5.5 VIBRATION MODES OF THE ENGINE BLOCK TEST SURFACES

(a) 1st bending mode block 1

(b) 1st bending mode block 3

(c) 2nd bending mode block 1

(d) 3rd vibration mode block 1

(e) 1st vibration mode block 4

(f) 2nd vibration mode block 4

The vibration modes for block 2 were similar to the corresponding ones for block 1.

to those of the other blocks. However similar results were obtained for the radiation efficiency for the same order mode on all blocks.

The non-classical plate modes of vibration investigated are illustrated in Fig. 3.7. The mode illustrated in Fig. 3.7a appears to be a combination of the classical (0,3) and (5,1) modes (which have finely separated resonant frequencies) and has a resonant frequency between the corresponding two classical mode resonant frequencies. The mode illustrated in Fig. 3.7b appears to be a combination of the (0,4) and (8,1) modes which again have narrowly separated resonant frequencies.

Results for the holographically determined values of the velocity ratio $\langle v^2 \rangle_{st} / \hat{v}_A^2$ (see Chapter 3) and for the corresponding sound pressure levels and antinodal acceleration levels measured in the reverberant room are listed in Table 5.1b for all the engine block modes considered. The results for the non-classical plate vibration modes are plotted as a function of wavenumber ratio in Fig. 5.6. The radiation efficiency corresponding to each mode is calculated as described in section 5.2. The same assumptions mentioned in section 5.1 are applicable to the calculation of the results for the non-classical plate and engine block vibration modes. The variations in the mean square velocity ratios for the same non-classical mode on different plates are considerable, probably due to the difficulty in repeating the exact driver and clamping conditions for each plate, a necessary condition as the drivers are considered to be responsible for the presence of the modes. The approximately determined radiation efficienc curve corresponding to the modes illustrated is shown in Fig. 5.6. The curve is a line of best fit through the experimentally determined data points for values of k/k_b less than 0.8 and is equal to unity at values of k/k_b greater than or equal to 0.8 as discussed earlier. From the Figure it can be seen that the radiation efficiency of the non-classical plate modes is greater than might be expected (from the trend shown in Figs. 2.6 and 2.7) for the classical (5,1) and (8,1) modes respectively. This

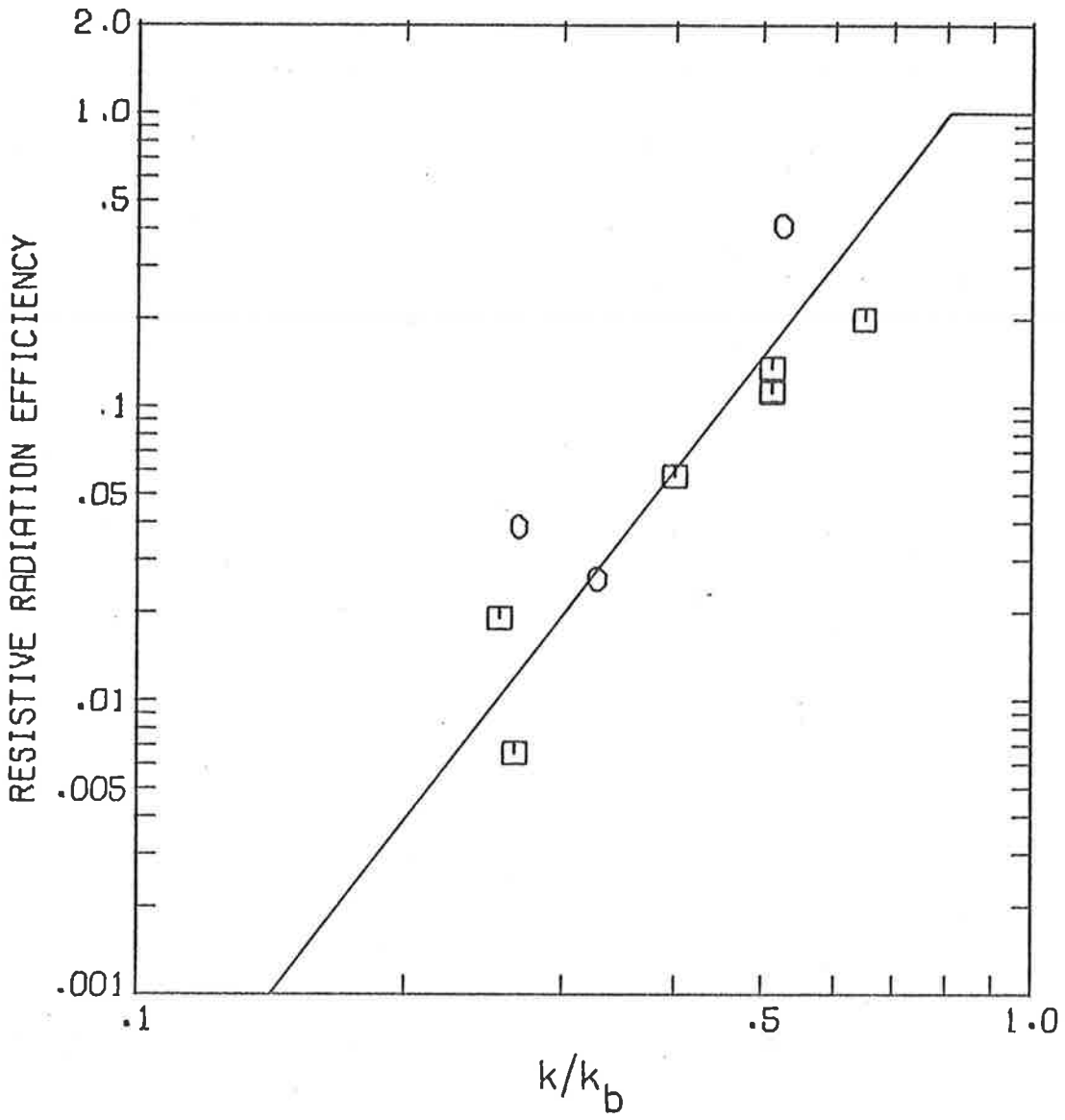

FIG.5.6 EXPERIMENTALLY DETERMINED RADIATION EFFICIENCIES FOR TWO NON-CLASSICAL PLATE VIBRATION MODES.

Table 5.1a : Radiation Efficiency Measurements for Non-Classical Plate Modes

Plate Radius = 0.1755 m.

Mode	frequency (Hz)	$\langle v^2 \rangle_{st} / \hat{v}_A$	Peak accel. level dB re. g(9.8m/s^2)	T_{60} (secs)	SPL re. 2 x 10^{-5}N/m^2	ka	k/k_b	σ
0,3:5,1	853	.161	+21	5.6	75.4	2.74	0.255	0.019
0,3:5,1	880	.42	20	5.5	73.8	2.85	0.265	0.0070
0,3:5,1	1715	.088	16	4.1	68.2	5.50	0.512	0.114
0,3:5,1	1714	.24	16	4.1	72.5	5.50	0.512	0.113
0,3:5,1	1714	.24	6	4.1	63.3	5.50	0.512	0.135
0,3:5,1	2172	.24	10	3.7	66.5	6.97	0.648	0.199
0,3:5,1	1339	.176	22	4.6	76.9	4.30	0.40	0.058
0,4:8,1	1565	.176	+15	4.3	64.8	5.02	0.33	0.026
0,4:8,1	1280	.135	+22	4.7	74.5	4.11	0.27	0.039
0,4:8,1	2518	.176	8	3.5	64.8	8.08	0.53	0.413

Table 5.1b : Radiation Efficiency Measurements for Engine Block Vibration Modes

Mode	Block No. (See Fig.5.3)	Block dimensions (m) $a_1 \times a_2$	Frequency (Hz)	$\langle v^2 \rangle_{st} / \hat{v}_A^2$	Peak accel. level dB re. $g(9.8m/s^2)$	T_{60} (secs)	SPL dB re. $2 \times 10^{-5} N/m^2$	$k\bar{a}$ $\bar{a} = \frac{(a_1^2 + a_2^2)^{\frac{1}{2}}}{2}$	k/k_b	σ
1st	1	.718 x .257	513	0.092	5	5.6	80.2	3.57	1.07	0.80
1st	2	.725 x .275	665	0.105	10	5.8	86.5	4.71	1.40	1.38
1st	3	.346 x .219	1331	0.059	10	4.5	75.5	4.98	1.34	2.60
2nd	1	.718 x .257	833	0.091	0	5.5	74.3	5.80	1.16	1.70
2nd	2	.725 x .275	1316	0.091	10	4.5	77.0	9.33	1.85	0.87
2nd	3	.346 x .219	1577	0.026	30	4.1	86.5	5.90	1.06	1.13
3rd	1	.718 x .257	1118	0.135	5	4.9	78.3	7.78	1.56	1.81

indicates that although the plate response is dominated by the (5,1) and (8,1) modes respectively, the radiated sound power is dominated by the more efficient (0,3) and (0,4) modal contributions. The values of k_b used in Fig. 5.6 were calculated using the theoretically determined plate bending wavenumbers of the classical (5,1) and (8.1) modes respectively, as these dominate the plate response. For the (5,1) mode $k_b a = 10.76$, for the (8,1) mode $k_b a = 15.24$, for the (0,3) mode $k_b a = 9.43$ and for the (0,4) mode, $k_b a = 12.57$.

The experimental data shown in Table 5.1b for the side surface of the engine blocks indicates that the radiation efficiencies for the low order modes are all in the region of unity, and generally greater than unity. These results are consistent with experimental results obtained by Chan and Anderton (1974) who performed tests on in-line diesel engine blocks under running conditions and obtained radiation efficiency values in excess of unity (for the frequency range considered here). This eliminates the possibility of establishing a radiation efficiency curve as demonstrated for the non-classical plate vibration modes, although in principle it should be possible to establish one, at least for the lowest order vibration mode, by measuring the sound power radiated by the block in forced vibration at lower frequencies and assuming the same mean square velocity distribution as for the lowest order resonant mode. In practice, this proposal was not practical due to the difficulties in ensuring that the forced response was the same as that corresponding to the lowest order resonant vibration mode. As the engine block was not firmly mounted, the forced response at frequencies below the first resonant frequency was dominated by a rocking motion of the whole block about its supports and this was difficult to eliminate. The conclusion which may be drawn from the radiation efficiencies of the engine block modes being approximately unity, is that sound radiated from the opposite side of the block will not interfere with sound radiated from the side tested. Thus the use of the baffle has served merely to prevent

sound from the opposite side from entering the reverberant room but it has not affected the radiation efficiency. In summary sound power radiated by the two sides in the low order modes is additive and may be calculated as though the two sides radiated independently as simple pistons of the same total area and with the same surface average mean square normal velocity. This conclusion was checked by making some measurements with the engine blocks placed in the reverberant room and a cover placed on the top and bottom of each block to prevent the interference of sound generated by the inside surfaces. The resultant increase in sound power level was in all cases about 3dB over that measured for the blocks mounted with one surface protruding from a reverberant room wall and vibrating with the same antinodal acceleration level, thus supporting the conclusion mentioned above.

A further conclusion may be drawn from this study. Since the radiation efficiencies for all of the low order modes of an engine block may be taken as unity, it should be quite possible to calculate the radiated sound power in the low frequency range using finite element analysis. Finite element analysis can be readily used to predict low order mode response and as this study shows, only the mean square average surface velocity, which could easily be obtained from the analysis, is required to compute the radiated sound power. As mentioned in Chapter 1 such detailed analysis is only required in the low frequency range where finite element analysis applies. In the higher frequency range quite acceptable statistical techniques are available. Thus the problem of predicting the sound power that will be radiated by an engine block appears to be essentially solved. What is now required is a procedure for estimating the distribution and amplitude of vibration in such a structure from first principles.

5.5 SUMMARY

The preceding discussion began with a comparison of measured and

predicted radiation efficiencies for the first few low order resonant vibration modes of a clamped edge circular plate mounted in an infinite rigid baffle. The theoretical predictions were for the plate radiating into an echo free field and this was simulated experimentally using a reverberant room containing a rotating diffuser. Discrepancies between theory and experiment were not fully explained. However suggestions which may account for most of the observed discrepancies were offered.

Experimentally measured radiation efficiencies for the plate model mounted in the end of a tube in the reverberant room were compared to those for the plate mounted in the reverberant room wall for the first six vibration modes. The differences obtained with this comparison were found to be slightly less than those which would have been predicted for simple sources in place of the plates.

In the second part of the discussion the radiation efficiency measuring technique was applied to two cases not readily amenable to theoretical analysis. It was shown how radiation efficiency measurements for the same vibration mode on a few surfaces of similar shape but not size could be used to predict the radiation efficiency for the same vibration mode on surfaces of the same shape but differing in size from the original surfaces. The two examples demonstrated were non-classical circular plate vibration modes and low order vibration modes of one side surface of some in-line engine blocks.

In the case of the engine blocks a scatter of ±3dB about a mean value of radiation efficiency of 1.6 is obtained. These results, although not completely understood, are consistent with previously published data (Chan and Anderton, 1974).

The radiation efficiency measurement technique described here is not limited to the particular examples considered, rather it is quite generally applicable.

PART II: INVESTIGATION OF THE RADIATION IMPEDANCE OF A SOURCE IN A REVERBERANT ROOM CONTAINING A ROTATING DIFFUSER

CHAPTER 6

DISCUSSION AND REVIEW OF PREVIOUS WORK

6.1 INTRODUCTION

One of the principal uses of a reverberant room is for the measurement of radiated sound power, for example as described earlier in Chapter 4. Measurements in a reverberant room are made subject to various conditions designed to ensure accuracy of measurement and that the average radiation impedance seen by the test source is essentially free field. The conditions which must be satisfied have generally been agreed upon, but some uncertainties persist and thus a copious literature exists devoted to an understanding of the use of reverberant rooms. In this chapter this literature will be briefly reviewed and summarized. In the remaining chapters, new information will be presented concerning the radiation impedance of pure tone sources looking into a reverberant room containing a rotating diffuser.

6.2 REVIEW OF PREVIOUS WORK

Measurements of sound power are always conducted in a reverberant room on the assumption that the field is diffuse. Only under the condition of diffuse field can a macroscopic theory be applied which allows calculation of the radiated sound power from appropriate measurements which may be carried out in the room.

The concept of diffuse field implies that sound propagation in all directions is equally likely; a condition which certainly is met in an echo-free space. However, in any reverberant enclosure there will always be preferred directions of sound propagation determined by the modes of the enclosure. Thus the diffuse field describes a limiting condition which is only approximated adequately when many modes of the enclosure are excited.

When many modes of an enclosure are excited at once the sound field is said to behave statistically as its various properties may be derived from statistical considerations. However, as the modal density of an enclosure is strongly frequency dependent and rapidly grows smaller as the frequency diminishes, it is clear that some difficulty will be experienced in achieving a diffuse sound field at low frequencies. Similarly difficulty may be expected at all frequencies as the bandwidth of the sound is narrowed, as this also tends to reduce the number of modes which are excited.

As a consequence of the dependence of the modal density of a room upon frequency, there is a lower limiting frequency for even broad band noise sources below which insufficient room modes will be excited in a frequency measurement band for the room to behave statistically. An estimate for this frequency, as a function of room volume and reverberation time, based on theoretical considerations together with some experimental evidence was presented by Schroeder (1962). This relation, which corresponds to a modal overlap index (see Bies and Hansen, 1976) in the room of three, may be written as,

$$f_c = 2000\ (T_{60}/V)^{\frac{1}{2}}\ .\ \text{Hz}\ . \qquad (6.1)$$

Subsequent work by Scharton (1967) and by Bies and Davies (1977) suggests that this limit may be reduced to a frequency corresponding to a modal overlap of one, at least for some measurements and for bands of noise. However, as the above expression implies that many room modes are excited simultaneously, frequency band excitation is implicit. The criterion thus cannot be expected to apply for the case of pure tones. Use of a rotating diffuser might alleviate the problem of room mode excitation but the question of whether a rotating diffuser will ensure good statistical behaviour above f_c, i.e. a diffuse field and free field radiation impedance, has not been resolved. The work in the remaining chapters of this thesis will show that a rotating diffuser will ensure approximately free field radiation impedance

for sources radiating at frequencies down to frequencies somewhat less than f_c.

The effects described above are particularly important for the measurement of sound power in tones in a reverberant room. The sound power radiated by a source is dependent upon the source internal impedance as well as the radiation impedance presented by the environment surrounding it. Generally the internal impedance of the source is unknown; thus it is important and in fact implicit in all sound power measurements that the radiation load be well defined, that is, that the radiation load be that of a free field. However, even though the assumption of free field radiation impedance is fundamental, it has received only limited theoretical attention and even less experimental confirmation.

Detailed numerical predictions for the sound power radiated by a pure tone monopole sound source in a reverberant room were published by Maling in 1967. He showed that at high frequencies, when many overlapping room modes are excited, the sound power radiated by the source, when averaged over many source positions, closely approximated the free field value. The accuracy of the approximation was dependent on the number of source positions used. At low frequencies when only a few room modes are excited, Maling showed that the sound power radiated by the source did not approximate the free field value when averaged over all source positions in the room. He also showed that the fluctuations of source power output with source position and frequency were strongly dependent on the absorption coefficient of the room walls, and were reduced by increasing the absorption coefficient.

In a second paper (Maling and Nordby, 1967) numerical results were given for the ratio of sound power radiated by a pure tone monopole sound source in a reverberant room to that radiated by the same source in an echo-free field, in the frequency range 200Hz to 2kHz, for a room of 230 m^3 volume. These predictions led to the following conclusion.

As the frequency of the pure tone source increases, the dependence of radiated sound power on source position becomes less and the radiated sound power, when averaged over a fixed number of source positions becomes closer to the free field value. The few experimental results presented support the broad conclusion that the source radiated sound power is dependent on source position in the room.

Waterhouse (1971) investigated theoretically and experimentally the sound power output of a source exciting a single room mode. He showed that in the limiting case of a very low frequency sound source, the sound power radiated into a hard walled room, when averaged over many source positions, showed no tendency to approach the free field value, and differed from free field by a factor dependent on the damping of the mode.

A rotating diffuser makes the measurement of a space average sound pressure level easier by reducing the spatial pressure fluctuations associated with the field of a pure tone source in a reverberant room. The motion of the diffuser causes the modal patterns within the room to continually change and the associated spatial pressure variations in consequence must also shift about in some regular but undefined way. The effect of this modal shifting at any measurement location must be similar to the effect of moving the measurement location over some cyclic but undefined spatial path. Thus the result is an improvement in the determination of the space average sound pressure.

A further spatial smoothing effect due to the rapid rotation of the diffuser can be expected because the continual shifting of modal patterns within the room must prevent any modes from reaching equilibrium. That is, the reverberant field within the room cannot be in steady state. The continual shifting of modes within the room and probably the lack of

energy equilibrium of any modes modulates the radiation impedance presented to the source which in turn amplitude modulates the energy output of the source. This amplitude modulation may be represented in the frequency domain as sidebands equal to the sum and difference of the source frequency and multiples of the fundamental rotational frequency of the diffuser.

The cyclic modulation of the radiation impedance for any given source position must be similar to the effect of moving the source over some cyclic but undefined path. Thus the use of a rotating diffuser for sound power measurements for a source in one particular position in a reverberant room must have a similar averaging effect as the use of a number of different source positions. In the remaining two chapters of this thesis it will be shown that a large rapidly rotating diffuser does have a strong effect on the radiation impedance of a pure tone source in a reverberant room.

In addition to the frequency sidebands generated by the amplitude modulation of the source power output, a diffuser with a significant component of motion in a direction generally normal to its reflecting surfaces could be expected to introduce some Doppler shifting of the source frequency within the room. However, a diffuser of the design used in Chapters 7 and 8 (Lubman 1971), which has no component of motion normal to its reflecting surface, cannot be expected to introduce any significant Doppler shifting of the field within the room.

A rotating diffuser is an old device which was probably first used by Sabine (1922) for the purpose of achieving a diffuse sound field in a reverberant room. However, criteria for its design are still sketchy and inconsistent among various authors. The quantitative effect of the

diffuser on the sound field was first experimentally investigated by Ebbing (1971) for the purpose of measuring sound power radiated by pure tone sound sources. He measured the acoustic impedance presented by a room containing a rotating diffuser to a specially constructed pure tone sound source which was restricted to the frequency range 100 - 240Hz. His measurements showed no significant dependence of near field pressure and velocity on angular position of the diffuser, contrary to the results reported in Chapter 8 of this thesis, but they did show a strong dependence of phase between pressure and velocity of his source on diffuser angular position, in agreement with the results reported in Chapter 8 of this thesis. Although Ebbing's calibration data showed that even in his very restricted frequency range some of his data lacked precision he was able to draw the following conclusions from his experimental work.

1. The impedance presented by the room to a pure tone sound source is a function of the diffuser angular position and the impedance fluctuations about a particular mean caused by rotation of the diffuser decrease as the diffuser rotational speed increases.

2. The rotation of the diffuser causes the room modal frequencies to be perturbed in a cyclic manner in synchronization with the angular orientation of the diffuser. This means that the diffuser causes a continual energy flow from one mode into another, and never allows the modes to be excited to the extent that would be achieved without the rotation of the diffuser. This results in a more uniform sound field in the room and a reduction of the impedance fluctuations as the diffuser speed increases.

3. Although the rotation of the diffuser reduces the variability of radiation impedance encountered as the source is moved about the room, it does not entirely eliminate the dependence of source power output on position in the room. However, the diffuser reduces the fluctuations in radiation impedance as a function of source position and frequency; thus

the uncertainty in the average radiation impedance presented to the source is also reduced.

4. To be effective, the major dimension of the rotating diffuser reflecting surfaces must be at least half a wavelength long at the lowest frequency of interest. Also the reflective surfaces must affect axial as well as tangential and oblique modes.

Some aspects of diffusion and diffusers in a reverberant room were considered by Dodd and Doak (1971), who used a computer simulation of a reverberant room to reach the following conclusions.

1. For sensible sound power measurements there must be an effective averaging over the receiver position and frequency, as well as over source position and orientation.

2. The source averaging may be accomplished using a rotating diffuser which should sweep through a volume of at least two to three cubic wavelengths and should be such as to provide effective scattering at the frequencies of interest. The diffuser recommended by Dodd and Doak is considerably larger than that recommended by Ebbing (see (4) above).

3. At low frequencies, highly directional pure tone sound sources will produce a spatially more erratic room response than that produced by a simple point source.

Sound diffusion in reverberant rooms has been discussed at length in general qualitative terms by Schulz (1971). He defined a diffuse sound field as one in which there is a uniform total energy density and an equal probability of energy flow in all directions. The reason he gives for the desirability of a diffuse sound field is that it enables the sound power level produced by the source to be related to the total absorption and space average sound pressure in the room. Methods to evaluate diffusion, ways to maximize diffusion and proposed methods to check on the adequacy of diffusion in a particular test facility were considered and the following

conclusion reached. In a large well designed room, the most effective way of enhancing the sound field diffusion is to use a moving vane diffuser. Such a diffuser achieves two effects:

1. It continuously changes the room shape in time resulting in a continual shift in room modal frequencies.

2. It continuously redirects the energy flow in space. The criterion given by Schulz for required diffuser dimensions to ensure adequate performance agrees essentially with that suggested by Dodd and Doak, mentioned earlier. He suggests that the minimum dimension of the diffuser should be approximately a wavelength of sound at the frequency of interest.

Reverberant sound fields have been considered statistically by Waterhouse (1968), who concluded that the accuracy of the value obtained for the space average of the sound pressure level improved as the number of sample points used and the bandwidth of the room excitation increased. He also concluded that continuous movement of the receiving point (essentially achieved using a rotating diffuser) resulted in an improvement in the value obtained for the space average sound pressure.

The statistical properties of reverberant sound fields were further considered by Lubman (1969 and 1971) who presented nomographs from which the accuracy of a spatially averaged sound pressure level could be determined in terms of signal bandwidth, room reverberation time and number of fixed microphones used (or length of traverse for a travelling microphone). He also found that use of a rotating diffuser greatly increased the statistical accuracy of the measured mean sound pressure level, especially when pure tones were considered. He suggested that the ratio of the expected pressure spatial variance with the diffuser stationary, divided by the measured pressure spatial variance with the diffuser in motion, might be used as a figure of merit for the evaluation of the effectiveness of a rotating diffuser. The possible effect of the diffuser on the radiation

impedance of a source in a reverberant room was not considered. The analysis of Lubman and Waterhouse assumed frequencies well above the lower bound (Schroeder, 1962) given by equation (6.1).

A review of the "state of the art" of reverberation room acoustics has been given by Waterhouse (1973). He concluded that more work was necessary on the theory and practice of rotating diffusers and also on the measurement of the sound power radiated by pure tone sound sources. This latter work was necessary especially in the area of the experimental determination of the difference between the source power output in the reverberant room (averaged over many source positions) and the power output in free space, so that the limitations of a particular measurement configuration could be determined.

Maling (1973) and Ebbing and Maling (1973) have described the basis of the American acoustic measurement standard ANSI S1.21 - 1972. In the first of the two papers, Maling suggests goals for measured standard deviations of the space average sound pressure level and gives corresponding required microphone traverse distances (or number of discrete microphone measuring positions required). Also tables recommending the number of different source positions which should be used are given as a function of reverberant room volume, room reverberation time and source frequency. In the second paper, Ebbing and Maling describe a procedure, involving lengthy experimental measurements, whereby a given test facility may be evaluated for its suitability for determining the sound power radiated by a pure tone sound source to a desired degree of accuracy. For each particular $\frac{1}{3}$ octave band tested, the test facility (which may include a rotating diffuser) is deemed to qualify for pure tone sound power measurements in that $\frac{1}{3}$ octave band if the following criterion is met. The standard deviation of the difference between the room sound pressure levels and the mean level for a specified number of different pure tones in the particular $\frac{1}{3}$ octave band must be less than a specified amount when a constant power output source is

used. This procedure provides an estimate of the measurement uncertainty but makes no provision for reducing the measurement uncertainty by some calibration procedure, nor does it provide any means for "making do" with a room that does not qualify, using some correction determined by calibration.

The precision of reverberant sound power measurements was reviewed by Lubman (1974). The spatial variance in sound pressure level in the room for low, mid-range and high frequency signals was discussed quantitatively and in detail. The variance in sound pressure level with source position, the effect of a rotating diffuser in reducing this variance and the spatial variance were briefly considered.

The effect of a rotating diffuser on the spatial variations of the sound pressure level in a reverberant room was summarized by Tichy (1974). The frequency and amplitude modulation caused by a rotating diffuser in the sound field produced by a pure tone source was considered. The source frequency component in the resulting sound field was shown to have a much higher amplitude than that of any sideband produced by diffuser rotation. Also, the effect of several different diffuser shapes and speeds on the normalised spatial variance in sound pressure level was presented as a function of modal density. The results show that the diffuser shape is important and the rotational speed should be greater than about 20 r.p.m.

The variance in sound pressure level as a function of microphone traverse length in a room containing a rotating diffuser was compared with numerical results published earlier (Lubman, 1969) for a room containing no diffuser. The data show that the diffuser has a considerable effect in reducing this variance.

Recently an alternative impedance-tube calibration procedure has been described which allows calibration of a reverberant room for the measurement of sound power in tones from a small source (Bies and Hansen, 1976). This procedure provides a means for estimating the sound power

radiated by a source, even for a room which does not qualify according to the American acoustic measurement standard ANSI S1.21 - 1972. Furthermore the method offers a means for measuring the radiation impedance of the mouth of the tube at a particular location in a reverberant room. The extension of the procedure for the measurement of the radiation impedance is the subject of the next chapter, Chapter 7.

In 1975 Hwang derived expressions for the sound field produced by a point monopole source in a rectangular enclosure with one wall in rectilinear time harmonic motion. He concluded that the sound field produced by the pure tone source is multitonal and that the frequency side-bands are due mainly to the Doppler shifted sound waves reflected from the moving wall. However, for a cylindrically shaped diffuser such as used in the experiments considered in this thesis it is difficult to imagine that Doppler frequency shift plays an important part in the generation of side-band frequencies, as the reflecting surfaces of the diffuser do not have a normal component of motion. In this case the side-band frequencies can be accounted for in terms of the modulation of the radiation impedance of the source as first suggested by Lubman (1971). This view is supported by the work contained in Chapters 7 and 8 of this thesis.

In a recent publication (Bies, 1976) the use of reverberant rooms for the measurement of sound power is discussed in detail and the requirements set forth in the appropriate standards are summarized.

At the Ninth International Congress on Acoustics, (1977) three papers relevant to the work discussed in this chapter and Chapters 7 & 8 were given.

1. de Vries et al showed that the sound power radiated by a monopole source in a reverberant room is always less than the free field value, even when averaged over all possible source positions. However, the difference between the power radiated into the reverberant room and the free field value becomes small at high frequencies.

2. Waterhouse showed that for a monopole source, many source positions are required to give an accurate measurement of the true mean for the radiated sound power averaged over all possible source positions.

3. Tichy reviewed recent developments in sound power measurements in reverberant rooms and suggested that, although a rotating diffuser can reduce errors in space average sound pressure level measurements, it has little effect on the source radiated sound power. The work described in Chapters 7 and 8 of this thesis shows that this conclusion is incorrect, at least for a cylindrically shaped rotating diffuser.

6.3 SUMMARY OF EARLIER WORK

To clarify the areas in which research still needs to be done, the earlier work which is described in detail in the foregoing section will be briefly summarized here. This previous work may be divided into four parts as follows.

1. Theoretical and experimental investigations of the radiation impedance presented to a pure tone sound source as a function of source frequency, source position and room characteristics are required.

Theoretical expressions have been derived and numerically evaluated for a pure tone monopole source. These calculations show that the impedance presented by the room to the source is dependent on source position but at high frequencies when averaged over many source positions, the impedance approaches the free field value as more source positions are considered. At low frequencies the limiting value for the impedance is not the free field value and is dependent on the room physical properties. However, more experimental work needs to be done to verify these theoretical predictions, especially for real sources with complicated directivity factors. It was also shown that as the frequency increased, the dependence of impedance on source position decreased. The low frequency limit at which the free field value for the impedance is no longer approximated to a sufficient degree

of accuracy is generally considered to be that given by the Schroeder cut off frequency f_c given by equation (6.1).

2. Investigation is required of the precision of measurement of sound power radiated by a source occupying a particular position in a reverberant room. For example, it may not be possible to move the source to several different positions within the room. This problem has been considered statistically as a function of source frequency, bandwidth, number of sound pressure level sampling positions (or length of a continuous traverse) and room modal density. More experimental data for pure tone sound sources is necessary to verify these estimates, especially at low frequencies where the statistical approach is questionable.

3. Investigations of the effect of a rotating diffuser on the average radiation impedance and on the precision of sound power measurement are required.

Some experimental investigations have indicated that the use of a rotating diffuser reduces the need to average over many source positions as well as reducing the variance of the sound pressure levels sampled along a given microphone traverse. However much work still remains to be done in quantitatively evaluating the effect of a rotating diffuser on both the impedance presented to a pure tone sound source and the accuracy of the determination of the space average sound pressure level from a given microphone traverse.

4. The procedure generally recommended for pure tone sound power measurement is described in ANSI S1.21 - 1972. However, no possibility is allowed for the use of a test facility which does not qualify as described for pure tone measurements and even for test facilities which do qualify, there is no guarantee that the source radiated sound power will be equal to the free field value and neither is any means described by which a given test facility may be calibrated to reduce the uncertainty in the result

obtained for the radiated sound power. Also, suggested means for estimating this level of uncertainty need experimental verification.

CHAPTER 7

IMPEDANCE TUBE MEASUREMENT OF THE RADIATION IMPEDANCE

7.1 INTRODUCTION

The purpose of the work described in this chapter is to determine under what circumstances, if any, there is negligible difference between free field radiation impedance and the radiation impedance presented to a source by a reverberant room containing a rotating diffuser. For this purpose measurements are reported of the radiation impedance presented to three different size pure tone sound sources mounted in the side wall of a reverberant room containing a cylindrical rotating diffuser. Average radiation impedance measurements are presented as a function of diffuser speed and source frequency. The average measurements are obtained from many "instantaneous" impedance measurements distributed over one complete diffuser revolution. Examples of impedance variations as a result of diffuser rotation are also presented.

The sources used for these experiments were,respectively, the mouths of a 0.101m diameter tube, a 0.156m diameter tube and a 0.43m diameter mouth of a conical horn, the throat of which was attached to the open end of the 0.101m tube. In each case the mouth of the source was mounted flush with a large baffle placed in the side wall of the reverberant room.

The radiation impedance presented to a tube mouth was determined as a function of angular position of the diffuser, by recording the standing wave field in the tube using a slowly traversing probe microphone and a high speed data acquisition system. The sound field in the impedance tube was sampled at a suitable rate to obtain enough data

points to define individual standing waves in the tube for selected angular positions of the diffuser. The number of angular positions selected ranged from 300 at a diffuser speed of 10 RPM to 60 at 50 RPM and 20 at 0 RPM as shown in Table 7.2. The number of points used to define each standing wave ranged between 50 and 150.

Measurements were conducted using the above mentioned sources over a frequency range from 100 Hz to 1000 Hz in frequency increments of 50 Hz and from 1000 Hz to 2000 Hz in frequency increments of 100 Hz. For comparison with free field theoretical predictions an average radiation impedance was determined for each source at each frequency considered, by averaging the "instantaneous" impedance measurements over one complete revolution of the diffuser. It was not possible to find the average impedance from the average standing wave traced out in the level recorder with the slowly moving microphone probe in the tube and a slow writing speed, because the impedance is not linearly related to the average standing wave.

As it is well known that a rotating diffuser acts as a frequency modulator (Lubman, 1971, Tichy, 1974) it could be argued that the presence of side band frequencies in the standing wave of the impedance tube used for the measurements reported here would tend to obscure the minimum in the standing wave. This would have the effect of reducing the apparent standing wave ratio and could introduce a serious systematic error in the determination of the radiation or throat impedance at the radiating end of the impedance tube. As this point is of fundamental importance it is given careful consideration. It is shown that the side band frequencies are fully accounted for by a negligible distortion in the source signal which may be described as a slowly varying amplitude modulated sine wave.

7.2 EXPERIMENTAL CONFIGURATION

The test facility used in all experiments was a rectangular reverberant room of 181.4 m^3 volume and 194.6 m^2 surface area. The room is illustrated in Figs. 7.1 and 7.2a. For the tests described here a rotating diffuser capable of continuously variable speed and stable operation up to 50 RPM was used. As shown in Figs. 7.1 and 7.2a, the diffuser is mounted in the ceiling of the reverberant room on a vertical shaft and driven externally to the room. It consists of a relatively light semi-circular cylinder of 3.5 m diameter and 2.4 m height, resulting in a swept volume of approximately 23 m^3. The surface density of the diffuser reflecting surface is 3.3 kg/m^2. According to Schultz (1971) a surface density of 4.9 kg/m^2 is necessary for sound having a frequency of 90 Hz to be reflected. Thus a density of 3.3 kg/m^2 may be considered to make the diffuser effective for reflecting sound at frequencies above about 130 Hz. According to Dodd and Doak (1971) the swept volume of 23 m^3 ensures that the diffuser is effective for modulating room modes at frequencies above about 160 Hz. In the tests described in this chapter rotational speeds of 10 RPM, 20 RPM, 30 RPM, 40 RPM and 50 RPM were investigated. Additionally, measurements were also made with the diffuser stationary at twenty equal increments of eighteen degrees rotation to provide static (0 RPM) data for comparison.

The room reverberant decay times in the $^1/_3$ octave bands of interest are listed in Table 7.1. They were measured using the abrupt sound source cut off method. The room was driven with two speakers located in diagonally opposite corners. The speakers, in turn, were driven with $^1/_3$ octave bands of noise. The sound pressure level was measured with a stationary microphone whose output was monitored on a level recorder. The 60dB decay time, T_{60}, (with the diffuser in motion)

Table 7.1 : Reverberant Room 60dB Decay Times for $\frac{1}{3}$ Octave Bands of Noise, (Measured 7th January, 1977).

$\frac{1}{3}$ octave band centre frequency (Hz)	Reverberation time T_{60} (secs)
100	4.5
125	5.2
160	5.3
200	5.1
250	5.2
315	4.8
400	4.9
500	5.8
630	5.5
800	5.6
1000	5.1
1250	4.7
1600	4.1
2000	3.8

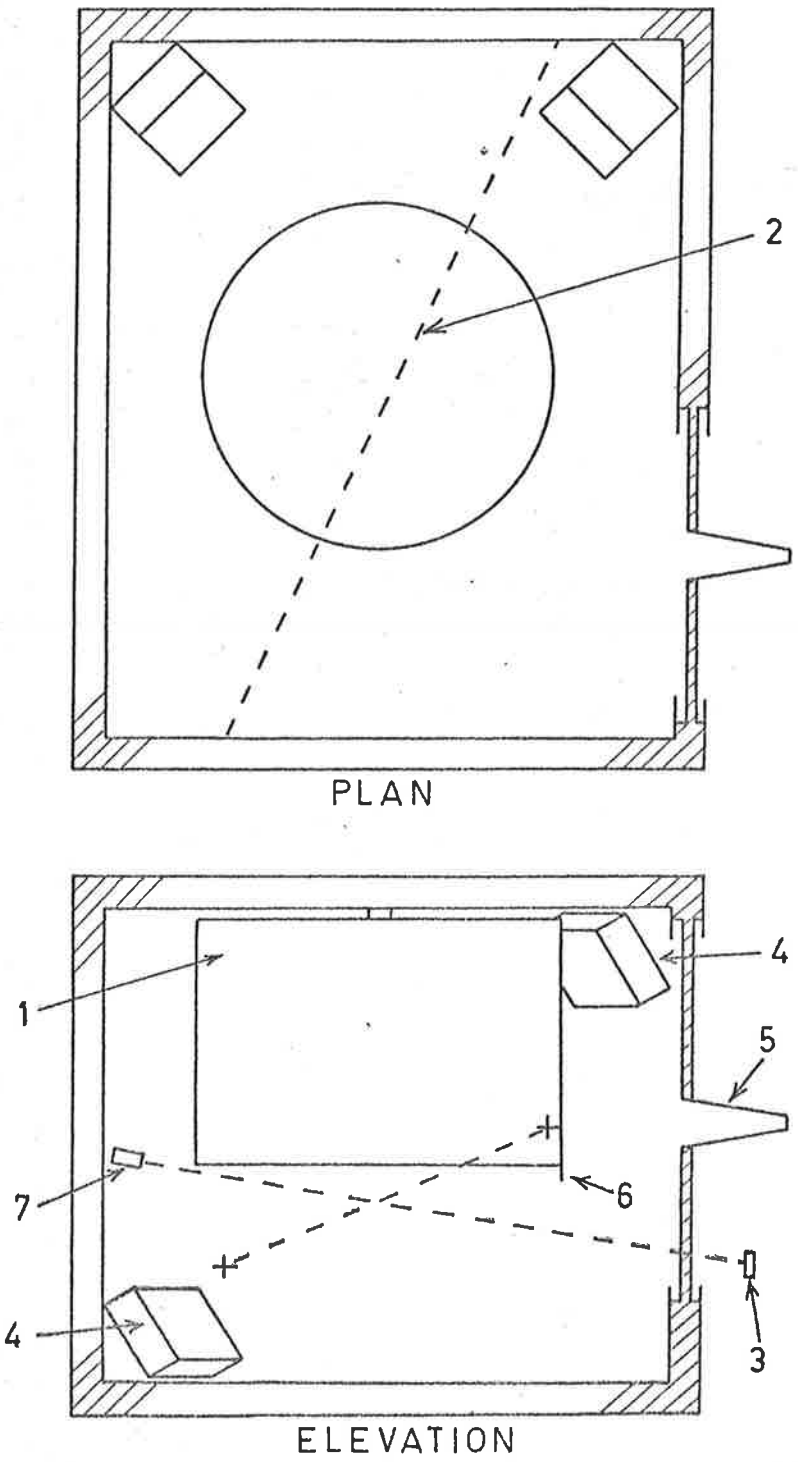

FIG. 7.1. REVERBERANT ROOM CONFIGURATION USED FOR RADIATION IMPEDANCE MEASUREMENTS.

1.Rotating diffuser. 2.Microphone traverse. 3.Photo-transistor. 4.Speaker. 5.Sound source. 6.Laser beam interruptor. 7.Laser light source.

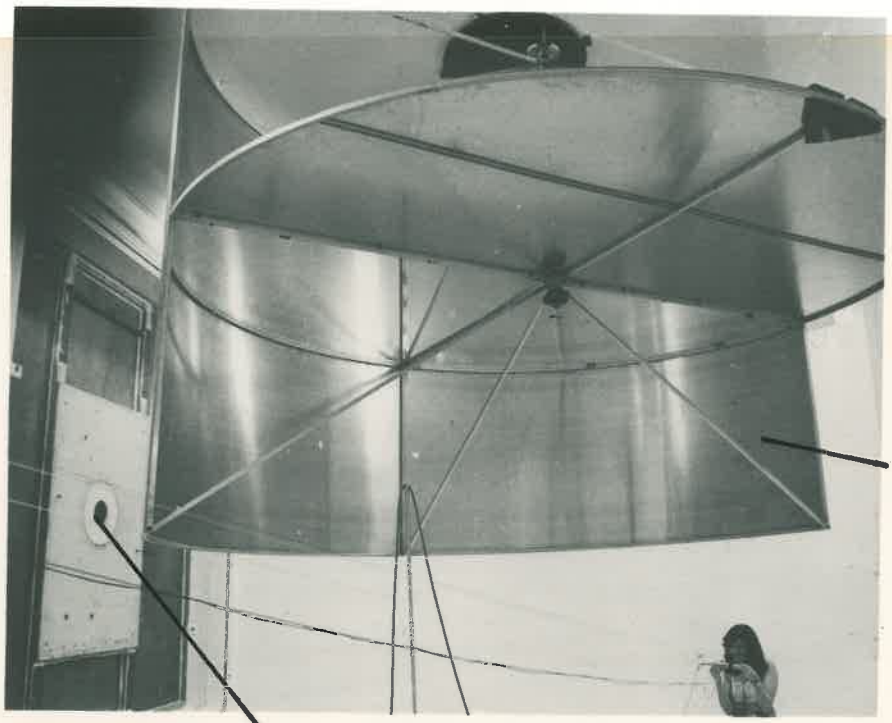

(a)

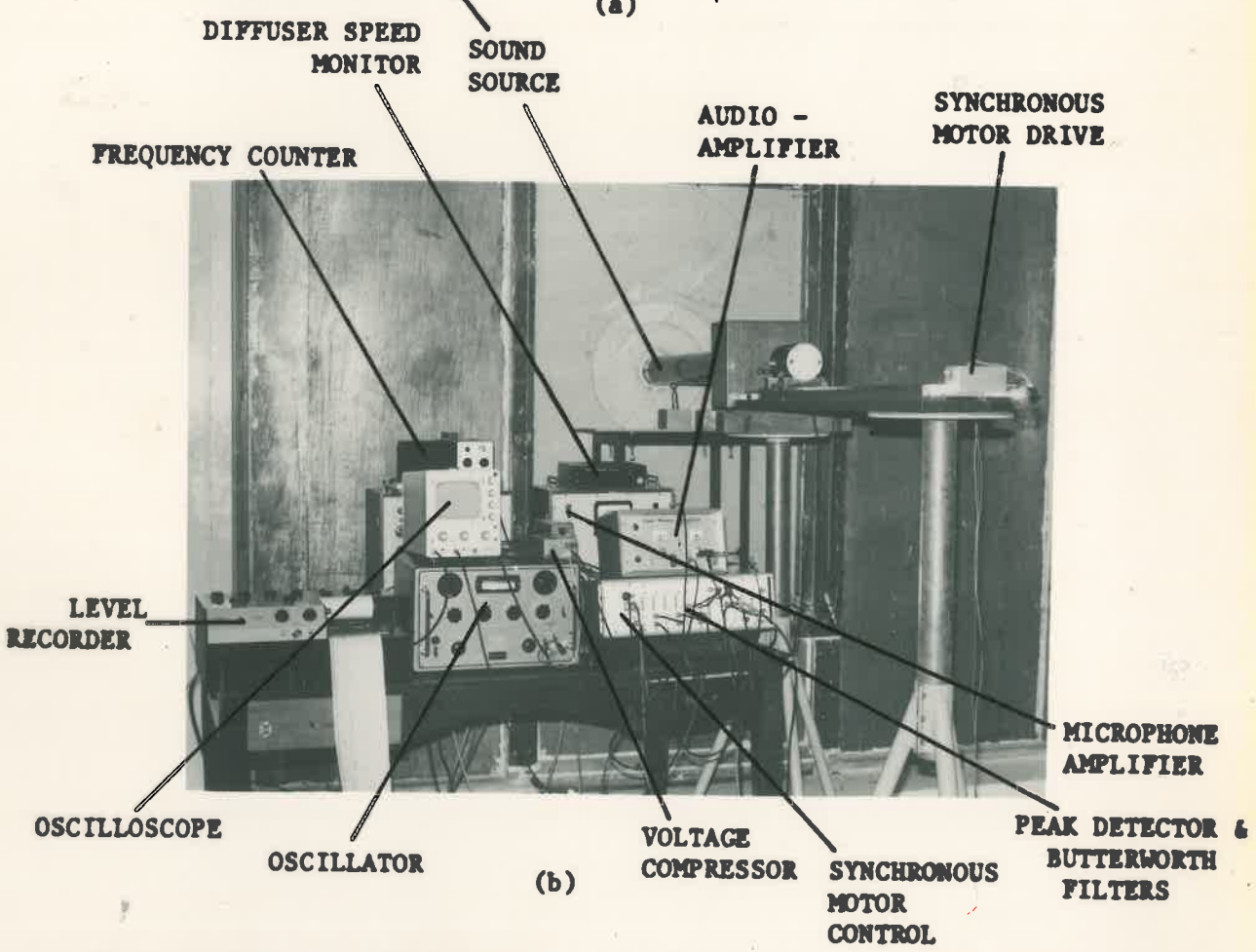

(b)

FIG. 7.2. EXPERIMENTAL ARRANGEMENT FOR IMPEDANCE TUBE SOUND SOURCE TESTS.

(a) Reverberant room arrangement.
(b) Signal generation & recording equipment external to the reverberant room. The data acquisition system is omitted here but is illustrated in Fig. 8.3.

was found by measuring the slope of the trace recorded by a level recorder when the sound from the speakers was abruptly shut off.

The measurements described in this chapter were made at a later date than were the measurements described in Chapter 4. In the time period between the earlier and later measurements of this chapter the reverberant room configuration was altered. The fixed speed rotating diffuser with a swept volume of 3 m^3 was replaced with a variable speed diffuser having a swept volume nearly eight times greater. Also the room walls were painted with a hard resin. These changes are thought to account for the differences in reverberation times reported in Tables 7.1 and 4.1.

The mouth of the sound source used for the radiation impedance measurements was mounted flush with the surface of a 0.019 m thick wooden baffle. This baffle was, in turn, mounted in a massive lead curtain wall which separated the test chamber from a smaller reverberant room, in which the source and associated electronic equipment were assembled. An assembled tube source and electronic test apparatus are shown in Fig. 7.2b. The location of the source mouth is the same as that of the sound source used for the experiments described in Chapter 4 and by Bies and Hansen (1976). The oscilloscope shown in Fig. 7.2b was used to continually monitor the peak detector signal which was derived from the microphone in the impedance tube. Observation of the signal at any one point in the tube showed that the amplitude fluctuations varied cyclically in synchronisation with the rotation of the diffuser. The level recorder shown in the Figure was used to trace out the time averaged standing wave in the impedance tube in order to obtain preliminary estimates of quantities required in the curve fitting procedure described in Section 7.4.

Impedance tubes of two different diameters were used for three tests; 0.156 m for test A and 0.101 m for tests B and C. The experimental arrangements for these tests are illustrated in Figs. 7.3a, b and c. The larger tube was used in the frequency range 100 Hz to 1200Hz, while the smaller tube was used in the range 1200Hz to 2000Hz. The upper frequency limit in each case was determined by the possibility of the onset of cross mode propagation in the tube.

The mouth of a conical horn was used as a sound source for a fourth test as illustrated in Fig. 7.3d. The horn mouth diameter was 0.430 m, the throat diameter was 0.101 m and the length was 1.127 m. For the tests the throat of the horn was attached to the mouth of the smaller of the two straight tubes and the impedance at the horn throat was determined by sampling the wave field in the tube. Consequently the upper limit of the frequency which could be tested was determined by the presence of higher order modes in the attached tube, rather than in the horn itself. This allowed the horn to be used at much higher frequencies (up to 2000Hz) than would have been possible if a straight tube having the same diameter as the horn mouth were used. Thus the conical horn made impedance measurements possible for a relatively large source. The horn was also advantageous at low frequencies, as it reduced the standing wave ratio in the impedance tube. This increased the accuracy of the pressure amplitude measurements, in the regions of pressure minima, as these measurements were made using a data acquisition system having a limited dynamic range.

For all tests, determination of the impedance presented to the source required that the sound field in the particular tube used be suitably sampled and recorded. The sound field in the large tube was sampled using a Bruel and Kjaer half inch condenser microphone attached

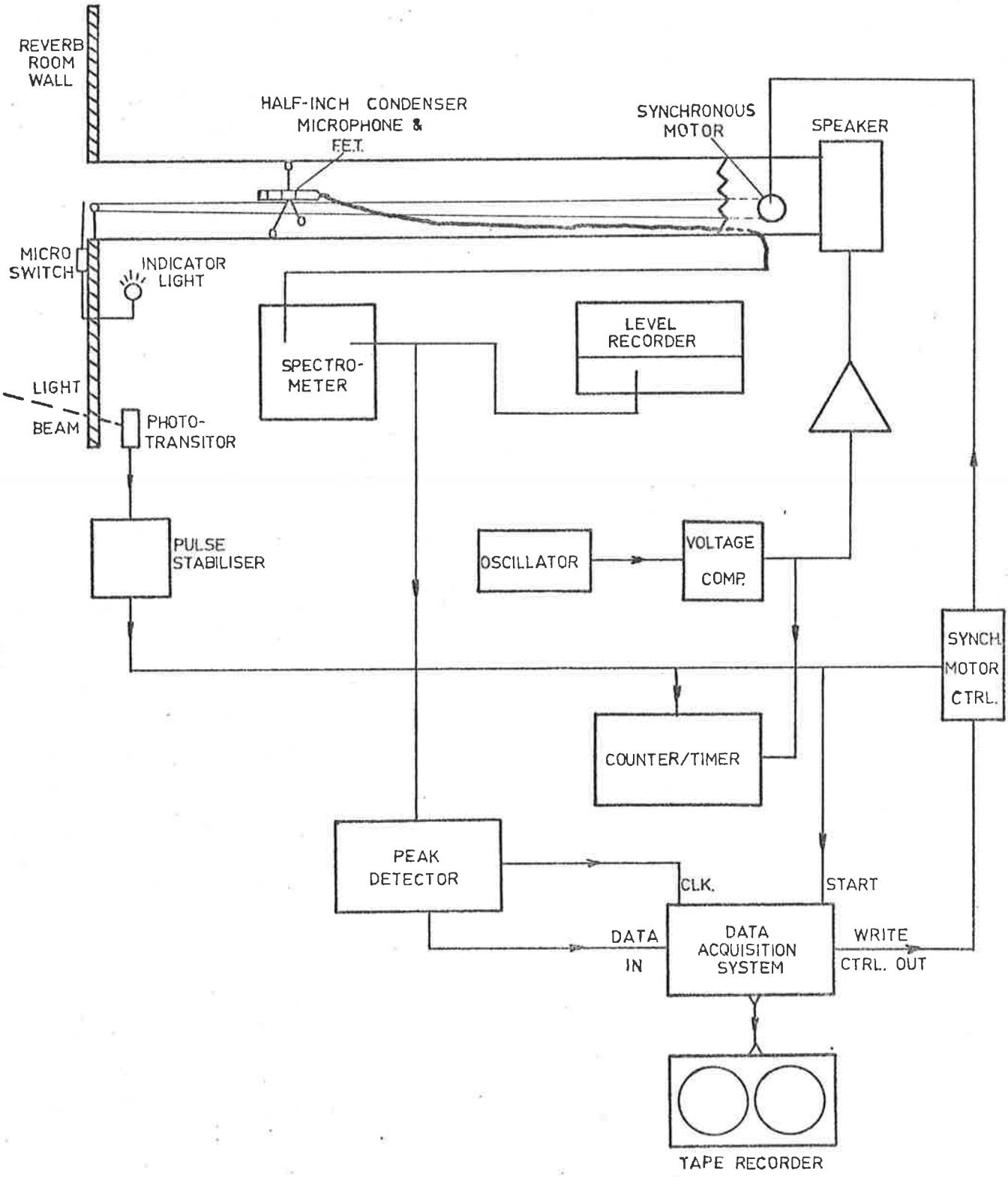

FIG. 7.3a. EXPERIMENTAL ARRANGEMENT FOR METHOD A.

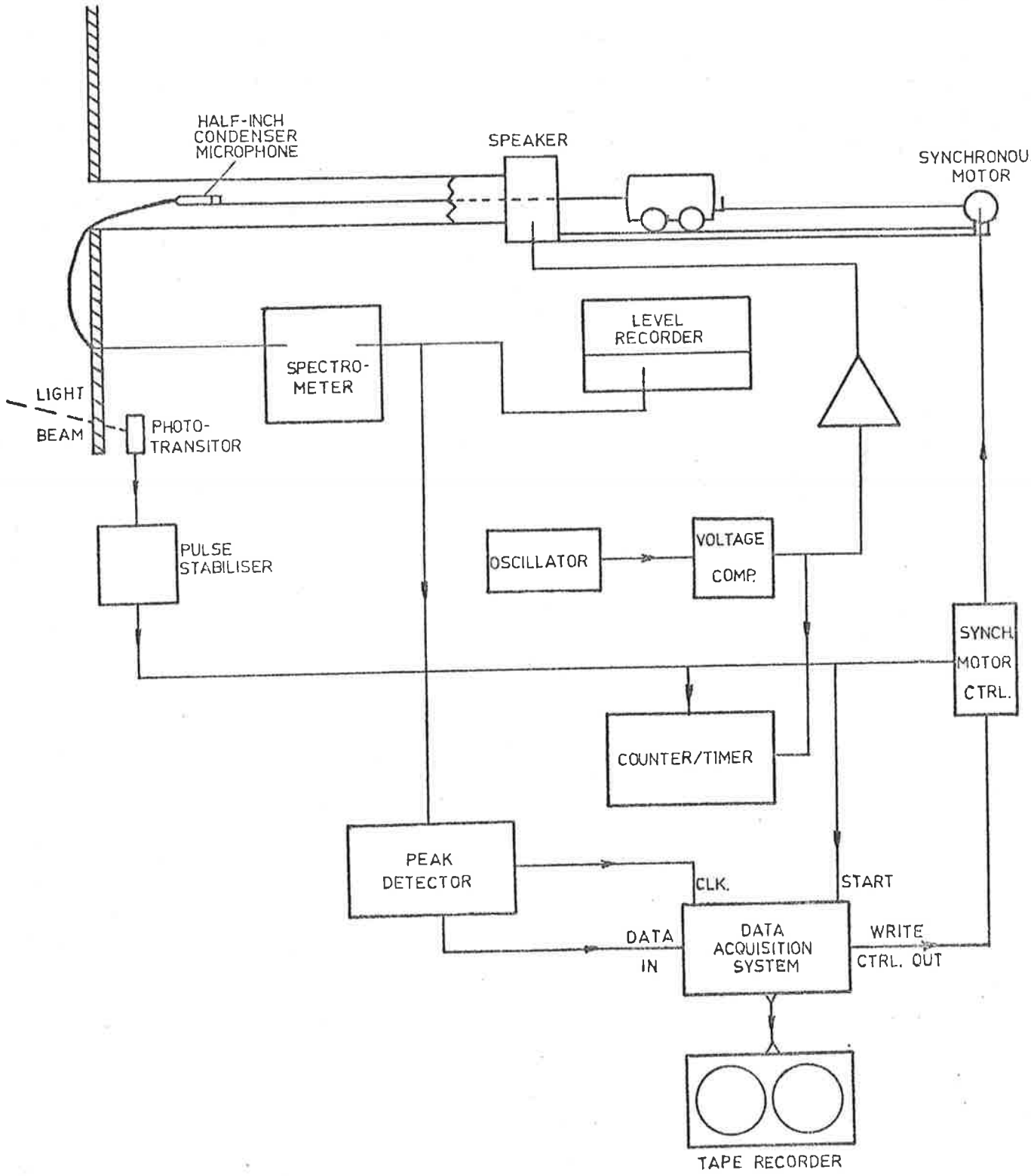

FIG. 7.3b. EXPERIMENTAL ARRANGEMENT FOR METHOD B.

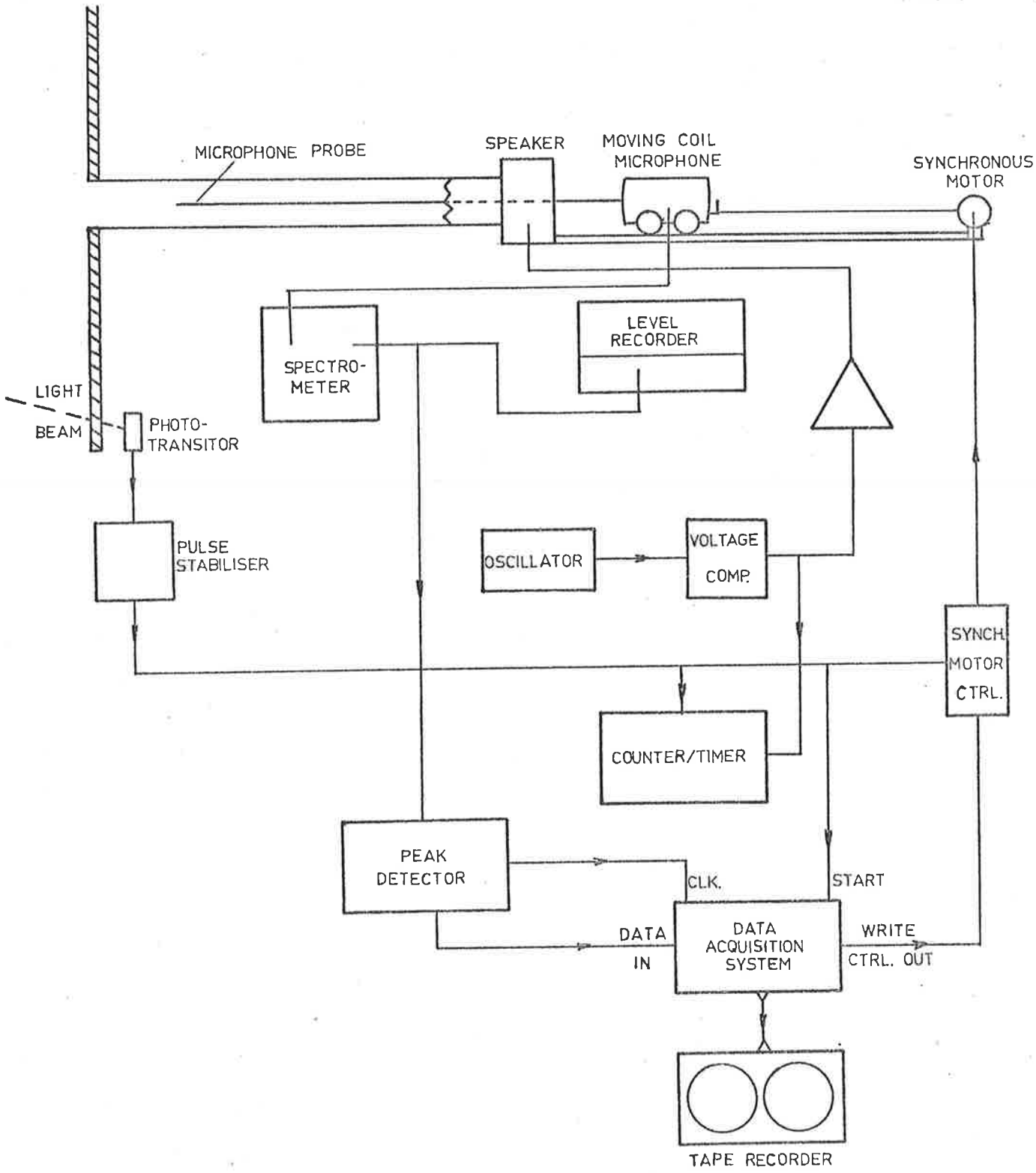

FIG. 7.3c. EXPERIMENTAL ARRANGEMENT FOR METHOD C.

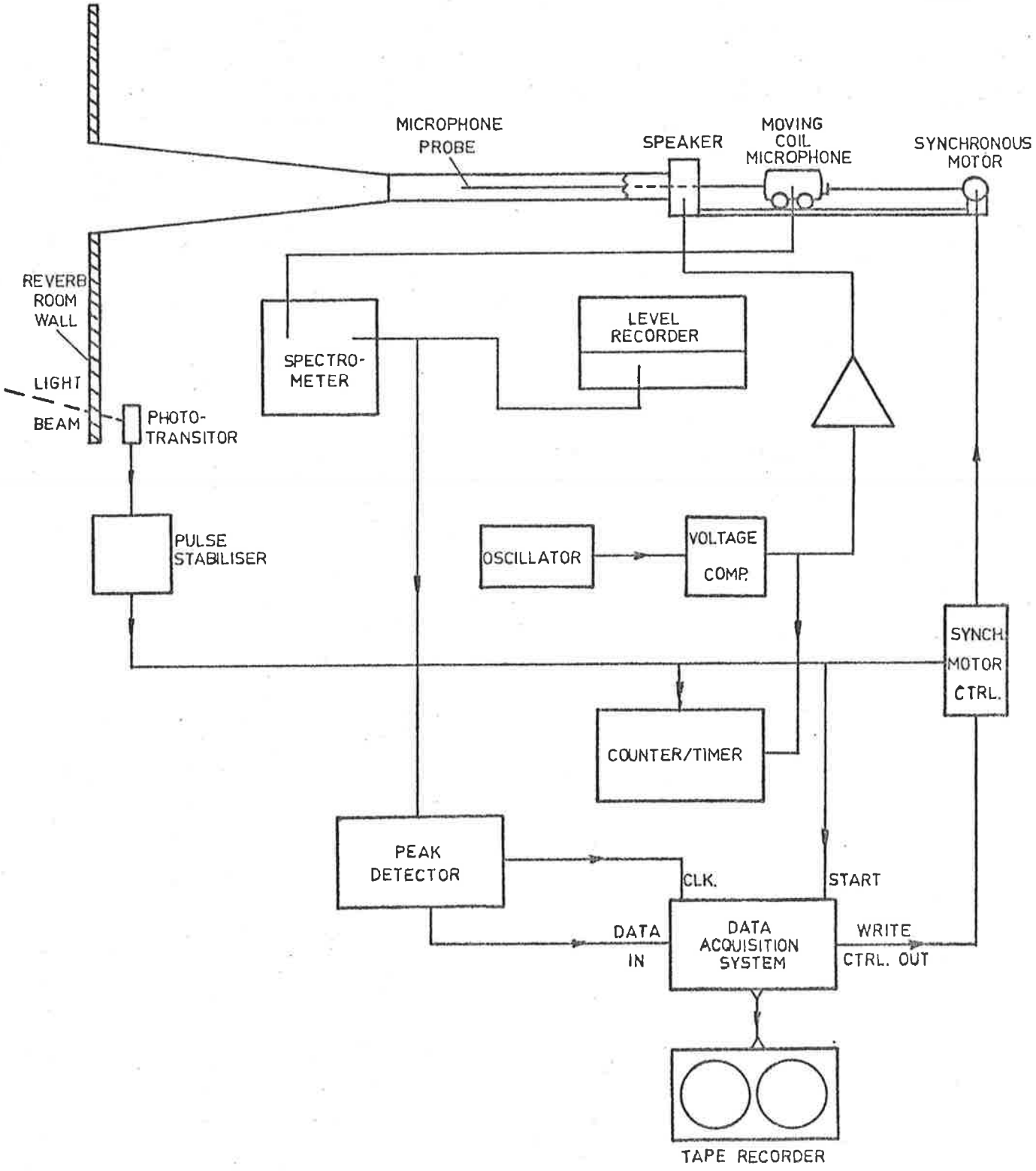

FIG. 7.3d. EXPERIMENTAL ARRANGEMENT FOR METHOD D.

through an FET to a Bruel and Kjaer spectrometer type 2112. The traversing arrangement used to move the microphone along the tube consisted of a string pulley system and carriage, and was contained completely within the tube as illustrated in Fig. 7.3a. The total cross sectional area of the microphone and traversing equipment in the tube was less than 2½% of the tube cross sectional area and was therefore considered to have a negligible effect on the sound field within the tube.

The sound field in the small tube was firstly sampled using a half inch condenser microphone, (test B), as described for the large tube. The cross sectional area of the microphone was about 7% of that of the tube. To ensure that the obstruction provided by the microphone had negligible effect on the sound field in the tube, the tests were repeated (test C) using a 5 mm diameter probe which had a cross sectional area of about 1% of that of the tube. The probe was attached to a moving coil microphone and carriage, which was mounted outside of the tube. The signal from the moving coil microphone was amplified using a Bruel and Kjaer spectrometer. The end of the probe in the impedance tube was closed and the sound field was sampled using two 0.25 mm diameter holes in the side wall of the probe. This enabled the tube cross sectional plane which was being sampled,to be located precisely. The non-linear frequency response of the probe was not a problem as absolute sound pressure levels were not needed for the radiation impedance calculations. The microphone probe was also used to sample the sound field in the tube when the conical horn was attached, (method D). In each of the tests mentioned above, the microphone signal was filtered using $^1/_3$ octave filters to obtain a good signal to noise ratio.

At a later date some of the measurements (involving the use of the small tube) were repeated using variable high and low pass 6 pole Butterworth filters instead of $^1/_3$ octave filters to ensure that the frequency of interest was centred in the pass band of the filter. The pass band used in the later measurements was several hundred Hz to ensure that any side band energy that may be present would not be excluded from the measurements. All of the earlier tests were repeatable to the order of accuracy of the measurements indicating that the use of the $^1/_3$ octave filters did not affect the results due to exclusion of side band energy.

The sound field in each impedance tube was generated using a 15 ohm, 20 watt speaker placed at the end of the tube. The signal to drive the speaker was generated using a Muirhead model D-650-B oscillator and the frequency of the signal was monitored using a Systron Donner model 6150 counter timer. In the frequency range considered the frequency stability of this oscillator was better than ±0.1Hz. However, the amplitude stability of the output voltage was not sufficient (between ±1% and ±2%). The amplitude stability was improved to ±0.05% by connecting a voltage compressor circuit to the oscillator output. This ensured that the stability of the sound source was within the limits demanded by the experiment.

All of the information required to determine the radiation impedance presented to the tube mouth was contained in the sound field in the tube. However, it was necessary to sample this sound field at the correct times and in the correct places in order to obtain meaningful results.

Sound levels at any given location in the impedance tube were observed to fluctuate in synchronization with the rotation of the diffuser. This indicated that it was essential to sychronize the

pressure measurements with the diffuser rotation. Furthermore as the information about the impedance to be measured was contained in the pressure distribution along the tube it was necessary to synchronize the pressure measurements with location in the tube. The synchronization of the rotation of the diffuser was accomplished by interrupting periodically a low power laser beam with a small pointer attached to the diffuser. The laser was directed on to a photo transistor which produced a signal to begin data sampling everytime the laser beam was interrupted. The synchronization of location along the impedance tube was accomplished using a constant speed mechanical drive to move the microphone and support carriage along the tube.

The microphone traverse in the large tube was driven externally to the tube using a small synchronous motor and gearbox, as shown in Fig. 7.3a. The drive shaft from the gearbox was attached directly to the pulley located in the tube near the speaker. The available microphone traverse length was 1.8 m and the traverse speeds used in the experiments were 51.1 mm/min, 155.6 mm/min and 259.4 mm/min. These speeds corresponded to nominal speeds of 1 RPM, 3 RPM and 5 RPM respectively for the output shaft of the gearbox attached to the synchronous motor.

In the small tube the traversing microphone was attached to a probe which, in turn, was attached to a carriage external to the tube, (see Figs. 7.3b, c and d). The carriage (and hence the microphone) was pulled along by a string wound up on a rotating drum driven through a gearbox by a small synchronous motor. The traverse speeds used were 25 mm/min, 75.5 mm/min and 125 mm/min corresponding to nominal speeds of 1 RPM, 3 RPM and 5 RPM respectively for the output shaft of the gearbox attached to the synchronous motor.

The use of the synchronous motors for driving the traverses resulted in constant microphone traverse speeds. Additionally the use of an automatic switching device enabled the microphone traverse to start at the same instant as the data acquisition system began acquiring data. The precision timing of the traverse start, together with the constant traverse speed, resulted in accurate determination of the microphone position corresponding to a given pressure measurement.

The traverse speed in all tests was changed simply by using different commercially available gearboxes attached to the synchronous motors. Changing traverse speeds required only a few minutes. At low frequencies and fast diffuser rotational speeds the faster traverse speeds were used, while at high frequencies and/or slow diffuser rotational speeds the slower traverse speeds were used. The traverse speed was adjusted so that, for any given diffuser angular position, the number of pressure measurements obtained for a microphone travel of half a wavelength of sound was between 50 and 150. Details of the microphone traverse drive, traverse positioning and starting procedures are outlined in Appendix 2.

The number of discrete angular positions of the rotating diffuser which corresponded to a series of pressure measurements was determined simply by the pressure measurement rate of 50 samples/sec and the diffuser rotational speed. The number of discrete angular positions for each diffuser rotational speed tested is listed in Table 7.2.

7.3 DATA ACQUISITION

This section describes instrumentation used to acquire data, criteria used to choose the method of acquisition of data and experimental procedures.

Table 7.2 : Data Used for Calculating Radiation Impedance as a Function of Diffuser Angular Position.

Diffuser Speed (r.p.m.)	No. of full revolutions per data set	No. of samples per rev. of diffuser
0	1	20
10	3	300
20	6	150
30	10	100
40	13	75
50	16	60

The data acquisition system used in the experiments has eight synchronous input channels and is capable of data sampling rates up to 50 kHz. The lower limit to the sample rate is determined by the external clock system used. The memory has a maximum size of 16,000 words, but in the experiments described here only 1,024 words of memory and a sample rate of 50 Hz were used. Each data word consists of eight bits resulting in a minimum error of approximately ±0.2% when the data value is a maximum (that is a data value corresponding to all bits on). It can be seen that a small data value where only the least significant bit is on has a possible error of ±50%.

The data to be recorded originated from either the condenser microphone in the impedance tube or the moving coil microphone attached to the small probe in the impedance tube. The signal from the moving coil microphone was amplified using a Bruel and Kjaer model 2112 spectrometer, while that from the condenser microphone was amplified using an FET and the same spectrometer. The output from the spectrometer was connected through a peak detector to one channel of the data acquisition system.

The peak detector circuit sampled the peak value of the sound pressure signal from the microphone amplifier (2112 spectrometer) and held it long enough for the data system to sample it. At the same time it sent a clock pulse to the data system when the peak value was ready to be sampled. The signal from the microphone amplifier was a.c. coupled and sinusoidal, eliminating the need to sample the negative as well as the positive peak. The number of peaks sampled was variable, using a front panel control, from one in one hundred to every one. The number of peaks sampled was varied in the tests as the frequency of the sound source varied so that at all times the sample rate was 50 samples/sec.

The use of a peak detector enabled instantaneous sampling of the acoustic pressure in the impedance tube, which permitted the instantaneous impedance presented by the room to the tube mouth to be calculated as a function of diffuser angular position.

Voltage levels in the peak detector were adjusted so that an r.m.s. full scale reading on the spectrometer corresponded to all bits on in the data system. The peak detector circuit contained a compression circuit so that voltage levels in excess of full scale were attenuated to the full scale value, thus preventing damage to valuable equipment.

When sound pressure measurements were made in the impedance tube, it was necessary to satisfy the following criteria to maximise the accuracy of the results obtained.

1. The maximum value of the sound pressure level in the impedance tube should correspond as nearly as possible to all bits on in the data system (that is, a full scale reading on the microphone amplifier) without clipping the signal.

2. The minimum value of the sound pressure level in the impedance tube should be well above either acoustic noise or electrical noise inherent in the measuring system.

During the experimental work, the sound power output from the speaker in the impedance tube was adjusted using the variable volume control on the driver amplifier until the above two criteria were satisfied. When the signal from the microphone was passed through a $^1/_3$ octave filter, a maximum sound pressure level of approximately 110dB in the impedance tube satisfied the above criteria.

As the recorded sound pressure data had to be synchronized with the angular rotation of the diffuser, it was necessary to ensure that the diffuser rotated at an essentially constant speed while data were acquired. The short term variations in diffuser rotational speed were

minimized by using a regulated d.c. power supply to drive the diffuser electrical motor. Long term variations in diffuser rotational speed were avoided by taking data sets in a sequence of short time intervals, where each interval began at the same angular position of the diffuser and lasted for a predetermined number of diffuser revolutions. The number of diffuser revolutions contained in each data set was determined by the diffuser rotational speed, the number of samples in each set and the sample rate. The diffuser rotational speed was monitored to the nearest millisec./rev using the counter timer mentioned earlier.

In all experiments the sample size, (or data set size) used for each block of data recorded in the data system memory was 1,024 words, as this proved by trial and error to best satisfy the following criteria.

1. The sample size should be small enough;

(a) to subsequently allow convenient computer analysis and

(b) to ensure that the diffuser rotational speed remains essentially constant during the sampling period.

2. The sample size should be such that slightly more than an integral number of diffuser revolutions occur during the acquisition of each data set. At the same time the sample size should be small enough so that it can be written on to magnetic tape in the time interval between the completion of acquiring a data set and the end of the last diffuser revolution included in the data set.

3. The sample size should be as large as possible;

(a) to minimize the total number of diffuser revolutions missed in a complete frequency run (as one is missed between each data set) and

(b) to reduce the total number of data blocks which have to be subsequently analysed.

4. A requirement of the data acquisition system is that the sample size be an integral multiple of 256.

The choice of a sample size of 1,024 words resulted in the number of complete diffuser revolutions included in one data set being as shown in Table 7.2. The additional data, corresponding to part of a diffuser revolution and which was recorded after the final complete diffuser revolution, was discarded during the data reduction procedure described in section 7.4. The time required to write a data block of 1,024 words on to magnetic tape was about 50 m sec, which set the minimum required time between the end of sampling a set of data and the beginning of the acquisition of the next set of data (beginning of the next revolution of the diffuser). Thus there was a lapse of one diffuser revolution between the end of one set of data and the beginning of the next. As the microphone in the impedance tube moved continually this resulted in small gaps in the standing wave data which are insignificant and show up as faint vertical white lines in Figs. 7.9b, 7.10b and 7.11b.

7.4 DATA REDUCTION

The acoustic pressure data were firstly translated using a CDC 6400 computer from eight bit words into integer numbers between 0 and 255. The actual acoustic pressure corresponding to a particular integer was determined by comparing that integer with the integer corresponding to the sound pressure produced by a Bruel and Kjaer pistonphone. For each frequency considered, the data which were recorded sequentially were reassembled by the computer into blocks of data which described the pressure distribution along the impedance tube for each angular position of the diffuser. Sufficient pressure measurements were made using the experimental procedures described earlier, so that at each frequency tested between 50 and 150 data points were available in each data block to define each standing wave in the impedance tube, for each considered angular position of the diffuser.

The blocks of data thus assembled were checked for validity by first plotting p as a function of x (distance from the mouth of the

impedance tube) for a few blocks in each frequency run and inspecting the plots to ensure that the electronic equipment had produced no obviously incorrect data. The data blocks were then fitted to a theoretical expressions (Beranek 1949b) describing the pressure distribution in a standing wave as follows,

$$p(x) = B\{\cosh[2(\alpha x+\psi_1)] + \cos[2(kx+\psi_2)]\}^{\frac{1}{2}} \quad . \qquad (7.1)$$

Values of x are zero at the tube mouth and negative between the tube mouth and the sound source. The values of x corresponding to particular values of sound pressure p were determined from the microphone travel speed, the pressure sampling rate and the number of samples taken prior to the one considered. When a condenser microphone was used, the actual pressure measuring plane was some distance in front of the microphone diaphragm and this was taken into account as described in Appendix 2. The microphone traverse and data sampling system were started simultaneously for each experimental run and the microphone traverse continued between the acquisition of data sets when the data were being written on to magnetic tape. Thus it was necessary to take into consideration in the curve fitting procedure the distance moved by the microphone during the diffuser revolution when the data were being written on to tape and none were being recorded.

As the quantity k (wavenumber) of equation (7.1) was already known, there remained four unknown quantities, B, α, ψ_1 and ψ_2. Values for these quantities were determined using a curve fitting procedure which is an extension of the basic procedure for two unknowns discussed by La Fara (1973). The principle of the procedure is as follows. The non-linear function (equation (7.1)) is first linearised using a Taylor's series expansion where only the first order terms are

retained. This approximation makes it convenient to use Newton's iteration procedure to find a solution for the unknown constants from initial estimates of each constant. The correction terms (to be added to each constant) evaluated in each iteration are found by minimizing the sum of the squares of the differences between the data and the Taylor's series expansion of the original function. The set of simultaneous linear equations obtained during each iteration step is solved for the correction terms using the Gauss-Jordan elimination method as described by La Fara (1973). The curve fitting procedure is complete when the evaluated correction terms become small enough to ignore. This curve fitting method usually converged to a solution with less than 0.1% error in about four or five iterations.

The success of the curve fitting procedure (which used approximately ¼ sec per data block of CDC 6400 computing time) depended on accurate preliminary estimates for values of the unknown quantities. These preliminary values were estimated from approximate measurements of the average sound pressure minimum value, (p_{min}), the average standing wave ratio SWR and distance (d_N) between the impedance tube mouth and first minimum sound pressure level in the tube. These approximate measurements were made using the paper trace which was recorded on the Bruel and Kjaer level recorder at the same time as the sound pressure in the tube was being sampled by the data acquisition system. The following equations (Beranek, 1949) were then used to obtain the preliminary estimates for ψ_1,ψ_2 , B and α .

$$\tanh \psi_1 = 10^{-SWR/20} \tag{7.2}$$

$$\psi_2 = - 2\pi d_N/\lambda - \pi/2 \tag{7.3}$$

$$B \simeq 10^{SWR/20.5} + p_{min} \tag{7.4}$$

$$\alpha \simeq 0.01, \quad d_N \text{ is negative.} \tag{7.5}$$

From the experimentally determined values of the four unknown constants of equation (7.1) it was possible to calculate the values of maximum and minimum sound pressure in the impedance tube for each angular position of the diffuser and for each test frequency used. This was done using relations derived by differentiating equation (7.1) with respect to x and setting the result equal to zero. The expressions thus obtained are as follows,

$$p_{max} = B[\cosh 2(\alpha D_m + \psi_1) + \cos 2(kD_m + \psi_2)]^{\frac{1}{2}} \tag{7.6}$$

and

$$p_{min} = B[\cosh 2(\alpha d_N + \psi_1) + \cos 2(kd_N + \psi_2)]^{\frac{1}{2}} , \tag{7.7}$$

where

$$d_N = [1/2k]\arcsin\{(\alpha/k)\sinh[2(\alpha d_N + \psi_1)]\} - \psi_2/k - N\lambda/4 \tag{7.8}$$

$$D_m = d_N + (\lambda/4)(-1)^N . \tag{7.9}$$

Equation (7.8) is solved iteratively using the value from the paper trace recording as the first estimate for d_N and values of α, ψ_1, ψ_2 which were found using the curve fitting procedure. The value of N used was either one or zero, depending on whether the initial estimate for d_N was greater than $\lambda/4$ or less than $\lambda/4$. Using these estimated values of d_N and D_m and the previously estimated values of α, ψ_1, ψ_2 and B, together with equations (7.6) and (7.7) values of p_{max} and p_{min} were calculated.

In order to calculate the radiation impedance the value of ψ_2 was recalculated using equation (7.3) from the value of d_N estimated using equation (7.8). This value of ψ_2, the previously estimated values of p_{max} and p_{min} and the following two equations (Beranek,

1949b) were then used to calculate the radiation impedance presented to the mouth of the impedance tube for each angular position of the rotating diffuser.

$$R/A\rho_0 c_0 = (p_{min}/p_{max})(1 + \tan^2\psi_2)/Den \qquad (7.10)$$

$$X/A\rho_0 c_0 = \tan\psi_2 [1 - (p_{min}/p_{max})^2]/Den, \qquad (7.11)$$

where

$$Den = (p_{min}/p_{max})^2 + \tan^2(\psi_2) \ . \qquad (7.12)$$

The reason for recalculating ψ_2 and using the ratio p_{min}/p_{max} instead of $\tanh \psi_1$ for the impedance calculations is that although the values of ψ_1, ψ_2, α and B obtained directly from the curve fitting procedure allow accurate estimation of the quantities p_{min}/p_{max} and d_N they are not necessarily related to the measured physical quantities of equations (7.2) to (7.5). In short, the curve fitting procedure is a convenient way to estimate the ratio p_{min}/p_{max} and d_N for each standing wave considered. These two quantities are then used together with the well known equations (7.3), (7.10), (7.11) and (7.12) to calculate the impedance presented to the tube mouth for each standing wave. The absorbtion α, in the tube was found by measurement to have a negligible effect on the ratio p_{min}/p_{max} over the frequency range considered.

The values of the real and imaginary parts of the impedance thus determined for each considered angular position of the rotating diffuser were averaged over one complete diffuser revolution to obtain mean values and standard deviations from the mean for each rotational speed of the diffuser, at each test frequency.

7.5 REVIEW OF RESULTS

For the purpose of data presentation in the figures to be discussed here, the real and imaginary parts of the measured radiation impedance have been normalized with respect to the characteristic impedance $\rho_0 c_0$, of the medium (air) and the source radiating area, A. Thus values of impedance are presented as dimensionless quantities. Average values of the normalized real and imaginary parts of the radiation impedance which were measured using an impedance tube are shown in Figs. 7.4. The data in the Figures are plotted at 50Hz intervals up to 500Hz and at 100Hz intervals thereafter.

In Figs. 7.4 the real and imaginary parts of the radiation impedance are to be compared with theoretical predictions for a piston source set in an infinite baffle radiating into a free field. The equations due to Morse (1948) which were used for these calculations are as follows.

$$R/A\rho_0 c_0 = 1 - 2J_1(w)/w \tag{7.13}$$

$$X/A\rho_0 c_0 = -(4/\pi)\int_0^{\pi/2} \sin(w\cos\psi)\sin^2\psi d\psi \tag{7.14}$$

$$w = 4\pi a/\lambda \tag{7.15}$$

a = tube radius .

The experimental data shown in Fig. 7.4a were obtained using the large diameter impedance tube with the test arrangement previously discussed and illustrated in Fig. 7.3a. The experimental data shown in Fig. 7.4b were obtained using the small diameter impedance tube with the test arrangement illustrated in Fig. 7.3b. In this case the pressure in the tube was sensed with a condenser microphone whose cross sectional area was about 7% of the cross sectional area of the tube, as previously mentioned.

To ensure that the obstruction offered by the microphone

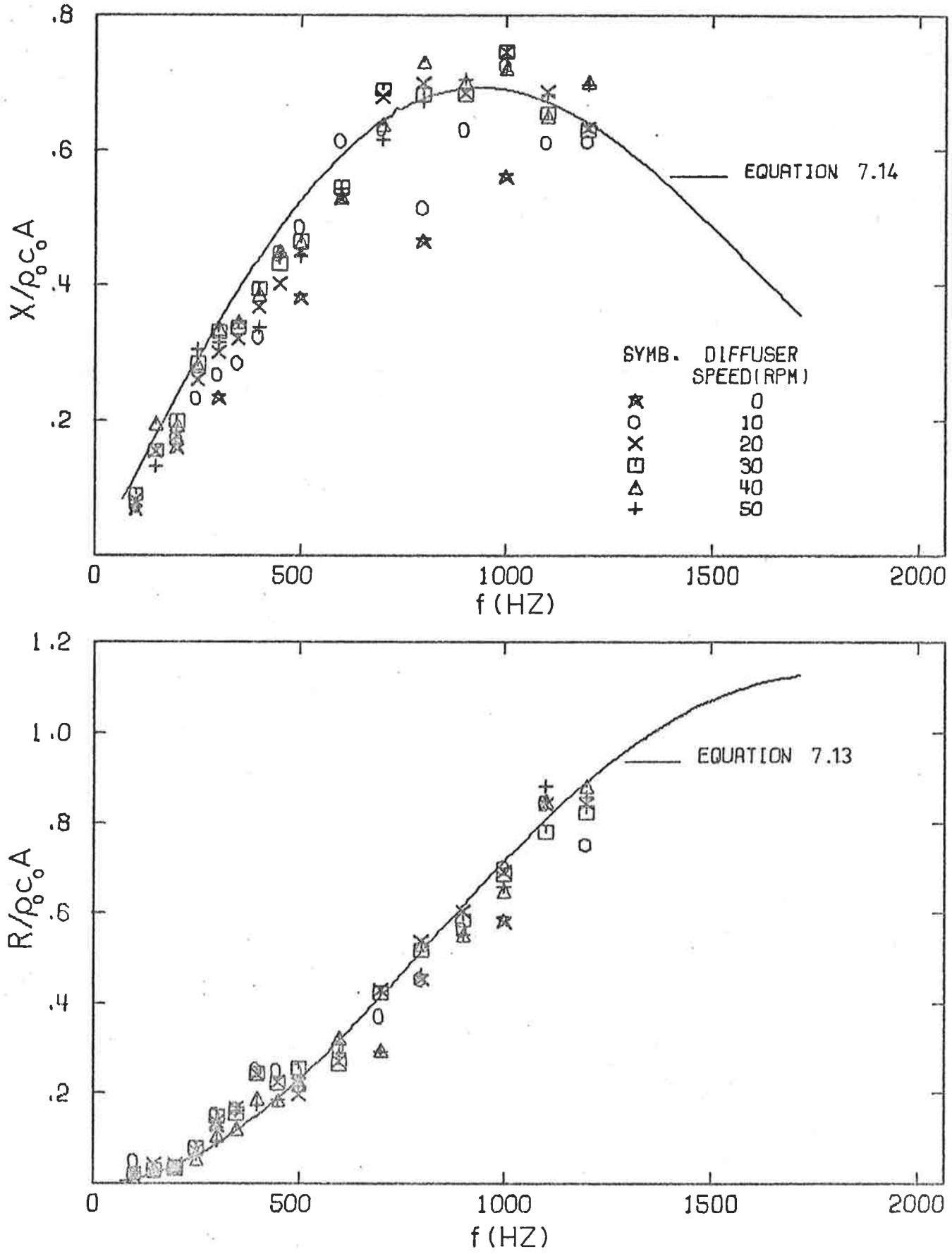

FIG. 7.4a. AV. TUBE MOUTH IMP. IN WALL OF REV. RM. (DATA ACQUIRED USING METHOD A)

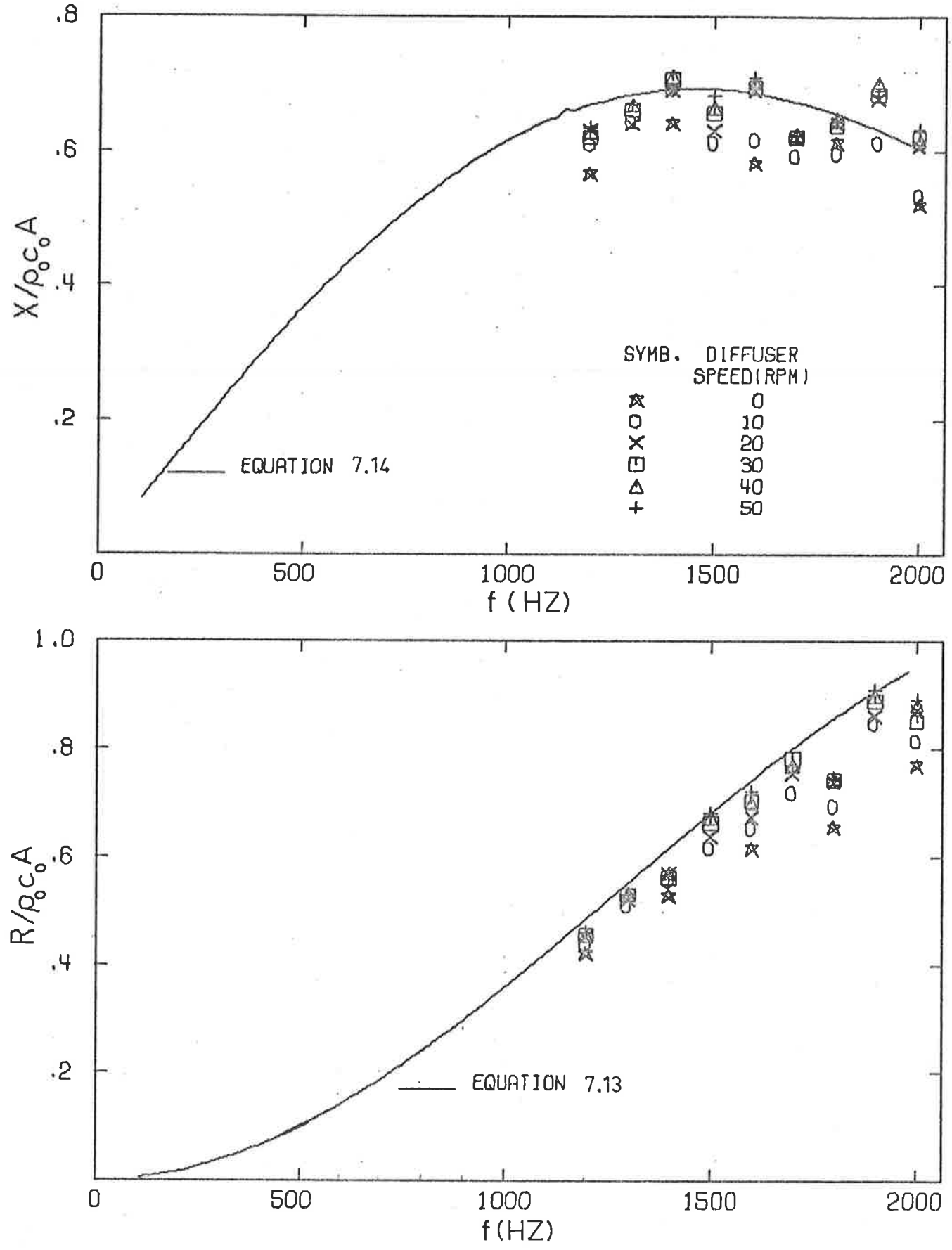

FIG. 7.4b. AV. TUBE MOUTH IMP. IN WALL OF REV. RM. (DATA ACQUIRED USING METHOD B)

probing the field within the tube was unimportant, the small tube measurements were repeated using the test arrangement illustrated in Fig. 7.3c. In this case the probe cross sectional area was less than 1% of the tube cross sectional area and the probe was arranged to extend beyond the measurement plane. The results for the latter measurements are shown in Fig. 7.4c. Comparison of the results for the small tube shown in Figs. 7.4b and c shows that the obstruction offered by the microphone was unimportant and the measurements were quite repeatable.

Inspection of Figs. 7.4a, b and c shows that the measured values all lie close to the predicted free field values. Further inspection shows that the measured values for the stationary diffuser lie furthest from the predicted free field values except in the frequency range below 500Hz for the large impedance tube shown in Fig. 7.4a. In this low frequency range the standing wave ratio in the impedance tube was quite large because of the very small value of radiation impedance. In consequence of the difficulty of accurately defining the acoustic pressure minimum in such a case the data are subject to relatively large error. On the basis of the data shown in the figures above 500Hz one may conclude that increasing the diffuser rotational speed to 20 or 30 RPM has the effect of shifting the time-average impedance toward its predicted free field value, while further increase in rotational speed has negligible effect.

With a diffuser rotational speed of 20 or 30 RPM the measured values of the real and imaginary parts of the radiation impedance at all frequencies above about 500Hz are within 0.5dB of the predicted value. Further inspection shows that the measured mean values of the real and imaginary parts of the radiation impedance of the large tube of 0.156 m diameter shown in Fig.7.4a are generally scattered about the predicted free field values, while in contrast the measured values using the small

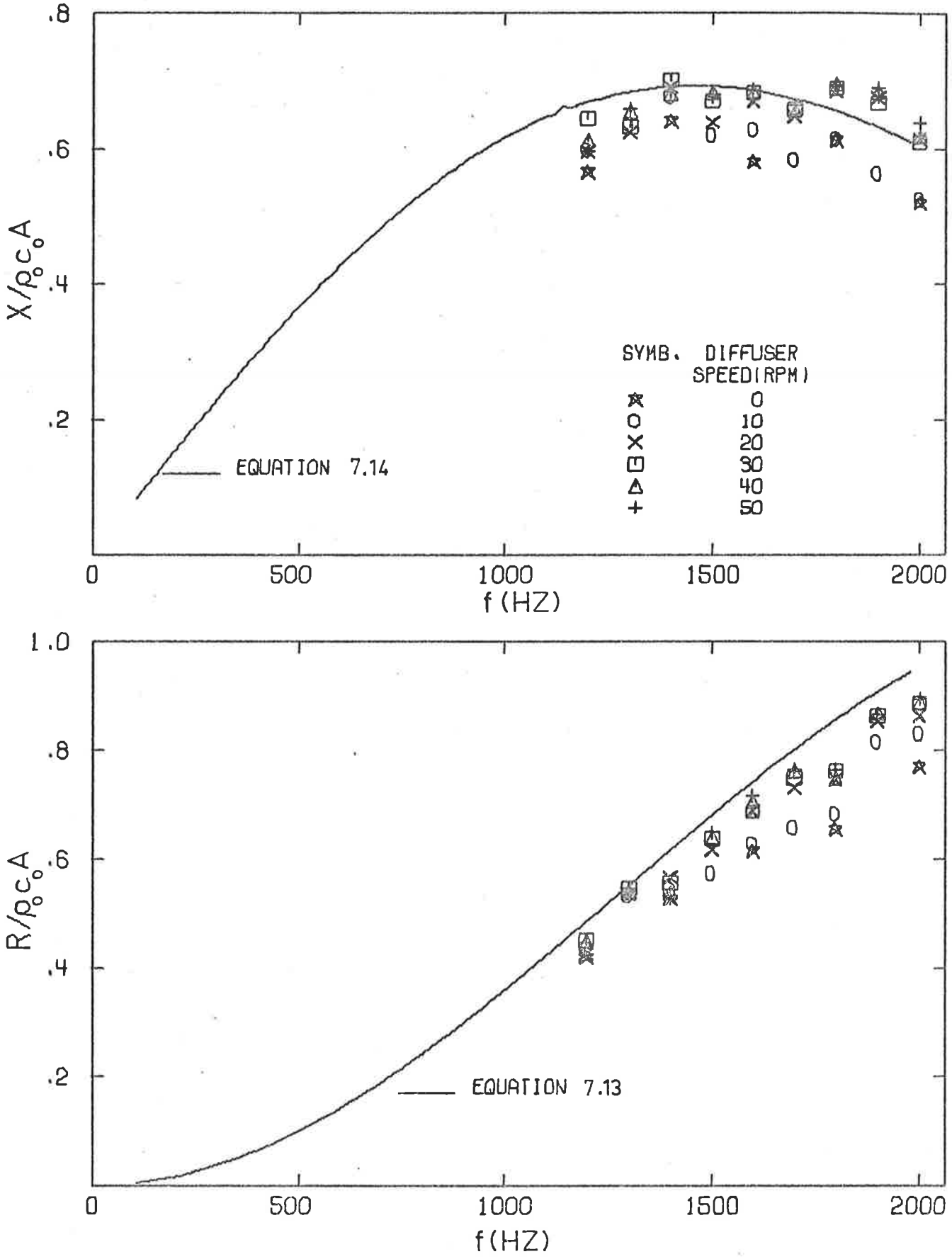

FIG. 7.4c. AV. TUBE MOUTH IMP. IN WALL OF REV. RM. (DATA ACQUIRED USING METHOD C)

impedance tube of 0.101 m diameter show a strong tendency to lie below the predicted free field values. This observation suggests that the effectiveness of the diffuser in producing, on average, a free field radiation impedance at the source, may be dependent upon the source size.

The observation that the effect of the rotating diffuser in producing on average free field conditions at the source may be dependent upon the source size suggested that the effect of the source size should be investigated. This might be done using a very small diameter impedance tube, but then the radiation impedance in the frequency range of interest would be very small. As mentioned earlier this implies that an accurate determination of the standing wave ratio in the tube would be very difficult. In this case reliable data probably could not be obtained. The alternative then was to use a large source. However, a large diameter impedance tube would be limited to too low a frequency range to be of interest. Thus the horn arrangement previously discussed and illustrated in Fig. 7.3d was used to obtain large source radiation impedance data. The measured normalised radiation impedance data for the horn throat are shown in Fig. 7.5a. The corresponding values for the impedance at the horn mouth, calculated from the measurements at the throat, are shown in Fig.7.5b. The horn mouth impedance calculations were carried out using the following equations (Hansen and Bies, 1979c).

$$R/A\rho c = \cos(\beta)[\cosh(\mu)\sinh(\mu)\cos(\beta)]/[\cosh^2(\mu)-\cos^2(k\ell+\gamma+\beta)] \quad (7.16)$$

$$X/A\rho c = \cos(\beta)[\cosh^2(\mu)\sin(\beta) + \sin(k\ell+\gamma)\cos(k\ell+\gamma+\beta)]/ [\cosh^2(\mu) - \cos^2(k\ell+\gamma+\beta)] \quad (7.17)$$

$$\beta \approx \tan^{-1}(1/k\ell) \quad (7.18)$$

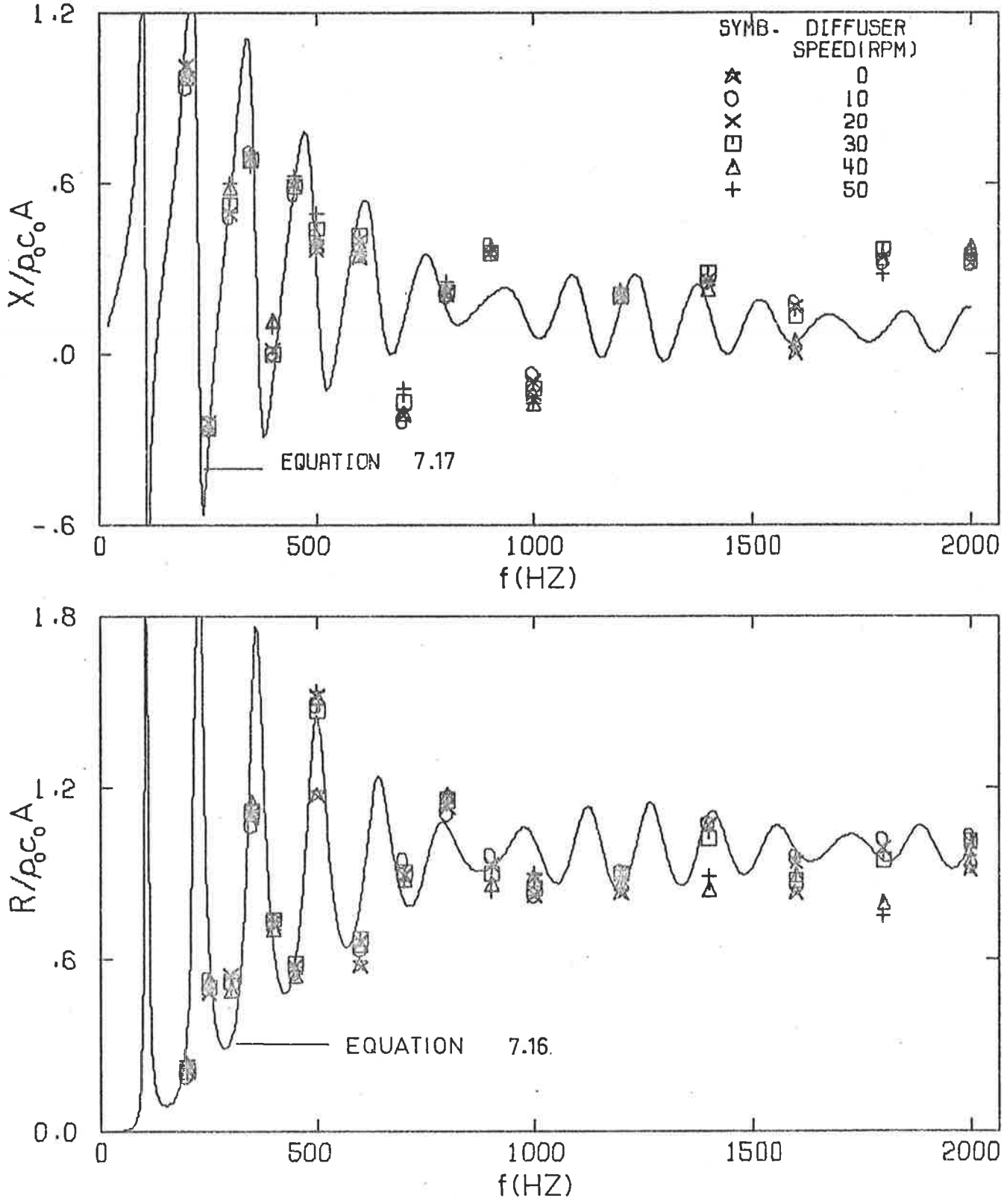

FIG. 7.5a. AV. HORN THROAT IMP. IN WALL OF REV. RM (DATA ACQUIRED USING METHOD D).

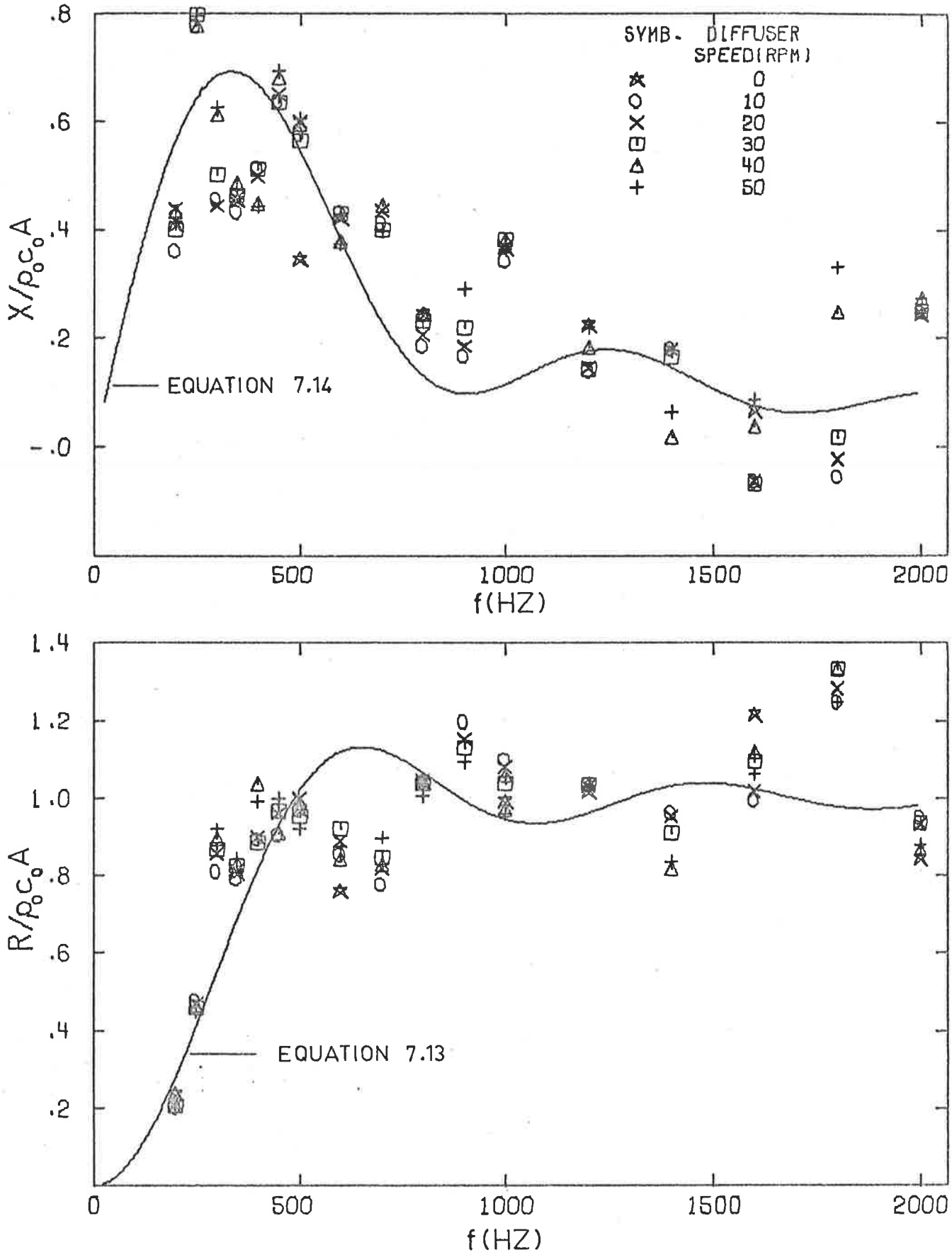

FIG. 7.5b. AVERAGE IMPEDANCE FOR MOUTH OF HORN IN WALL OF REVERBERANT ROOM, DERIVED FROM MEASUREMENTS AT THROAT.

The above equations give exactly the same results as those given by Morse (1948) but they are in a more convenient form for the required computation. Measured values of the real and imaginary parts of the horn throat impedance were inserted and the length ℓ from the horn apex was set equal to the distance from the apex to the plane of the throat. The unknown quantities μ and γ were determined using equations (7.16) and (7.17). These values were then used to calculate the impedance at the mouth by setting the length equal to the distance from the horn apex to the plane of the mouth. It should be noted that in the reported analysis (Hansen and Bies, 1979c) it is shown that the distance ℓ varies over every plane normal to the horn axis but following Morse (1948) it has been assumed that this variable distance may be approximated by the axial distance from the horn apex to the plane considered.

The spread in the experimental data shown in Fig. 7.5a for the horn throat is attributed to insufficient measurement accuracy, especially in the location of the position of the horn throat. In Fig. 7.5b it can be seen that the data are neither consistently above nor below the free field predictions, but they are generally within 1dB of the predicted value over the frequency range considered (200 Hz to 2000 Hz). The spread in the data shown in the Figure is expected from the spread shown by the horn data if it is remembered that both the resistive and reactive parts of the throat measurements are needed to determine each of the resistive and reactive parts of the mouth impedance. Experimental impedance measurements made in an anechoic room show a similar spread and divergence from the predictions of theory, (Hansen and Bies, 1979c). Thus it is difficult to tell whether or not small differences between free field theory and experiment for this particular model are due to measurement uncertainties or lack of free

field simulation by the reverberant room and rotating diffuser.

Comparison of the results shown in Figs. 7.4a, 7.4b and 7.5b suggests that the agreement between measured impedance values and free field predictions may be dependent on the source size. As the source size is reduced, there appears to be a tendency for the measured average impedance to fall below the theoretical predictions for an echo free field. This suggests that at least for frequencies above f_c there may be a lower limit to the size of the sources whose radiation impedance will be significantly affected by the diffuser and for which the reverberant room will present essentially free field impedance conditions. In fact it has been shown by Smith and Bailey (1973) that for a pure tone source in a reverberant room containing no rotating diffuser the number of source positions required to obtain an average radiation impedance close to free field at a given frequency becomes greater as the source size is reduced. As it is assumed that the function of the rotating diffuser is essentially to average the radiation impedance over several source positions, then the trends in the results presented here are consistent with the work of Smith and Bailey. The effect of source size is investigated more extensively in Chapter 8.

The effect of the diffuser on the impedance presented to the source is indicated by the data shown in Figs. 7.6a and b. These Figures show the standard deviations in the impedance measurements associated with one complete rotation of the diffuser. Reference to Table 7.2 shows that they are the result of a large number of measurements at each frequency and angular rotation speed, ranging from a minimum of twenty static measurements to three hundred measurements at an angular speed of 10 RPM. As the two sets of small impedance tube measurements (methods B and C) were effectively indistinguishable, only one set has been included in Fig. 7.6a.

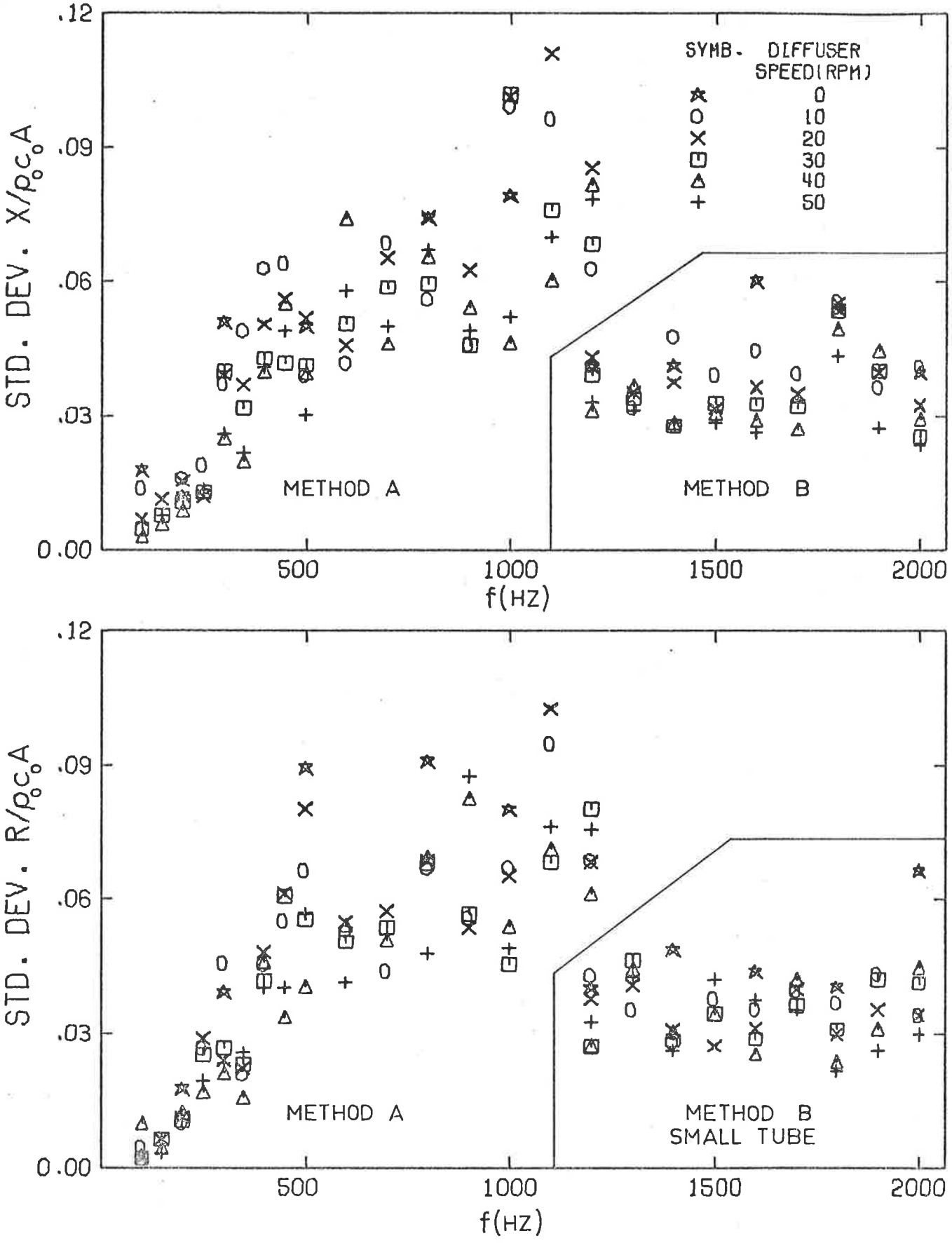

FIG. 7.6a. STANDARD DEVIATIONS FOR THE VARIATIONS IN SOURCE RADIATION IMPEDANCE CAUSED BY ROTATION OF THE DIFFUSER.
(DATA ACQUIRED USING METHODS A&B).

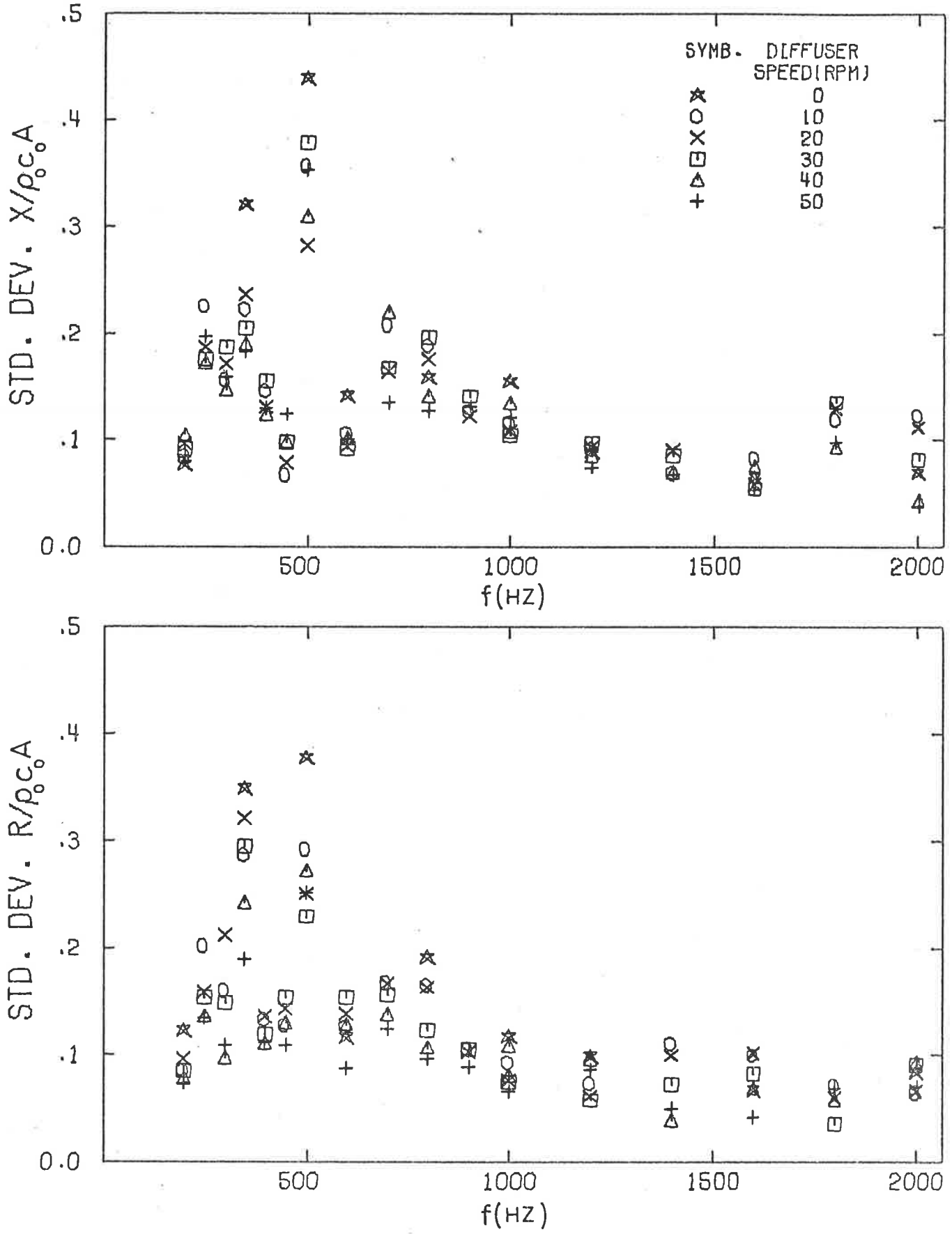

FIG. 7.6b. STANDARD DEVIATIONS FOR THE VARIATIONS IN HORN THROAT IMPEDANCE CAUSED BY ROTATION OF THE DIFFUSER.
(DATA ACQUIRED USING METHOD D).

The data of Figs. 7.6a and b may be divided approximately into two frequency ranges. Above about 500Hz the measured standard deviations seem to range about mean values independent of frequency. At 500Hz and lower frequencies, the measured standard deviations exhibit apparent frequency dependence. It is of interest to note that the mean values of standard deviation in the rotational speed range of 20 to 30 RPM are respectively 0.035 for the small tube, 0.062 for the large tube and 0.105 for the horn, while the diameters of these three sources are respectively 0.101 m, 0.156 m and 0.430 m. A linear dependence of standard deviation on source linear dimension is suggested by the data in the high frequency range above 500Hz.

In the frequency range of 500Hz and lower frequencies the large impedance tube data of Fig. 7.6a clearly show that the standard deviation diminishes with frequency. This is to be expected as the magnitude of the measured values of radiation impedance also diminishes, as indicated by Figs. 7.4a, b and c. The behaviour of the horn throat data of Fig. 7.6b in the low frequency range is attributable to the very large standing wave structure in the horn, as indicated by the data of Fig. 7.5a. Similarly the relatively small standing wave structure in the horn at frequencies above 500Hz may be offered as justification for the tacit assumption above, that we may directly associate the measured standard deviation of the throat impedance measurements with the standard deviation of the mouth impedance estimates based on the throat data.

It was noted earlier that a diffuser rotational speed of between 20 and 30 RPM seemed to be optimal in providing a source radiation impedance close to a predicted free field value. Further increase of rotational speed seemed to have only a marginal effect as shown, for example, by the data of Figs. 7.4b and c. It is of interest to discover whether

the rotational speed has any discernable effect upon the measured standard deviation. Initial inspection of the data of Figs. 7.6a and b suggests no dependence of the standard deviation on rotational speed. However, closer inspection shows that in the high frequency range the static measurements are predominantly associated with the large values of standard deviation whereas the 50 RPM measurements are predominantly associated with the small values of standard deviation.

The average impedance values discussed above are based upon from 20 to 300 measurements depending upon the diffuser rotational speed as shown in Table 7.2. It is of interest to plot the measured values of impedance upon which these averages are based as a function of diffuser angular position. Some representative values of the normalized real and imaginary parts of the radiation impedance are shown in Figs. 7.7. When interpreting these Figures it should be kept in mind that the number of data points used to construct these curves vary from 20 at 0 RPM to 300 at 10 RPM and 60 at 50 RPM so that the general smoothing of the curves from 10 RPM to 50 RPM may be an artifact of the smaller data sample.

No consistent trends are shown by the curves of Figs. 7.7. However some of the families of curves do show a general resemblance and a gradual transition from one form to another with rotational speed. They are all consistent with the computed mean and standard deviation values given earlier.

7.6 ERROR ANALYSIS

7.6.1 Discussion of the fundamental assumptions

Measurements of the sound field in the impedance tube are made on the assumption that the variations in the sound pressure distribution in the tube are synchronous with the angular position of

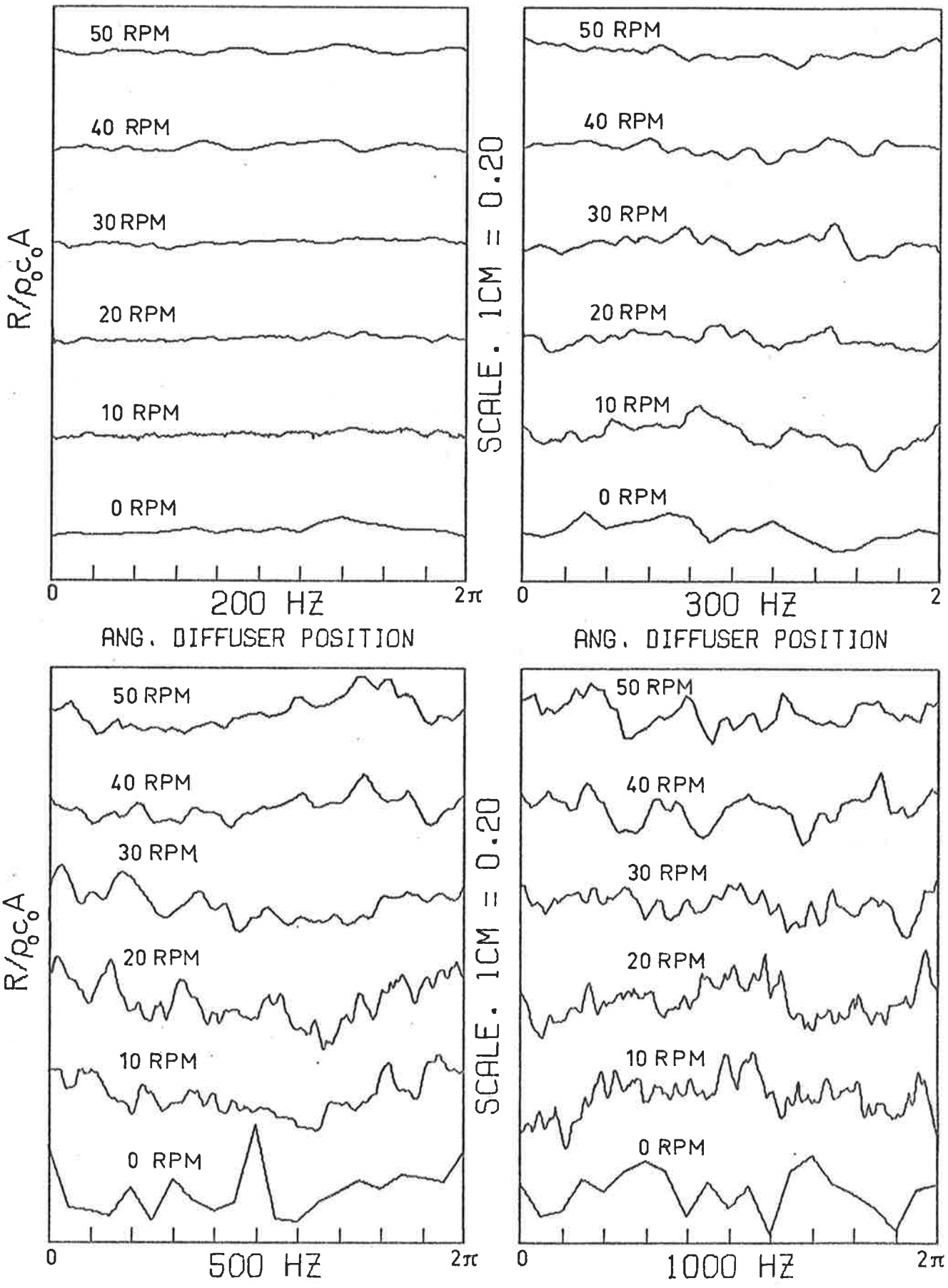

FIG. 7.7a. VARIATION OF TUBE MOUTH RESISTIVE IMP. WITH ANGULAR POSITION OF ROTATING DIFFUSER IN REVERBERANT ROOM. (DATA ACQUIRED USING METHOD A).

See table 7.2 for complementary information.

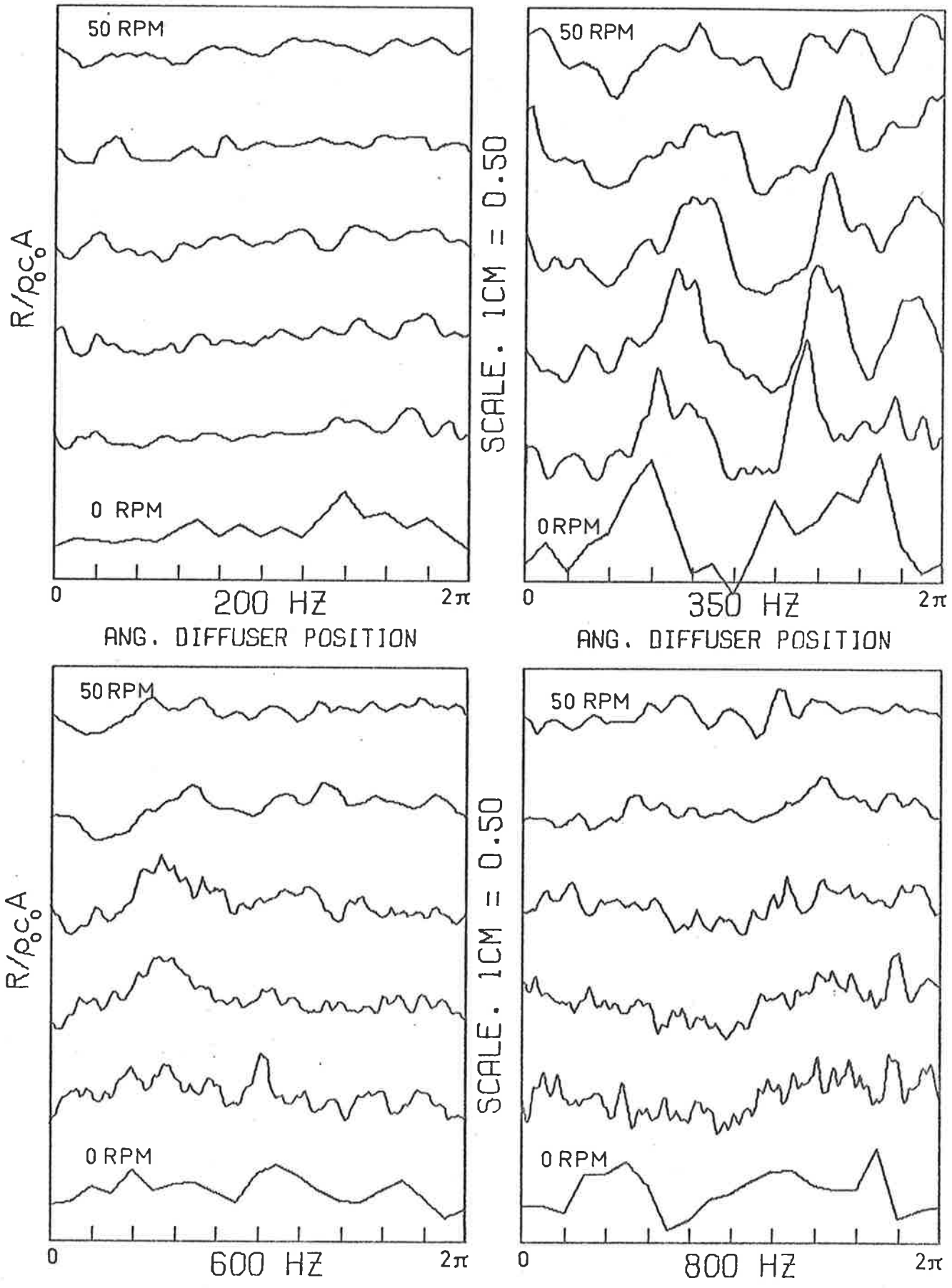

FIG. 7.7b. VARIATION OF HORN THROAT RESISTIVE IMP WITH ANGULAR POSITION OF ROTATING DIFFUSER IN REVERBERANT ROOM. (DATA ACQUIRED USING METHOD D).

the rotating diffuser. This assumption is valid if two further assumptions are satisfied. The first is that the impedance changes presented to the tube mouth are slow enough and the time constant for the tube is small enough such that the standing wave field present at any given time in the tube can be related to the instantaneous impedance at the tube mouth using equations (7.1) to (7.12).

During the measurement procedure, the length of standing wave sampled was approximately $c_0/2f$, where f is the source frequency and c_0 the speed of sound in free space. This corresponded to one complete cycle of the standing wave in the tube which repeated itself at intervals of $\lambda/2$. According to Morse and Ingard (1968) the time it takes for the standing wave at a point x from the tube mouth to be affected by the impedance at the tube mouth is given by x/c_0. The maximum value of x used in the measurements was approximately $\lambda/2$, resulting in a maximum time lag of $\lambda/2c_0$ seconds. Thus in order for the impedance measurements to be valid, the impedance presented to the tube mouth should not change significantly in $\lambda/2c_0$ seconds. The worst case is for a diffuser speed of 50 RPM. In $\lambda/2c_0$ seconds, the diffuser circumference moves a distance of approximately 0.016λ which is shown later to be insignificant. When the conical horn is attached to the tube mouth the time lag is increased by L/c_0 where L is the horn length, equal to 1.127 m. At 2000 Hz and a diffuser speed of 50 RPM (worst case), this additional time lag corresponds to a diffuser circumferential movement of approximately 0.17λ. This movement is later shown to be significant and may account for a large scatter in the results for the conical horn measurements for the higher frequencies. However, it should be remembered that the 0.17λ above is a worst case situation and in most cases the movement is much less than this. For

example at a frequency of 1000 Hz and a diffuser speed of 20 RPM the movement would be 0.04λ which is considered to be insignificant.

The second assumption is that the instantaneous impedance presented to the tube mouth by the room is a function of the angular position of the rotating diffuser. This does not imply that the sound field in the room needs to be quasi stationary. It merely implies that the sound field in the room reaches dynamic equilibrium, an assumption which is not unreasonable.

A further assumption is that sideband energy generated by the doppler shift in sound waves reflected off the rotating diffuser and fed back up the impedance tube (Waterhouse, 1978) is negligible. As the diffuser is cylindrical in shape it is unlikely that any significant sidebands will be produced by a doppler shift in waves reflected from the diffuser surfaces. This is because all surface movement is in the plane of the moving surface rather than normal to it. However as the diffuser amplitude modulates the impedance presented to the tube mouth, it must amplitude modulate the sound field in the tube.

If the amplitude modulation produced by the diffuser is sinusoidal then the convolution integral shows that a frequency analysis of the amplitude modulated signal will consist of the original signal frequency and two side bands, one above and one below the signal frequency, and separated from the signal frequency by the reciprocal of the diffuser period. The amplitude modulation produced by the diffuser is <u>not</u> sinusoidal, but it can be Fourier analysed into a sum of a number of sinusoidal components, with frequencies equal to multiples of the reciprocal of the period of diffuser revolution. Thus the amplitude modulation produced by the diffuser results in a number of frequency sidebands spaced equally above and below the signal frequency at intervals equal to the reciprocal of the diffuser period of revolution.

The presence of acoustic energy in these sidebands is a source of error for two reasons. Firstly as $^1/_3$ octave filters were used, not all of the energy in the total signal was measured. Secondly a pure tone theoretical curve was fitted to the experimental data.

It can be demonstrated that these errors are negligible. For each frequency considered the signals from stationary microphones located at the approximate standing wave minima and maxima were recorded in analogue form on a magnetic tape as the diffuser rotated. On playback, the tape speed was increased by a factor of four and the resulting signal was frequency analysed using an FFT analyser with 0.2 Hz filters.

In effect this was equivalent to analysing the original signal with 0.05 Hz filters. However the required analysis time was considerably reduced by speeding up the tape and using a correspondingly larger analysis bandwidth. The energy level in the frequency band containing the signal frequency was typically 20 to 25dB higher than that in any other band for measurements at a standing wave maximum. For measurements at a standing wave minimum the energy in the signal frequency band was typically 15 dB higher. At very low frequencies (100 to 200 Hz) the level differences between the signal frequency band and the sidebands were a little smaller. An example of a frequency analysis plot for the signal in the small impedance tube is shown in Fig. 7.8a. The test frequency is 800Hz and the diffuser rotational speed was 30 RPM. In Fig. 7.8b a frequency analysis plot is presented for the signal in the small impedance tube with the conical horn attached. The test frequency in this case is 300Hz and the diffuser rotational speed is 30 RPM.

The frequencies marked in the figures are those corresponding to the original recorded signal. The upper trace in each figure is an analysis of the signal at or near the pressure minimum in the impedance tube while the lower trace represents the signal at or near the pressure maximum. As the diffuser rotational speed was 30 RPM, the sidebands due

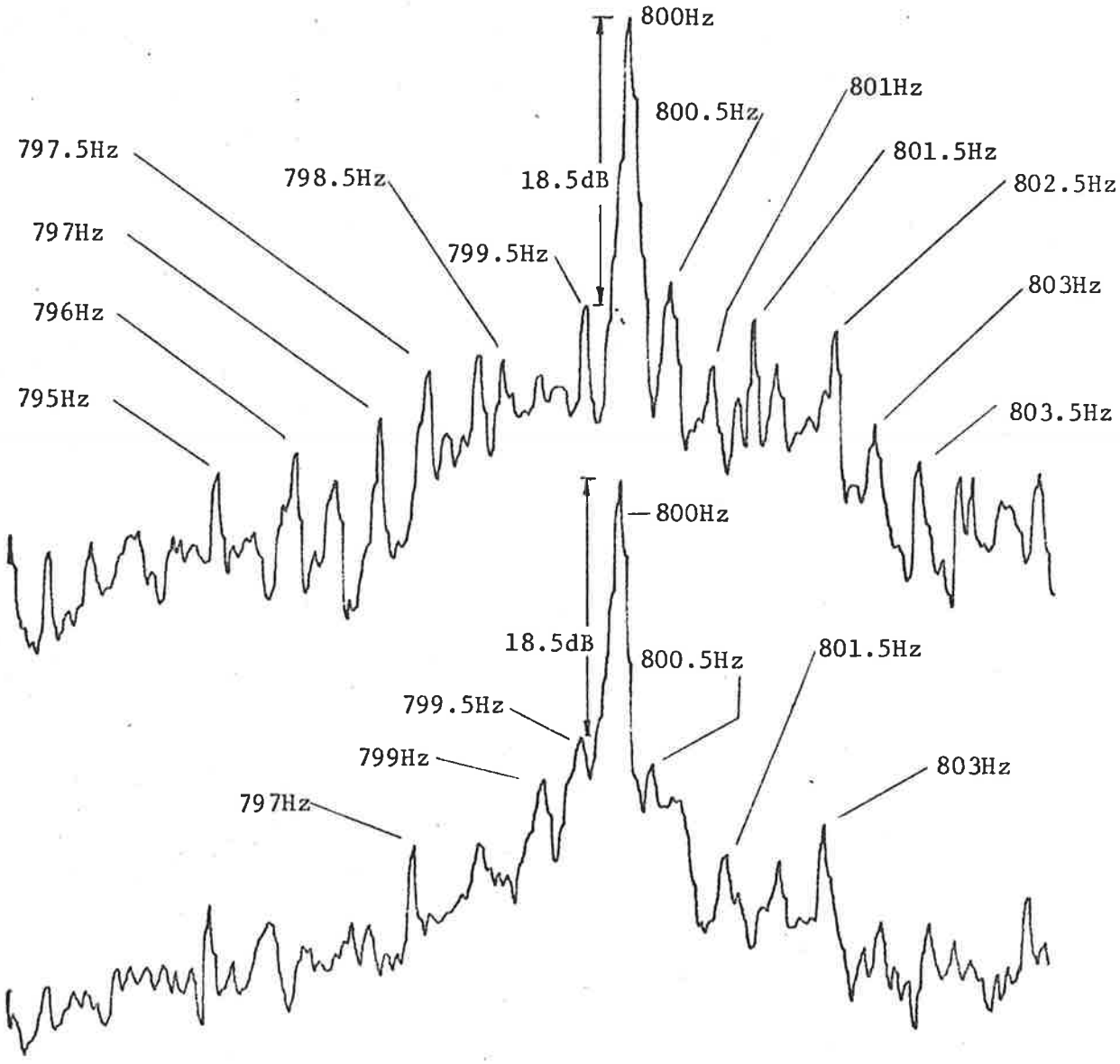

FIG. 7.8(a) FREQUENCY ANALYSIS OF THE ACOUSTIC PRESSURE SIGNAL IN THE SMALL IMPEDANCE TUBE.
The upper curve represents a measurement close to a pressure minimum in the tube while the lower curve represents a measurement close to a pressure maximum.
Signal frequency = 800 Hz.
Diffuser rotational speed = 30 RPM.

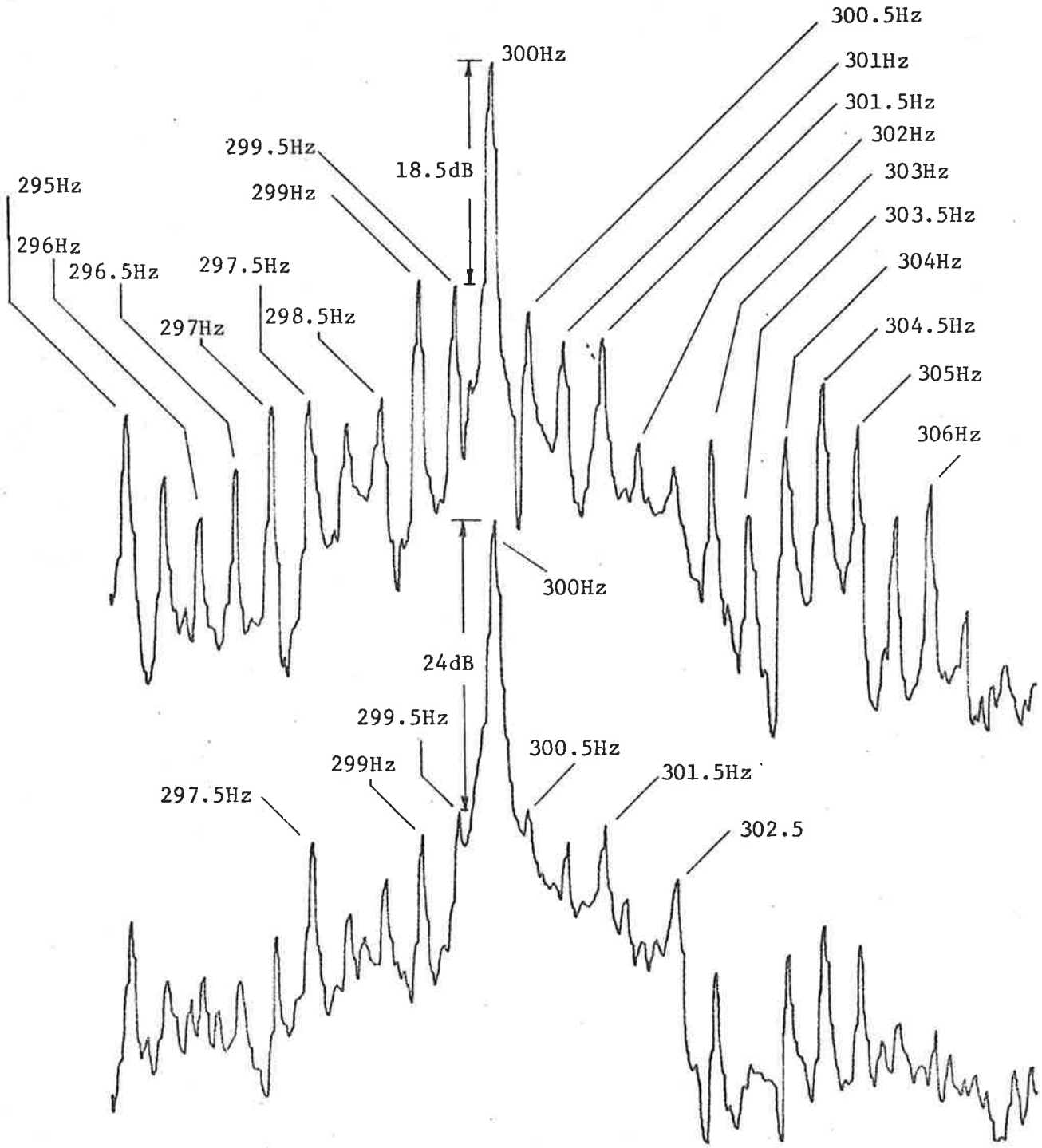

FIG. 7.8 (b) FREQUENCY ANALYSIS OF THE ACOUSTIC PRESSURE SIGNAL IN THE SMALL IMPEDANCE TUBE WITH THE CONICAL HORN ATTACHED.
The upper curve represents a measurement close to a pressure minimum in the tube while the lower curve represents a measurement close to a pressure maximum.
Signal frequency = 300 Hz.
Diffuser rotational speed = 30 RPM.

to amplitude modulation are separated by ½ Hz. These are clearly visible. It can also be seen that the level of energy in the sidebands is well below the level at the signal frequency and in addition all of the significant energy is contained in the sidebands a few Hz either side of the signal frequency. Thus a $^1/_3$ octave filter did not exclude any significant sound energy. As a test for the validity of using the $^1/_3$ octave filters, many of the experiments were later repeated using Butterworth high and low pass filters and allowing a bandwidth of at least 200 Hz either side of the signal frequency. The difference in results obtained using the two methods was in the bounds of experimental error in all cases tested. It is realised that large errors would be expected at frequencies furthest from the centre frequencies of the $^1/_3$ octave filters. However, even at these frequencies the difference in results obtained using the two methods was not measurable.

As the sideband energy was found to be relatively small it is considered that the distortion in the standing waves in the tube due to the presence of sidebands will be small and not measurable. The validity of the assumptions discussed above is demonstrated by the excellent fit of the theoretical pure tone standing wave equation (7.1) to the experimental standing wave data as illustrated in Figs. 7.9, 7.10 and 7.11 where the pressure amplitude as a function of distance along the impedance tube is plotted for three different angular positions of the rotating diffuser and for two different sources. Both the abscissa and ordinate scales are linear. The symbols represent the experimentally measured data and the solid lines are the theoretical curves fitted to the data. In Fig. 7.9a the source is the small impedance tube, the frequency is 1200 Hz and the diffuser speed is 20 RPM.

The small amount of scatter in the data is attributable to variations in the diffuser rotational speed during the experiment which were of the order of $\pm$0.2%, or $\pm$2.2cm of diffuser circumferential movement

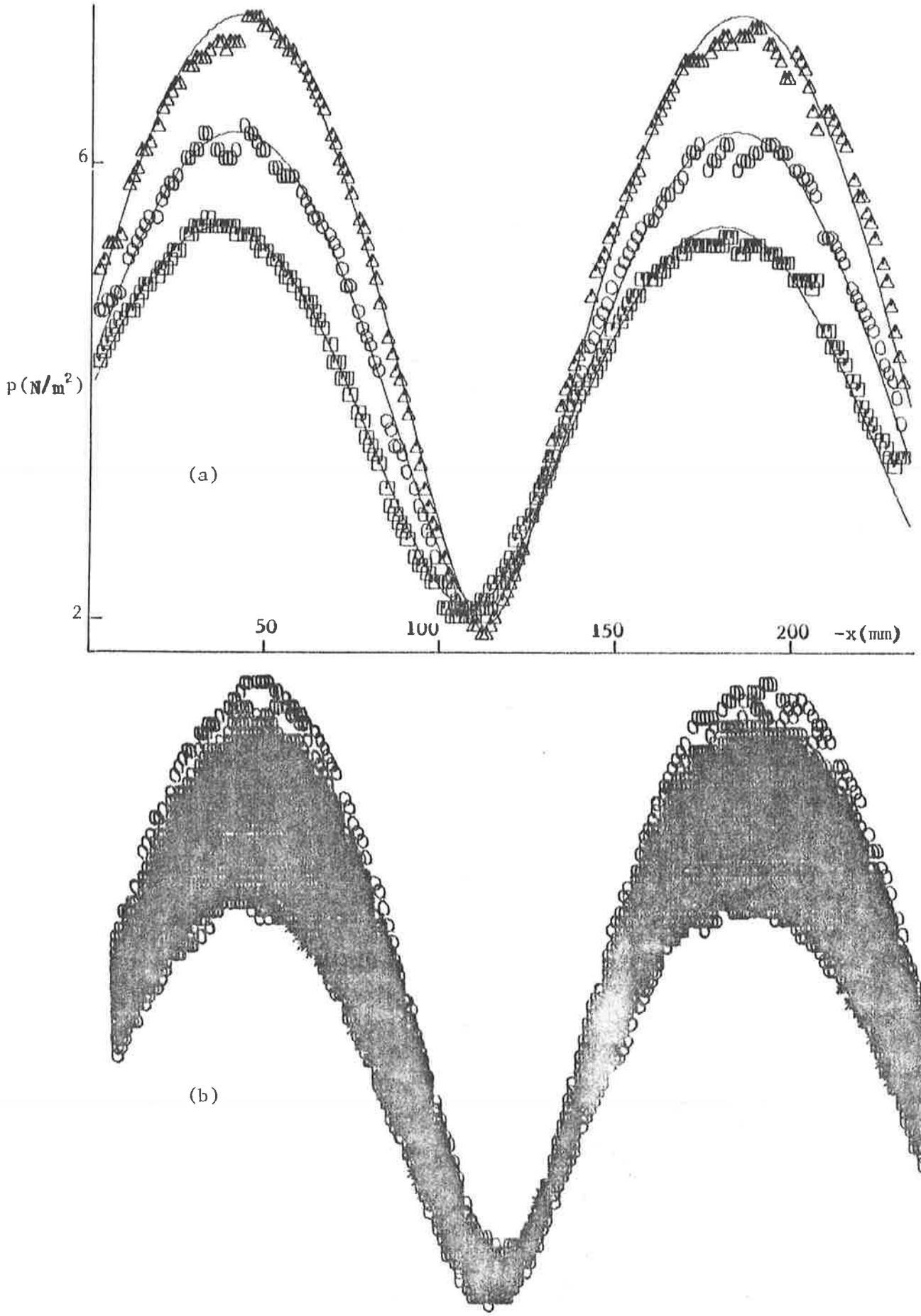

FIG.7.9 (a) STANDING WAVE DATA AND FITTED THEORETICAL CURVES CORRESPONDING TO THREE DIFFERENT DIFFUSER ANGULAR POSITIONS.
(b) COMPLETE DATA SET FOR ALL ANGULAR POSITIONS.
Small impedance tube sound source - 1200 Hz, diffuser speed - 20 RPM

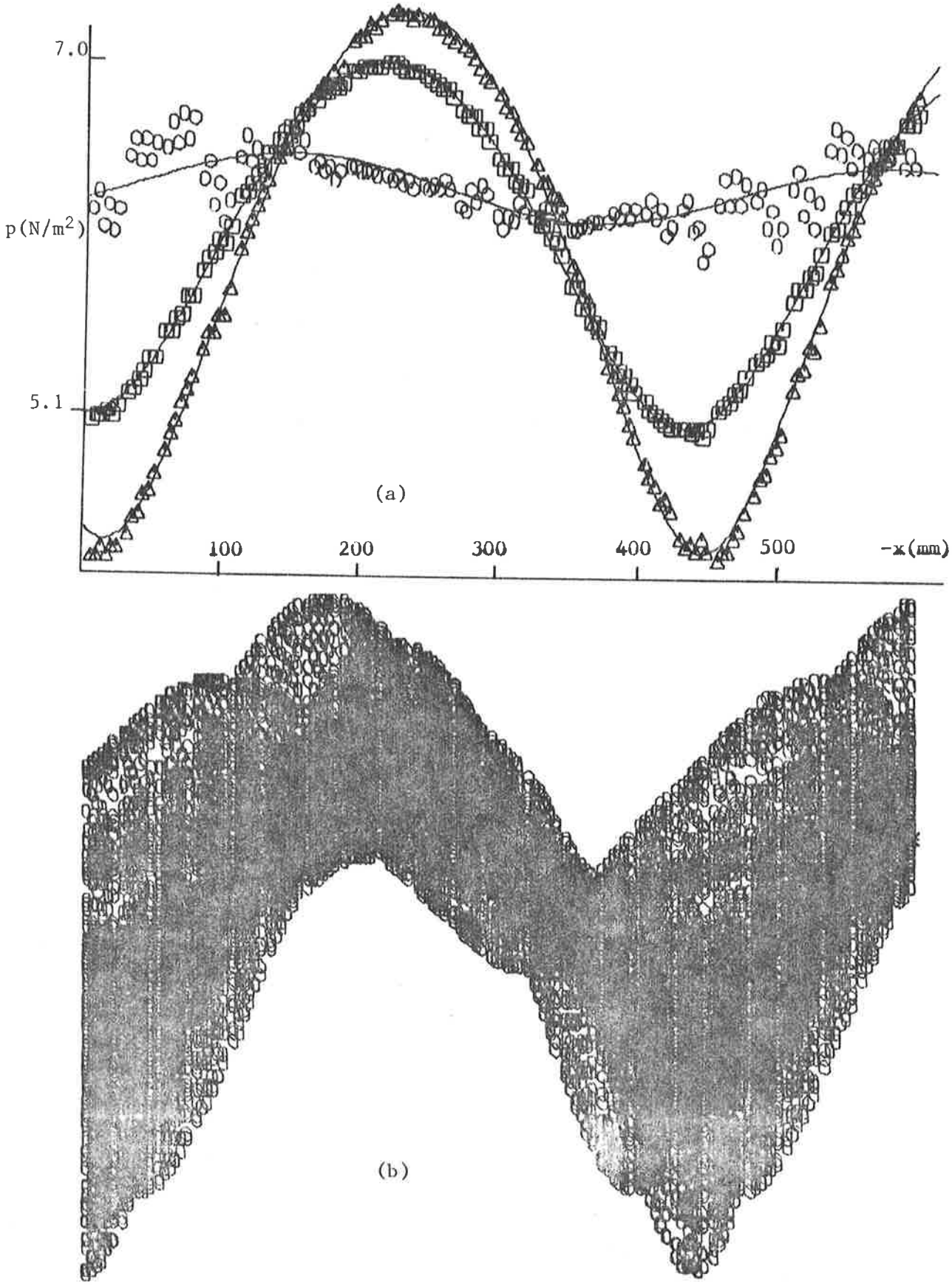

FIG.7.10 (a) STANDING WAVE DATA AND FITTED THEORETICAL CURVES CORRESPONDING TO THREE DIFFERENT DIFFUSER DYNAMIC ANGULAR POSITIONS.
(b) COMPLETE DATA SET FOR ALL ANGULAR POSITIONS.
Conical horn attached to small impedance tube source - 400 Hz diffuser speed - 20 RPM.

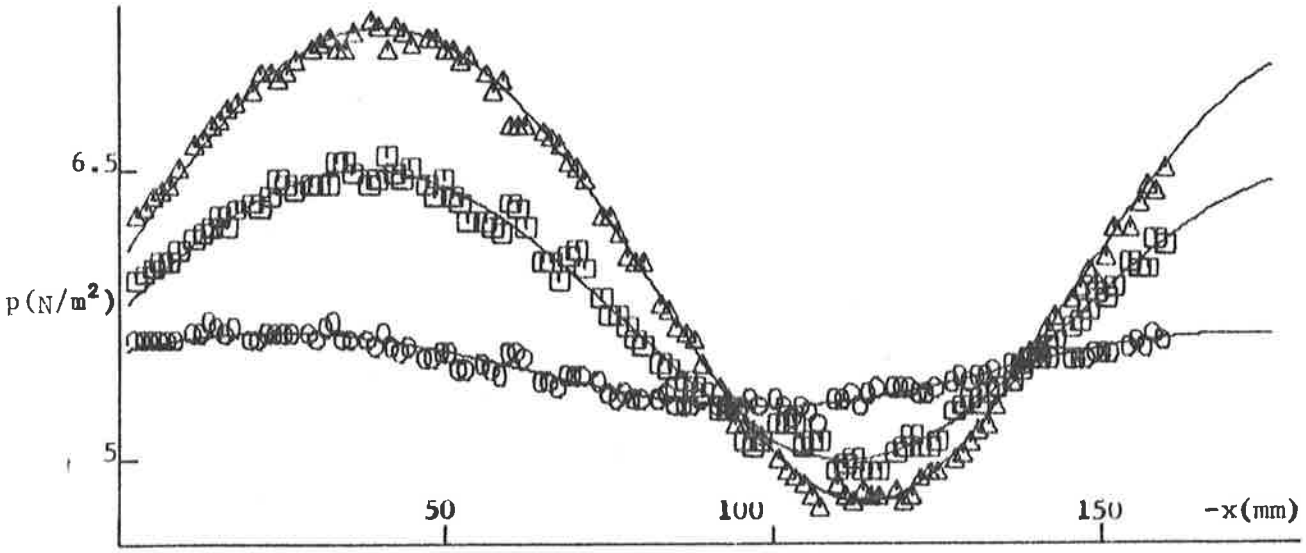

(a)

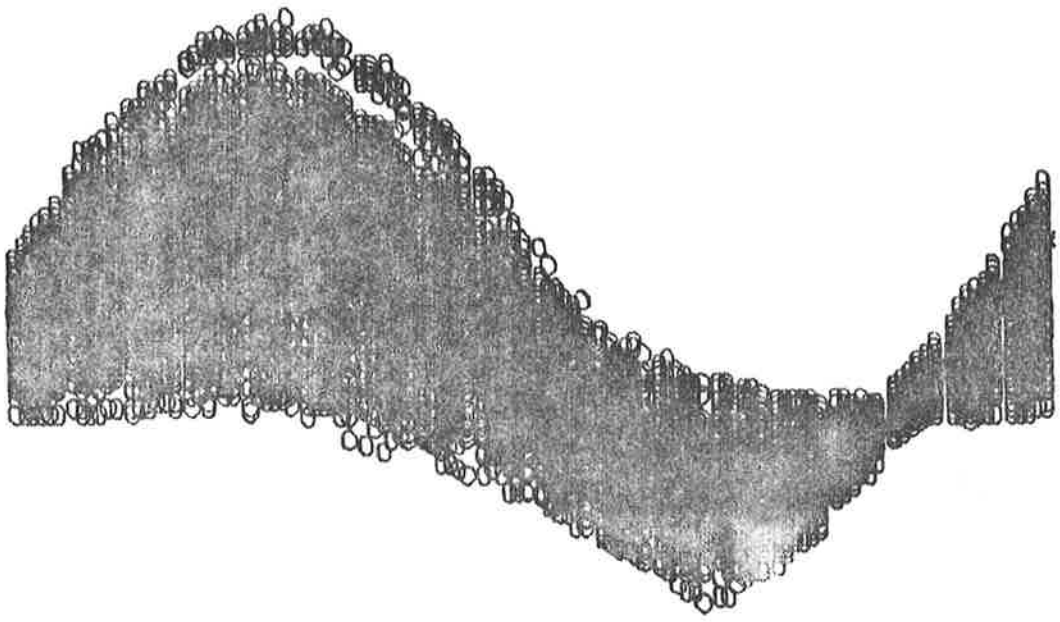

(b)

FIG.7.11 (a) STANDING WAVE DATA AND FITTED THEORETICAL CURVES CORRESPONDING TO THREE DIFFERENT DIFFUSER DYNAMIC ANGULAR POSITIONS.
(b) COMPLETE DATA SET FOR ALL ANGULAR POSITIONS.
Conical horn attached to small impedance tube source - 1200 Hz
diffuser speed - 20 RPM.

which is ± 0.08 of a wavelength at 1200 Hz. The conclusion that the scatter in the data was due to small variations in diffuser rotational speed was supported by the observation of a much greater scatter when an artificial speed change of 1% was introduced into the data sorting program. The scatter in the data due to diffuser speed variations also indicates that a very small circumferential movement (of the order of ± 0.1 wavelength) of the diffuser can produce a significant and measurable change in the radiation impedance presented to the sound source.

In Fig. 7.9b the standing wave data collected over one complete revolution of the diffuser are shown. The data for the three different angular diffuser positions shown in Fig. 7.9a were derived from these data as described in section 7.4. A similar set of data as that shown in Fig. 7.9b was obtained at each test frequency for each diffuser rotational speed considered. Each data set typically consists of between 10,000 and 20,000 discrete values, all of which are used in the impedance calculations described in section 7.4.

Each data value p corresponds to a particular known distance x along the impedance tube and a particular known dynamic angular position θ of the rotating diffuser. From a knowledge of x and θ for each data value, it is possible to sort the data into sets of p vs x where each set corresponds to a particular value of angular diffuser position θ. The data sets, p vs x represent standing waves which are evaluated as described in section 7.4 to give radiation impedance as a function of diffuser angular position.

In Figs. 7.10 and 7.11 similar results are presented for measurements in the tube when the conical horn was attached to the tube mouth. In both cases the diffuser speed is 20 RPM and in Fig. 7.10 the test frequency is 400 Hz while in Fig. 7.11 it is 1200 Hz.

7.6.2 Measurement errors

The first source of measurement error considered is the use of an "instantaneous" measurement of the peak value of the time varying sinusoidal signal in the impedance tube as a means for calucating the "instantaneous" r.m.s. value of the signal. As the signal level was continuously changing, an error is present in the calculated r.m.s. value. (It is shown in Appendix 3 that at all times this error is less than 0.09dB, and can be regarded as negligible). Note that as the frequency sidebands generated in the tube are due to amplitude modulation of the signal frequency, the above error estimate also takes into account errors in the estimate of the r.m.s. signal level due to energy existing in sidebands, which is not fully accounted for in the peak measurement.

A second source of error is in the measurement of the standing wave ratio in the tube and the estimation of the distance of the first pressure minimum from the tube mouth.

It is well known that for an open tube the radiation impedance becomes smaller as the frequency decreases (see Fig. 7.4). This implies that the standing wave ratio in the tube becomes larger which results in greater inaccuracies in the detection of the correct level and position of the standing wave minimum. For this reason measurements were not carried out in the small tube at low frequencies (except when it was terminated with a conical horn). Also for this reason the results measured at low frequencies (between 100 Hz and 200 Hz) for the large tube are not very accurate. The accuracy in measurement of the position of the standing wave minimum was approximately $\pm$1mm when a horn was not used and $\pm$2mm when a horn was used. Additionally, the accuracy in the determination of the standing wave ratio may be taken as about $\pm$0.3dB as the data acquisition system had 8 bits and most standing wave ratios were smaller than 10dB. Using a Smith chart the accuracy to be expected as a function of frequency was calculated and is listed for various frequencies and standing wave ratios in Table 7.3.

TABLE 7.3 (a) EXPECTED IMPEDANCE MEASUREMENT ERRORS DUE TO UNCERTAINTIES IN THE MEASUREMENT OF d_N AND THE STANDING WAVE RATIO, (SMALL TUBE SOUND SOURCE, DIFFUSER SPEED 30 RPM).

f(Hz)	Calculated Value		Measurement Uncertainty		Calculated Error	
	$\bar{R}/A\rho_o c_o$	$\bar{X}/A\rho_o c_o$	Δd_N(mm)	ΔSWR(dB)	$\Delta R/A\rho_o c_o$	$\Delta X/A\rho_o c_o$
1200	0.371	0.392	0	0.3	.012	.004
			1	0	.006	.023
1500	0.536	0.417	0	0.3	.015	.008
			1	0	.013	.025
2000	0.704	0.427	0	0.3	.018	.016
			1	0	.022	.026

TABLE 7.3 (b) EXPECTED IMPEDANCE MEASUREMENT ERRORS DUE TO UNCERTAINTIES IN THE MEASUREMENT OF d_N AND THE STANDING WAVE RATIO. (LARGE TUBE SOUND SOURCE, DIFFUSER SPEED 30 RPM).

f(Hz)	Calculated Value		Measurement Uncertainty		Calculated Error	
	$\overline{R}/A\rho_o c_o$	$\overline{X}/A\rho_o c_o$	Δd_N(mm)	ΔSWR(dB)	$\Delta R/A\rho_o c_o$	$\Delta X/A\rho_o c_o$
250	.068	.232	0	0.3	.002	-
			1	0	-	.005
500	.260	.408	0	0.3	.009	.001
			1	0	.002	.010
800	.467	.565	0	0.3	.015	.007
			1	0	.009	.017
1200	.675	.467	0	0.3	.018	.014
			1	0	.015	.018

TABLE 7.3 (c) EXPECTED IMPEDANCE MEASUREMENT ERRORS DUE TO UNCERTAINTIES IN THE MEASUREMENT OF d_N AND THE STANDING WAVE RATIO, (CONICAL HORN SOUND SOURCE - THROAT ATTACHED TO SMALL IMPEDANCE TUBE, DIFFUSER SPEED 30 RPM)

f(Hz)	Calculated Value		Measurement Uncertainty		Calculated Error	
	$\overline{R}/A\rho_o c_o$	$\overline{X}/A\rho_o c_o$	Δd_N(mm)	ΔSWR(dB)	$\Delta R/A\rho_o c_o$	$\Delta X/A\rho_o c_o$
250	0.548	-0.311	0	0.3	.017	.007
			2	0	.003	.008
500	1.32	0.478	0	0.3	.012	.043
			2	0	.030	.009
1000	0.905	-0.161	0	0.3	.019	.025
			2	0	.012	.007
2000	0.869	0.272	0	0.3	.017	.024
			2	0	.034	.026

7.7 SUMMARY

The radiation impedances of three simple pure tone sources placed in the side wall of a reverberant room containing a rotating diffuser have been measured as a function of frequency and diffuser rotational speed using an ordinary impedance tube, a high speed data acquisition system and a CDC6400 computer. The impedance was shown to vary cyclically with rotation of the diffuser in an unpredictable way. For frequencies above the Schroeder large room limit, diffuser speeds 20 RPM and above and a source size of 0.156m or greater the impedance values were observed to fluctuate by a small amount about the free field predictions. On the other hand, for a source of 0.101 in diameter values of radiation impedance of the order of 0.5 dB less than predicted for free field were consistently observed, suggesting that for small sources the average radiation impedance may be dependent on source size. For diffuser speeds of 10 RPM and less the deviations of measured values of impedance from free field predictions were found to be considerably greater than those measured for diffuser speeds greater than 20 RPM for all sources considered.

Scatter in the standing wave data was shown to be attributed to small variations of ±0.2% in the diffuser rotational speed. Due to the high sensitivity of source radiation impedance to diffuser angular position, the variations in rotational speed should be kept at least to this level if useful measurements of the type reported here are to be obtained. As might be expected measurements at higher frequencies are more sensitive to variations in the rotational speed.

By careful attention to many details the method used for the measurements has yielded much useful information not previously available. However, the questions raised by the results of the experiments will probably have to be investigated by other means as the techniques used

here do not seem amenable to further extension due, in part, to difficulty in obtaining a sufficient degree of measurement precision. The various choices were very nearly optimal and the information returned seens about the best that can be expected using an impedance tube.

CHAPTER 8

NEAR FIELD MEASUREMENT OF THE RADIATION IMPEDANCE

8.1 INTRODUCTION

In the previous chapter the experimental results indicated that the extent of the effect of the rotating diffuser on sound radiation from a pure tone source might be a function of source size. The purpose of the experiments described here is to investigate the effect of source size and to obtain more accurate measurements for the variations in radiated sound power as a function of angular diffuser position. The sound sources used here were simply supported edge square plates of various sizes and thicknesses, vibrating in their fundamental resonant mode. The experimental procedure involves the measurement of the nearfield sound pressure levels adjacent to the square plate sound source and over a sufficiently fine grid. At each measurement point on the plate the sound pressure level is sampled (using a peak detector circuit), at a rate of between 80 and 100 Hz for approximately 1½ revolutions of the rotating diffuser. Each pressure sample so obtained corresponds to a particular angular position of the rotating diffuser. At each measurement point the sampling begins at the same angular position of the diffuser. Thus each particular angular diffuser position is represented by one pressure sample at each sampling point on the plate. Each time a pressure measurement is made a corresponding measurement is recorded of the signal from an accelerometer fixed to a single reference point on the plate. The phase between the two signals is also recorded. When this data is combined with velocity amplitude distribution data obtained from a time averaged hologram it

is possible to calculate accurately the average surface radiation efficiency as a function of diffuser angular position. The procedure allows both the real and imaginary parts of the plate radiation efficiency averaged over one diffuser revolution to be calculated as well as the extent of the variations encountered over a single diffuser revolution.

The microphone is automatically moved from point to point during the measurement procedure using a stepping motor-ball screw arrangement. The experimental procedure and result calculations are fully described later.

8.2 REVIEW OF PREVIOUS WORK

The problem of deducing sound power information from sound pressure level measurements in the near field of a sound source has always been complicated by the presence of the reactive sound field. The intensity of the reactive part of the sound field is proportional to the product of the pressure and the in quadrature component of the particle velocity while the intensity of the resistive part of the sound field is proportional to the product of the pressure and the in phase component of the particle velocity. The sound pressure level produced in the far field by a source is determined entirely by the resistive component of the sound field near to the source.

Thus sound power levels determined from sound pressure level measurements made near to the source are useful only if the intensity of the reactive sound field is small compared with the intensity of the resistive sound field at the measurement point. This is generally true if the frequency of the radiated sound is well above the frequency at which the real or resistive part of the source radiation efficiency is unity.

Over the past 25 years many attempts have been made to produce a sound intensity meter which is capable of measuring only the resistive sound field. Only recently have these attempts met with much success. In 1977 and 1978 F. Fahy presented a successful procedure for acoustic intensity measurement. For the measurements he uses two condenser microphones and a portable sound level meter fitted with octave band filters. The measurement procedure is based on the principle that the particle velocity is related to the pressure gradient at a particular point by the equation

$$\frac{\partial p}{\partial x} = - \rho \, \partial v/\partial t \quad . \qquad (8.1)$$

This principle together with suitable signal processing of the two microphone signals allows a measurement of the resistive acoustic intensity to be obtained. More recently Chung (1978) has used a similar approach and in addition he has shown how the intensity spectrum may be determined by measuring the imaginary part of the cross spectrum between the two microphone signals.

A second method for the measurement of acoustic intensity at a vibrating surface has been used by Brito and Lyon (1976, 1977) and Macadam (1976). They rely on point wise exploration of a surface with an accelerometer and microphone to obtain an overall picture of the sound field adjacent to a vibrating surface. This method also allows location of far field acoustic sources on the vibrating surface if the experimenter is patient enough to explore the surface in sufficient detail. Alternatively, sources of far field noise can be located using acoustic holography (Graham, 1969; Watson, 1971, 1973; Watson and Hannon, 1974; Watson and King, 1976; Ueha, et al., 1975). Acoustic holography is advantageous in some instances because it can image aero-

dynamic and moving sources but it has the disadvantage that the wavelength of the sound must be much smaller than the source being imaged (Rayleigh, 1879).

The basis of the experimental procedure used for the work of this chapter has been reported by the author and his thesis advisor in a previous paper (Hansen and Bies, 1978, 1979e) where a method for the measurement of both the resistive and reactive parts of the intensity produced by a vibrating surface radiating pure tone sound is described.

The procedure described makes use of surface pressure measurements in an anechoic room and a time averaged hologram of the vibration mode to compute the complex acoustic intensity at every point on the vibrating surface. The surface radiation efficiency is then calculated by averaging the distribution of the complex intensity over the vibrating surface. The measurements also allow quantitative location on the vibrating surface of acoustic sources which radiated energy to the far field, with good precision and resolution provided the resistive part of the acoustic intensity is positive for all parts of the surface.

The measurement procedure is based upon the following considerations. Continuity of the acoustic medium (air) requires that the acoustic normal velocity in the fluid immediately adjacent to the surface is equal to the normal surface velocity. Therefore the real part of the acoustic intensity in the fluid immediately adjacent to a particular sample point on the vibrating surface may be calculated as the product of the acoustic pressure in the fluid and the in phase normal surface velocity at that point, while the imaginary part may be calculated as the product of the acoustic pressure and the in quadrature normal surface velocity

The sound sources used in the initial verification of the technique were edge clamped circular plates vibrating in low order modes and the side surfaces of some in line engine blocks vibrating in each of two lowest

order modes. The interesting phenomenon of an area of negative resistive intensity at the plate centre was predicted and experimentally verified for some of the clamped edge circular plates vibrating in the 0,2 mode. Areas of negative intensity were also observed on the engine blocks suggesting that the phenomenon may not be uncommon. The experimental method reported allows far greater detailed investigation of a surface than would be possible when using surface acceleration measurements as described by Brito and Lyon and Macadam, because of the necessity in the latter case for point-wise exploration of the surface and the need for good point contact of the accelerometer with the surface at each point tested.

8.3 EXPERIMENTAL PROCEDURE

The sound sources used in the experiments were four simply supported edge square plates and one rectangular plate. The plate sizes used are listed in Table 8.1. The plates were supported using a shim arrangement (Ochs and Snowdon, 1975) as illustrated in Figure 8.1. The shim thickness to width ratio h/b is an important consideration for obtaining a simply supported edge condition. If the ratio is too small the plate edges are not sufficiently constrained against movement normal to the plate surface, resulting in a distortion of the fundamental vibration mode shape. If the ratio is too large then the plate is not free to rotate at its edge and the result is an edge condition somewhere between clamped and simply supported. Values of h and b which represent a compromise between the above two extremes are listed in Table 8.1 for each test plate.

The first part of the experimental procedure entailed taking a time-averaged hologram of the surface of the plate vibrating in its

TABLE 8.1 SQUARE AND RECTANGULAR EXPERIMENTAL PLATE CHARACTERISTICS

Plate Dimensions (mm)	Plate Thickness (mm)	Measured resonant frequency for 1,1 mode (Hz)	Predicted resonant frequency for 1,1 mode (Hz)	Shim Width b(mm)	Shim Thickness h(mm)	No. of Measurement Points in Plate N	No. of Diffuser Angular Positions Considered L
102 x 102	.60	270	277	20	.13	361	180
102 x 102	.81	371	374	20	.13	361	185
152 x 152	1.2	251	250	20	.26	841	157
152 x 152	1.6	337	334	20	.26	841	168
253 x 253	3.0	231	226	25	.52	625	154
253 x 253	5.0	381	376	25	.52	625	184
378 x 378	10.1	336	344	25	1.0	1369	168
633 x 379	10.1	247	230	25	2.0	1025	164
376 x 376	8.15	281	277	25	1.0	1369	187

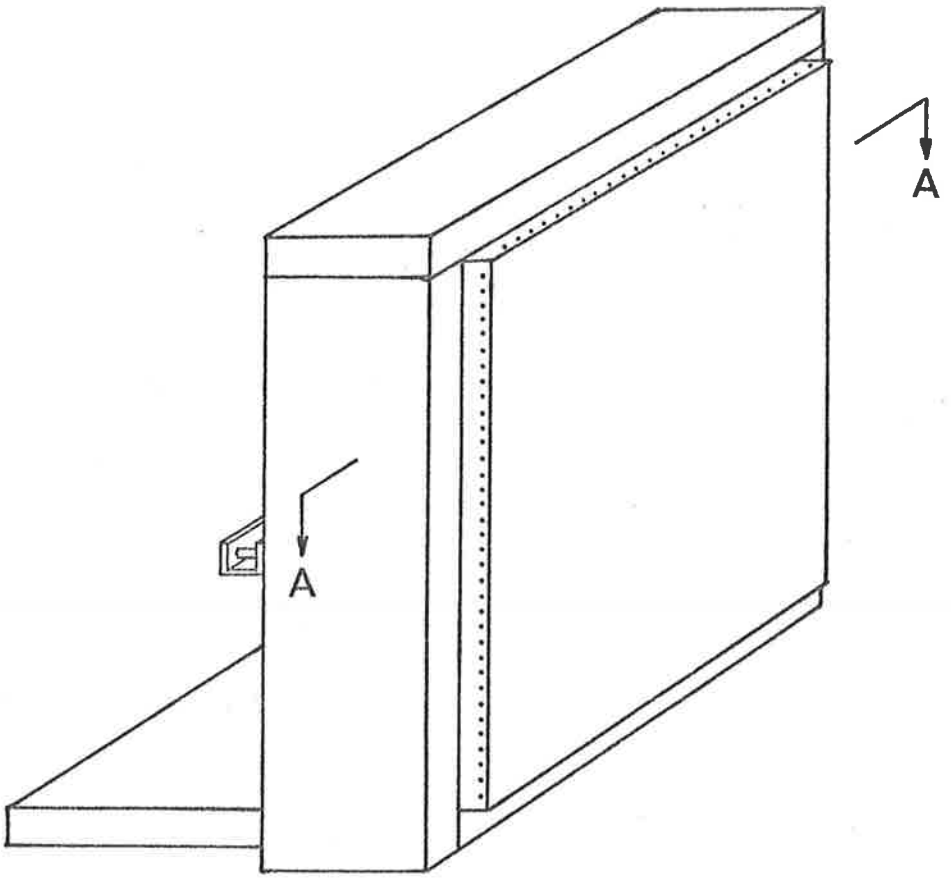

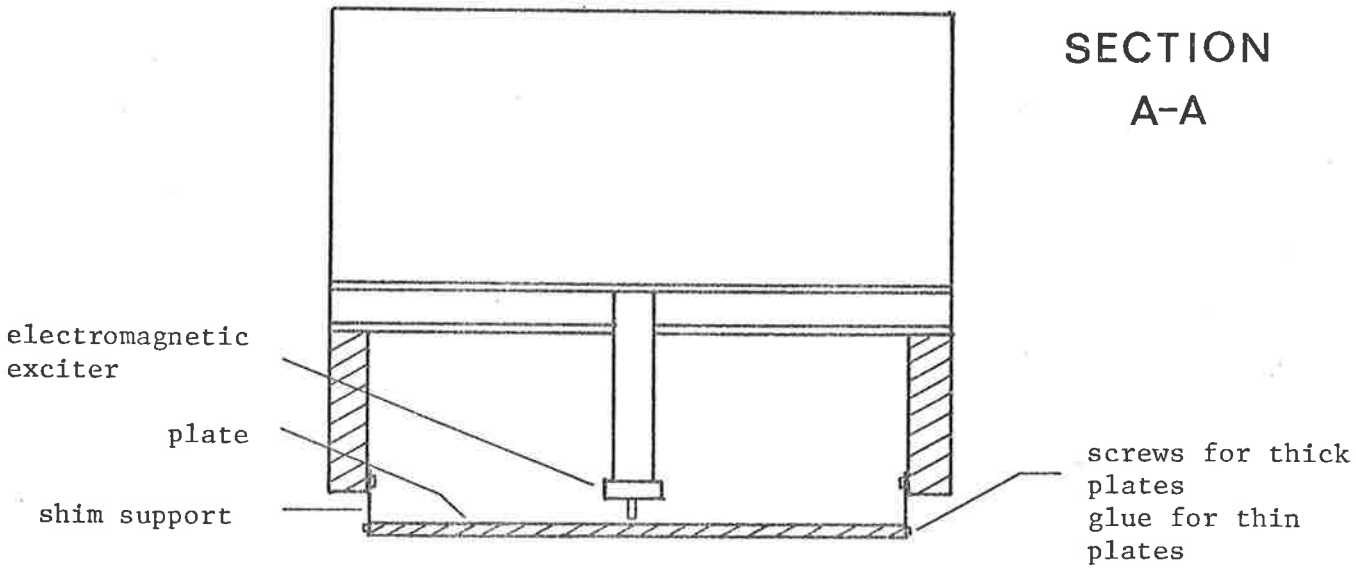

FIG. 8.1 PLATE SUPPORT AND EXCITATION ARRANGEMENT

fundamental resonant mode. The procedure used is the same as that described in Chapter 3. A photograph of an image reconstructed from a time-averaged hologram of one of the plates vibrating in its fundamental resonant mode is shown in Figure 8.2.

Photographs of the images reconstructed from the time-averaged holograms were analysed by using an electronic data tablet connected through a micro processor to a 6400 computer. The individual fringes were identified and traced as a sequence of co-ordinates into computer memory by using the data tablet. The data tablet and associated hardware allowed automatic sequential sampling of fringe co-ordinates at a selectable rate as the fringe was traced with a tracer. The fringe identification information and associated sequences of fringe co-ordinates stored in memory were subsequently used by the computer to determine the surface normal velocity distribution. The apparatus used for analyzing the holograms and storing the information in computer memory is fully described elsewhere, Tonin (1978).

For the next part of the measurement procedure the test plates were mounted in the side wall of the reverberant room containing the same rotating diffuser as described in Chapter 7. The plate location was also the same as that used for the sound sources described in Chapter 7. An accelerometer was placed at some reference point on the plate. A quarter inch condensor microphone was automatically scanned over the plate surface, spending enough time at each sample point on the plate for the diffuser to rotate through at least one revolution. The number of sample points on the plates ranged from 361 for the smaller plates to 1369 for the larger plates, and are listed in Table 8.1. The spacing between the sample points varied from 5 mm for the smaller plates to 10 mm for the larger plates. The microphone was placed so that its

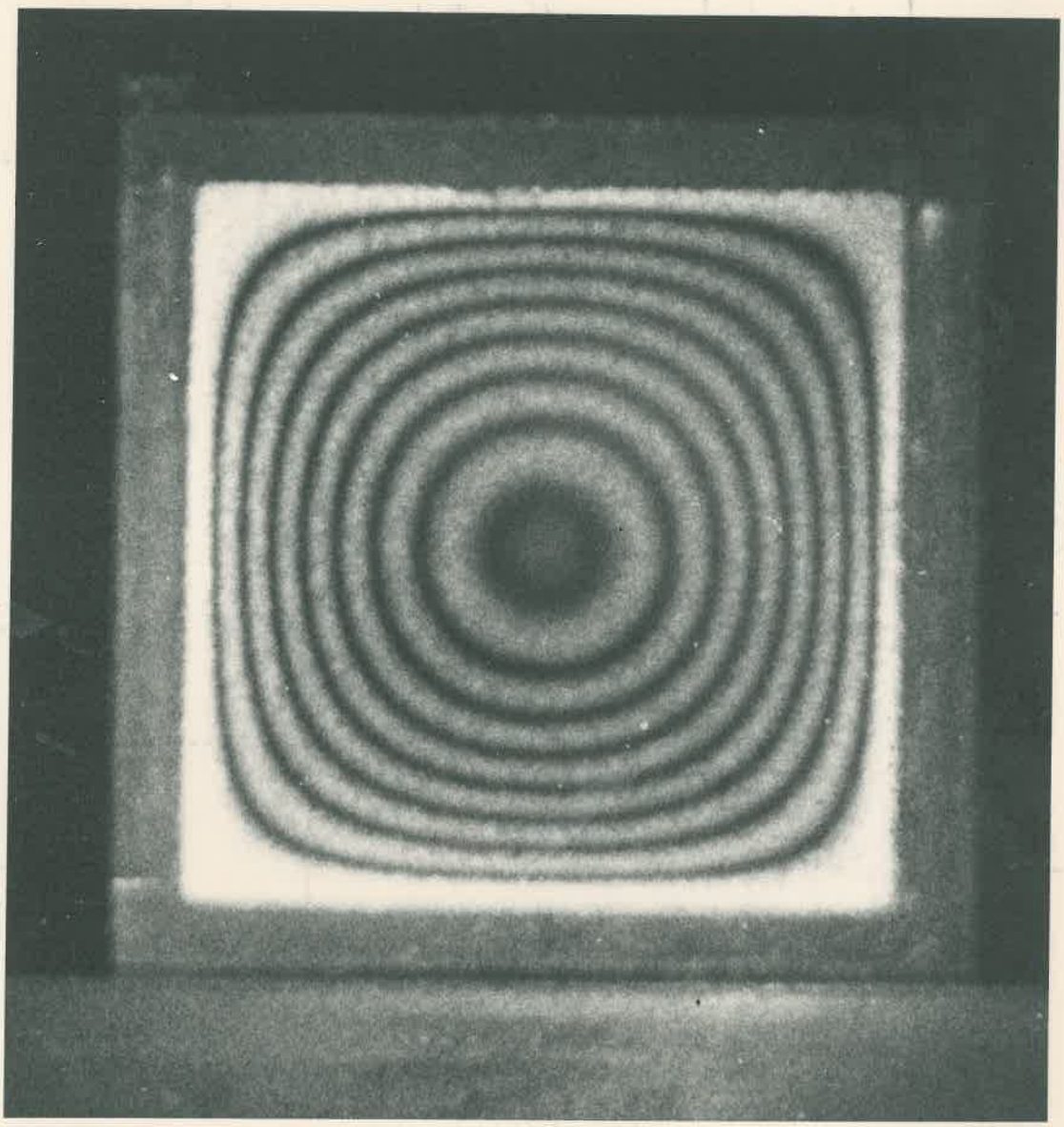

FIG. 8.2. RECONSTRUCTED IMAGE FROM A TIME AVERAGED HOLOGRAM OF A SIMPLY SUPPORTED SQUARE PLATE VIBRATING IN ITS FUNDAMENTAL MODE.

diaphragm was approximately 3 mm from the vibrating plate at all times. This distance was used because measurements in an impedance tube reported in Appendix 2 indicated that due to diffraction affects the microphone actually samples the pressure field at a distance of approximately 3 mm in front of its diaphragm.

The microphone was mechanically moved back and forth across the plate surface by using an electronically controlled stepping motor-ball screw system illustrated in Figure 8.3. The microphone was positioned well above the traverse mechanism thus minimizing the interference with the sound field near the test surface. The 12.5 mm diameter hollow post supporting the microphone was isolated from the traverse mechanism and internally damped to minimize microphone vibration transmitted from the horizontal traversing movement.

During the scanning procedure the microphone moved horizontally in steps of 5 mm or 10 mm, depending on the plate size. At each sample point on the plate the signal from the microphone and accelerometer, together with the phase difference signal was continuously recorded as the diffuser rotated through approximately 1½ revolutions. To minimize the amount of data stored, the signals from the accelerometer and microphone were passed through a peak detector unit resulting in only the peak levels of the sinusoidal signals being recorded. The number of peaks sampled was then reduced using a data rejection system so that in most cases between 80 and 100 peaks were sampled per second. The pressure and acceleration signals were passed through high and low pass Butterworth filters before entering the peak detector units. The filters were calibrated for phase shift at each test frequency. The phase shift between the two signals was detected digitally by measuring the time difference between the zero crossing

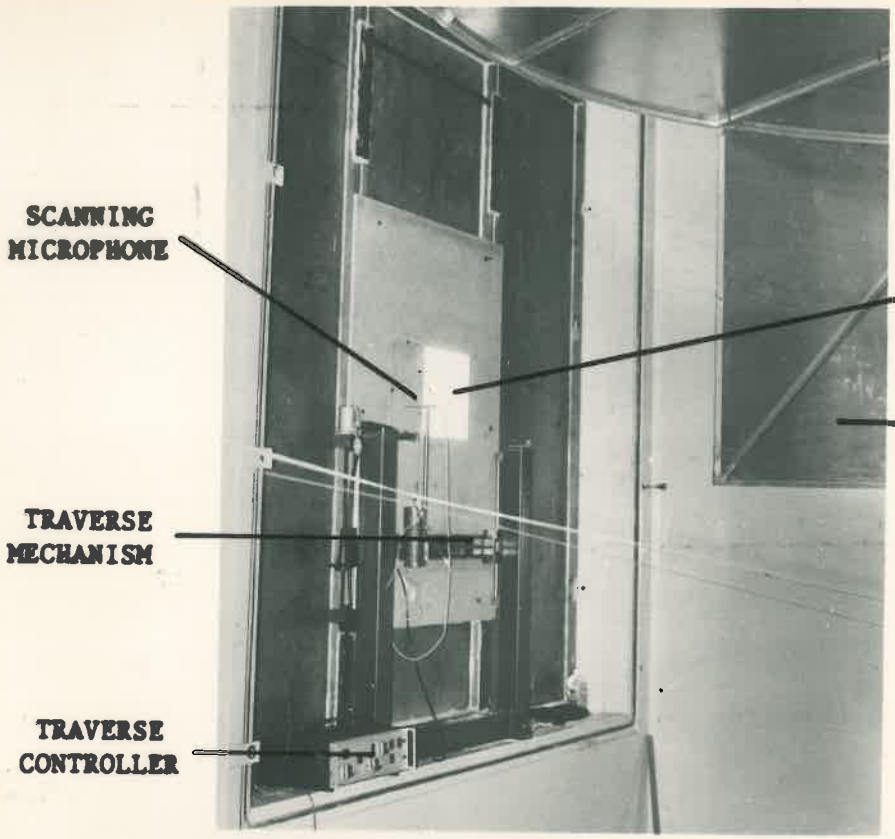

(a)

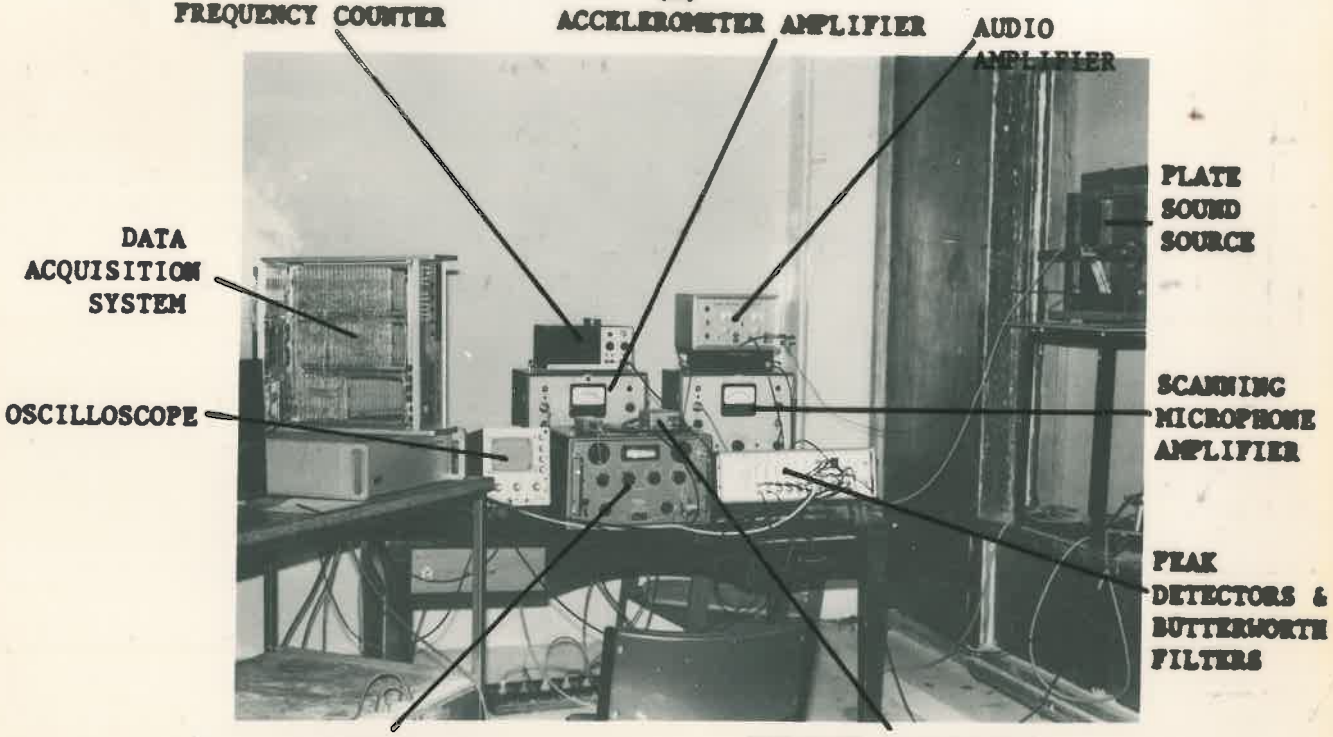

(b)

FIG. 8.3. EXPERIMENTAL ARRANGEMENT FOR SQUARE PLATE SOUND SOURCE TESTS.

(a) Reverberant room arrangement.
(b) Signal generation and recording equipment external to the reverberant room.

point of each signal. A fast counter was initiated by the downwards zero crossing of the pressure signal and stopped by the downwards zero crossing of the accelerometer signal. When the counter stopped its output was latched and a short time later was recorded. The phase sample rate was the same as the pressure and acceleration amplitude sample rate. The signals from the two peak detectors and phase detector were recorded simultaneously using a high speed multi-channel data acquisition system (Brown, 1975). As the microphone moved from one sample point to another the data system memory was written on to magnetic tape. At each sample point the angular position of the diffuser was always the same at the instant data began to be acquired. This was achieved by using the signal from a photo transistor to start the data acquisition system. The photo transistor was activated by using a small spigot attached to a point of the rotating diffuser to interrupt a laser beam. The signal from the photo transistor was interlocked with a signal from the microphone traverse so that the photo transistor signal could only get through after the microphone traverse had stopped moving.

At the completion of each horizontal traverse the microphone automatically moved downwards a distance of 5 mm or 10 mm, depending on the horizontal step size. The horizontal traverse then proceeded to move in the opposite direction until it once again reached its original starting point. The process was repeated until the whole plate had been scanned.

The above measurements were repeated with the plate mounted in a large baffle in an anechoic room so that the reverberation room measurements would have a basis for comparison. The test procedure was similar except that there was no rotating diffuser to vary the signal with time for a given sample point.

A schematic design of the experimental arrangement is shown in Figure 8.4.

The plates were excited electromagnetically at the plate centre using a Muirhead model D-650-B oscillator and audio amplifier. The amplitude of vibration of the plate during the microphone scanning time (which could be up to 2½ hours) was kept constant by using a voltage compression circuit between the oscillator and the electromagnetic exciter to reduce the voltage fluctuations to the electromagnetic exciter to less than .01%. The frequency stability of the oscillator used was better than .02%. However, due to the analysis technique used (described in section 8.3) small variations in plate vibration amplitude during the microphone scanning process do not affect the results obtained.

8.4 DATA ANALYSIS AND COMPUTATION OF RESULTS

The analogue inputs to the data system were connected to eight bit analogue to digital converters which resulted in a possible error of less than ½% for maximum levels (10 volts). The smallest signals recorded were from the microphone when it was near the edge of the plate and were of the order of 1 volt resulting in a 4% measurement error.

The phase input to the data acquisition system was a 16 bit digital input with an accuracy of ± ½ μ sec and a maximum time interval measurement capability of 0.03 seconds. At 200 Hz this represented a phase measurement error of 0.04 degrees. This accuracy was greatly reduced by both high and low frequency noise on the pressure and acceleration signals. The low frequency noise, generated mainly by the rotating diffuser drive and also by the microphone amplifier and power supply

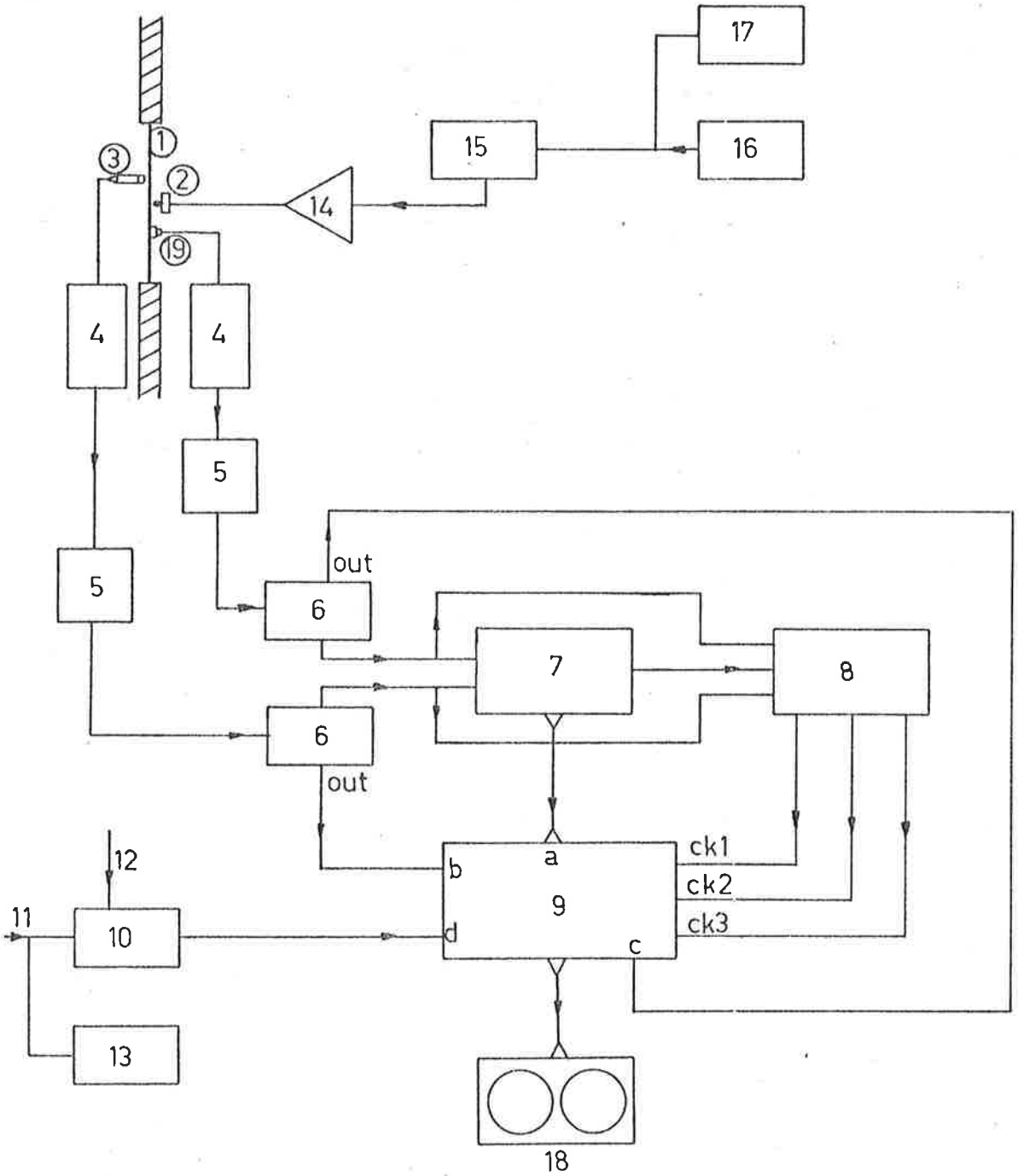

Figure 8.4. DATA ACQUISITION ARRANGEMENT.

1. Vibrating plate. 2. Electromagnetic exciter. 3. ¼-inch Bruel & Kjaer condenser microphone and FET. 4. Microphone amplifier and power supply. 5. High and low pass 6 pole Butterworth filter. 6. Peak detector. 7. Phase detector. 8. Data rejector. 9. Data acquisition system, (a) Channel 3 digital input, (b) Channel 1 analogue input, (c) Channel 2 analogue input, (d) external start to begin sampling data. 10. Logic for external starting of data acquisition system. 11. Signal from photo transistor. 12. Signal from microphone traverse mechanism. 13. Diffuser speed timer. 14. Audio amplifier. 15. Voltage compression circuit. 16. Oscillator. 17. Frequency counter. 18. Tape Recorder. 19. Accelerometer.

was minimized by using a step variable high pass 6 pole Butterworth filter with the 3 dB cut off at least 100 Hz below the signal frequency. The high frequency noise generated by the microphone amplifier and power supply was minimized using a low pass 6 pole Butterworth filter with its 3 dB cut off frequency at 800 Hz.

It is realized that the signal recorded by the microphone in the reverberant room would be slightly distorted due to the presence of side bands generated by rotation of the diffuser. A frequency analysis of the recorded signal showed that the level of the highest side band was at least 15 dB below the signal frequency. Also all of the significant sideband energy was contained in the frequency range of a few tens of Hz either side of the signal frequency; thus all the significant side band energy would be contained in the pass band of the filters used. As shown in Chapter 7 the side bands are produced by an amplitude modulation of the radiated sound power. Thus it follows that the phase measurement is unaffected by the side band distortion of the waveform as the phase measurement relies entirely on zero crossing points which remain undistorted. The error in calculating the rms pressure signal from the peak signal can also be shown to be insignificantly affected by the side band distortion of the waveform using the same calculations as in Chapter 7, even if the energy in the side bands was much more than it was actually found to be. The conclusion which may be drawn from this discussion is that errors in the measurements produced by the presence of diffuser generated sideband frequencies are so small as to be insignificant.

A convenient way to express the experimental results is in terms of the plate radiation efficiency which may be regarded as a normalised form of the radiation impedance. The plate radiation efficiency is defined by

$$\sigma = \frac{W}{\langle v^2 \rangle_{St} A \rho_0 c_0} \quad . \tag{8.2}$$

The radiation efficiency is averaged over the whole plate for each considered angular position of the rotating diffuser. Thus for the j^{th} angular position of the diffuser we have

$$\sigma_j = [1/A\rho_0 c_0][A/N_p] \sum_{n=1}^{N} \{I_{n,j} / [\langle v^2 \rangle_{St}]_{n,j}\} \tag{8.3}$$

where

$$I_{n,j} = \tfrac{1}{2}[\hat{p}\hat{v} \cos \phi_{p-v} + i\hat{p}\hat{v} \sin \phi_{p-v}]_{n,j} \tag{8.4}$$

where the subscript n denotes the n^{th} measurement point on the plate and the subscript j denotes the j^{th} angular position of the rotating diffuser. N is the number of measurement points on the plate and L is the number of diffuser angular positions considered (see Table 8.1). The average radiation efficiency for one complete diffuser revolution is calculated by averaging the values for each of the considered angular positions. Thus

$$\sigma = \frac{1}{L} \sum_{j=1}^{L} \sigma_j \quad . \tag{8.5}$$

The first part of the analysis required the determination of the normal surface velocity amplitude and phase at each point where corresponding sound pressure measurements had been recorded during the microphone traverse. As described earlier the reconstructed image from a time-averaged hologram was traced fringe by fringe into computer memory. The result was strings of co-ordinates corresponding to increments of surface displacement. For the analysis to proceed it was necessary to translate this displacement information into a grid, corresponding to the sound pressure measurement grid, of velocity

amplitude and phase information relative to the measured acceleration at the location of the single reference accelerometer.

The surface displacement amplitude at a given point was found by using linear interpolation with the nearest recorded data points on each of the two nearest fringes. It was then expressed as a ratio of displacement amplitude at the given point to the displacement amplitude at the location of the reference accelerometer. The ratio of mean square plate displacement to displacement amplitude squared at the reference accelerometer location was also calculated by averaging over all points on the measurement grid, and was equal to the ratio of the mean square plate velocity to velocity amplitude squared. The linear interpolation method described above gave extremely accurate and reliable results with the largest errors occurring near the plate edge. In summary then the hologram was used to determine the ratios $\hat{v}/\hat{v}_{ref}$ and $\langle v^2\rangle_{St}/\hat{v}^2_{ref}$ for each grid point on the plate.

The second part of the computations consisted of analysing the recorded pressure amplitude, acceleration amplitude and pressure-acceleration phase data to obtain $\hat{p}$, $\hat{a}_{ref}$ and $\phi_{p\text{-}a_{ref}}$ for each pressure measurement. The ratio of acoustic intensity to mean square plate surface velocity corresponding to each pressure measurement was obtained by combining the above measured quantities as follows

$$I/\langle v^2\rangle_{St} = \tfrac{1}{2}[1/\langle v^2\rangle_{St}]\,[\hat{p}\hat{v}\cos\phi_{p\text{-}v} + i\hat{p}\hat{v}\sin\phi_{p\text{-}v}] \qquad (8.6)$$

i.e.

$$I/\langle v^2\rangle_{St} = [\hat{p}/2]\,[\hat{v}/\hat{v}_{ref}]\,[\hat{v}^2_{ref}/\langle v^2\rangle_{St}]\,[2\pi f/\hat{a}_{ref}]\,[\cos\phi_{p\text{-}v} + i\sin\phi_{p\text{-}v}] \qquad (8.7)$$

where

$$\phi_{p\text{-}v} = \phi_{p\text{-}a_{ref}} + \pi/2 - \phi_{y\text{-}y_{ref}} \text{ radians} . \qquad (8.8)$$

The quantities on the RHS of equations (8.7) and (8.8) were all measured experimentally. The instantaneous ratio $I/\langle v^2 \rangle_{St}$ was calculated for each considered angular position of the rotating diffuser and for each pressure measurement location on the plate surface. When the quantity $I/\langle v^2 \rangle_{St}$ was divided by $\rho_0 c_0$ and averaged over all measurement points on the plate for each considered angular diffuser position, the plate radiation efficiency as a function of diffuser angular position was obtained. The time averaged radiation efficiency was then obtained by averaging over one complete diffuser revolution.

The calculations for the anechoic room measurements were similar but the results for a given pressure measurement location were constant as no rotating diffuser was present.

8.5 REVIEW OF RESULTS AND CONCLUSIONS

The main purposes of the measurements in the reverberant room were to find how the rotating diffuser affects the sound radiation efficiency of a source in the room and to observe if this effect is a function of source size as well as frequency. Another reason for the measurements was to find how closely the source radiation efficiency, averaged over one diffuser revolution, approximated the radiation efficiency measured in an echo free field; and whether or not better agreement with free field measurements was obtained for larger sources than for smaller sources.

The radiation efficiency results are presented in Figures 8.5 and 8.6. The average values measured in the reverberant room and in the anechoic room are shown as symbols and the variation in the values over one diffuser revolution is shown as a vertical line through the symbols. In Figure 8.5 the theoretical curve is taken from work

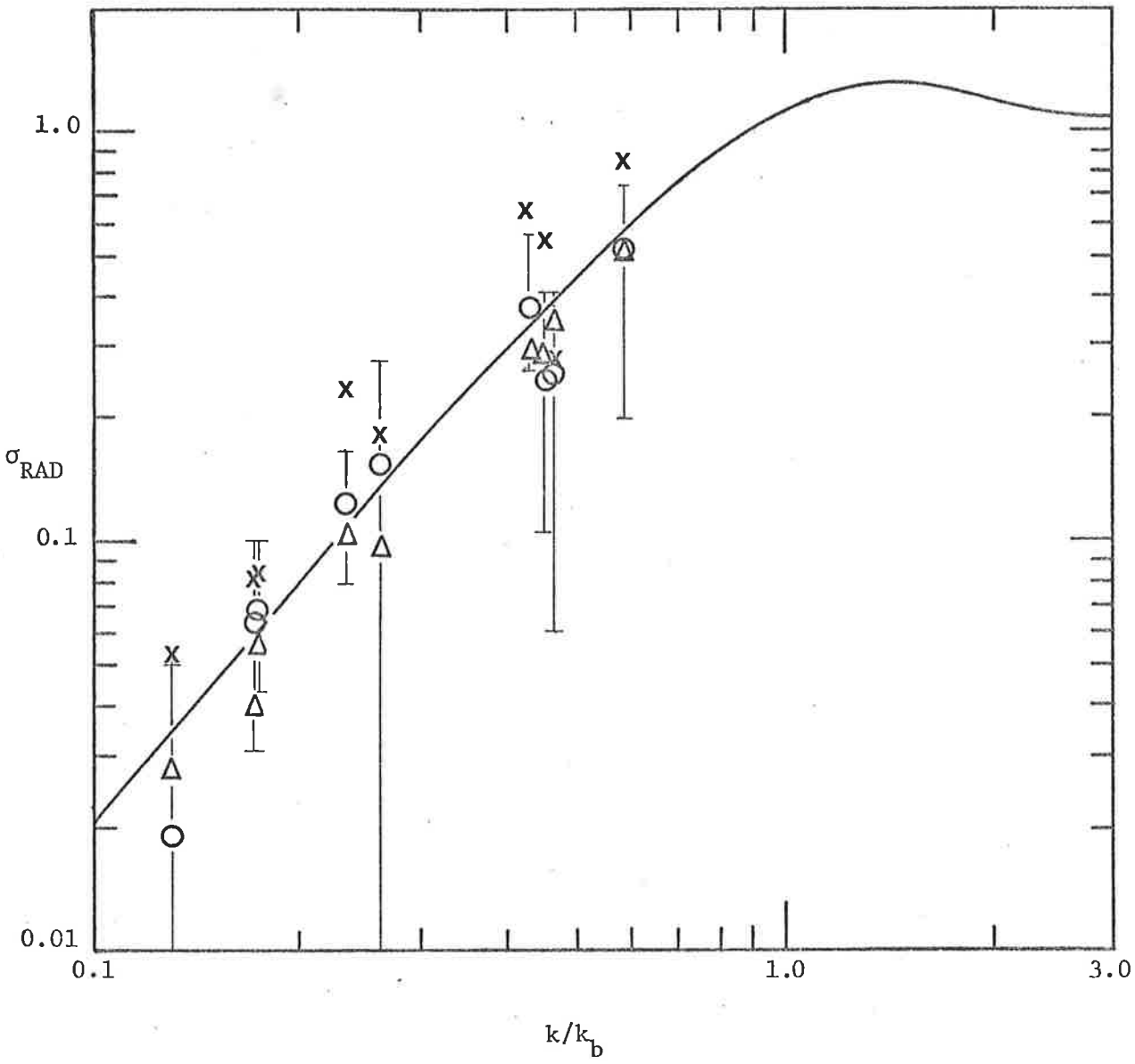

—— = Theory (Wallace)

Δ = Anechoic room data

O = Reverb room data averaged over one diffuser revolution

I = Reverb room data variation during one diffuser revolution

X = Calculations from measurements of space average SPL and T_{60}

FIG.8.5 RADIATION EFFICIENCY FOR A SIMPLY SUPPORTED EDGE SQUARE PLATE (1,1 MODE)

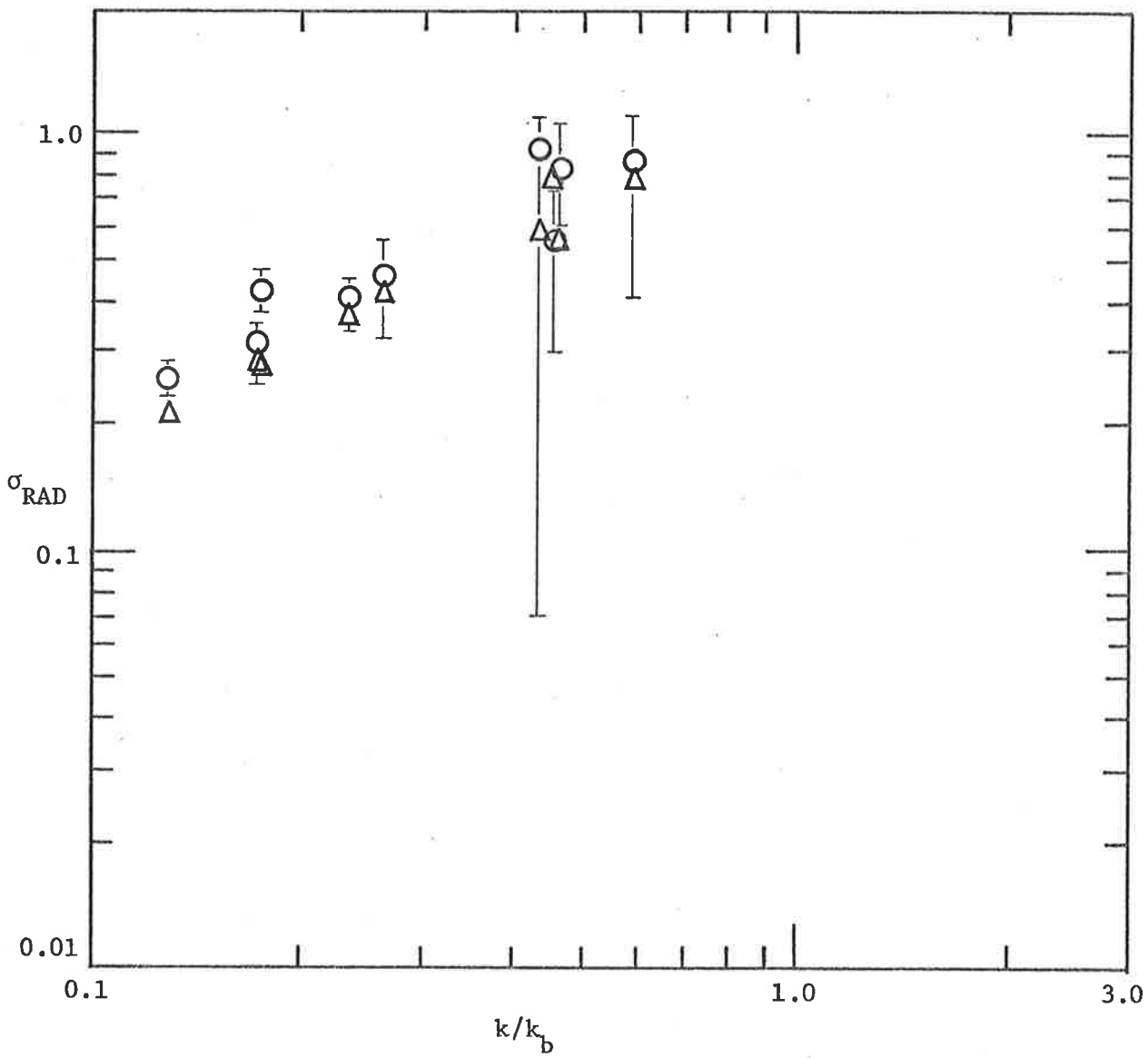

Δ = Anechoic room data

O = Reverb room data averaged over one diffuser revolution

| = Reverb room data variation during one diffuser revolution

FIG. 8.6 MEASURED REACTIVE RADIATION EFFICIENCY FOR A SIMPLY SUPPORTED EDGE SQUARE PLATE. (1,1 MODE)

published by Wallace (1972). As discussed by Wallace, the wave number ratio k/k_b on the abscissa of the plot may be defined as

$$k/k_b = [2\pi f/c_0][(m\pi/a_1)^2 + (n\pi/a_2)^2]^{-\frac{1}{2}} \quad . \tag{8.9}$$

The predicted values of plate resonant frequency listed in Table 8.1 were calculated from the following equation derived using Classical plate theory.

$$f = 0.48\ c_L\ h[1/a_1^2 + 1/a_2^2]\ \text{Hz} \quad . \tag{8.10}$$

The agreement between theory, reverberant room measurements and anechoic room measurement is for the real part of the radiation efficiency excellent, within 1 dB for 4 out of the 9 test plates, within 2 dB for 4 and within 3 dB for one of the test plates. The agreement between reverberant field and free field measurements for the imaginary part is equally as good.

The data show no obvious trend which suggests that the effect of the diffuser on the source radiation impedance is a function of source size. This may be due to the fact that it was not possible to use identical exciting frequencies for each source size because it was necessary to drive the plates at resonance to obtain a sufficiently large microphone signal to noise ratio. Even if it were possible to excite the plates sufficiently at frequencies below the 1,1 mode resonant frequencies, difficulty would have been encountered in achieving a simply supported edge condition due to the excessive exciting forces which would be required. As all the radiation efficiencies measured for the square plate sources in the reverberant room were very close to free field predictions, it appears that very much smaller sound sources need to be tested to find whether or not the diffuser effect

decreases significantly if the source size becomes small enough. However, it was not practical to test smaller sources than those Listed in Table 8.1 using the experimental method reported here. It appears from the data reported here that if a conclusive result is to be obtained about the source size effect it would be necessary to test very small sources and very large sources radiating at identical frequencies.

In order to check on the accuracy of the measurements reported in Chapter 5, the real part of the source radiation efficiency was calculated by measuring the room reverberation times and the space averaged sound pressure levels (using a linear microphone traverse) as described in that Chapter and Chapter 4.

The results are shown as **X** in Figure 8.5. It can be seen that the data are consistently high, indicating insufficient accuracy in the measurements of the room reverberation times and the space average sound pressure levels. These inaccuracies are consistent with results obtained using an impedance tube calibration procedure described in an earlier paper (Bies and Hansen, 1976).

Typical plots showing the variation of plate radiation efficiency as a function of diffuser angular position are presented in Figures 8.7 and 8.8. Note that the pattern repeats itself after one complete revolution, indicating that a unique value of the source radiation impedance exists for a particular angular position of the rotating diffuser. From Figs. 8.7 & 8.8 it can be seen that the absolute values of both the real and imaginary parts of the radiation efficiency vary more for the larger plates than for the smaller plates during one diffuser revolution. However, the variation in the ratio of the value of the radiation efficiency, corresponding to a given angular position of the rotating diffuser, to the mean value of the radiation efficiency

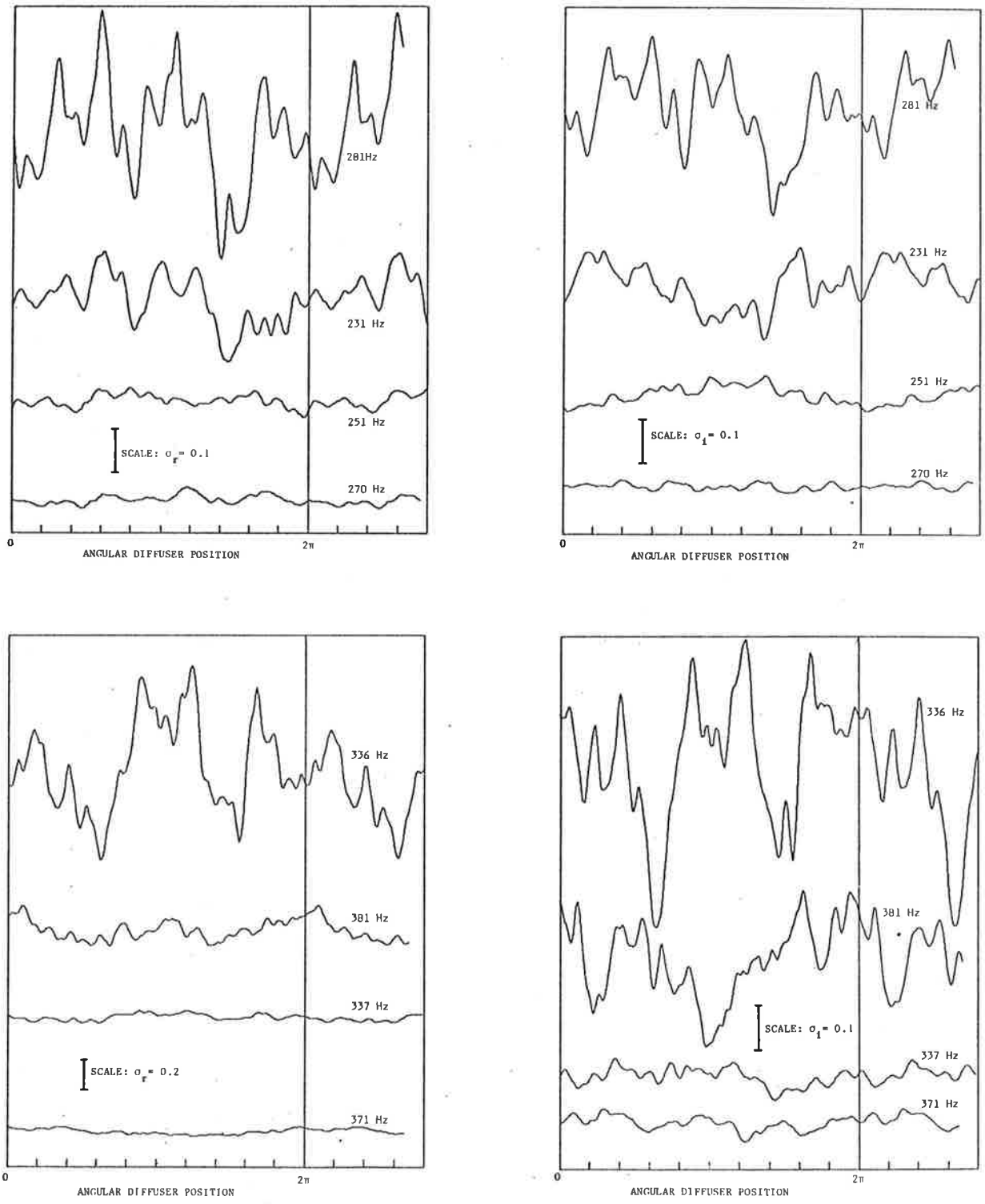

RESISTIVE

REACTIVE

FIG. 8.7 VARIATIONS IN THE ABSOLUTE VALUES OF THE RESISTIVE AND REACTIVE PLATE RADIATION EFFICIENCIES AS A FUNCTION OF DIFFUSER ANGULAR POSITION.

Source size increases from the lower curve to the upper curve in each case.

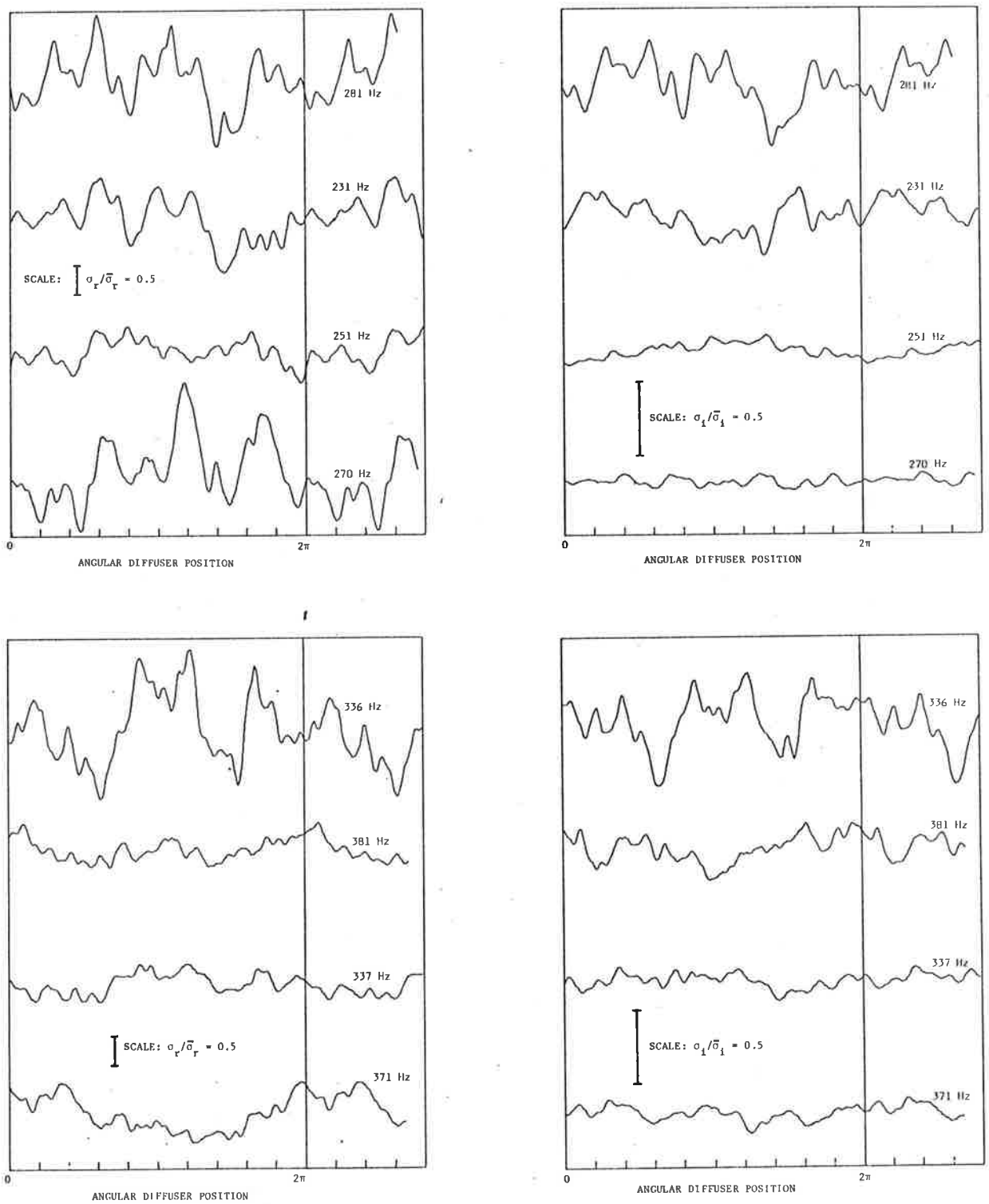

RESISTIVE REACTIVE

FIG.8.8 VARIATIONS IN THE NORMALIZED VALUES OF THE RESISTIVE AND REACTIVE PLATE RADIATION EFFICIENCIES AS A FUNCTION OF DIFFUSER ANGULAR POSITION.
Source size increases from the lower curve to the upper curve in each case.

(averaged over one diffuser revolution) does not appear to depend on plate size.

The results of the measurements prove without doubt that the rotating diffuser does significantly vary the radiation efficiency of the source and hence the power radiated by the source in the room. In all cases the real part of radiation efficiency varied about the measured free field value although in some cases the imaginary part did not. The substantial effect of the rotating diffuser on the power radiated by the source in the reverberant room is clearly shown in Fig. 8.9. In this figure values of $I/\rho_0 c_0 \langle v^2 \rangle_{st}$, measured on a central horizontal line across one of the plates, are plotted for several different diffuser angular positions. Different symbols correspond to different dynamic angular positions of the diffuser rotating at 30 rpm. The angular diffuser positions considered in the figure are separated by an angle represented by a circumferential movement of the diffuser of approximately $\lambda/4$. The results in the figure represent the largest variation which could be found for a given angular position change of the diffuser, for the particular plate considered. The scatter in the data is attributed to both inaccuracy in pressure-acceleration phase measurements and to errors in determining the precise angular position of the diffuser due to slight variations in speed.

It is realized that if the diffuser distorted the 1,1 resonant mode shape of the plates, by loading some parts of a given plate differently to other parts then meaningful results would not have been obtained. The uniformity of the variation in radiation loading on the plates as the diffuser rotated was checked by monitoring the outputs of several accelerometers placed at random on a given plate, using a multi-channel

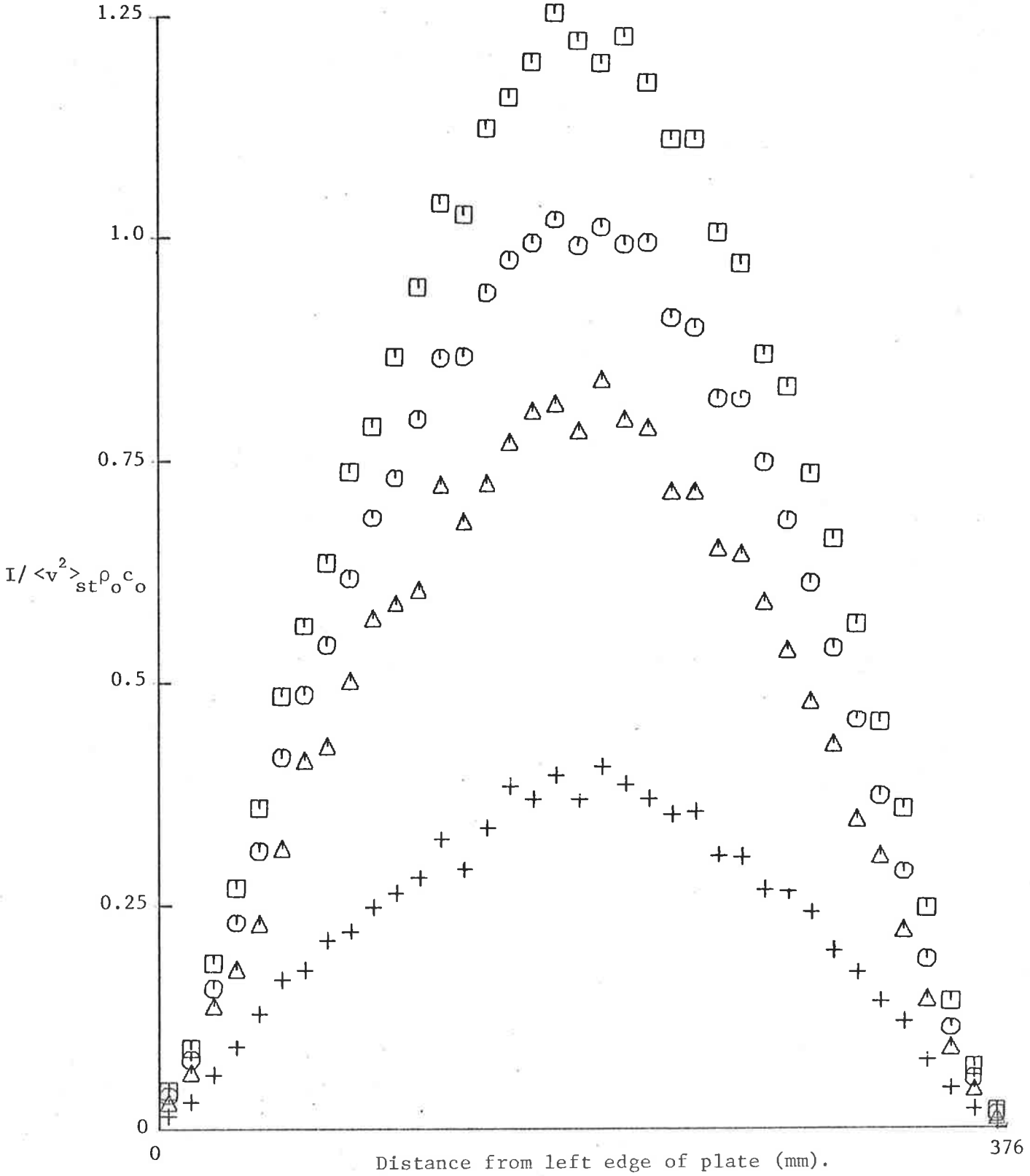

FIG. 8.9 VALUES OF THE QUANTITY $I/\langle v^2\rangle_{st}\rho_o c_o$ PLOTTED ACROSS THE CENTRE OF ONE OF THE PLATES FOR FOUR DIFFERENT ANGULAR POSITIONS OF THE DIFFUSER. THE ANGULAR SEPARATION BETWEEN EACH ADJACENT POSITION IS EQUIVALENT TO A LENGTH OF APPROXIMATELY $\lambda/4$ AROUND THE DIFFUSER CIRCUMFERENCE.
Plate size = 376mm x 376mm x 8.15mm.

oscillope and checking that the acceleration signals were all varying synchronously.

8.6 SUMMARY

A new method has been developed for the measurement of the complex radiation efficiency of a modally vibrating surface. The method was used to investigate the effect of a rotating diffuser on the complex radiation efficiency of various size sources in a reverberant room. The sources used were simply supported edge square plates vibrating in their fundamental resonant mode.

The data show conclusively that the effect of the rotating diffuser is substantial and also that the diffuser enables the average value of the source radiation efficiency to approach very close to the free field value, at least in the frequency range over which the tests were conducted.

It was found that for the range of source sizes tested the effect of the diffuser on the source radiation efficiency was not dependent on source size. The test sources ranged in size from a 0.1m x 0.1m square plate to a 0.63m x 0.38m rectangular plate.

APPENDIX 1

FAR FIELD EVALUATION OF THE RAYLEIGH INTEGRAL

In the following analysis, the real part of the radiated sound field is calculated by evaluating the Rayleigh Integral (Rayleigh, 1878c) at a sufficient distance from the plate such that the acoustic pressure and particle velocity may be considered to be in phase.

The well known solution for radiation from a circular piston (Junger and Feit, 1972) in an infinite wall is used as a model. However, the plate surface velocity is modelled according to the vibration mode being considered and results are presented in a non-dimensional form. The appropriate surface velocity distributions are obtained from Section 2.2.

The integral expression given by Rayleigh is as follows,

$$\phi = -(1/2\pi) \int\int_A \frac{d\phi}{dn} \frac{e^{-ikr'}}{r'} dA. \qquad (A1.1)$$

For the vibrating plates this expression may be rewritten as,

$$\phi(R,\alpha,\theta',t) = (e^{i\omega t}/2\pi) \int\int_A \hat{v}(r_0,\theta) \frac{e^{-ikr'}}{r'} dA , \qquad (A1.2)$$

where positive time dependence has been used and where (R,α,θ') are spherical coordinates and (r_0,θ) are polar coordinates on the plate surface. The coordinates are illustrated in Fig. A1.1. In equation (A1.2), $\phi(R,\alpha,\theta',t)$ is the velocity potential at a point $P(R,\alpha,\theta')$ at time t due to velocity amplitude distribution $\hat{v}(r_0\theta)$ on the plate surface.

In the far field r' (the distance from point P to a point on the plate surface) in the denominator of equation (A1.2) may be replaced with R. However, only terms which are much less than unity may be neglected in the argument of the exponential term of equation (A1.2). Thus r' in the exponential term will be replaced by (Junger and Feit, 1972):

$$r' = R - r_0 \sin\alpha \cos(\theta' - \theta). \qquad (A1.3)$$

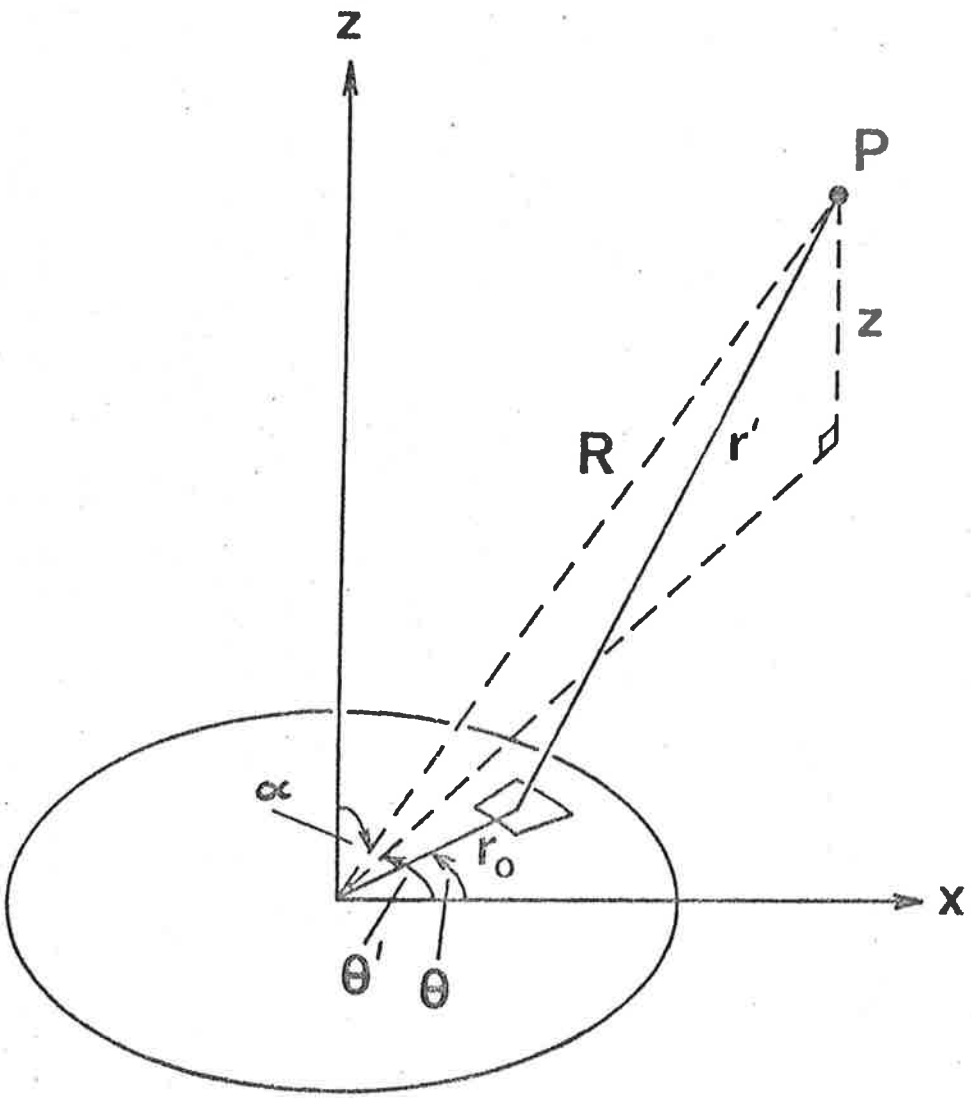

FIG. A1.1 COORDINATE SYSTEM USED FOR THE FAR FIELD EVALUATION OF THE RAYLEIGH INTEGRAL.

With these approximations, equation (A1.2) may be written as,

$$\phi(R,\alpha,\theta',t) = (e^{i\omega t}/2\pi R) \int_0^{2\pi}\int_0^a \hat{v}(r_o,\theta) \exp[-ikR + ikr_o \sin\alpha \cos(\theta'-\theta)]\, r_o\, dr_o\, d\theta . \tag{A1.4}$$

Using equation (2.3) the quantity $\hat{v}(r_o,\theta)$ may be written as,

$$\hat{v}(r_o,\theta) = i\omega a D_{mj} \Theta_m(\theta) H_{mj}(u) . \tag{A1.5}$$

Replacing r_o with ua and using equation (A1.5) we may rewrite equation (A1.4) as,

$$p_{mj}(R,\alpha,\theta',t) = -\{\rho_o \omega^2 a^3 D_{mj} \exp[i(\omega t - kR)]/2\pi R\}$$

$$\times \int_0^{2\pi}\int_0^1 H_{mj}(u)\, \Theta_m(\theta) \exp[ikau \sin\alpha \cos(\theta' - \theta)]\, u\, du\, d\theta , \tag{A1.6}$$

where the following well known relationship between acoustic pressure and velocity potential has been used,

$$p(R,\alpha,\theta',t) = \rho_o \frac{\partial \phi(R,\alpha,\theta',t)}{\partial t} . \tag{A1.7}$$

Using the procedures outlined by McLachlan (1941), and the following Bessel Function identity,

$$\exp[iz \cos(\theta' - \theta)] = J_o(z) + 2 \sum_{n=1}^{\infty} i^n J_n(z) \cos[m(\theta' - \theta)] , \tag{A1.8}$$

the integral with respect to θ in equation (A1.6) may be evaluated and written as,

$$\int_0^{2\pi} \Theta_m(\theta) \exp[ikau \sin\alpha \cos(\theta' - \theta)]\, d\theta = 2\pi i^m \Theta_m(\theta') J_m(kau \sin\alpha) . \tag{A1.9}$$

Using equation (A1.9), equation (A1.6) may be written as,

$$p(R,\alpha,\theta',t) = -i^m \rho_o \omega^2 a^3 D_{mj} \Theta_m(\theta') \exp[\,i(\omega t - kR)\,]\,\Delta/R, \tag{A1.10}$$

where,

$$\Delta = \int_o^1 H_{mj}(u)\, J_m(kau \sin\alpha)\, u\, du\,. \tag{A1.11}$$

If Classical Theory is used to describe the plate vibrations then equation (2.4) may be used to define $H_{mj}(u)$ in equation (A1.11). If Mindlin-Timoshenko Plate Theory is used then $H_{mj}(u)$ is replaced by $H_{tmj}(u)$ which is defined by equation (2.42). The use of known Bessel Function relations (McLachlan, 1941) allows the integration of equation (A1.11)in either case. The results of the integration considering the various possibilities are summarized in table A1.1. The terms used are also summarized in the table.

According to equation (A1.10)the modulus of the pressure amplitude may be expressed as,

$$|\,p_{mj}(R,\alpha,\theta')\,| = \rho_o \omega^2 a^3 \Theta_m(\theta')\, D_{mj}\, \Delta/R. \tag{A1.12}$$

As illustrated by Wallace (1972) for rectangular plates, the acoustic power radiated into the far field may be obtained by integrating the acoustic intensity over a hemispherical surface located in the far field. The acoustic intensity may be written in terms of the modulus of the pressure amplitude of equation (A1.12). Thus the real part of the acoustic power radiated by the plate vibrating in mode (m,j) is given by the following integral,

$$W_{mj} = \int_o^{2\pi} \int_o^{\pi/2} \frac{|\,p_{mj}(R,\alpha,\theta')\,|^2}{2\rho_o c_o} R^2 \sin\alpha\, d\alpha\, d\theta'. \tag{A1.13}$$

Substitution of equation (A1.12)into (A1.13) and integrating gives for the

Table A1.1: Summary of Integration of Equation (A1.11)

Expressions for Δ

	$x \neq z$ $y \neq z$	$x = z$ $y \neq z$	$x \neq z$ $y = z$	$x = z$ $y = z$
Mindlin-Timoshenko Plate Theory $x = \delta_{1mj}a$; $y = \delta_{2mj}a$; $z = ka.\sin\alpha$.				
$ka < (k_T c_s/\bar{\gamma} c_o)$	F_1-F_2	F_3-F_2	F_1-F_2	F_3-F_2
$ka \geqslant (k_T c_s/\bar{\gamma} c_o)$	F_1-F_4	F_3-F_4	F_1-F_5	F_3-F_5
Classical Plate Theory $x = y = \pi\beta_{mj}$ $z = ka.\sin\alpha$	F_1-F_2	-	-	F_3-F_2

$$F_1 = [x J_m(z) J_{m+1}(x) - z J_m(x) J_{m+1}(z)] / [x^2 - z^2]$$

$$F_2 = [J_m(x)][y J_m(z) I_{m+1}(y) + z I_m(y) J_{m+1}(z)] / [I_m(y)(y^2 + z^2)]$$

$$F_3 = 0.5[J_m^2(x) - (2m/x) J_m(x) J_{m+1}(x) + J_{m+1)}^2(x)]$$

$$F_4 = [J_m(x)][yJ_m(z) J_{m+1}(y) - z J_m(y) J_{m+1}(z)] / [J_m(y)(y^2 - z^2)]$$

$$F_5 = 0.5[J_m^2(y) - (2m/y) J_m(y) J_{m+1}(y) + J_{m+1}^2(y)][J_m(x)/J_m(y)]$$

power radiated,

$$W_{mj} = (\rho_0 \omega^4 a^6 D_{mj}^2 \pi / c_0 \epsilon_m) \int_0^{\pi/2} \Delta^2 \sin \alpha \, d\alpha. \qquad (A1.14)$$

Substitution of equations (A1.14) and either (2.16b), (2.16c) or (2.48) into equation (1.1) gives the following expression for the radiation efficiency,

$$\sigma_{mj} = [(ka)^2 / F_{mj}] \int_0^{\pi/2} \Delta^2 \sin \alpha \, d\alpha \, . \qquad (A1.15)$$

If Classical plate theory is used to describe the plate vibrations then

$$F_{mj} = J_m^2(\pi \beta_{mj}) \qquad (A1.16)$$

for clamped edge plates and

$$F_{mj} = J_m^2(\pi \beta_{mj}) P_{mj} \qquad (A1.17)$$

for simply supported edge plates.

If M-T Plate Theory is used then

$$F_{mj} = g_{mj} \, . \, [\text{Equation (2.49) or (2.50)}] \qquad (A1.18)$$

The integral in equation (A1.15) was evaluated numerically and values of σ_{mj} were calculated for the first seven low order vibration modes for ka values in the range of 0.1 to 40. The results were calculated and plotted using the CDC 6400 computer and are shown in Fig. 2.5.

APPENDIX 2

DESCRIPTION OF MICROPHONE TRAVERSE USED FOR THE EXPERIMENTS DESCRIBED IN CHAPTER 7

The purpose of this section is to describe the mechanics involved in starting the impedance tube microphone traverse in the correct position and at the same time as the data system begins to acquire data. For the following discussion reference should be made to the block diagrams shown in Figs. 8.3a to d.

Referring to Figs. 8.3a to d, the data system ignores all start pulses from the diffuser interruption of the laser beam until the acquire and/or the write button is depressed. If it is required to write the data on to magnetic tape immediately when the data system memory has been filled, both the acquire and write buttons must be depressed at the same time. The data system then begins to sample when the laser beam is next interrupted by the diffuser.

The automatic traverse start was designed so that it is immune to start pulses until the write button on the data acquisition system is depressed. When the write button is depressed, the traverse will start on the next start pulse from the laser beam interruption, at the same time as the data system begins to sample. The traverse control circuit is immune to further start pulses until the write button on the data system is again depressed. Depressing the write button this second time completes the acquisition of data and stops the microphone traverse. The traverse is then manually returned to a point in front of the start point. A switch on the traverse motor control then allows the traverse to be driven exactly on to the start point without requiring the data system to be activated. This eliminates any problems with backlash in the traverse drive gears. The system is then ready to repeat the cycle just described.

For measurements using the small tube the microphone is placed

at its start position in the tube (at the plane of the tube mouth) by correctly positioning the microphone carriage which is external to the tube. In the case of the large tube all the traverse gear is located in the tube and the correct positioning of the microphone at the start of the traverse is achieved using a microswitch attached to a light emitting diode as illustrated in Fig. 8.3a. These two methods enable the positional accuracy of the microphone traverse start position to be better than ¼ mm.

When a condenser microphone is used to sample the acoustic pressure in the impedance tube, allowance has to be made for the fact that the actual sampling cross-sectional plane is some distance in front of the microphone diaphragm. This distance was found by experimenting with the microphone in a tube terminated with a rigid end and observing the positions of the first two minimum sound pressure levels. The required correction was taken as equal to the difference between the measured position of the minimum closest to the rigid termination and an estimate of one quarter wavelength at the frequency tested. The quarter wavelength was estimated based on the measured temperature and checked by comparison with the measured half wavelength between the two measured minima. For all of the test frequencies (between 100Hz and 2000Hz) the distance between the sampling plane and the diaphragm of the half inch microphone was found to be 4.5 mm ± 0.5 mm. Similar tests on a quarter inch condenser microphone showed this distance to be 3 mm ± 1 mm at all frequencies tested (between 200Hz and 1200Hz).

When the microphone probe was used instead of the condenser microphone, this problem was eliminated by closing off the end of the probe and using two small holes in the side of the probe to sample the acoustic pressure, thus ensuring that the sampling plane was the same as the plane containing the two holes.

APPENDIX 3

CALCULATION OF THE ERROR IN ESTIMATING THE INSTANTANEOUS rms VALUE OF A TIME VARYING SINUSOIDAL SIGNAL FROM A MEASUREMENT OF ITS PEAK VALUE

The rms value of a sinusoidal signal of constant amplitude is related to the peak value as follows

$$p_{rms} = p_{peak}/\sqrt{2} \qquad \text{(A3.1)}$$

If the sinusoidal signal varies in amplitude with time the right hand side of equation (A3.1) will not be a true estimate of the rms value. The error will be dependent on the rate and amount of amplitude variation of the sinusoidal signal.

The error involved in using equation (A3.1) to estimate the rms value of one cycle of a time varying sinusoidal signal may be estimated as follows. As a first approximation let us postulate that the amplitude of the sinusoidal signal is increasing such that the amplitude after one cycle is (1+a) times what it was at the beginning of that cycle. The mean square value of such a signal having unit amplitude to begin with is given by,

$$p_{rms}^2 = \frac{1}{2\pi}\int_0^{2\pi} \left\{(1+ax/2\pi)\ \sin x\right\}^2 dx \qquad \text{(A3.2)}$$

Expanding and integrating gives,

$$p_{rms}^2 = \tfrac{1}{2} + a/2 + a^2/6 \qquad \text{(A3.3)}$$

If the amplitude were constant the mean square value would be

$$p_{rms}^2 = \tfrac{1}{2}$$

The error involved in using a single peak measurement is the difference in the two estimates of the mean square value;

that is,

$$E = a/2 + a^2/6 \qquad \text{(A3.4)}$$

where E is the mean square error.

Thus for a time varying pressure signal, the error in sound pressure level would be

$$E_L = 10 \log_{10} \{a + a^2/3 + 1\} \text{ dB.} \qquad \text{(A3.5)}$$

For the experiments described in chapter 7 the largest error corresponded to a diffuser speed of 50 RPM. Values of a were measured for successive samples in each set of data recorded as described in chapter 7. The maximum value of a for each data set was then chosen for the error calculations. This maximum value of a varied from 0.003 to 0.02 and was a function of the position of the microphone in the impedance tube at the time a particular data set was chosen. The largest measured value of a was 0.02 and this value is used in the following error calculations.

Substituting for a=0.02 in equation (A3.5) gives

$$E_L = 10 \text{ Log}_{10} [0.02 + 0.00007 + 1] = 0.09 \text{ dB.}$$

It should be remembered that this is an upper bound estimate and in most cases the error was considerably less than this.

It is interesting to estimate the variation in signal amplitude corresponding to a = 0.02, in terms of dB per signal wavelength of translation of the diffuser rim. For a diffuser rotational speed of Ω revolutions per second the number of signal cycles in a translation of the outer rim of the diffuser of one wavelength of sound at the signal frequency is given by

$$N_c = c_o/\pi D\Omega \qquad \text{(A3.6)}$$

where D is the diffuser diameter (= 3.5m)

c_o = speed of sound in air (m/sec)

At diffuser speed of 50 RPM, N_c = 37 cycles.

For a value of a = 0.02, the signal variation is 0.17dB/cycle. Thus for a

diffuser speed of 50 RPM the signal variation is 6.4dB/wavelength of translation of the diffuser rim.

REFERENCES

ALPER, S. (1970 — Radiation from the forced harmonic vibrations of a clamped circular plate in an acoustic fluid. Ph.D. Thesis, Graduate School of Engineering and Architecture, Catholic University of America.

ALPER, S. & MAGRAB, E. (1970) — Radiation from the forced harmonic vibrations of a clamped circular plate in an acoustic fluid. J. Acoust. Soc. Am. 48, 681-691.

A.N.S.I. STANDARD S1.21 (1972) — Methods for the determination of sound power levels of small sources in reverberation rooms. American National Standards Institute, New York.

ARCHBOLD, E. & ENNOS, A. (1968) — Observation of surface vibration modes by stroboscopic hologram interferometry. Nature, 217, 942-943.

BERANEK, L. (1949a) — Acoustic measurements. (John Wiley and Sons, New York) p. 48.

BERANEK, L. (1949b) — Ibid, Chap. 7, pp. 317-324.

BERANEK, L. (1971a) — Noise and vibration control (McGraw Hill, New York) pp. 146-150.

BERANEK, L. (1971b) — Ibid, pp. 290-294.

BIES, D. (1974) — The investigation of the used of holography for the study of vibrating and acoustically radiating surfaces. Noise Shock and Vibration Conference, Monash University, Australia.

BIES, D. (1976) — Uses of anechoic and reverberant rooms. Noise Control Engineering, 7, 154-163.

BIES, D. & HANSEN, C. (1976) — Impedance tube calibration of a reverberant room for the measurement of sound power in tones. J. Acoust. Soc. Am. 59, 1393-1398.

BIES, D. (1978) — Private communication.

BIES, D. & DAVIES, J. (1977) — Investigation of the measurement of transmission loss, J. Sound and Vibration, 53, 203-222.

BRITO, J. (1977) — Sound intensity patterns for vibrating surfaces. 9th International Congress on Acoustics, Madrid, 1, 317.

BRITO, J. & LYON, R. (1976) — Sound intensity patterns for vibrating plates. Acoustical Society of America, 92nd Meeting.

BROWN, G., GRANT, R. & STROKE, G. (1969) — Theory of holographic interferometry. J. Acoust. Soc. Am. 45, 1166-1179.

BROWN, G. (1975) — Institution of Engineers, South Australian Design Award 1975. Department of Mechanical Engineering, University of Adelaide.

BUTUSOV, M. (1974) — Time-averaged holographic vibrometry; features of interference pattern recording. Optics and Spectroscopy 37, 301-303.

CHAN, C. & ANDERTON, D. (1974) — Correlation between engine block surface vibration and radiated noise of in-line diesel engines. Noise Control Engineering, 2, 16-24.

CREMER, L., HECKL, M., & UNGAR, E. (1973a) — Structure borne sound. (Springer Verlag, Berlin.) Chap. 4, p.201.

CREMER, L. et al (1973b) — Ibid, Chap. 1, pp. 5-7.

DE VRIES, D. (1977) — On the sound power radiated by a velocity monopole under reverberant and under free field conditions. 9th International Congress on Acoustics, 1, 127.

DODD, S. & DOAK, P. (1971) — Some aspects of the theory of diffusion and diffusers. J. Sound and Vibration 16, 89-98.

EBBING, C. (1971) — Experimental evaluation of moving sound diffusers for reverberant rooms. J. Sound and Vibration 16, 99-118.

EBBING, C. & MALING, G. (1973) — Reverberation room qualification for determination of sound power of sources of discrete frequency sound. J. Acoust. Soc. Am. 54, 935-949.

EVENSEN, D. & APRAHAMIAN, R. (1970) — Application of holography to vibrations, transient response and wave propagation. N.A.S.A. - C.R. - 1671.

FAGAN, W., WADDELL, P., & McCRACKEN, W. (1972) The study of vibration patterns using real-time hologram interferometry. Optics and Laser Technology, 4, 167-172.

FAHY, F. (1977) Noise Control Engineering, 9, 155-162. A technique for measuring sound intensity with a sound level meter.

FAHY, F. (1978) Measurements with an intensity meter of the acoustic power of a small machine in a room. J. of Sound and Vibration, 3, 311-322.

FLAMMER, C. (1957) Oblate spheroidal wave functions. (Stanford University Press: Stanford, California.) Chap. 1-4.

FRYER, P.A. (1970) Vibration analysis by holography. Rep. Prog. Phys. 33, 489-531.

GRAHAM, T. (1969) Long wavelength acoustic holography. Ph.D. Thesis, The Pennsylvania State University.

GROVER, E. & LALER, N. (1973) Low noise engine design at I.S.V.R. J. Sound Vib. 28, 403-431.

HANSEN, C. & BIES, D. (1976) Optical holography for the study of sound radiation from vibrating surfaces. J. Acoust. Soc. Am., 60, 543-555.

HANSEN, C. & BIES, D. (1979) Near field determination of the complex radiation efficiency and acoustic intensity distribution for a resonantly vibrating surface. J. Sound Vib., 62, 93-110.

HANSEN, C. (1979a) Computation of oblate spheroidal wave functions. Department of Mechanical Engineering, University of Adelaide, report TN 1/79.

HANSEN, C. (1979b) Notes on Holography, Department of Mechanical Engineering, University of Adelaide, report TN 2/79.

HANSEN, C. & BIES, D. (1979c) Conical horn analysis - Preliminary Report, Department of Mechanical Engineering, University of Adelaide, report Tn 3/79.

HANSEN, C. (1979d) — On the accuracy of simple source theory for the prediction of surface radiation efficiencies. Department of Mechanical Engineering, University of Adelaide, report TN 4/79.

HANSEN, C. & BIES, D. (1979e) — Near field determination of the complex radiation efficiency and acoustic intensity distribution for a resonantly vibrating surface. Department of Mechanical Engineering, University of Adelaide, report TN 5/79.

JAMES, R. (1976) — An investigation into the use of holography for the study of sound radiation from vibrating surfaces. M.E. Thesis, Dept. Mechanical Eng. University of Adelaide.

JUNGER, M. & FEIT, D. (1972) — Sound, structures & their interaction. (M.I.T. Press: Cambridge, Massachusetts) pp.73-80.

KHANNA, S., TONNDORF, J. & JANECKA, I. (1973) — Vibration patterns examined by real time and time-averaged holography. J. Acoust. Soc. Am., 54, 1686-1693.

KINSLER, L. & FREY, A. (1962) — Fundamentals of acoustics. (John Wiley and Sons: New York) pp.173-176.

LA FARA, R. (1973) — Computer methods for science and engineering. (Hayden Book Co.: Rochelle Park, New Jersey) pp.148-156.

LAX, M. (1944) — The effect of radiation on the vibrations of a circular diaphragm. J. Acoust. Soc. Am., 16, 5-13.

LIEM, S., HAZELL, C. & BLASKO, J. (1973) — Vibrational analysis of circular cylinders by holographic interferometry. J. Sound and Vibration 29, 475-481.

LEISSA, A. (1969) — Vibrations of plates. NASA SP-160.

LEVINE H. & SCHWINGER, J. (1948) — On the radiation of sound from an unflanged circular pipe. Physics Review, 73- 383-406.

LUBMAN, D. (1969) — Fluctuations of sound with position in a reverberant room. J. Acoust. Soc. Am. 44, 1491-1502.

LUBMAN, D. (1971) — Spatial averaging in sound power measurements. J. Sound and Vibration, 16, 43-58.

LUBMAN, D. (1974) Precision of reverberant sound power measurements. J. Acoust. Soc. Am. 56, 523-533.

LYON, R. (1975) Statistical energy analysis of dynamical systems: theory and applications. (M.I.T. Press: Cambridge, Massachusetts.)

McLACHLAN, N.W. (1941) Bessel functions for engineers. (Oxford University Press: London.)

MACADAM, J.A. (1976) The measurement of sound radiation from room surfaces in lightweight buildings. App. Acoustics, 9, 103-118.

MAIDANIK, G. (1962) Response of ribbed panels to reverberant acoustic fields. J. Acoust. Soc. Am., 34, 809-826.

MALING, G. (1967) Calculation of the acoustic power radiated by a monopole in a reverberation chamber. J. Acoust. Soc. Am., 42, 859-865.

MALING, G. & NORDBY, K. (1967) Reverberation chamber determination of the acoustic power of pure tone sources. I.B.M. J.of Research and Development 11, 492-501.

MALING, G. (1973) Guidelines for the determination of the average sound power radiated by discrete frequency sources in a reverberation room. J. Acoust. Soc. Am. 53, 1064-1069.

MINDLIN, R. (1951) Influence of rotatory inertia and shear on the flexural motions of isotropic, elastic plates. A.S.M.E. J.of Applied Mechanics, 18, 31-38.

MINDLIN, R. & DERESIEWICZ (1954) Thickness-shear and flexural vibrations of a circular disc. J. Applied Physics, 25, 1329-1332.

MONAHAN, M. & BROMLEY, K. (1968) Vibration analysis by holographic interferometry. J. Acoust. Soc. Am. 44, 1225-1231.

MOON, P. & SPENCER, D. (1961) Field theory handbook. (Springer-Verlag: Berlin) pp.31-32.

MORSE, P. (1948) Vibration and sound. (McGraw-Hill Inc.: New York) 2nd ed., Chap. 6, pp.265-288.

MORSE, P. & INGARD, K. (1968a) Theoretical acoustics (McGraw-Hill Inc.: New York) Chap. 5.3.

MORSE, P. & INGARD, K. (1968b) Ibid, Chap. 7, pp.315-317.

OCHS, J. & SNOWDON, J. (1975) Transmissibility across simply supported thin plates, 1. Rectangular and square plates with and without damping layers. J. Acoust. Soc. Am., 58, 832-840.

POWELL, R. & STETSON, K. (1965) Interferometric vibrational analysis by wavefront reconstruction. J. Opt. Soc. Am., 55, 1593-1598.

PRASAD, M., PATTABIRAMAN, J. & RAO, B. (1975) On acoustic near field measurements, J. Sound and Vibration, 40, 415-423.

LORD RAYLEIGH (1878a) Theory of sound Vol. I. (Macmillan and Co.: London) Chap.10.

LORD RAYLEIGH (1878b) Ibid, p.258.

LORD RAYLEIGH (1878c) Theory of sound Vol. II. (Macmillan and Co: London) Chap. 14, p.95.

LORD RAYLEIGH (1879) Investigations in Optics with special reference to the spectroscope. Philosophical Magazine, series 5, 8, 261-274.

ROPPER, A. (1974) Effect of the forcing function on the vibratory modes of a circular membrane. J. Acoust. Soc. Am., 56, 673-676.

SABINE, W. (1972) Collected paper on acoustics. (Harvard University Press: Harvard. 3rd Ed.) p.247.

SCHARTON, T. (1967) Techniques for improving the low frequency performance of small reverberation chambers. Bolt, Beranek and Newman, Inc., report prepared under contract number N.A.S. 5-21003 for N.A.S.A.

SCHROEDER, M. (1962) Frequency correlation functions of frequency responses in rooms. J. Acoust. Soc. Am. 34, 1819-1823.

SCHULZ, T. (1971) Diffusion in reverberant rooms. J. Sound and Vibration, 16, 17-18.

SHAJENKO, P. & JOHNSON, C. (1968) Stroboscopic holographic interferometry. Applied Physics Letters 13, 44-45.

SMITH, W. BAILEY, J. (1973) Experimental investigation of the statistics of sound power radiation in a reverberant room. J. Acoust. Soc. Am. 54, 950-955.

STETSON, K. & TAYLOR, P. (1971) The use of normal mode theory in vibration analysis with application to an asymmetrical circular disc. J. Physics E., Scientific Instruments 4, 1009-1015.

TICHY, J. (1974) Effect of rotating diffusers and sampling techniques in sound-pressure averaging in reverberation rooms. J. Acoust. Soc. Am., 56, 137-143.

TICHY, J. (1977) Recent developments in sound power measurements in reverberation rooms. 9th International Congress on Acoustics, Madrid, 1, 188 .

TIMOSHENKO, S. (1921) On the correction for shear on the differential equation for transverse vibrations of prismatic bars. Philosophical Magazine, Series 6, 41, 744-746.

TONIN, R. & BIES, D. (1977) Time-averaged holography for the study of three dimensional vibrations. J. Sound and Vibration, 52, 315-323.

TONIN, R. (1978) Time-averaged holography for the study of three-dimensional vibrations. Ph.D. Thesis, Dept. of Mech. Eng., University of Adelaide.

TUSCHAK, P. & ALLAIRE, R. (1975) Axisymmetric vibrations of a cylindrical resonator measured by holographic interferometry. Exp. Mech., 15, 81-88.

UEHA, S., FUJINAMI, M., UMEZAWA, K. & TSUJIUCHI, J. (1975) Mapping of noise-like sound sources with acoustical holography. Applied Optics 14, 1478-1479.

VIKRAM, C. (1972) A triple-exposure technique to reduce recording time in stroboscopic holographic interferometry. Optics Communications, 6, 295-296.

WALLACE, C. (1972) Radiation resistance of a rectangular panel. J. Acoust. Soc. Am., 51, 946-952.

WATERHOUSE, R. (1968) Statistical properties of reverberant sound fields. J. Acoust. Soc. Am. 43, 1436-1444.

WATERHOUSE, R. (1971) Power output of a point single source exciting a single cartesian mode. J. Acoust. Soc. Am., 49, 9-16.

WATERHOUSE, R. (1973) Noise measurement in reverberant rooms. J. Acoust. Soc. Am., 54, 931-934.

WATERHOUSE, R. (1977) Estimates of monopole power radiated in a reverberation chamber. 9th International Congress on Acoustics, Madrid, 1, 191.

WATERHOUSE, R. (1978) Private communication.

WATRASIEWICZ, B. & SPICER, P. (1968) Vibration analysis by stroboscopic holography. Nature 217, 1142-1143.

WATSON, E. (1971) Detection of sound radiation from plates using long wavelength acoustical holography. Ph.D. Thesis, The Pennsylvania State University.

WATSON, E. (1973) Detection of acoustic sources using long wavelength acoustical holography. J. Acoust. Soc. Am., 54, 685-691.

WATSON, E. & HANNON, R. (1974) Sound radiation from a circular steel plate driven on the edge. J. Acoust. Soc. Am. 56, 683-685.

WATSON, E. & KING, W. (1976) On the use of acoustical holography to locate sound sources in complex structures. J. Sound and Vibration, 48, 157-168.

WILSON, A. & STROPE, D. (1970) Time-average holographic interferometry of a circular plate vibrating simultaneously in two rationally related modes. J. Opt. Soc. Am., 60, 1162-1165.

ZAIDEL, A. (1969) Holographic strobe method for studying vibrations. Soviet Physics - Technical Physics, 13, 1470-1473.